INFLUENCE OF DEFORMABLE GEOFOAM BUFFERS ON THE STATIC AND DYNAMIC BEHAVIORS OF CANTILEVER RETAINING WALLS

A THESIS SUBMITTED TO
THE GRADUATE SCHOOL OF NATURAL AND APPLIED SCIENCES
OF
MIDDLE EAST TECHNICAL UNIVERSITY

BY

ÖZGÜR LÜTFİ ERTUĞRUL

IN PARTIAL FULFILLMENT OF THE REQUIREMENTS
FOR
THE DEGREE OF DOCTOR OF PHILOSOPHY
IN
CIVIL ENGINEERING

SEPTEMBER, 2011

Approval of the thesis:

INFLUENCE OF DEFORMABLE GEOFOAM BUFFERS ON THE STATIC AND DYNAMIC BEHAVIORS OF CANTILEVER EARTH RETAINING WALLS

submitted by **ÖZGÜR LÜTFİ ERTUĞRUL** in partial fulfillment of the requirements for the degree of **Doctor of Philosophy in Civil Engineering Department, Middle East Technical University** by,

Prof. Dr. Canan ÖZGEN _____
Dean, Graduate School of **Natural and Applied Sciences**

Prof. Dr. Güney ÖZCEBE _____
Head of Department, **Civil Engineering**

Prof. Dr. M. Yener ÖZKAN _____
Supervisor, **Civil Engineering Dept., METU**

Examining Committee Members:

Prof. Dr. Erdal ÇOKÇA _____
Civil Engineering Dept., METU

Prof. Dr. M. Yener ÖZKAN _____
Civil Engineering Dept., METU

Prof. Dr. Celal KARPUZ _____
Mining Engineering Dept., METU

Prof. Dr. K. Önder ÇETİN _____
Civil Engineering Dept., METU

Assoc. Prof. Dr. S.Oğuzhan AKBAŞ _____
Civil Engineering Dept., Gazi University

Date: **19/09/2011**

I hereby declare that all information in this document has been obtained and presented in accordance with academic rules and ethical conduct. I also declare that, as required by these rules and conduct, I have fully cited and referenced all material and results that are not original to this work.

Name, Last name : Özgür Lütfi ERTUĞRUL

Signature :

ABSTRACT

INFLUENCE OF DEFORMABLE GEOFOAM BUFERS ON THE STATIC AND DYNAMIC BEHAVIORS OF CANTILEVER RETAINING WALLS

ERTUĞRUL, Özgür Lütfi

Ph.D., Department of Civil Engineering

Supervisor: Prof. Dr. M.Yener ÖZKAN

September 2011, 281 pages

Static and dynamic interaction mechanism of the retained soil-compressible geofoam buffer and yielding retaining structures requires further investigation. The present study, initiated on this motive, discusses the results of 1-g physical model tests and numerical analyses of cantilever retaining walls with and without deformable geofoam buffers between the wall and cohesionless granular backfill. 0.7m high walls with various wall thicknesses were utilized in the physical modeling. Dynamic tests were carried out by using a laminar container placed on a uni-axial shaking table.

Influence of buffer thickness, geofoam type and wall flexibility as well as base excitation characteristics on the lateral earth pressures and flexural wall deflections were under concern. Outcomes of the analyses performed with FLAC-2D (v6.0) finite difference code were validated against the results of the physical model tests. It was observed that the arching effect induced in the retained soil by the lateral compression of the lower half of the geofoam buffer has a positive effect, as this zone is able to absorb a portion of the total unbalanced lateral force exerted by the backfill thus causing a reduction in the static and seismic lateral wall pressures.

Relative thickness and stiffness of the geofoam buffer appear to be the most dominant factors affecting the reduction in earth thrust. Lateral earth pressure coefficients determined from physical model tests were compared with those calculated using methods available in the literature. Good agreement was observed between the predictions. Graphs were provided to estimate the static and dynamic lateral earth pressure coefficients for various combinations of wall stiffness and buffer characteristics.

Analysis of a 6m high prototype cantilever wall subjected to an excitation recorded in August 17, 1999 Kocaeli earthquake by finite difference method exhibited the contribution of geofoam buffers on seismic performance of cantilever earth retaining walls. It was observed that the presence of an EPS geofoam inclusion provides a reduction of the permanent flexural wall deflections as well as total seismic thrust likely to be experienced by the wall during an earthquake.

Keywords: Geofoam buffer, 1-g physical model test, shaking table, cantilever retaining wall, numerical modeling

ÖZ

DEFORME OLABİLEN GEOFOAM ARA KATMANI KULLANIMININ ANKASTRE İSTİNAT DUVARLARININ STATİK VE DİNAMİK DAVRANIŞLARI ÜZERİNDEKİ ETKiLERİ

Ertuğrul, Özgür Lütfi

Doktora, İnşaat Mühendisliği Bölümü

Tez Yöneticisi : Prof. Dr. M. Yener ÖZKAN

Eylül 2011, 281 sayfa

İksa edilen zemin, deforme olabilen geofoam tabakası ve esnek istinat duvarları arasında oluşan statik ve dinamik etkileşim mekanizmasının belirlenmesi için yeni araştırmalar gereklidir. Bu çalışmada, bahsedilen amaç doğrultusunda, duvar gövdesi ile kohezyonsuz granüler dolgu arasında geofoam katmanı bulunan veya bulunmayan ankastre istinat duvarı modelleri ile yapılan küçük ölçekli deneysel ve nümerik modelleme çalışmalarının sonuçları tartışılmaktadır. Fiziksel modellemede, 0.7m yüksekliğinde ve farklı kalınlıklara haiz olan duvarlar kullanılmaktadır. Dinamik deneyler, tek eksenli sarsma tablası üzerinde yeralan bir laminer kutuda gerçekleştirilmiştir.

Geofoam tabaka cinsi ve kalınlığı, duvar esnekliği ve dinamik yer hareketi özelliklerinin, yanal zemin basınçları ve duvar sehimleri üzerindeki etkileri incelenmektedir. Bir sonlu farklar metodu yazılımı olan FLAC-2D (v6.0) programı ile elde edilen bulgular, deneysel çalışmanın sonuçları ile doğrulanmaktadır. Duvar ile kohezyonsuz zemin arasında yer alan geofoam tabakasının sıkışması neticesinde, iksa edilen zeminin özellikle alt yarısında yoğunlaşan yatay zemin hareketleri, kemerlenme etkisi oluşturmaktadır. Bu etki, kohezyonsuz dolgu tarafından uygulanan dengelenmemiş kuvvetlerin bir kısmını absorbe ederek statik ve dinamik yanal basınçların azaltılmasında olumlu etki gösterebilmektedir.

Kullanılan geofoam katmanının rölatif kalınlığı ve esnekliği, yanal zemin itkisinin azaltılması hususunda en önemli etkiye sahiptir. Model deneyler neticesinde elde edilen yanal zemin basıncı katsayılarının, literatürde yeralan metotlar ile elde edilen sonuçlarla karşılaştırıldığında oldukça tutarlı olduğu gözlenmektedir. Duvar esnekliği ve geofoam katman özelliklerinin çeşitli kombinasyonları için, statik ve dinamik yanal basınç katsayılarının tahmini amacıyla grafikler sunulmaktadır.

6m yüksekliğindeki bir prototip ankastre istinat duvarının 17 Ağustos 1999 depreminde kaydedilen bir yer hareketine maruz kalması durumu için oluşturulan sonlu farklar modeli ile yapılan analizler, duvar ile kohezyonsuz dolgu arasında yeralan geofoam ara katmanının, istinat yapısının sismik performansına katkısını ortaya koymaktadır. Kullanılan EPS geofoam tabakasının, deprem anında duvarın maruz kalacağı toplam sismik itkide ve kalıcı duvar sehimlerinde düşüş sağlayabildiği gözlenmiştir.

Anahtar Kelimeler: Geofoam ara katmanı, 1-g fiziksel model deney, sarsma tablası, ankastre istinat duvarı, numerik modelleme

ACKNOWLEDGMENTS

I wish to express my gratitude to my supervisor Prof. Dr. M.Yener Özkan for his guidance, encouragement and valuable insight throughout the research. His wise attitude enlightened me in all stages of my graduate studies.

I highly benefited from the studies conducted under Dr. Aurelian Trandafir's supervision during my residence in U.S. and would like to express my sincere thanks to Dr. Trandafir for providing his valuable comments and suggestions as well as the numerical modeling software used in this Ph.D. thesis study.

Finally, I would like to express the most grateful thanks to my wife and family, for their continuous patience and support.

TABLE OF CONTENTS

LIST OF TABLES

TABLES

LIST OF FIGURES

FIGURES

LIST OF SYMBOLS

P_{AE}	Active dynamic earth thrust
δ	the angle between the normal to the wall and direction of P_{AE}
θ	the angle between the wall stem and the vertical axis
$\bar{d}_{perm}$	Mean value of permissible displacement according to method of Whitman and Liao (1985)
a_y	Yield acceleration according to method of Whitman and Liao (1985)
ΔK_{AE}	Dynamic earth pressure coefficient
EPS	Expanded polystyrene
XPS	Extruded polystyrene
e_{max}	Maximum void ratio
e_{min}	Minimum void ratio
t	Deformable buffer thickness
H	Wall height
t_{ci}	Minimum Required deformable buffer thickness according to analytical method of Partos and Kazaniwsky (1987)
E_{ci}	Young's modulus of the geofoam
Δ_a	amount of deformation necessary to mobilize the active stress conditions in the retained soil
K_a	coefficient of active earth pressure
δ	interface friction angle between the geofoam and soil
γ_t	total unit weight of the retained soil
t_{cie}	Minimum required deformable buffer thickness for seismic loading
R_θ	linear rotational spring constant
M_{ci}	resisting moment per unit length of the wall according to Horvath (1997)
d_θ	Relative soil-wall stiffness according to Veletsos and Younan (1994b)
G_s	shear modulus of the retained soil
ϑ_s	Poisson's ratio
E_s	Young's modulus of the soil retained
k_{N_i}	Normal stiffness according to the method of Bathurst et al. (2007b)

k_{S_i}	Shear stiffness according to the method of Bathurst et al. (2007b)
β	mass damping factor
$\dot{u}_1$	Velocity in horizontal direction
$\dot{u}_2$	Velocity in the vertical direction
OI	Oxygen index of geofoam
E_i, E_p	Initial stiffness, plastic stiffness of geofoam according to Koerner (2005)
K_o	Coefficient of lateral pressure at rest
E_{ti}	the initial tangent modulus of geofoam in MPa
μ, ϑ	Poisson's ratio of EPS geofoam
s	Strain rate applied in triaxial tests in mm/min (Ossa and Romo, 2009)
σ_3	Confining stress
σ_y	Yield stress of geofoam in kPa
G_0	Small strain shear modulus of geofoam
γ_C	cyclic shear strain (%)
D_0	initial damping ratio
$(\sigma_a-\sigma_r)_{static}$	initial static deviator stress
σ_a	Major principal stress
σ_r	Minor principal stress
SSR	static stress ratio $((\sigma_a-\sigma_r)_{static}/(\sigma_a-\sigma_r)_{yield})$
CDSR	Cyclic deviator stress ratio $(\Delta(\sigma_a-\sigma_r)_{cyclic}/(\sigma_a-\sigma_r)_{static}).\ (\sigma_a-\sigma_r)_{yield}$
λ	Damping ratio
i_p	The isolation efficiency of the buffer in terms of total lateral force
P_o	lateral wall thrust in absence of compressible inclusion
P	reduced thrust due to the presence of the compressible layer
d_w	Relative wall flexibility
P_{static}	Static lateral thrust (in kN/m)
K_{exp}	lateral earth pressure coefficients back calculated from physical tests
φ	Internal friction angle of the backfill
K_a	coefficient of lateral active pressure (K_a) calculated by Rankine's theory
d_o	horizontal deflection of the wall top for the absence of geofoam buffer
d	horizontal deflection of the wall top for the presence of geofoam buffer
δ_h	Horizontal deflection at the wall top

β_j	Low pass filter coefficients
ω_b	Cut-off frequency
i_δ	The isolation efficiency in terms of dynamic lateral displacements
η	Amplification factor
f_1	The first fundamental frequency of an equivalent one-dimensional and linear elastic soil column
f_1^*	Fundamental frequency of the wall-backfill system
$i_{\Delta p}$	dynamic earth thrust reduction efficiency
$\Delta P_{w/o\ inc}$	dynamic increment of the wall thrust without geofoam buffer
$\Delta P_{w/inc}$	dynamic increment of the wall thrust with geofoam buffer
E_{inc}/t_{inc}	Relative stiffness of the buffer (Ratio of buffer elastic modulus to buffer thickness)
$(K_{ae})_{exp}$	seismic lateral earth pressure coefficients back calculated from tests
E_{50}	The static modulus corresponding to the 50% of the deviator stress at yield

CHAPTER 1

INTRODUCTION

1.1 General

The application of expanded polystyrene (EPS) geofoam as compressible inclusion has gained widespread popularity in geotechnical engineering. Early applications of EPS geofoam as compressible inclusions in geotechnical projects have been documented in Germany during 1970s. They were also used extensively in Holland and Japan to reduce stresses acting on buried pipelines due to consolidation settlements of soils as well as earthquake induced lateral stresses on retaining structures (Beinbrech and Hohwiller, 2000). According to Horvath (2008), the compressible inclusion function of geofoam is basically defined as placement of a low-stiffness material intentionally between two stiffer materials (i.e. retaining wall and the backfill) to provide reduction in the lateral forces on the earth-retaining walls. Geofoam buffers of low stiffness installed vertically against rigid non-yielding retaining structures provide lateral displacements in the backfill due to the low stiffness of the geofoam. According to the classical theories of lateral earth pressure, displacements in a retained soil mass mobilize a greater portion of the available shear strength of the material and reduce the unbalanced lateral forces acting on the retaining structure. Horvath (2008) indicated that lateral compression of the deformable geofoam buffers leads to soil arching which has an additional positive effect on the load reduction mechanism. Therefore, presence of a compressible inclusion behind a rigid non-yielding wall makes contribution to economical design of the wall by providing controlled yielding in the backfill material. Geofoam products made of EPS (expanded polystyrene) and XPS (extruded polystyrene) are considered as suitable materials for the deformable buffer function between the retaining walls

and the retained backfill since their physical properties may be adjusted easily to fulfill the required stress-strain behavior and material density. In addition to these, Horvath (1997) documented more than thirty years of proven durability of geofoam in several geotechnical applications.

Field experiments demonstrated the significant effect of compressible buffers in reducing the lateral earth pressures behind rigid non-yielding retaining walls (Partos and Kazaniwsky, 1987). Reduction of compaction induced lateral earth pressures on retaining walls by using geofoam like materials has also been demonstrated by Reeves and Filz (2000) using large scale physical tests. Ertugrul and Trandafir (2010) presented result of small scale model tests on 0.7m high cantilever retaining wall models with geofoam buffers of various thicknesses. Numerical analyses were performed using plane strain finite element models of the test setup. Results are validated against lateral stress data of small scale tests. The behavior of the retained soil mass and the compressible inclusion are reasonably well predicted using an elasto-plastic model for the soil and linear elastic formulation for the geofoam. Stress measurements and results of numerical analyses indicate significant reduction in earth thrust in the presence of compressible inclusions installed behind the wall.

Numerical sensitivity studies based on finite-element analysis addressing the static load reduction on rigid walls with geofoam buffers have been reported in the literature (Karpurapu and Bathurst, 1992; Trandafir et al. 2010a*).* Trandafir et al. (2010b) presented the results of a finite element modeling study discussing the reduction in horizontal earth pressures against a 9-m high rigid wall with a 0.6-m thick EPS buffer against the wall, retaining a cohesionless soil mass. In a recent study, Ertugrul and Trandafir (2011) proposed design charts based on their parametric study perfomed using a finite element code validated against the reduced scale physical model tests.

1.2 Motivation of the study

Retaining structures play an important role in the modern infrastructure such as transportation systems, energy plants, lifelines, and several other constructed facilities. Although these structures are prone to catastrophic failures during earthquakes due to excess dynamic earth pressures, design of retaining systems

against seismic loads does not take enough importance in many geotechnical projects.

In seismic design of retaining structures, traditional approaches generally provide limited predictions on soil movements and interactions between soil and structure. Seismic stabilities of these structures designed according to traditional approaches are generally questionable. On the other hand, appropriate design against the increased lateral seismic earth forces may result in significant increase in the construction costs. Hence, new innovative methods or design procedures are becoming a necessity for the static and seismic performance improvement of the retaining walls. In this context, seismic isolation of retaining structures by deformable buffers has evolved as an extension of the studies on reduction of static earth pressures (Athanasopoulos et al., 2007). Utilization of expanded polystyrene geofoam as seismic buffer for rigid non-yielding walls were proved to be beneficial since the retaining structure interacts with the backfill through a hybrid type of interaction mechanism occurring during the earthquake excitation (Hazarika et al., 2003). The compressibility of the geofoam material may provide absorption of a portion of the seismic thrust depending on the wall flexibility, buffer thickness, and stiffness. Based on these previous studies, the motivation of this research is basically the seismic performance improvement of the earth retaining structures including flexible and yielding cantilever earth retaining walls.

1.3 Scope of the Study

Static and dynamic interaction mechanisms of the retained soil-compressible geofoam buffer and retaining structures require further investigation. Use of numerical simulation techniques in conjunction with physical modeling may provide valuable insight towards a better understanding of this interaction mechanism. The outcomes of such a study may contribute to the better design of retaining walls with deformable geofoam buffers. The present study, initiated on this motive, discusses the results of physical model tests performed on various cantilever retaining wall models with and without geofoam compressible buffers. The influence of relative flexibility of the wall as well as the thickness and stiffness of the compressible buffer placed between the cohesionless backfill and the wall stem were investigated in this context. The static and dynamic characterization of the materials used in physical modeling study was made through extensive

laboratory testing. A series of numerical simulations were performed using the general finite difference method software FLAC 2D v6.0 (Itasca, 2008). The results of the numerical modeling study assist the planning of the physical test series and selection of the materials. The outcomes may also provide insight about the influence of parameters such as buffer stiffness and thickness on the static and dynamic response of retaining walls. The behavior of a real scale cantilever wall subjected to an earthquake excitation was briefly investigated using the finite difference code.

CHAPTER 2

PREVIOUS STUDIES ON THE SEISMIC RESPONSE OF RETAINING WALLS

2.1 General

Earth retaining structures, such as gravity retaining walls, bridge abutments, anchored bulkheads, cantilevered reinforced concrete walls, and mechanically stabilized earth walls are integral components of modern world infrastructure. They exist as key elements of harbors, transportation systems, power plants lifelines and several other constructed facilities having various levels of importance to the mankind. They have been widely used in seismically active areas and in many historic earthquakes, failure and excessive deformations of these structures were reported due to seismic forces. In some cases, failure of retaining walls triggered further catastrophic failures of other civil engineering structures.

2.2 Studies on the seismic earth pressures on retaining walls

Seismic behavior of retaining walls has been a field of interest since the beginning of 1900's. From that time different researchers, compiled damage data for the retaining walls in previous strong earthquakes. The damage characteristics vary according to the type of the retaining walls and magnitude of the earthquakes. Primarily permanent deformations and/or rotations occur in retaining walls after a strong shaking episode. In some cases, only small deformation occurs, in others collapse occurs with large physical and economic consequences. A brief summary on recorded damage data for a group of strong earthquakes is shown in Table 2-1.

Table 2-1 Retaining Wall Damage Due to Past Strong Earthquakes
(After Stadler, 1997)

Earthquake	Date	Magnitude.	Damage/Failure
Kitaizu, Japan	1930	7,1	Failure of gravity walls (approx. 26 ft of mvt)
Tonankai, Japan	1944	8,2	Sliding of retaining wall. Outward movement of bulkhead with relieving platform (10-13 ft. of mvt.).
Tokachioi, Japan	1952	7,8	Outward movement of gravity wall (approx. 18 ft. of mvt)
Chile	1960	8,5	Complete overturning of gravity walls (>15 ft of mvt.) Outward movement of anchored bulkheads
Alaska, USA	1964	8,4	Lateral displacement of bridge abutments. Spreading and settlement of abutment fills.
Niigata, Japan	1964	7,5	Complete failure of 4.4 miles of earth retaining waterfront structures (sheet pile and gravity walls)
San Fernando, USA	1971	6,2	Severely damaged flood control channels (L-type reinforced concrete sections),
Friuli, Italy	1976	6,5	Complete collapse of retaining wall due to liquefied backfill.
Tangshan, China	1976	7,8	Lateral movement of bridge abutments. Buckling of superstructures.

Table 2.1 (continued) Retaining Wall Damage Due to Past Strong Earthquakes (After Stadler, 1997)

Loma Prieta, USA	1989	7,1	Vertical cracking of reinforced concrete walls. Formation of gaps between top of walls and backfill soil.
Northridge, USA	1994	6,7	Continuous cracking and differential settlement of concrete crib walls.
Hyogoken-Nanbu, Japan	1995	7,2	Overturning and outward tilting with subsequent backfill settlement of gravity walls. Complete failure of stem of reinforced concrete cantilever retaining walls.

Researchers proposed various analytical and numerical models to predict the dynamic behavior of these structures. Besides the analytical and numerical studies, physical modeling studies have been performed to investigate the dynamic soil-structure interaction and to verify the analytical and numerical modeling studies. Previous physical modeling studies have been conducted on 1-g and centrifuge environments. Nowadays use of centrifuge techniques are considered to be more reliable because they are one step better to represent the stress dependency of soils. Steedman and Zeng (1991) conducted several centrifuge tests to observe the seismic effects on cantilever retaining walls. Based on the results of centrifuge tests, an analytical approach known as Steedman-Zeng Method was validated.

Centrifuge testing has its own limitations due to small size of the models and requirement of small scale instrumentation. Due to the limited model size, even a lightweight pressure sensor mounted on a retaining wall model may affect the response of the model structure. Hausler (2002) reports that there may be changes in the stress distribution observed in the centrifuge models due to the increasing radius of rotation at different coordinates of the model. In addition to

these disadvantages, the container-side wall effects with the neighboring soil may lead to unrealistic behavior.

2.2.1 Analytical Methods for Calculating Seismic Pressures on Retaining Walls

According to Kramer (1996), a common approach to design retaining walls against seismic loads involves estimating the loads imposed on the wall during earthquake excitations and then ensuring that the wall can resist these anticipated loads. However, loading conditions on the retaining walls depend on several factors such as modes of wall movement, physical properties of the soil and flexibility of the retaining structure. Numerous analytical solutions towards the problem of dynamic lateral earth pressure on retaining walls have been proposed up to now. According to Nazarian and Hadjian (1979), the analytical solutions can be divided into four broad categories based on their methodologies. The categories include:

1. Rigid plastic methods (Mononobe-Okabe Approach, Steedman-Zeng Method etc.)
2. Elastic Methods (Veletsos and Younan, 1994a)
3. Elasto-plastic methods
4. Nonlinear solution methods

Typically, the magnitude of the anticipated retaining wall deflection determines which analysis method should be used. The rigid plastic and elastic methods represent the two extremes of displacement. A fundamental assumption of the rigid plastic methods is relatively large displacement which leads to the formation of active wedge in the retained backfill material. However, elastic solutions assume very small displacements in the retained medium. For displacements between these two extremes, elasto-plastic and nonlinear methods are appropriate. Numerical modeling technique implemented with elasto-plastic and non-linear methods are typically used when the intermediate displacement conditions are expected. A summary of the relevant work in each of these categories is presented in the following sections.

2.2.1.1 Mononobe-Okabe Method

It is a rather approximate method which was developed in Japan in the 1920's by Okabe (1924) and Mononobe and Matsuo (1929) to determine the resultant of

dynamic lateral earth pressures. Still widely used, this approach is called the Mononobe-Okabe (M-O) Method. It is based on Coulomb's classical earth pressure theory for dry cohesionless backfill. Coulomb's theory was modified by treating the inertial forces due to horizontal and vertical backfill accelerations as additional static forces. The model used for the Mononobe-Okabe method of analysis is shown in Figure 2-1. In this analysis, pseudo static accelerations are applied to a Coulomb active or passive wedge. The pseudo static soil thrust is then obtained from force equilibrium of the wedge. Seed and Whitman (1970) summarized the fundamental assumptions of Mononobe-Okabe method:

(a) The driving soil wedge and the retaining structure act as rigid bodies and therefore experience uniform accelerations throughout the respective bodies.

(b) Wall movement is sufficient to ensure either active or passive conditions.

(c) The driving soil wedge inducing the lateral earth pressures is formed by a planar failure surface starting at the heel of the wall and extending to the free surface of the backfill. Along this failure plane the maximum shear strength of the backfill is mobilized.

(d) When the minimum soil pressures are developed, the soil wedge behind the wall is at the point of failure and the maximum shear strength developed along the failure surface.

(e) The point of application of the seismic lateral thrust is at *H/3* above the base of the wall where *H* is the wall height.

As demonstrated by Seed and Whitman (1970), the dynamic earth pressures may be determined from analogous static conditions. Accordingly, the Mononobe-Okabe expressions for dynamic earth pressures can be derived from the Coulomb's expressions for static earth pressures. The analogous static conditions are achieved by rotating the wall-backfill system by an angle ψ, such that the vector sum of the horizontal and vertical inertial coefficients (k_h and k_v, respectively) is oriented vertically, where:

$$\tan(\psi) = \frac{k_h}{1 - k_v} \qquad 2\text{-}1$$

In regard to the mathematical expressions, Mononobe-Okabe expressions can be derived from the Coulomb's expressions by replacing the static values for the total unit weight of the soil (γ_t), height of the wall (*H*), inclination of the backfill (β), and inclination of the wall face from the vertical (θ), with the corresponding dynamic values (i.e., $\gamma_{td}, H_d, \beta_d$ and θ_d). For the active dynamic conditions, the modified Coulomb's expressions are as follows:

$$P_{AE} = \frac{1}{2}\gamma_{td} H_d^2 K_a(\beta_d, \theta_d) = \frac{1}{2}\gamma_t H^2.(1-k_v).K_{AE} \qquad 2\text{-}2$$

$$K_{AE} = \frac{\cos^2(\phi-\theta-\psi)}{\cos(\psi).\cos^2(\theta).\cos(\delta+\theta+\psi).\left[1+\sqrt{\frac{\sin(\phi+\delta).\sin(\phi-\beta-\psi)}{\cos(\delta+\theta+\psi).\cos(\beta-\theta)}}\right]^2} \qquad 2\text{-}3$$

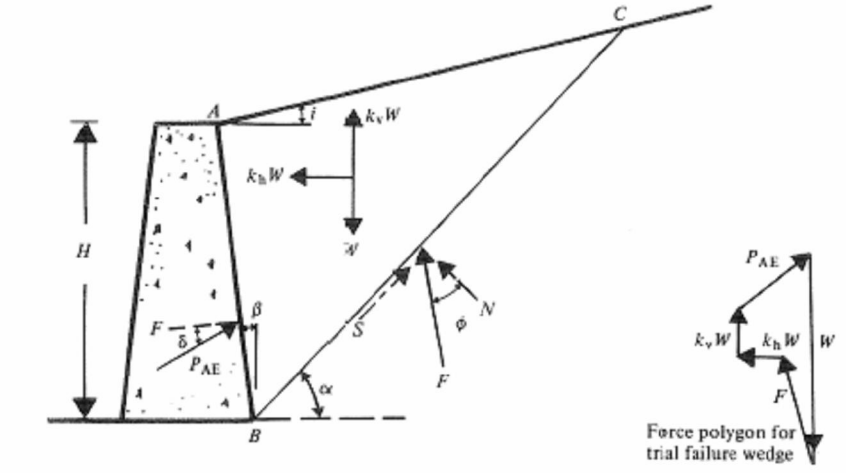

Figure 2-1 Forces acting on active failure wedge according to Mononobe-Okabe Approach (Das, 1983)

Although M-O analysis implies that the total active thrust should act at a point *H/3* above the base of the wall height, *H*, experimental results suggest that it actually acts at a higher point under the dynamic loading conditions. The total active thrust calculated by Eq. 2-3 can be divided into a static component, P_A and a dynamic component ΔP_{AE} as shown in Eq.2-4:

$$P_{AE} = P_A + \Delta P_{AE} \qquad 2\text{-}4$$

The static component is known to act at *H/3* above the base of the wall. Seed and Whitman (1970) suggested that the dynamic component be taken to act at approximately 0.6*H*. Hence, the total active thrust will act at a height:

$$h = \frac{P_A H/3 + \Delta P_{AE}.(0.6H)}{P_{AE}} \qquad 2\text{-}5$$

above the base of the wall. The value of *h* depends on the relative magnitudes of P_A and P_{AE}. Generally it occurs near the mid height of the wall.

2.2.1.2 Steedman and Zeng Method

Mononobe-Okabe method accounts the dynamic nature of earthquake loading in a very approximate way. A finer approximation was suggested by Steedman and Zeng (1990). This method involves a pseudo dynamic analysis approach which accounts for phase differences and amplification effects developing during an earthquake (Kramer, 1996). If the active wedge shown in Figure 2-2 is considered, acceleration at a depth z can be expressed as follows:

$$a(z,t) = a_h \sin\left[\omega\left(t - \frac{H-z}{v_s}\right)\right] \qquad 2\text{-}6$$

where a_h= amplitude of harmonic horizontal input acceleration, ω= cyclic frequency of harmonic input motion, t = time, v_s = velocity of vertically propagating harmonic shear wave, H = height of the wall, z = depth (from wall top)

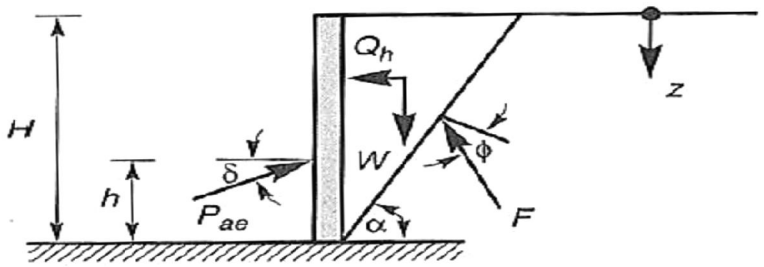

Figure 2-2 Forces acting on active failure wedge according to Steedman-Zeng Approach (Kramer, 1996)

The mass of a thin element in the active wedge is:

$$m(z) = \frac{\gamma}{g}.\frac{H-z}{\tan\alpha}dz \qquad 2\text{-}7$$

where γ is the unit weight of the backfill material and g is the gravitational acceleration. The total inertial force acting on the wall can therefore be found as:

$$Q_h(t) = \int_0^H m(z).a(z,t).dz = \frac{\lambda\gamma a_h}{4\pi^2 g\tan(\alpha)}\left[2\pi H\cos\omega\zeta + \lambda\left(\sin\omega\zeta - \sin\omega t\right)\right] \qquad 2\text{-}8$$

where

$$\lambda = \frac{2\pi v_s}{\omega} \qquad 2\text{-}9$$

$$\zeta = t - \frac{H}{v_s} \qquad 2\text{-}10$$

By resolving the forces on the wedge, the total soil thrust is calculated as follows:

$$P_{AE}(t) = \frac{Q_h(t)\cos(\alpha-\phi) + W\sin(\alpha-\phi)}{\cos(\delta+\phi-\alpha)} \qquad 2\text{-}11$$

By differentiation, the total earth pressure distribution is computed as follows:

$$P_{AE}(t) = \frac{\gamma z}{\tan\alpha}\frac{\sin(\alpha-\phi)}{\cos(\delta+\phi-\alpha)} + \frac{k_h \gamma z}{\tan\alpha}\frac{\cos(\alpha-\phi)}{\cos(\delta+\phi-\alpha)}\sin\left(\omega\left(t-\frac{z}{V_s}\right)\right) \qquad 2\text{-}12$$

The height of application of total thrust is estimated according to the following formula:

$$h_d = H - \frac{2\pi^2 H^2 \cos\omega\zeta + 2\pi\lambda H \sin\omega\zeta - \lambda^2\left(\cos\omega\zeta - \cos\omega t\right)}{2\pi H\cos\omega\zeta + \pi\lambda\left(\sin\omega\zeta - \sin\omega t\right)} \qquad 2\text{-}13$$

Backfill amplification effects can also be reflected to the equations by expressing a_h as a function of depth rather than using a constant acceleration value thought the height of the backfill. The results of Steedman-Zeng method shows good agreement with the centrifuge results but this method does not possess the ability to represent the effects of wall flexibility on dynamic pressures.

2.2.1.3 Elastic Methods Based on Wave Theory

Elastic solutions are applicable to non-yielding walls where displacements do not cause plastic displacements in the soil body. Matsuo and Ohara (1960) determined an approximate elastic solution for the dynamic soil pressure on a rigid wall using a two-dimensional analytical model. In their approach, bending of the stem due to the flexibility of the wall was not considered and no vertical displacement of the soil mass was allowed. Assuming the wall was stationary, lateral soil stresses were derived using classical wave theory. Tajimi (1973) derived lateral earth pressures induced by a harmonically forced rigid-wall in translation and base rotation by employing a quarter infinite field and two-dimensional elastic wave theory. The formulation of this problem is illustrated in Figure 2-3. The results are given in the form of equations and charts. The solutions may also be used to calculate the approximate impedance functions for embedded structures. However, the boundary conditions used in Tajimi approach are such that the solutions are not directly relevant to the problem of base shaking of a wall-soil system of finite size (Steedman 1984). In another study, Scott (1973) studied the dynamic behavior of a rigid retaining wall by modeling the soil backfill as a one-dimensional, elastic, shear beam attached to the wall by Winkler springs. This model is depicted in Figure 2-4. The methodology was proposed for two soil conditions: constant soil properties with depth and shear modulus

increasing nonlinearly with depth. Results indicated that the first mode of vibration is primarily responsible for the pressures on the wall.

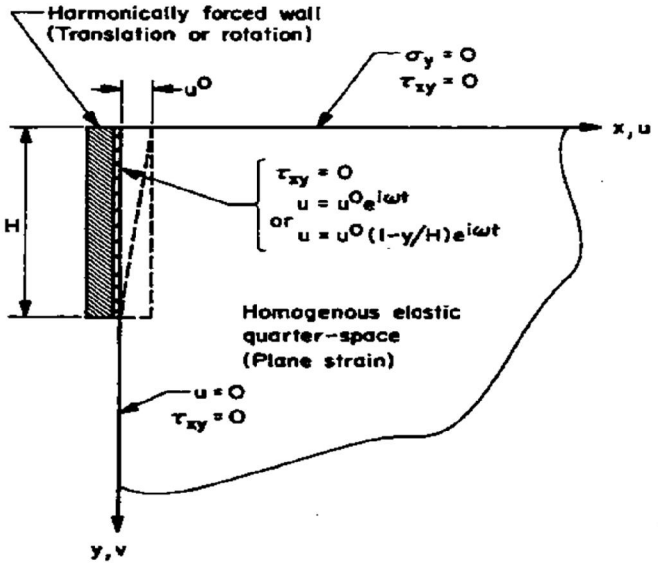

Figure 2-3 Tajimi's Problem (Wood, 1973)

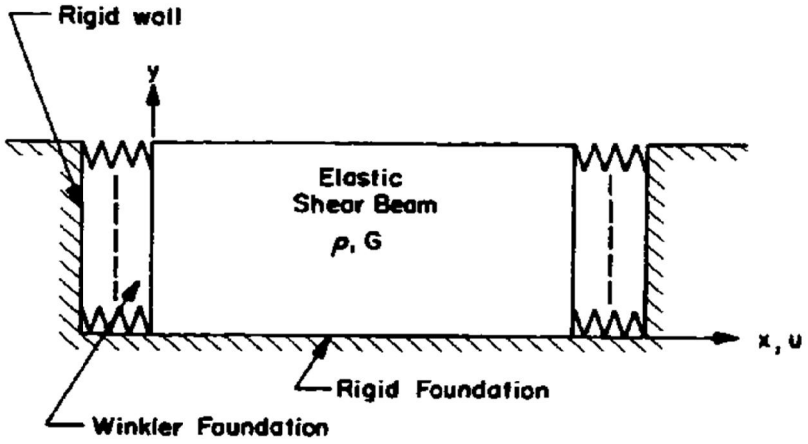

Figure 2-4 Scott's Model (Wood, 1973)

According to his solution, the first-mode dynamic pressure increment distribution is a cosine function which is decreasing with depth from a maximum at the surface to zero at the base. The resultant force was observed to act at approximately 2*H*/3 from the base of the wall.

Wood (1973) has presented an extensive study of the behavior of rigid soil retaining structures subjected to earthquake motions. The study was based on

linear elastic theory and idealized representations of wall-soil systems. The normal mode solution for the free vibration of the elastic solid medium was derived and solutions for the cases of arbitrary horizontal forcing of the rigid boundaries and a uniform horizontal body force were presented. The boundary conditions for the case of a uniform horizontal body force were illustrated in Figure 2-5. Results were presented as normalized pressure profiles (Figure 2-6).

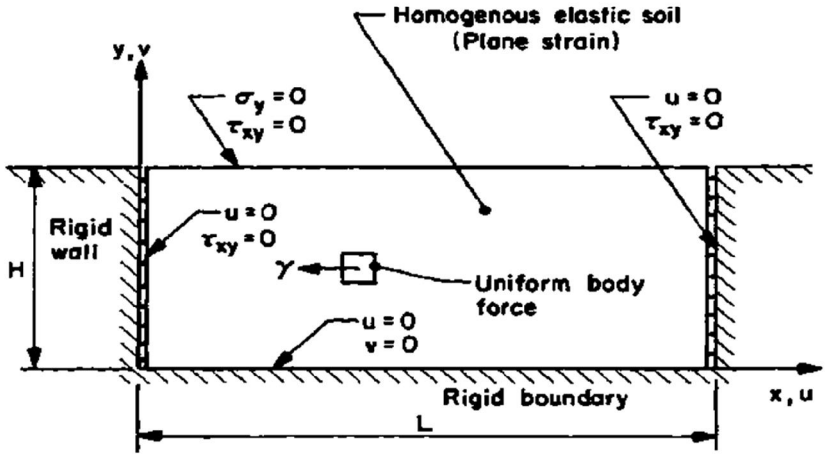

Figure 2-5 Wood's Model (Nazarian and Hadjian, 1979)

Analytical solutions were augmented by finite element solutions for those cases where analytical results would be difficult to obtain. Veletsos and Younan (1994) studied the dynamic behavior of rigid retaining walls. The response of the walls retaining semi-infinite, uniform, visco-elastic stratum of soil having constant thickness which has excited by both harmonic and transient excitations were investigated by assuming constant and frequency dependent parameters.

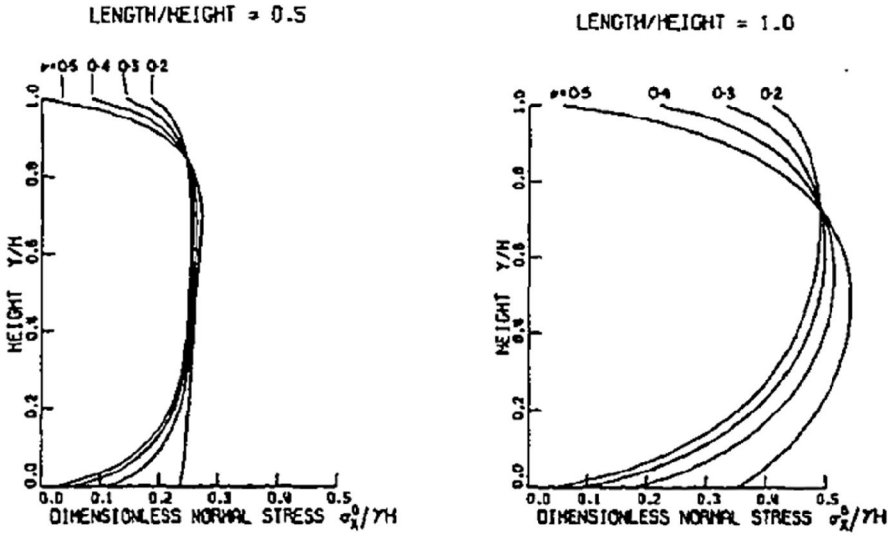

Figure 2-6 Pressure Distributions for 1-g Static Horizontal Body Force (Wood, 1973)

Based on the results, frequency independent parameters were proposed to obtain more generalized characteristics. In the analyses, radiation damping of the medium was ignored and the wall pressures were considered to be proportional with the relative motions of the soil at the far field. In another study, Veletsos and Younan (1997) carried analytical studies to examine the effect of wall and base stiffness on the wall pressures and distributions. The model of their study is depicted in Figure 2-7. Authors stated that wall pressures induced by ground shaking are quite sensitive to wall flexibilities. An increase of the wall flexibility decreased the proportion of the inertial forces transmitted to the wall. The base shear for a wall having a realistic flexibility value is more than 50 % lower than those obtained for a fixed base rigid wall. The amount of decrease in the overturning moments was observed to be even larger. Wall pressures for different wall flexibilities are shown in Figure 2-8. In this figure, η axis of the graph is the dimensionless vertical position coordinate which is equal to *y/H*, d_θ denotes the relative flexibility of the rotational base constrained and the retained medium, d_w ,the relative flexibility of the wall and the retained medium, ρ, mass density of the soil medium, *H*, height of the wall and $\ddot{X}_g$, maximum ground acceleration.

Elastic methods are providing valuable insight into the dynamic behavior of retaining walls in most cases, however the solutions become complicated when the soil-structure interaction effects considered for complex geometries. Besides,

one of the main limitations of the elastic methods is the assumption of complete bonding in the soil-wall interface which causes unexpected behavior due to tensile forces occurring in this boundary.

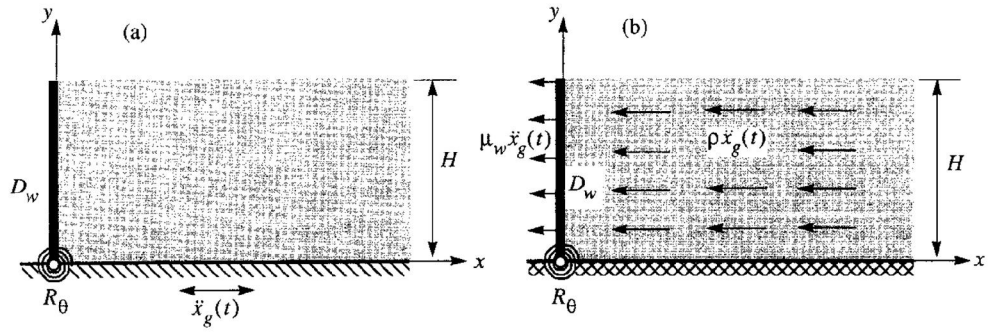

Figure 2-7 (a) Base-Excited System (b) Force – Excited System (Veletsos and Younan, 1997)

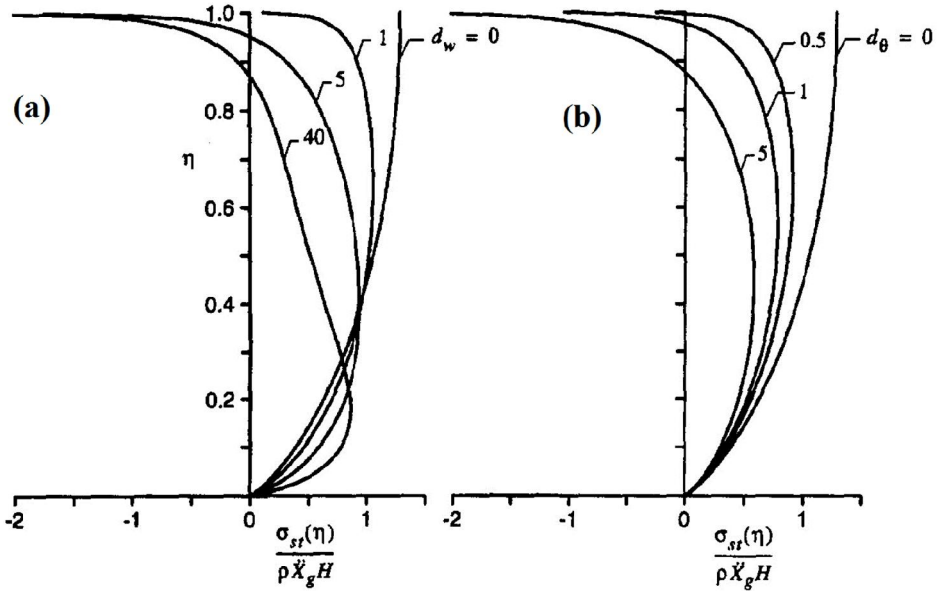

Figure 2-8 Distributions of Wall Pressure for Statically Excited Systems with different Wall and Base Flexibilities (a) for d_θ=0 (b) for d_w=0 (Veletsos and Younan, 1997)

2.2.1.4 Numerical Methods with elasto-plastic and nonlinear models

Clough and Duncan (1971) performed finite element modeling studies to inspect the behavior of the soil-wall interface. In a following study, Wood (1973) modeled various retaining wall-backfill systems with linear, plane-strain finite elements and compared the results with analytical calculations. Good agreement was reported between numerical predictions and analytically calculated soil pressures. Aggour

and Brown (1973) studied the effects of wall flexibility, soil moduli, backfill length and backfill shape on the dynamic earth pressure distribution. Two-dimensional, plane strain analyses were performed for a 6m high wall with the backfill extending to 60 meters. Wall thicknesses varied as 0.4m 0.6m and 1.2m. Sinusoidal excitations having amplitude of 0.1g and various frequencies were applied as the input acceleration in the dynamic finite element analyses. Byrne and Salgado (1981) derived a simple elasto-plastic model to be used in numerical analyses. In their study, soil was modeled by spring elements and forces were calculated based on the active and passive earth pressure coefficients. Nadim and Whitman (1982) considered some of the limitations of the sliding block model using a finite element formulation. They recommended that the limiting displacement method should be used for design purposes with modifications to the design acceleration. Siddharthan and Maragakis (1989) studied the dynamic behavior of flexible walls supporting dry sand backfill. Soil response under dynamic loading was modeled as nonlinear and hysteretic. The model also accounted for the increase in lateral stresses and settlements related to grain slip caused by cyclic loads, the soil was represented by plane-strain, iso-parametric elements and the wall was represented by beam elements. Sinusoidal base excitations were applied to the base of the models. A centrifuge test of an aluminum wall model retaining dry sand was modeled numerically (Steedman, 1984). Computed and measured dynamic bending moments showed good agreement. Finite element model developed in their study was further used to investigate the effect of different backfill densities and wall flexibility values on the wall response. They concluded that the base bending moment was smaller and the deflection was higher for the more flexible walls. Finn et al. (1989) presented a numerical method of analysis for cantilever retaining walls and compared the results with centrifuge test data. The finite element code employed a nonlinear dynamic effective stress analysis method. Deformations, bending moments, and accelerations were numerically estimated and compared with the centrifuge test results. Good agreement was found between the two. Bakeer et al. (1990) performed finite element analyses in order to investigate the dynamic pressures and the point of application for different wall movement modes. Failure modes involving translation, rotation about the top and rotation about the bottom were investigated. It was observed that dynamic lateral earth pressure coefficients are generally higher than those predicted by Mononobe-Okabe approach for all wall movement modes (Figure 2-9 and Figure 2-10). For rotation around top and

horizontal translation modes, location of the resultant thrust was observed to be higher than the one third of the wall height; whereas for the rotation around base mode, location of the thrust was lower when compared to the estimations of Mononobe-Okabe method for small acceleration values. Bakeer et al. (1990) used results of shaking table tests to verify their finite element analysis results. The comparison of their studies with experimental data indicated good agreement.

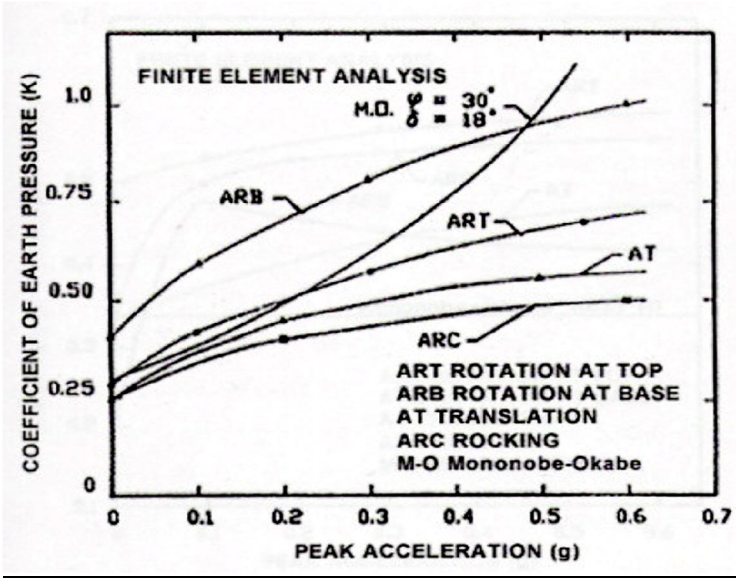

Figure 2-9 Finite Element analysis results for coefficient of earth pressure for different wall movement modes (Bakeer et al., 1990)

Gazetas et al. (2004) investigated the dynamic earth pressures on various kinds of earth retaining structures such as L-shaped reinforced-concrete walls, piled walls with horizontal or strongly inclined anchors, and reinforced soil walls. In their analyses, base excitations of either high or moderately low dominant frequencies having a peak value of 0.4g are applied for short durations. Stress-strain behavior of the retained backfill at dry conditions were modeled with either Mohr-Coulomb or linear elastic models. According to analyses results, the observed failure modes for the cantilever walls were depicted in Figure 2-11. Gazetas et al. (2004) compared pressure distributions for a theoretical rigid non-sliding wall with the ones of a very flexible type non-sliding wall. A considerable decrease in pressure distributions were observed for the flexible wall case.

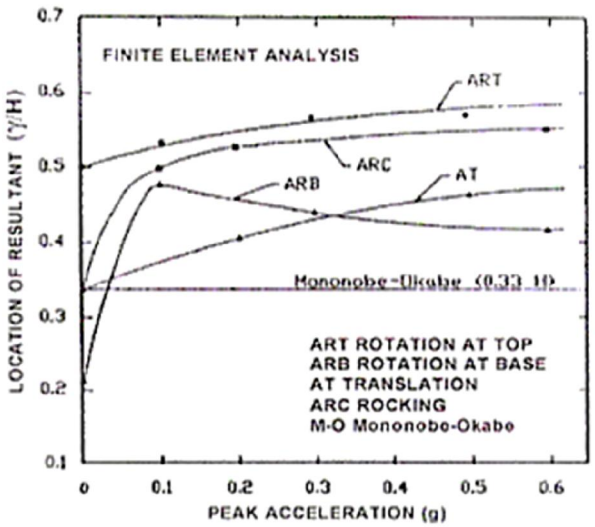

Figure 2-10 Finite element results of the application point of the resultant for different wall modes (Bakeer et al., 1990)

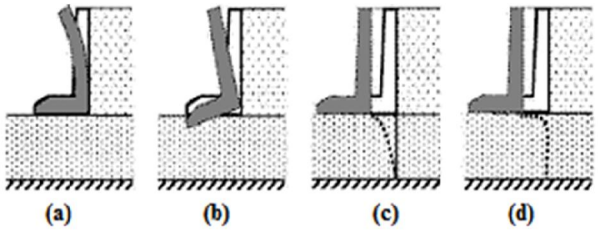

Figure 2-11 Possible modes of displacement of an L-shaped wall: (a) structural flexure, (b) base rotation, (c) base translation, and (d) sliding (Gazetas, et al., 2004)

Gazetas et al. (2004) compared results of a numerical analysis of a reinforced soil zone with centrifuge experiment results of Koseki (2002) in a quantitative manner. A visual comparison of the soil wedge at failure from finite element analysis and the centrifuge experiments is depicted in Figure 2-13. As observed from the Figure 2-13, the soil tends to move as a block and with the failure mechanism developing behind the wall. According to the numerical analysis results, the dynamic wall pressures are low as long as the soil behavior remains in the linear range, but when the soil wedge behind the wall occurs, or in other words, when failure mechanism activates, significant increase occurs in the dynamic wall pressures.

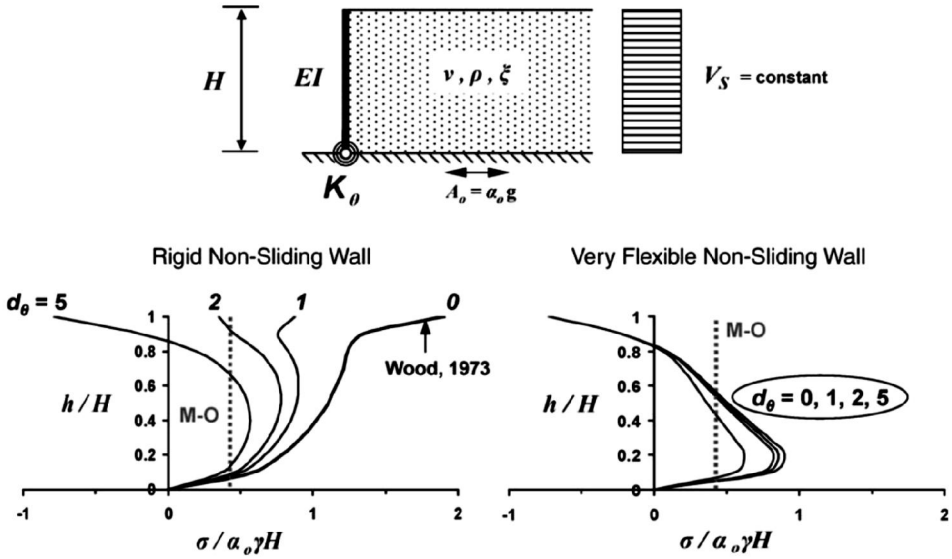

Figure 2-12 Elastic dynamic earth-pressure distribution of a pseudo-statically excited one-layer system for a non-sliding wall (Gazetas et al., 2004)

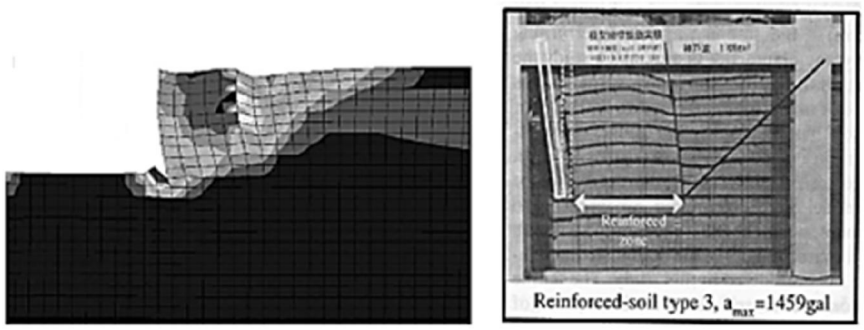

Figure 2-13 A quantitative comparison of finite element analysis and centrifuge experiments (Gazetas et al., 2004)

In a following study, Veletsos and Younan (2003) developed their previous effort on the dynamic response of cantilever retaining walls by performing comprehensive numerical analyses investigating effect of various parameters including the characteristics of the input motions. The response quantities involved the displacements of the wall relative to the base, the dynamic wall pressures, and the total wall force, base shear and base moment. Psarrapoulos (2005) conducted finite element analyses to verify the elastic solutions of Veletsos and Younan (2003) by investigating the parametric effects such as flexural wall rigidity and the rocking base compliance on the response of 8m high retaining walls. In the numerical analyses, the soil was modeled as either a homogeneous

or an inhomogeneous media. The systems investigated in this study are shown in Figure 2-14.

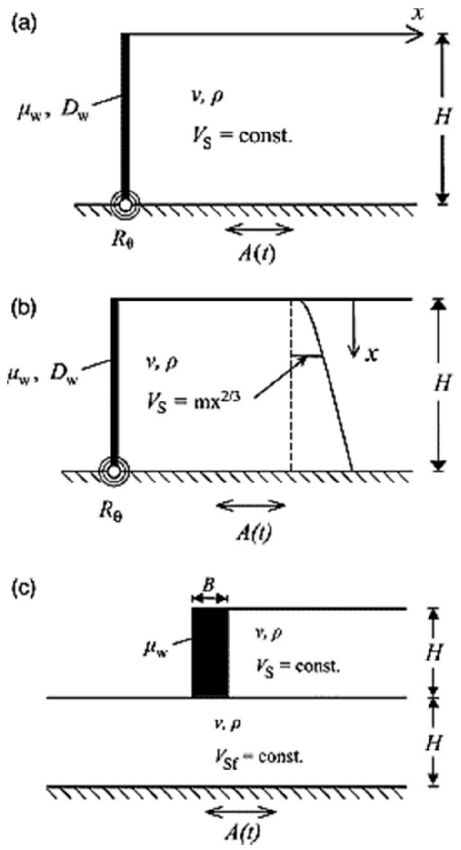

Figure 2-14 (a) Flexible wall (homogeneous soil layer), (b) flexible wall (inhomogeneous soil layer) and (c) rigid gravity wall in a two-layer soil system (Psarrapoulos, 2005)

The excitations are given as a base excitation of sinusoidal acceleration time history having frequencies of maximum three times the natural frequency of the considered soil stratum. The distribution of the dynamic earth pressures on rigid and flexible walls were observed to be in agreement with the estimations of available analytical methods. It was observed that the soil pressure profiles in the dynamic case are very dependent on the wall flexibilities and the rotational base constraints of the modeled walls as depicted in Figure 2-15. Green and Olgun (2008) performed nonlinear, explicit finite difference analyses to determine the seismic response of cantilever retaining walls and compared the wall pressures with values obtained by Mononobe-Okabe methodology. The numerical model consisted of a 6m high concrete cantilever wall resting on 3m thick foundation soil.

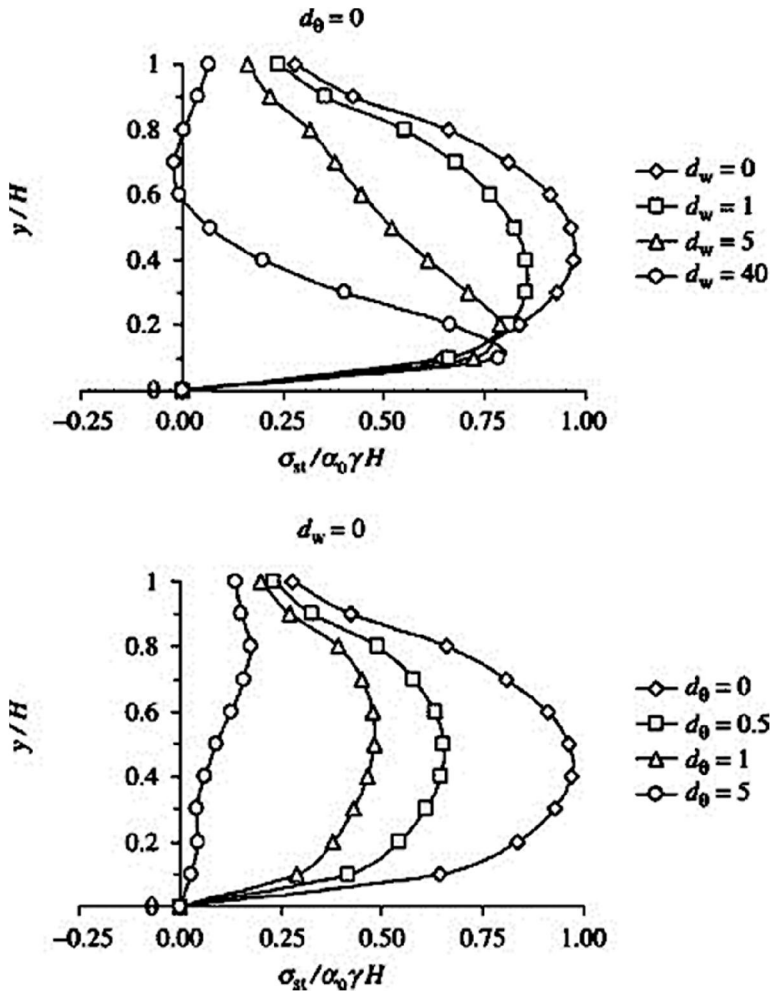

Figure 2-15 Earth pressure distributions for walls with different wall and base flexibilities (Psarrapoulos, 2005)

Stress-strain behavior of the geo-materials was simulated by an elasto-plastic constitutive model, in conjunction with Mohr-Coulomb yield criterion. The wall was modeled using elastic beam elements. Finite difference mesh used in their study was depicted in Figure 2-16(a). The model consisted of four sub-grids, namely the backfill, foundation soil, left and right absorbent boundaries. Wall-soil interfaces were modeled using the non-linear hyperbolic model proposed by Gomez et al. (2000). In the analyses, 3% Rayleigh damping was defined by setting the central frequency equal to the small-strain fundamental frequency of the retaining wall-system. Additional hysteretic damping was also present in the system due to utilization of elasto-plastic constitutive model with Mohr-Coulomb yield criterion. According to Figure 2-16(b), failure wedge is not monolithic and slip planes occurs at several inclinations.

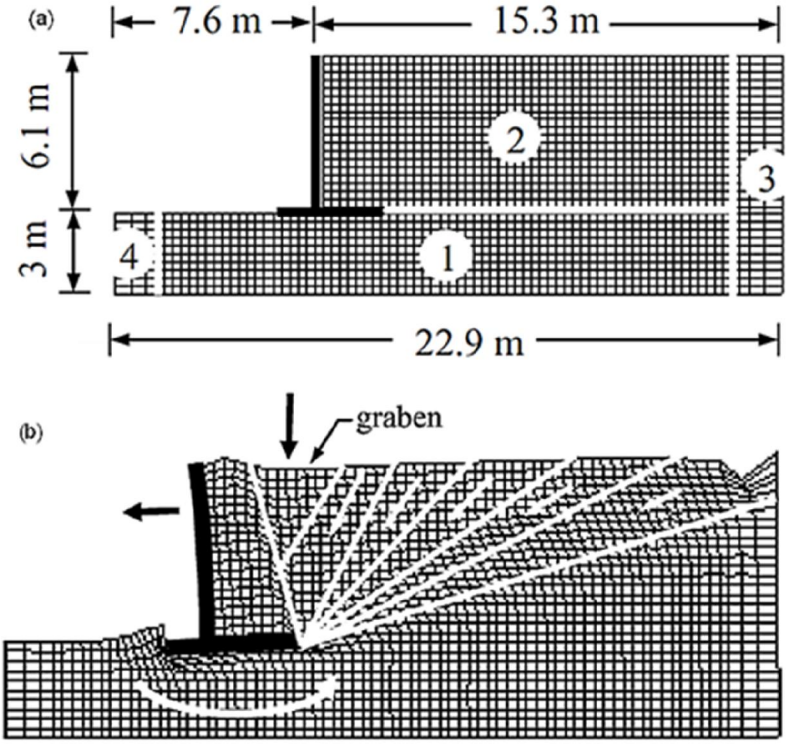

Figure 2-16 (a) Original Finite difference mesh used in the analyses of a cantilever retaining wall (b) Deformed mesh after base excitation (Green and Olgun, 2008)

Lateral stresses on the wall stem computed by finite difference analyses did not agree with those predicted by Mononobe-Okabe Approach. Authors attributed the reason of this deviation to the relative flexibility of the wall and the non-monolithic motion of the driving soil wedge which is considered as a contradiction with the main assumptions of the Mononobe-Okabe Approach.

2.2.1.5 Displacement Based Methods

In many of the cases, post-earthquake serviceability of retaining structures is under concern. Large permanent displacements may be acceptable in some walls, but some of them are sensitive to very small displacements. By considering these factors, some methodologies were developed by previous researchers.

Richards and Elms (1977) proposed a technique based on the allowable permanent wall displacements. According to their method, using the simplified Mononobe-Okabe formulation, a yielding wall may be designed using either a limit-equilibrium force approach (conventional retaining wall design) or an

approach that permits movement of the wall up to tolerable amounts. In their study, evaluation of the yield acceleration for the retaining wall is required to estimate the wall displacements by Eq. (2-14). The active dynamic thrust (P_{AE}) acting on the wall is estimated by using Mononobe-Okabe approach and writing the equilibrium equation in the horizontal direction, yield acceleration was determined iteratively and calculated values were used to estimate permanent block displacements. Using the data provided by Franklin and Chang (1977), a function that predicts the maximum displacement for a maximum earthquake velocity was presented. Predictions of the permanent wall displacements with this methodology provided close results with the maximum displacements estimated by Newmark method (Newmark, 1965).

$$a_y = \left[tan\,\Phi_b - \frac{P_{AE}\,cos(\delta+\theta) - P_{AE}\,sin(\delta+\theta)}{W} \right] g \qquad 2\text{-}14$$

$$d_{perm} = 0.087 \frac{v_{max}^2 a_{max}^3}{a_y^4} \qquad 2\text{-}15$$

where δ is the angle between the normal to the wall and P_{AE}, θ is the angle between the wall stem and the vertical axis. Richards-Elms approach may also be used to determine the seismic lateral thrust acting on the retaining walls. Based on a certain amount of permissible displacement, the designer can calculate an acceleration coefficient value somewhat less than the maximum. Lateral force is determined by M-0 method using the reduced acceleration coefficient. However, inertia forces due to the wall mass should also be considered. To account for uncertainties, a safety factor of 1.5 should be applied to the weight of the wall.

In a following study, Whitman and Liao (1985) identified several errors related to the simplifications involved in the Richards-Elms approach. Dynamic response of the backfill, several kinematic factors, tilting mechanism and the effect of vertical accelerations were neglected in the Richards-Elms methodology. Following studies indicated that these simplifications may lead to significant uncertainty in the calculation of permanent displacements. For example, Nadim (1982) reported that significant increase was observed in permanent wall displacements when the predominant frequency of the earthquake coincides with the natural frequency of the retaining wall-backfill system. Studies of combined tilting and sliding generally increase wall displacements compared to sliding-only models. Besides,

consideration of the vertical accelerations produces slightly larger displacements compared to the analyses without vertical excitation component. Whitman and Liao (1985) studied the effects of these sources on the predicted permanent wall displacements and quantified by a log-normal distribution having a mean value of:

$$\bar{d}_{perm} = \frac{37 v_{max}^2}{a_{max}} exp\left(\frac{-9.4 a_y}{a_{max}}\right) \quad \text{2-16}$$

The effects of uncertainty due to statistical variability of the ground motions and the soil properties such as friction angle and cohesion on the permanent wall displacements were also investigated and modified versions of Eq.2-16 were proposed.

2.3 Experimental Studies on the seismic response of retaining walls

Experimental studies are classified as 1-g shake table and centrifuge tests. Results of 1-g shaking table tests provide valuable insight towards understanding the seismic behavior of cantilever retaining walls. However the effective stresses in the small scale laboratory tests are significantly lower compared to those in the prototype. Several important parameters related with the soil behavior such as shear modulus and damping ratio are dependent on effective stress levels on the geo-materials. Owing to this stress-dependent nature of soils, 1-g physical tests may lead to questionable conclusions; however results serve to investigate a qualitative behavior of the retaining walls. Due to the insufficient ability of 1-g tests to replicate the in-situ stress conditions, utilization of geotechnical centrifuge in retaining wall problems have become widespread in the recent years. This method allows a more realistic replication of the prototype conditions in the controlled laboratory environment (Stadler, 1996). In the following sections, the physical modeling studies on the seismic behavior of retaining walls are summarized.

2.3.1 1-g Shaking Table Experiments

After the proposal of the Mononobe-Okabe methodology, several researchers carried out 1-g shaking table tests to investigate the applicability and validity of this analytical approach (Matsuo (1941), Matsuo and Ohara (1960), Ishii et al.

(1960), Sherif et al. (1982), Sherif and Fang (1984)). Commonly, all of these researchers investigated the behavior of small-scale retaining wall models subjected to harmonic base excitations and observed that Mononobe-Okabe approach provides reasonably well predictions of the lateral dynamic earth thrust, however pressure distribution along the wall stem and naturally the point of application of the resultant thrust are not in good agreement with predictions of analytical approaches.

Calisan (1999) performed 1-g shake table tests on gravity retaining walls with various weights and come up with similar findings with the previous researchers. In a more recent study, Watanabe et.al. (2003) conducted 1-g shaking table tests to evaluate seismic stability of different types of retaining walls against high seismic loads. Six different retaining wall types were tested under irregular excitations. The wall models consisted of three conventional retaining walls involving cantilever, gravity and leaning type as well as three types of reinforced earth retaining walls with different reinforcement arrangements. The height of the wall stem was 530mm and the width of the wall foundations was 230mm for the cantilever wall model. Test results indicated that major failure planes occurred at two different orientations, where the second slip surface occurred at higher amplitude excitations. This was explained by the effects of strain localization in the backfill and associated post-peak reduction in the shear resistance from peak to residual values along the previously formed failure plane. Yunatci (2003) investigated the seismic behavior of laterally braced sheet pile walls. Model walls made from steel having 3mm thickness and 65cm height were supported by wooden bracings at three levels (Figure 2-17). The model was subjected to sinusoidal base motions with acceleration amplitudes between 0.05g to 0.40g. Dynamic earth pressures on the walls and the accelerations in the backfill were recorded in each test. Amplifications ranging between 1.6 and 2.4 were observed in the tests. Lateral dynamic thrust values were in agreement with the predictions of Mononobe-Okabe approach in the acceleration amplitude range of 0.15g to 0.25g. For lower acceleration amplitudes, results were above the theoretical values. Residual stresses remained after the termination of the seismic event. Cilingir (2005) conducted tests on laterally braced walls retaining cohesionless backfills. Input acceleration applied to the wall base was kept between 0.03g to 0.27g. The effects of surcharge and wall stiffness on the dynamic lateral pressures were investigated and results were compared with those of the

analytical methods available in the literature. It was observed that surcharge significantly increases the dynamic lateral pressures on the walls. No clear relationship was observed between the point of application of the dynamic thrust and the surcharge magnitude. Lateral dynamic pressures on the flexible walls were observed to be lower compared to the stiffer walls.

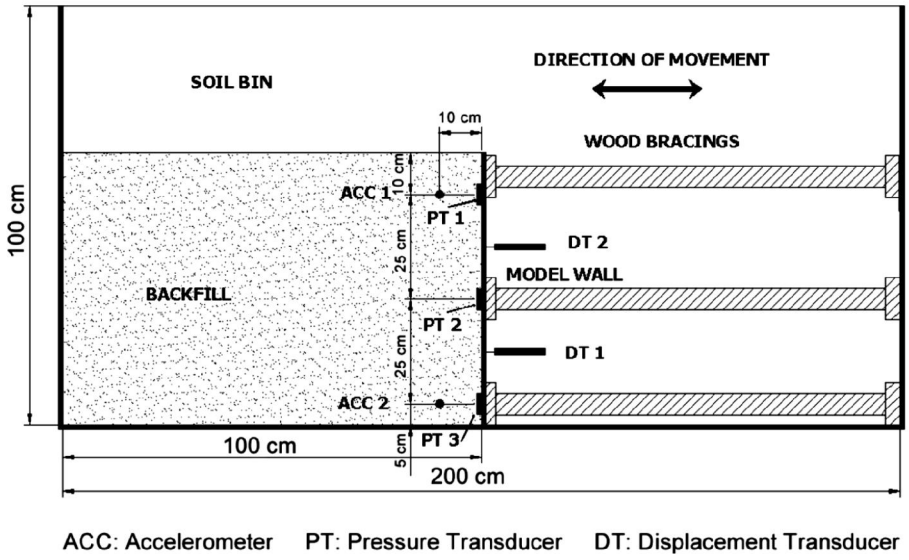

Figure 2-17 Model set-up of braced wall (Yunatci, 2003)

Ling et al. (2005) presented results of large scale shaking table tests in 2.8m high flexible geosynthetic reinforced walls. The walls were excited with the record of Kobe earthquake scaled to 0.4g and 0.86g, respectively. Very little horizontal deformation was observed in the walls for both of the excitation phases. Part of the lateral deformation and the tensile stresses in the reinforcements were recovered at the end of the ground shaking.

2.3.2 Centrifuge tests

Modeling of the retaining wall problems by geotechnical centrifuge facility offers an alternative way to physical testing with 1-g shake table. The better ability of simulating the prototype conditions in the laboratory environments designates the most important advantage of the centrifuge testing. It provides a cost effective way of simulating soil-structure interaction problems compared to full-scale model testing. Results of physical modeling studies performed in centrifuge environment

provide means of validation for the numerical modeling techniques or analytical methods. However, there are inherent limitations regarding to centrifuge modeling. According to Hausler (2002), increasing radius of rotation at different coordinates of the centrifuge set-up affects the observed stress distributions on the model retaining walls. The container-side wall effects with the neighboring soil may lead to unrealistic behavior; however this effect was minimized by the use of laminar containers and low friction membranes.

Ortiz et al. (1983) carried out centrifuge tests to investigate seismic response of a model cantilever wall retaining 97.5mm high backfill. Tests were performed for medium dense, dry sand under 50g acceleration environment. Model walls were made of aluminum and represented a very flexible cantilever model, at least six times more flexible than a corresponding concrete wall. Large increases in the bending moments were observed at the end of the excitations. They observed a broad agreement with the Mononobe-Okabe predictions and commented that the point of application of the dynamic force was H/3 above the wall base. Similarly, Bolton and Steedman (1982) carried out dynamic centrifuge experiments on cantilever wall models made from concrete and steel. Their results were generally in agreement with predictions made by Mononobe-Okabe approach. In another study, Steedman (1984) performed tests on cantilever model walls retaining dense and dry backfill on Cambridge Geotechnical Centrifuge. Measured dynamic forces were in agreement with the values calculated by Mononobe-Okabe Approach. In a more recent study, Zeng (1990) conducted nine centrifuge tests on Cambridge Centrifuge Facility. In this study, cantilever and anchored retaining walls with dry and saturated cohesionless backfill materials were tested. Based on their centrifuge modeling studies Steedman and Zeng (1991) observed that failure may occur in cantilever walls retaining saturated backfills due to the strain softening resulted from pore pressure build-up. They also reported that dynamic amplification and attenuation of the input motion through the backfill significantly change the distribution of the dynamic lateral forces acting on the wall stem. Stadler (1996) carried out 14 dynamic centrifuge tests on cantilever retaining walls. According to their test results, static pressure distribution was approximately triangular; however incremental dynamic stresses exhibit a varying profile ranging between triangular to rectangular in shape. Stadler (1996) suggested the reduction of acceleration coefficient (20% to 70% of the original) in the Mononobe-Okabe equations to achieve a better agreement of the results. The

quality of predictions made using Mononobe-Okabe methods was dependent on the wall flexibility incorporated with wall height. Author indicated that for stiffer walls which have flexibility of less than 0.05in^2/lb/inch, the lateral dynamic thrust was under predicted by Mononobe-Okabe approach. However, for more flexible walls, analytical approach over predict the actual behavior.

In a more recent study, Al Atik and Sitar (2010) performed series of centrifuge tests on rigid and flexible cantilever walls connected to stiff floor slabs. The models were designed to represent the prototype structures of Bay Area Rapid Transit System (BART). Dry, medium dense backfills were prepared by dry pluviation technique. Relative density of the material after pluviation was measured as 73%. Shaking events consisted of scaled ground motions of Loma Prieta, Kobe and Kocaeli earthquakes. The peak ground acceleration of the scaled input motions ranged from 0.1g to 0.87g with a predominant period of 0.2s to 0.62s. Authors simulated behavior of the retaining walls observed in the centrifuge tests by two dimensional plane strain finite element analyses developed on the OpenSees platform. Results indicated that finite element analysis is able to capture the behavior with a good agreement. The findings of the physical modeling study and numerical analysis results indicated that maximum dynamic earth pressures increase with depth and approximated by a triangular distribution. The application point of the dynamic thrust was observed to act at 1/3H which was originally suggested by Mononobe and Matsuo (1929) and Okabe (1926). The dynamic earth pressure coefficients (ΔK_{AE}) were depicted in Figure 2-18. Investigation of the dynamic interaction between the wall and the backfill depicted that maximum dynamic earth pressures and wall inertia forces do not occur at the same time. Authors expressed that dynamic earth pressures were significantly overestimated for the current design methods based on Mononobe-Okabe Approach since in this method it is assumed that maximum dynamic earth pressure and wall inertia force occur at the same time.

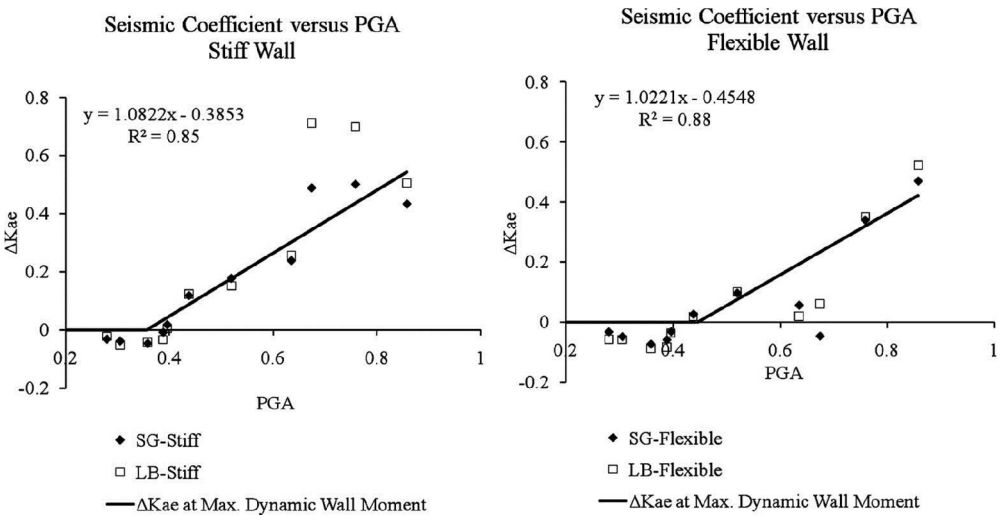

Figure 2-18 Dynamic earth pressure coefficients for stiff and flexible cantilever walls (Al Atik and Sitar, 2010)

2.4 Geofoam in geotechnical applications

During the last few decades, there is an increasing interest on lightweight geosynthetics by the geotechnical engineers and academics (Negussey, 1998). Horvath (1995) proposed the generic term “geofoam” for polystyrene foams used in geotechnical field. Later the new definition of the word included all the cellular geosynthetics created by an expansion process. According to ASTM (2005), geofoam is defined as “block or planar rigid cellular foam polymeric material used in geotechnical engineering applications”. Multifunctional use of the geofoam in geotechnical engineering projects increases the cost effectiveness of the material. Most common geofoam types are made of expanded polystyrene (EPS) or extruded polystyrene (XPS); however EPS has become the most well-known and commonly used geofoam product. EPS was invented in 1950 at BASF Company in Ludwigshafen, Germany. It is a type of foamed plastic formed by the expansion of polystyrene resin beads in a molding process according to ASTM D7180-05. Due to the characteristics of the manufacturing methodology, a cellular and lightweight material is produced. In the first stage of the manufacturing process, polystyrene beads are preheated under a controlled steam input. This phase is accompanied by the volumetric expansion of the beads due to the pentane gas trapped inside the beads. The density of the final product is determined during this stage. Diameter of the polystyrene cells may become three to four times greater than the initial diameter at the end of steam heating. Density adjustment of the material depends on the length of the heating time. The material called the

“prepuff” is stored in a ventilated container in order to release the excess moisture. Prepuff is poured into molds where steam is injected from the side walls. In this stage, additional volumetric expansion occurs. Cells are tightly squeezed forming relatively rigid EPS blocks. Dimensions of the final product depend on the size of the steam injection mold.

Applications of EPS in road construction were practiced in Germany in late 1950’s shortly after the discovery of the material. Later, EPS geofoam have been used in geotechnical applications in a number of countries in the world such as Norway, the Netherlands, the United States, Japan, and Malaysia (Elragi, 2000). EPS was considered as the most suitable geofoam due to its low density (1/50 to 1/100 of natural fills) and high compressive strength which is sufficient to support loads in many geotechnical applications (Hazarika, 2001). Range of applications of EPS geofoam involve rapid embankment construction over compressible soils (Farnsworth et al., 2008), slope stability (Jutkofsky et al., 2000), reduction of static and dynamic lateral earth pressures on retaining structures (Horvath 1991,1997,2008; Hazarika and Okuzono 2004; Hatami and Withoeft 2008; Zarnani and Bathurst 2007,2008), sub-base fills in highway constructions (Stark, 2004). Beinbrech and Hohwiller (2000) indicate the technical and economic benefits provided by geofoam in applications such as absorption of deformations to reduce lateral earth pressures acting on engineering structures, redistribution of stresses on pipelines, reduction of overburden soil pressure by inducing arching in the soil and attenuation of vibrations due to human activity such as railroad and vehicle traffic, construction activities etc. According to the author, EPS is considered as a suitable material due to its low density, good thermal insulation, superior vibration absorbing characteristics, and lateral deformation properties.

One of the first geotechnical projects with EPS geofoam was performed in Norway in 1965 (AabФe, 2000). In 1972, a road embankment for the portions of a highway adjoining a bridge in Norway is filled by EPS geofoam. Frydenlund and AabФe (1996) reports that progressive settlements in the order of 20-30 cm were observed in road embankments, however settlements were successfully reduced after geofoam lightweight fill application. Beinbrech and Hohwiller (2000) reports frequent use of EPS geofoam since 1970’s in northern lowlands of Germany where soil mechanical properties are not suitable for construction activities. In 1995, the code of practice for the use of EPS geofoam in the construction of highway embankments was published in Germany. Besides the use of EPS

geofoam in highway embankments, several profitable applications such as pressure reduction on pipelines, isolation of underground structures and garages from vibrations, mitigation of vibrations due to railroad and subway traffic etc. were reported in the rest of Germany (Beinbrech and Hillmann, 1998).

Years of practical experience with polymeric geofoam proved its ability to withstand vertical and lateral stresses when used in the construction of earthworks. The stability, durability and resistance to moisture and deterioration are the superior properties of rigid cellular geofoam. Since the bulk density of the geofoam can be adjusted according to the diverse range of applications. The swelling pressures on base slabs of buildings can be reduced by placing deformable geofoam cushions between the structural elements and soils.

Geofoam may be used as a countermeasure for earthquake induced displacements on the buried pipelines and underground structures. For the seismic applications, elasticated geofoam products has a better ability to attenuate earthquake forces since the elastic portion of this type of geofoam may reach up to 10%.

Presence of a pipe structure beneath the soil causes additional loads to be concentrated on the pipe thus causing a relief of stresses in the surrounding soils. Placing a deformable layer of geofoam causes a rearrangement of vertical stresses over the buried pipes (Beinbrech and Hohwiller, 2000). Displacements induced in the soil owing to the presence of EPS compressible layer enable mobilization of the soil shear strength and relieve the stress concentrations on the pipelines. In Figure 2-19, typical applications of geofoam on pipelines were illustrated. The positive effect of EPS geofoam layer in reducing stress concentrations on the roof of the buried pipelines was proved by Vaslestad et al. (1994) by tests and analytical calculations.

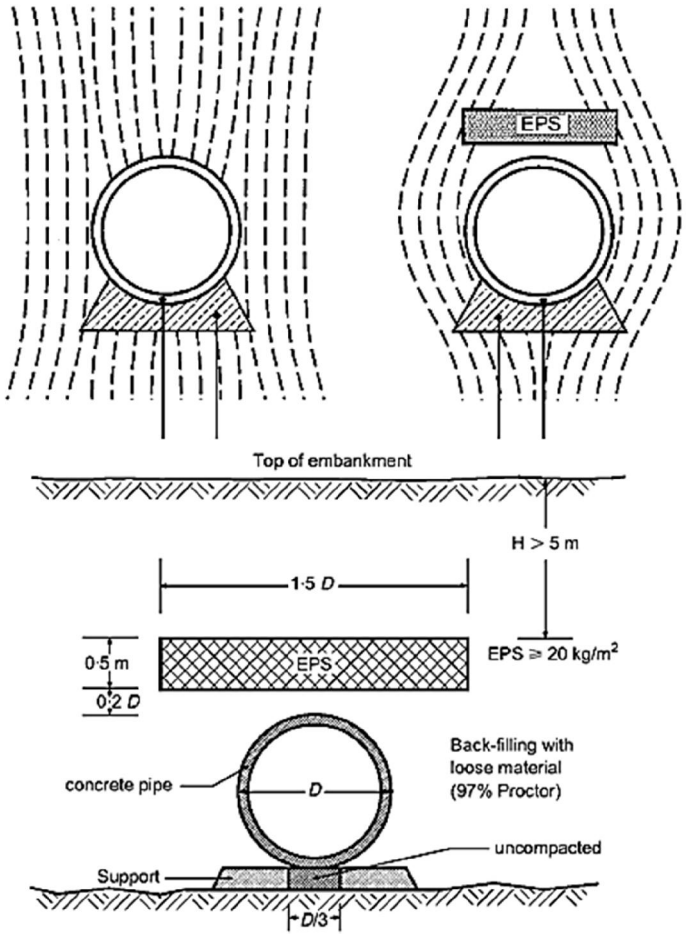

Figure 2-19 Applications of EPS geofoam to reduce vertical overburden stress on pipelines (Beinbrech and Hohwiller, 2000)

The damping characteristics of the geofoam make it a feasible choice for impact and vibration isolation. Placement of a geofoam layer beneath the railway tracks and additionally placement of vertical geofoam layer in front of the basement of the buildings subjected to railway traffic vibrations may attenuate ground borne vibration disturbance. In Figure 2-20, application of geofoam for vibration reduction purposes were depicted. Beinbrech and Hohwiller (2000) report the construction of geofoam vibration barriers for railroad tracks in Grenoble. Entire track bed of a portion of a light transit railway system which was passing through a business and residential district was filled with EPS geofoam. Measurements indicated that an improvement of 24dB in the critical frequency range of 20Hz to 40Hz was observed in structure-borne noise along the portion of the railway isolated with compressible geofoam inclusion. Trenches filled with low acoustic impedance properties such as EPS are proved to be very effective in preventing

propagation of vibratory forces by reducing the amplitude of Rayleigh waves (Davies, 1994), (Itoh, et al., 2005). In a more recent study, Murillo et al. (2009) conducted centrifuge testing to investigate the effect of vertical trenches filled with EPS geofoam on transmission of traffic induced vibrations in soils. The vibration reduction was quantified by a ratio (A_{RR}). Results indicated A_{RR} ratios between 0.2 to 1.8 depending on the barrier depth and the distance between the source and the barrier.

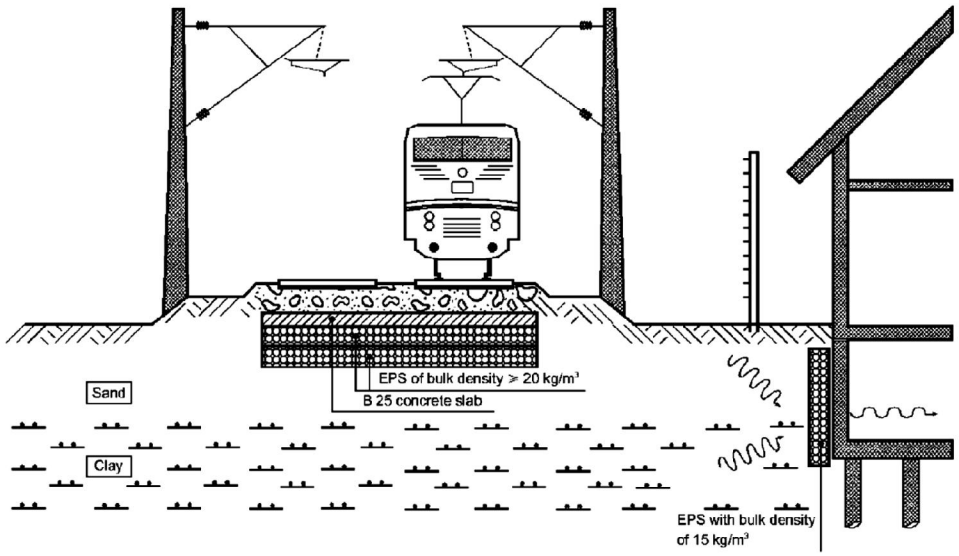

Figure 2-20 Vibration isolation of a building from a railroad activity in the vicinity of the structure (Beinbrech and Hohwiller, 2000)

Applications of geofoam in geotechnical projects in the USA have become quite popular in the recent years. One of the largest EPS geofoam project in the States was successfully completed during reconstruction of Interstate-15 Highway in Salt Lake City, Utah. A photograph of a lightweight fill application from I-15 reconstruction project is shown in Figure 2-21. Utah Department of Transportation (UDOT) initiated a large construction consortium for the reconstruction of I-15 in the Salt Lake Valley prior to the 2002 Winter Olympic Games (Newman et al., 2010). A 26 km. portion of the I-15 was reconstructed involving several bridges and more than 160 mechanically stabilized earth walls. To accelerate the reconstruction project, novel geotechnical technologies were implemented. These techniques involve lime cement column supported embankments, two stage MSE walls and lightweight embankments with scoria and geofoam products.

Figure 2-21 Lightweight fill application of EPS geofoam in reconstruction project of Interstate-15 in Utah

Authors reported that placement of high embankments had potential to produce primary consolidation settlements of more than 1m at many portions of the construction field due to the high compressibility of soft clays in Salt Lake City Valley. Settlements also carried the risk of damaging important utility lines crossing the Interstate Highway in several locations. Lightweight embankment constructions carried a major role in order to prevent the damage to the infrastructure due to the reconstruction project. To monitor the performance of the geofoam embankments, several portions of the fills were instrumented by researchers from University of Utah and Syracuse University. Horizontal and vertical pressures were monitored in the geofoam fills and underlying soils. Vertical displacements related to the static and creep loading was also monitored through instrumentation arrays for a period of 7 years. The data obtained from these devices at three typical lightweight EPS fill application areas were discussed by Bartlett and Farnsworth (2004).

Newman et al. (2010) compared the measurements of the instrumentation arrays with results of numerical models performed with Fast Lagrangian Analysis of Continua (FLAC) finite difference code. A bilinear material behavior is implemented in FLAC code to take into account the effects of EPS block curvature and resulting initial gap which causes unequal surface contact and stress distribution through EPS blocks. This fact significantly increased the complexity of the numerical modeling process. Results indicated that FLAC

simulations overestimated the stress measurements taken from instrumentation array which is in accordance with the findings of Elragi (2000). In general, FLAC analyses produced reasonably well estimations of field measurements and provide valuable insight into EPS geofoam behavior in lightweight fill applications.

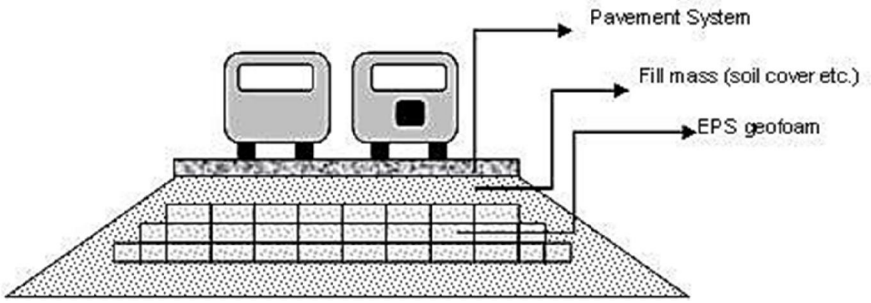

Figure 2-22 A schematic representation of vibration protection and lightweight fill by EPS geofoam in the track bed of light rail system

EPS block geofoam provided successful performance in slope stabilization projects. A typical sketch of EPS-block geofoam used for the slope application is shown in Fig.2.23. In Japan, treatment of slopes by EPS geofoam started from mid-1980's. Performance of EPS-treated slopes was discussed in 1996 during International Symposium on EPS geofoam held in Tokyo, Japan. Based on the available application experience and laboratory testing, a procedure for the use of EPS in slope stabilization was proposed by Tsukamoto (1996). In the United States, slope stabilization projects involving EPS geofoam have also been widespread throughout the continent in the recent decades. Some examples of these projects are Highway 160 in Colorado (Yeh and Gilmore, 1992), Bayfield County Trunk Highway in Wisconsin (Reuter and Rutz, 2001), State Route 44 in Alabama (Alabama Department of Transportation, 2004) and State Route 23A in New York (Jutkofsky, et al., 2000). These case histories demonstrate significant improvements in stability of slopes treated with EPS geofoam. Based on the current state of the art techniques, Arellano et al. (2010) presented a framework for the design of EPS-block geofoam fills for the slope stabilization and repair based on the American National Cooperative Highway Research Program (Stark et al., 2004).

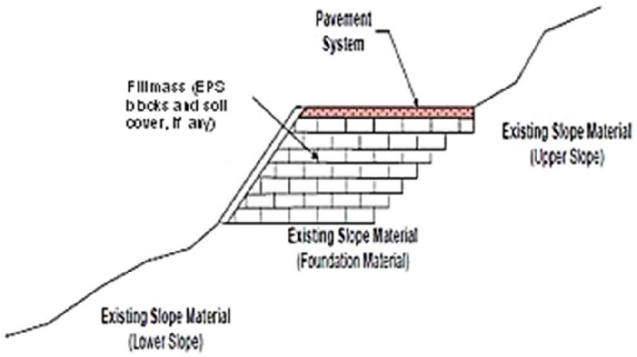

Figure 2-23 Major components of an EPS geofoam slope system (Arellano, et al., 2010)

2.5 Reduction of lateral earth pressures on retaining systems by geofoam buffers

Earth retaining walls can be classified into two broad categories: Non- yielding walls and yielding walls. Non-yielding walls are constrained or incapable against horizontal rigid body displacements and structural deformations due to the design loads (Horvath, 2008). Yielding walls may have the ability to deform and /or displace under earth forces. It is assumed that active stress state was being developed in the backfills retained by yielding walls.

Displacement of the mobilized soil wedge behind a retaining wall is the main factor controlling the lateral earth forces. The amount of displacement required for the backfill material to achieve active state stress conditions depends on the soil strength parameters. Traditional retaining wall design has always focused on reinforcement of the structure to resist the powerful lateral load factors that are exerted by extremely heavy earthen backfills. According to Horvath (1997), a condition called “controlled yielding” is created in the retained soil mass by installing a layer of compressible inclusion behind non-yielding retaining walls. This condition would allow lateral strain in the backfill which leads the mobilization of soil shear strength to achieve active state even if the retaining structure is non-yielding and rigid. As backfill material approach to active stress state as a result of lateral displacements provided by the compression of the less stiff material, lateral forces transferred to retaining structure are reduced (Karpurapu and Bathurst, 1992).

Utilization of geofoam products can provide stress reduction on retaining walls through the following primary mechanisms (Horvath, 2008):

- The lightweight fill function provides stress reduction due to the low density of the geofoam product as compared to the retained soils. The density of a typical geofoam product can be as low as 1% of the natural geomaterials. Strains occurring in geofoam materials are low in typical lightweight fill applications.
- Compressible inclusion function of the geofoam takes its use due to the low stiffness of the material as compared to the retained backfill. The strains in the geofoam material are high compared to the lightweight fill applications.

Materials such as glass-fiber and cardboard have been used in several applications to reduce lateral earth pressures (Rehnman and Broms, 1972); (Edgar et al., 1989). However, Horvath (1997) indicated that stress-strain characteristics of glass-fiber and cardboard are not as predictable as the properties of geofoam and there may be unexpected deformations due to bio-degradation of materials such as cardboard and hay. Contrary to these materials, EPS geofoam does not suffer bio-degradation and unpredictable deformations due to uncertainties in stress-strain behavior. Horvath (1997) reported more than 30 years of proven durability of EPS geofoam in geotechnical applications.

Early applications of EPS geofoam as compressible cushions in geotechnical projects have been documented in Germany during 1970s. Geofoam compressible inclusions were also used extensively in Holland and Japan to reduce stresses acting on buried pipelines due to consolidation settlements of soils as well as earthquake induced lateral stresses on retaining structures (Beinbrech and Hohwiller, 2000). During recent years, use of expanded polystyrene (EPS) geofoam replaced the previous materials used as compressible inclusions. High compression ability of the EPS geofoam provides its use as a compressible inclusion behind retaining walls to reduce lateral pressures. Conceptual sketches for several applications of EPS geofoam to reduce earth forces are depicted in Figure 2-24. Deformable geofoam buffers of low stiffness installed against the rigid retaining structure compress under the lateral earth pressures exerted by the retained soil mass. This process of controlled yielding will allow for a certain lateral deformation of the retained soil

mass thus mobilizing the soil shear resistance and bringing the soil mass close to the active failure state (Horvath, 2008).

Field experiments demonstrated the significant effect of compressible inclusions in reducing the lateral earth pressures behind rigid non-yielding retaining walls (Partos and Kazaniwsky, 1987). Matsuda et al. (1996) reported the application of a 0.5-m strip of EPS geofoam to reduce the static earth pressure acting on a 14-m high bridge abutment. Their results from finite-element analyses showed 85% reduction in overall bending moments along the bridge abutment for a geofoam density of 12 kg/m^3, and 70% reduction for a geofoam density of 20 kg/m^3. Additionally, numerical sensitivity studies based on finite-element analysis addressing the static load reduction on rigid walls with geofoam inclusion have been reported in the literature (Karpurapu and Bathurst, 1992), (Trandafir et al., 2010b), (Ertugrul and Trandafir, 2011).

In a recent study, Ikizler et al. (2008) carried out small scale physical lab tests to investigate static earth pressures against rigid non-yielding walls in expansive soils. According to their experimental results, placing a geofoam panel between the retaining wall and backfill was effective in reducing the lateral earth pressures due to swelling. In a more recent study, Trandafir et al. (2010a) presented the results of a finite element modeling study discussing the reduction in horizontal earth pressures against a 9-m high rigid wall with a 0.6-m thick EPS panel against the wall, retaining a cohesionless soil mass.

It is noteworthy that most of the studies addressing the use of compressible inclusions behind earth retaining structures were concerned with the controlled yielding of the backfill material against rigid non-yielding walls, whereas only a small number of published papers deal with the potential use of compressible inclusions behind yielding and flexible walls. In earlier investigations, Mcgown and Andrawes (1987) and (McGown et al., 1988) had shown that the lateral earth pressures acting on yielding walls retaining unreinforced and reinforced backfills may be reduced to minimum by controlled lateral boundary yielding.

In a more recent study, Hatami and Withoeft (2008) pointed out that there is a significant potential for using geofoam to reduce lateral earth pressures on mechanically stabilized earth (MSE) walls. According to the results of their numerical analyses, placing geofoam panels behind the reinforced zone of flexible

MSE walls can reduce the lateral earth pressures by up to 50% depending on the geofoam thickness and stiffness.

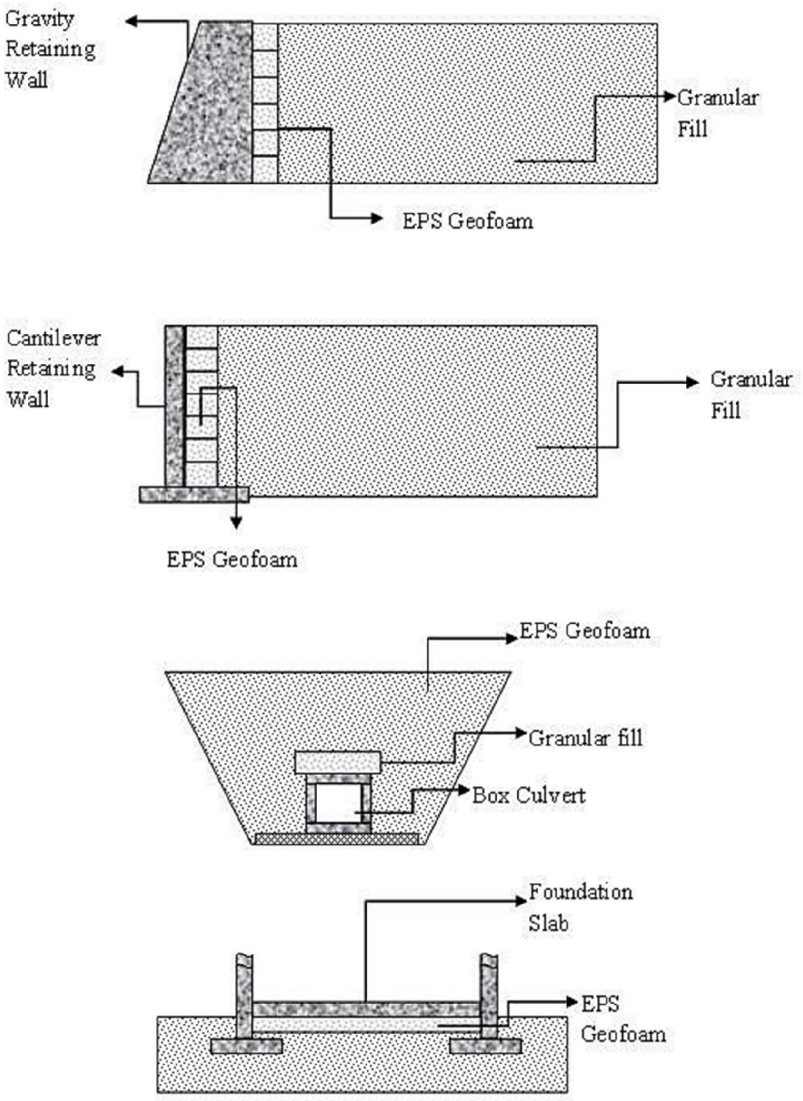

Figure 2-24 Common applications of EPS geofoam in order to reduce earth forces

2.6 Physical and numerical modeling studies on the reduction of static lateral earth pressures

McGown et al. (1988) investigated the effect of wall flexibility and presence of compressible inclusions on lateral earth pressures. Results of small scale model tests performed in University of Strathclyde were discussed in this study. In the

laboratory tests, a pin model served as a two dimensional analogue to sand backfill to a 0.5 m high yielding wall. The pin model was considered as a suitable representation of two dimensional plane strain geometry of a retaining wall. In this model, brass pins with diameters of 2, 3 and 4 mm and length of 70.5 mm were stacked as the backfill material. Shear box tests performed on the brass rods indicated a friction angle of approximately 26° which was similar to that of loose sand. From these studies, principal idea of using a compressible inclusion between the retained backfill and retaining wall was developed.

Horvath (1991a) carried out finite element analyses of an idealized 3m high rigid wall to investigate the effect of geofoam thickness on the lateral forces. According to their study, presence of an inclusion having a thickness of 1.67% of the wall height could reduce the lateral pressures on a rigid wall retaining unreinforced backfill as low as active stress conditions estimated by Rankine's theory. Presence of an inclusion having thickness of 20% of the wall height further reduced the lateral forces compared to the first case. It is also indicated that combination of the geofoam with stiff reinforcements in the retained soil reduced the lateral earth pressure acting on the wall to negligible values. In the same study, Horvath (1991a) introduced the concept of "Reduced Earth Pressure Wall (REP-Wall)" instead of the generic use of compressible inclusion. In this approach, the basic idea is to match the displacement of the retained soil mass required to mobilize the active state of stress by the deformation of the compressible inclusion (Figure 2-25). The deformation of the compressible material installed between the wall and the backfill depends on the stress-deformation characteristics of the material. Horvath (1997) indicated the potential use of REP-Wall concept on existing inadequately constructed retaining structures as well as new constructions. Author proposed placing a compressible inclusion between the wall and the retained soil to induce controlled yielding of the soil. This technique was considered to be more cost-effective alternative compared to rebuilding the existing structure according to modern design criteria. It was reported that this method has been verified by several small-scale model tests, large scale model testing at instrumented retaining walls and numerical modeling studies.

In a following study by Horvath (1991b), efficiency of the geofoam compressible inclusion for a retained backfill with a surcharge is investigated. Analyses results showed that structural demand for a rigid retaining wall subjected to surcharge

loading on the backfill is substantially reduced by usage of compressible inclusions.

Karpurapu and Bathurst (1992) performed a numerical modeling study in order to simulate the results of small scale model tests performed in the University of Strathclyde. After validating a numerical code, they performed numerical parametric studies to develop a series of design charts for the selection of thickness and stiffness of a compressible inclusion in order to initiate static active stress conditions in the soil for a given wall height and soil type.

Hatami and Withoeft (2008) investigated the efficiency of geofoam inclusions to reduce lateral earth pressures behind the reinforced zone of mechanically stabilized earth walls (MSE walls) by using FLAC Finite Difference Code (Figure 2-26). The constitutive model which they have used in the study was validated against the small scale test results of MSE walls performed in the University of Strathclyde. FLAC predictions and the measured results were in harmony for all the model configurations. The results of their study indicated significant reduction on lateral earth forces acting on the reinforced soil mass depending on the thickness and stiffness attributes of the geofoam panels. The lateral thrust and overturning moments decreased as much as 31% and 26%, respectively. The results of this study indicated that even in flexible earth structures such as MSE walls, inclusion of a compressible geofoam layer would result in beneficial effect on lateral wall pressures and displacements.

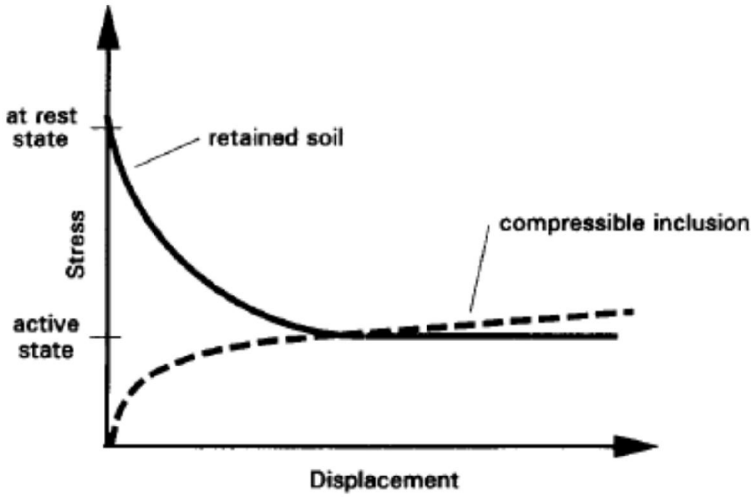

Figure 2-25 REP-Wall Concept (Horvath, 1997)

2.7 Function of EPS geofoam materials as seismic buffers behind the retaining systems

Retaining structures play an important role in the modern infrastructure such as transportation systems, energy plants, lifelines, and several other constructed facilities. Although these structures are prone to catastrophic failures during earthquakes due to excess dynamic earth pressures, design of retaining systems against seismic loads does not take enough importance in several projects. Considering the damage of the devastating earthquakes on retaining structures, seismic performance improvement of the retaining structures against seismic hazard is of utmost importance.

In seismic design of retaining structures, traditional approaches generally provide limited predictions on soil movements and interactions between soil and structure. On the other hand, appropriate design against the increased lateral and seismic earth forces may result in significant increase in the construction costs. Hence, new innovative methods or design procedures are becoming a necessity besides the conventional approaches in seismic design of retaining walls. In this context, seismic isolation of retaining structures by compressible inclusions has evolved as an extension of the theory on reduction of static earth pressures (Athanasopoulos et al., 2007). Typical application of EPS geofoam seismic buffers are shown in Figure 2-27. Based on the results of the studies on static earth force reduction by compressible inclusions, utilization of expanded polystyrene geofoam as seismic buffer between the wall and the backfill could be beneficial hence the structure will interact with the backfill soil through a hybrid type of interaction mechanism occurring during the earthquake excitation (Hazarika et al., 2003).

Implementation of compressible inclusions on existing aseismically designed retaining structures is quite feasible in terms of application time and effort as compared to rebuilding the existing structure. Inglis et al. (1996) documented the first field use of a compressible inclusion in order to reduce earthquake induced forces against a rigid basement wall. EPS geofoam boards with varying thicknesses were installed against a 9m high basement wall at site in Vancouver, Canada.

Hazarika (2001) reported that EPS geofoam can provide lower seismic forces when used behind retaining walls hence it may be considered as a cost effective solution in the earthquake resistant design of soil retaining facilities. Author

indicated that survey studies performed in ten different sites in Kobe, Japan after Hyogo-ken Nanbu earthquake revealed that none of the structures supported by EPS geofoam suffer any direct damage due to the earthquake. Laboratory experiments and field studies have been performed in various research institutes in Japan in order to assess the short and long term behavior of EPS geofoam and its earthquake resistant performance. Based on the outcomes of these studies, a seismic design method using EPS geofoam was placed in current Japan earthquake resistant design code.

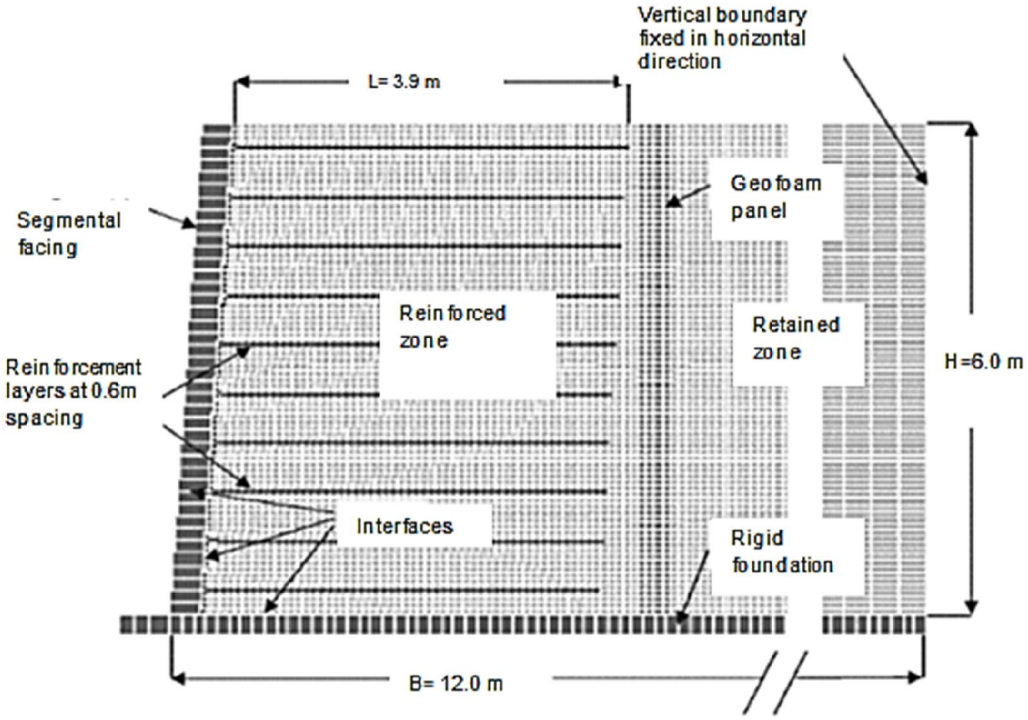

Figure 2-26 FLAC numerical grid (Hatami and Withoeft, 2008)

According to the damage assessment studies performed for the earthquakes occurred in 1994 and 1995 in Japan, the performance of geotechnical structures involving EPS geofoam were found to be satisfactory in most of the cases (Hotta et al.,1996) and (Kuroda et al., 1994). During Hyogo-Ken-Nanbu Earthquake, several infrastructural elements of the Kobe City were damaged. Embankments made of lightweight EPS geofoam fills resisted to earthquake forces and no direct damage was observed due to failure of geotechnical structures where EPS geofoam was used as a construction material.

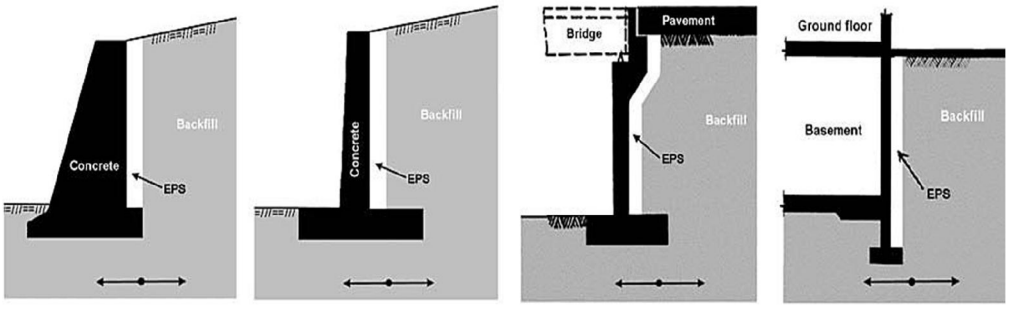

Figure 2-27 Use of EPS geofoam buffers for reducing seismic lateral forces (Athanasopoulos et al.,2007)

2.7.1 Physical modeling studies related to performance of geofoam seismic buffers

Hazarika et al. (2003) performed 1-g shake table tests on rigid and non-yielding reduced scale retaining wall models. Dynamic wall pressures were measured in the absence of a compressible buffer and with a compressible cushion installed between the back face of the rigid wall and the backfill. Uniformly graded fine dry Toyoura sand was used as backfill material. Shaking table used in the experiments was square shaped with sides being 1.5m long. Actuator system was capable of providing simultaneous horizontal and vertical excitations to a mass of 1 tons up to an acceleration level of 1.5g in a frequency range of 0Hz to 100 Hz. In the experiments additional surcharge of 4.5kPa was applied with an air mat to increase the vertical stress levels in the backfill. This additional vertical stress would help to measure earth pressures with higher resolution. The instrumented model walls were excited with a frequency of 3.3 Hz for a period of three minutes. Test setup used in 1-g tests is depicted in Figure 2-28. Four different wall models were tested in this study to investigate the effect of geofoam buffer layers on dynamic earth forces. In the control test, only cohesionless backfill existed behind the retaining wall model. In the following tests, cushion layers having thicknesses of 0.02*H*, 0.05*H* and 0.08*H* were installed behind the wall model In all of the tests, surcharge load of 4.5kPa was applied by using an air mat, however confining stresses were quite low for initiating deformations in the geofoam cushions required to mobilize the soil wedge. Due to this reason, urethane was utilized as the compressible inclusion in the tests. The density of urethane used in the tests was 22kg/m^3, and the elastic modulus of the material was 1/40th of the elastic modulus of EPS geofoam having the same density. In Figure 2-29, time histories for the lateral stresses recorded at the base of the model wall were compared for

two cases and it is observed that presence of urethane provided significant reduction in total dynamic pressures. Authors indicated that an increasing trend was observed in the lateral stresses as the backfill relative density increases due to vibration densification for the case without compressible inclusion. However, the presence of a compressible cushion with a thickness of 0.08*H* significantly affects the lateral stresses. The reduction efficiency of the seismic cushions increase with an increase in the relative density of the backfill. Same tendency was observed for all of the acceleration levels tested (0.2g to 0.8g). Although the results provide a good understanding on the function of compressible inclusions on earth pressures, one important shortcoming of carrying out the tests with urethane arises due to the difference between the constitutive behavior of the EPS geofoam and urethane.

Bathurst et al. (2007a) performed 1-g shake table tests to investigate effect of vertical compressible inclusion on dynamic lateral earth pressures. Rigid wall models of 1m height were tested in their study. Cross section of the test setup was depicted in Figure 2-30. Physical tests were conducted on a 2.7m by 2.7 m shaking table located at Royal Military College of Canada. Maximum displacement capacity of the hydraulic actuator of the shaking system was ±75 mm. Maximum payload can be excited up to ±2g at a frequency range of 1-13 Hz. Wall models were located in a strong box with dimension of 2.5m×1.4m×1.3m (length, width, height) which was rigidly connected to the shaking table.

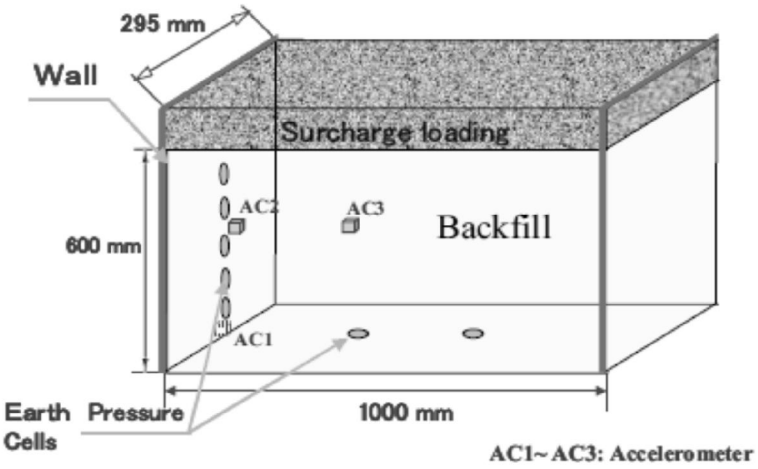

Figure 2-28 Test setup (Hazarika and Okuzono, 2004)

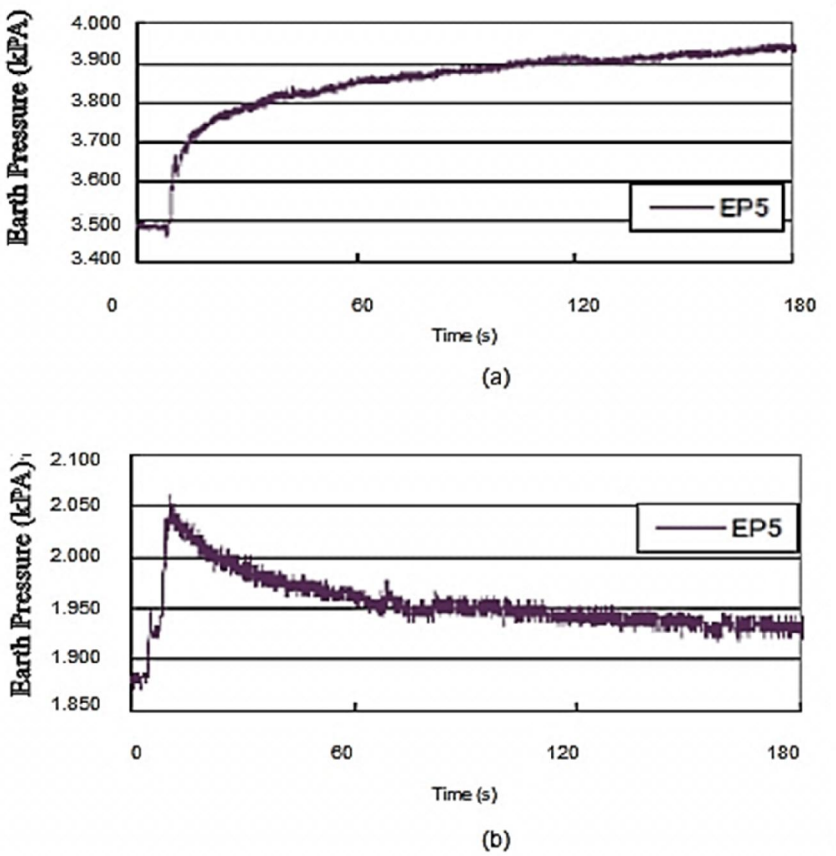

Figure 2-29 Stress time histories at wall base for 0.4g excitation (a) no compressible inclusion (b) cushion thickness of 0.08H (Hazarika et al., 2003)

Use of friction reducing membrane on rigid lateral bracings helped to provide plane strain boundary conditions. Excitation was applied only in the horizontal direction. The dimensions of the backfill were selected to prevent any interference with a potential wedge formation which can be computed by Mononobe-Okabe analysis. The sides of the box were rigidly braced which can be considered as an energy reflecting boundary. Dry silica free olivine sand having unit weight of 15.5kN/m^3 was retained as backfill material during the tests. It was composed of angular to sub-angular particles with specific gravity of 2.88. Three commercially available EPS materials with densities of 16 kg/m^3, 14 kg/m^3 and 6kg/m^3 materials were tested in their study. Elastic modulus values of the material ranged between 1.6MPa to 4.7MPa according to manufacturer's literature. The first material (density of 16kg/m^3) was classified as Type I according to ASTM-C 578-06 Standard Specifications. The second product was an elasticized type EPS geofoam. The linear elastic range of this material was significantly high as compared to regular EPS geofoam used in geotechnical applications. Non-elasticized EPS products have a linear elastic range up to 1% whereas the

behavior of the elasticized EPS is linear up to 40%. However, the yield strength of the elasticized EPS was lower compared to the regular EPS having the same density. The third product was in Type IX range according to ASTM-C 578-06. The density of the material was lowered from 12 kg/m^3 to 6 kg/m^3 by partially coring the EPS boards before installing on the wall model.

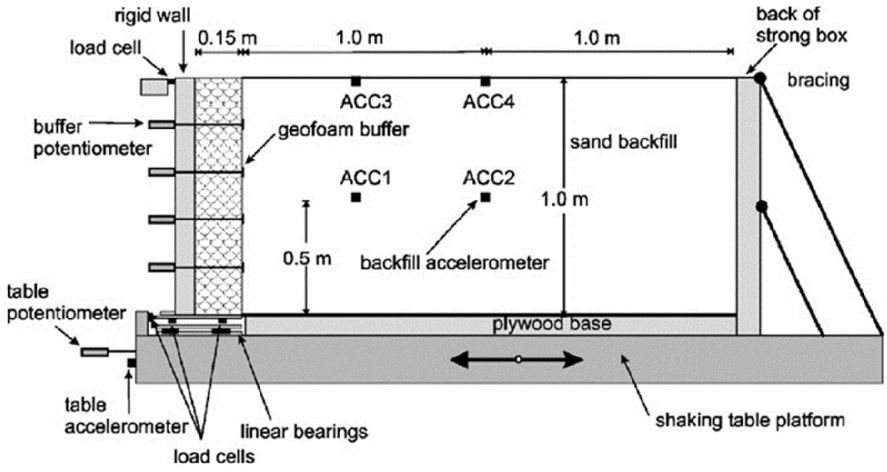

Figure 2-30 Cross-section of the test arrangement and the related instrumentation (Bathurst et al., 2007a)

The initial tangent modulus values of the EPS materials were estimated as 4.7MPa for the type I material, 0.27MPa for elasticized EPS and 1.6MPa for type IX material (50% of the material removed). In another study carried on by Zarnani and Bathurst (2009a), the results of the tests performed by Bathurst et al. (2007a) were replicated by a numerical model made by using FLAC software (Itasca 2008). In this study, the elastic modulus values of the EPS geofoam were back calculated as 4.8MPa for the type I material, 1.30MPa for elasticized EPS and 0.6MPa for type IX material. Seven different wall configurations were tested with first one being the control test configuration without buffer. Placement of the EPS cushions was depicted in Figure 2-31. During the tests, sand was placed in lifts of 200mm. Compaction of each lift was achieved by applying a base excitation for a duration of 90 seconds at 9 Hz frequency and peak acceleration amplitude of 0.1g. A total of 19 measurement instruments were placed in the model to obtain the lateral pressures on the wall, the accelerations throughout the backfill and the displacements of the wall and rigid box. Models were excited by a stepped-amplitude sinusoidal acceleration time history with a frequency of 5Hz. The maximum base acceleration was 0.8g. According to the author, this excitation record would affect the retaining wall more aggressively compared to an

equivalent true earthquake record. The excitation with 5Hz frequency for a 1/6 scale model was interpreted as 2Hz at the prototype scale considering the scaling relationships provided by Iai (1989). According to the authors, this would be representative of medium to high frequency earthquakes and meet the required parameters for the North American seismic design codes. Results of the study indicated that rigid retaining structures with a deformable buffer were exposed to lower horizontal loads than the ones without seismic buffer. The geofoam buffer with smallest density provided the highest reduction in dynamic forces. Reduction ratio reached up to 31% for the peak acceleration amplitude of 0.7g.

A more recent study was performed on the effects of deformable cushions on seismic displacement of the gravity quay walls (Moghadam et al. 2009). 1-g model tests were performed on models of caisson quay walls. The walls were tested for backfill only and with deformable buffer cases. Crushed silica sand (e_{max}=0.943 and e_{min}=0.603) was used as the backfill. Angle of internal friction was determined as 40°. The dimensions of the prototype caisson wall were designated as 12 meters in height and 7 meters in width. Displacement reducer panels were made of hollow polypropylene sheets of 3 mm thickness which are commercially being used in packaging industry. Researchers indicated that the polypropylene material does not produce enough stiffness and durability for the real scale geotechnical applications however it is a good alternative of EPS geofoam in the model tests to produce compression deformations in the cushion layer considering the low confining stresses due to limited height of the model wall. In the dynamic tests, model test setup was excited with sinusoidal base motions with 3 Hz and 8Hz frequency for duration of 10 seconds. According to the scaling relationships proposed by (Iai 1989), the base motion accounts for low frequency earthquake excitations.

(a)

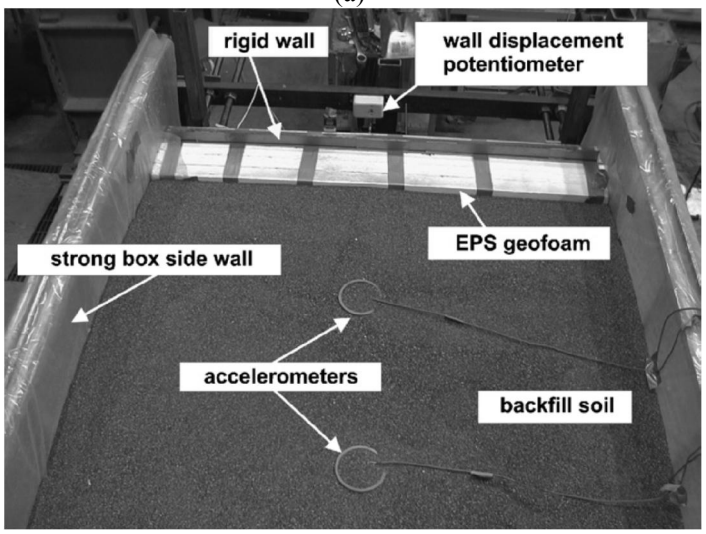

(b)

Figure 2-31 (a) Placement of EPS buffer (Bathurst et al., 2007a) (b) Sandwiched geofoam buffer

The results of the tests were discussed qualitatively since precise scaled-down models couldn't be obtained due to the complexity of soil and structural behavior. Results indicated that deformation cushions effectively reduce lateral deformations induced by the seismic forces. Performance of the compressible cushions increases as the compression of the cushion increases. The behavior observed in the tests was reproduced by numerical analyses with a good correlation.

2.7.2 Numerical studies related to performance of geofoam seismic buffers

Hazarika (2001) performed numerical modeling studies to investigate the effect of geofoam as a compressible seismic buffer for retaining walls. In their study, 10m high retaining wall models retaining dry cohesionless backfill material was subjected to harmonic loads as well as an earthquake loading similar to Hyogo-ken Nanbu earthquake excitation. Yielding and non-yielding type walls were simulated in the numerical study. Non yielding wall model was restricted against translation and rocking, whereas yielding wall models are free to make lateral translation and rocking motion around the top. Harmonic motions have 0.2g acceleration amplitude with 3.5Hz frequency. The North-South component of the Hyogo-ken Nanbu Earthquake recorded at Port Island in Japan was scaled to 0.2g to and applied as earthquake input motion. Numerical Rayleigh damping was applied to take into account of soil damping. A special constitutive model was developed and used based on localization of the materials. Comparison of the lateral forces for the presence and absence of the EPS geofoam inclusion are depicted in Figure 2-32. Lateral earth pressure profile for the upper one fifth of the wall did not exhibit significant variation for the EPS buffer and no buffer cases; however stresses are observed to decrease significantly with increasing depth for the EPS geofoam case. Authors attribute this decrease to the effect of confining stress on the EPS behavior.

Armstrong and Alfaro (2003) carried out numerical analyses with FLAC code to investigate the lateral thrust reduction efficiency of 10m high rigid retaining wall (Figure 2-33). Analyses were repeated for two different backfill interface friction angles (30° and 35°) and four different buffer thickness values (250mm, 500mm, 750mm and 1000mm). Initial elastic modulus of the geofoam material having a density of 30 kg/m^3 was taken as 4MPa and Poisson's ratio is considered as 0.1. Rayleigh damping of 5% was applied to the system in order to simulate the damping behavior of the geomaterials. Sinusoidal dynamic excitation was applied to the base of the system as a velocity time history having peak velocity amplitude of 0.2m/s and 1.5Hz frequency. Results were given in terms of lateral stresses normalized with vertical pressures in order to assess the effect of EPS inclusion for various thickness values (Figure 2-34).

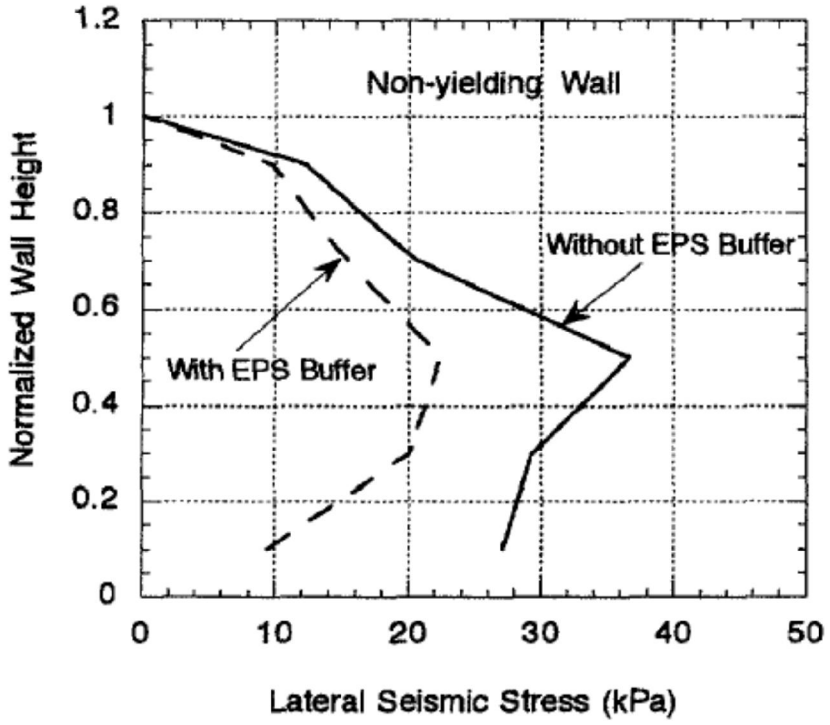

Figure 2-32 Seismic lateral force with and without compressible inclusion (Hazarika, 2001)

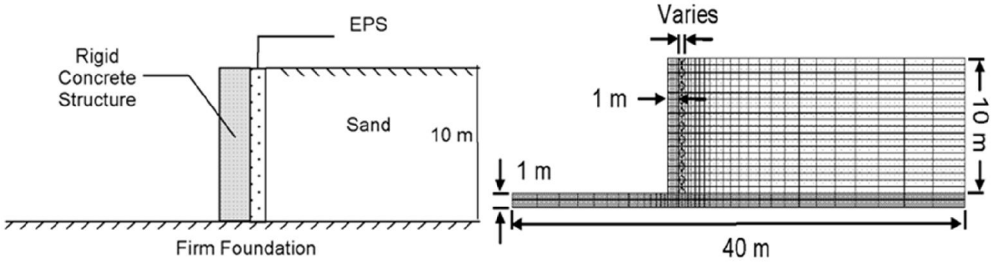

Figure 2-33 Numerical idealization of the problem (Armstrong and Alfaro, 2003)

According to the results of the numerical modeling study, presence of a compressible inclusion provided reductions in the passive seismic thrust acting on the wall model however it did not affect the active seismic thrust significantly. There was a limiting thickness of deformable buffer at which no significant additional reduction is observed in seismic thrust values. The stress distributions on the walls were in agreement with the values calculated using the method proposed by Zhang et al. (1998).

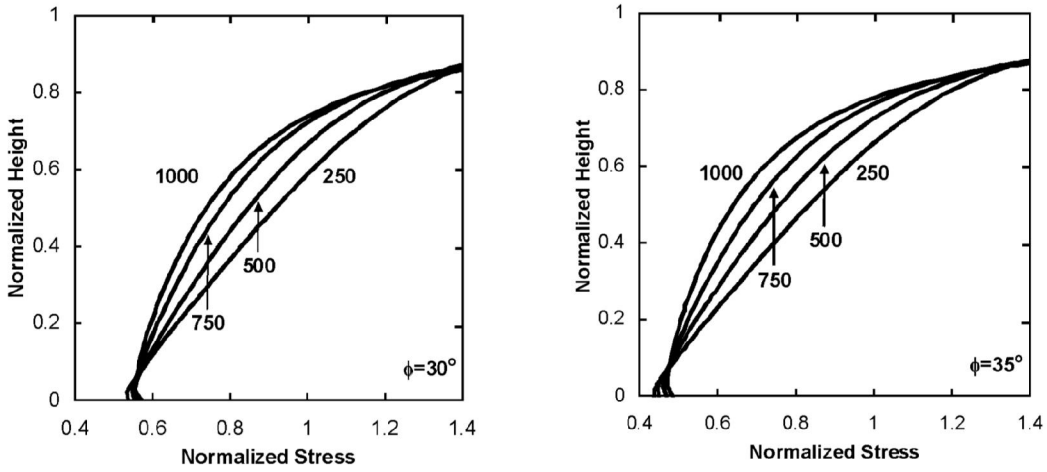

Figure 2-34 Normalized stress profiles for various inclusion thicknesses (Armstrong and Alfaro, 2003)

Athanasopoulos et al. (2007) investigated the efficiency of EPS compressible buffers by numerical seismic response analyses. The idealized wall models were excited with harmonic base motions of varying frequency and amplitude. To validate the numerical model, small scale shaking table tests carried out by Zarnani and Bathurst (2007) were simulated. Comparison of the wall thrust with and without EPS inclusion were shown in Figure 2-30. A satisfactory agreement was observed between the results.

In another study, Athanasopoulos et al. (2007) conducted a series of numerical analyses to investigate various parameters that may affect the response of the retaining walls with deformable EPS geofoam buffers. In the analyses, nonlinear material behavior models were assigned to the retained soil and the EPS geofoam installed between the vertical wall and the backfill. Hysteretic damping of the soil and the geofoam were taken into account. Damping curve for the EPS geofoam of this study was constructed based on the data obtained through resonant column (for small strains) and cyclic triaxial tests (moderate to large strains). The wall was modeled as a vertical elastic beam with some finite rigidity. The frequency of the input excitation ranged from 0.5Hz to 20Hz whereas the amplitudes of the harmonic acceleration records were taken as 0.1g, 0.3g, and 0.5g, respectively. Several parametric analyses were carried out to investigate the effect of the shape and thickness of the compressible inclusion, flexibility of the wall height and attributes of the input excitation on isolation efficiency.

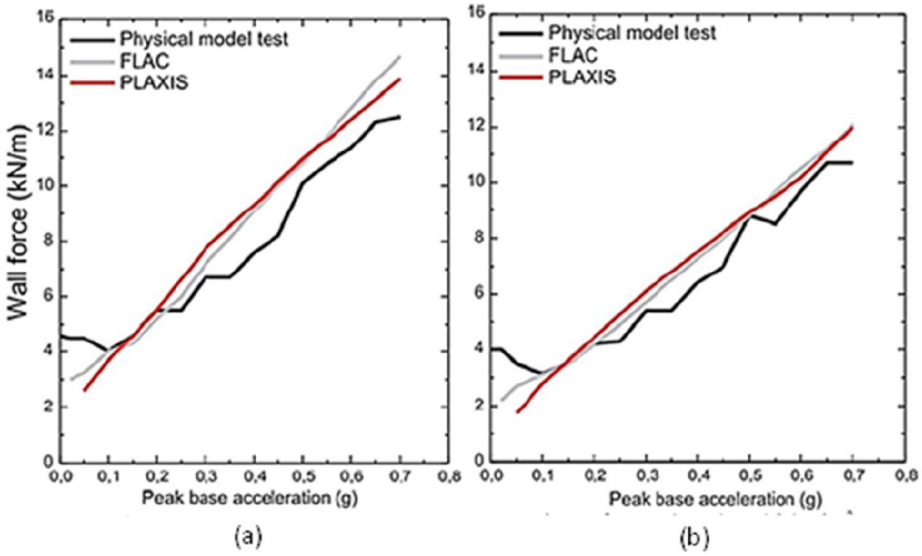

Figure 2-35 Comparison of measured and calculated earth forces in the shaking table test (a) no geofoam buffer (b) with geofoam buffer

Results were quantified by the isolation efficiency ratio (defined as the ratio of the seismic thrust with EPS case to the seismic thrust without EPS inclusion). In the finite element simulations, wall height varied between 4m to 8m whereas the thickness of the geofoam inclusion varied between 0.05H to 0.4H. Analyses were repeated for three different geofoam densities (15 kg/m^3, 20 kg/m^3 and 25 kg/m^3). Effect of wall flexibility on the isolation efficiency was investigated by modifying the stiffness of the structural elements. It was found that the isolation efficiency for a flexible wall is 16% better compared to a perfectly rigid wall case. As another note, increase in the wall height caused a reduction in isolation efficiency especially for stronger base acceleration amplitudes. However, the validity of this observation may be questionable hence the natural frequency of the wall-backfill system changes as the wall height increase. Deformable buffers exhibit good isolation performance when the predominant frequency of the input motion remains less than 30% or greater than 200% of the fundamental frequency of the system. The results have revealed that the isolation efficiency was reduced sharply in the vicinity of the fundamental frequency of the system. Authors indicated that low stiffness of the geofoam is the main factor affecting buffer performance. Density of the deformable material was not observed to affect the load attenuation for the two identical cases where the stiffness of the geofoam was kept constant and the density was varied. In this study, design charts were proposed for the selection of the inclusion properties for 50% reduction of the

seismic wall thrust. Results of a recent numerical modeling study related with the seismic performance of EPS geofoam buffers were reported by Zarnani and Bathurst (2009a). The influence of geofoam properties, buffer thickness, wall height, and attributes of the base excitation on response of rigid non-yielding retaining walls was investigated in this study. Geomaterials were modeled with elastic perfectly plastic Mohr-Coulomb yield criterion. Different from the study conducted by Athanasopoulos et al. (2007), varying amplitude sinusoidal base accelerations were used as the input excitations. Analyses were carried out by FLAC v.5 code (Itasca, 2008). Rigid non-yielding wall model did not possess any lateral or rotational degrees of freedom. In the simulations, wall height varied from 1m to 9m. Dimensions of the finite difference mesh were selected based on the previous experience of the researchers on the modeling reinforced soil retaining walls. The width of the grid was taken as five times of the model height. Authors indicated that this ratio is an optimum value in terms of computation time and disturbance of the results due to the size of the geometry. To minimize the effect of grid size, same grid density was selected in all of the analyses. The relative thickness (*t/H*) value was designated as the ratio of the inclusion thickness to the wall stem height and relative thickness values were taken as 0.025, 0.05, 0.1, 0.2 and 0.4. Backfill was modeled as an elasto-plastic material with Mohr-Coulomb failure criterion. The fundamental frequency of the backfill was calculated by considering the one dimensional linear elastic assumption as well as using the relationship suggested by Wu (1994) for two dimensional models. Based on the classification of ASTM D6817-06 (ASTM, 2006), physical properties of EPS19, EPS22 and EPS29 type geofoam having minimum density values of 18.4 kg/m^3 , 21.6 kg/m^3 and 28.8kg/m^3 were considered in the numerical analyses. Mechanical behavior of EPS geofoam was simulated with linear elastic model. Yield strength, Young's modulus, and Poisson's ratio values of the EPS geofoam were estimated using the correlations given by (Horvath 1995). Zero thickness interface elements were introduced in the model in order to simulate the interaction of the geofoam with wall and the retained soil. Based on the previous experimental study of Zarnani and Bathurst (2007), interface friction angle between the geofoam and the backfill was back-calculated as 20°. Interface normal and shear stiffness parameters were selected to optimize the calculation speed and stability of the numerical method. In the analyses, a variable amplitude sinusoidal excitation record was selected because of the relative simplicity of this type of record compared to an actual earthquake accelogram. Authors indicated

that a harmonic type excitation with a constant or stepped acceleration amplitude is more aggressive compared to an actual earthquake record with the same peak acceleration level. This horizontal acceleration record was applied to the base of the system and the two vertical boundaries of the model. Peak acceleration amplitude was 0.7g and frequency range of the excitation was varied between 0.7Hz to 21 Hz. Comparison of the buffer performance was made through isolation efficiency ratio. This parameter was computed as the difference of the total thrust acting to the wall with and without geofoam buffer. Evolution of lateral wall forces for a 3m high wall was depicted in Figure 2-36 (Zarnani and Bathurst, 2009a). The positive role of EPS geofoam on reducing lateral wall forces can be clearly observed in this figure. Presence of the geofoam layer having a thickness of 5% of the wall height provided more than 25% reduction of thrust. Further increase in layer thickness contributes to reduction efficiency however the rate of reduction decreases. In Figure 2-37, isolation efficiency of geofoam inclusions for various frequencies of the base excitation was depicted (Zarnani and Bathurst, 2009a). A decreasing trend was reported in efficiency values when base excitation frequency approaches to the natural frequency of the wall-soil system. The thickness of the geofoam inclusion is found to be effective in dynamic lateral force acting on the wall. Approximately 40% reduction was observed for a seismic buffer having thickness of 0.2H. Authors observed that the type of geofoam does not cause significant change in the response for walls excited below their fundamental frequency. Additionally, it was reported that increasing buffer thickness causes an increase in the isolation efficiency of the inclusion. Researchers also suggested use of geofoam materials having stiffness values smaller than 50 MN/m^3 for efficient reduction in lateral seismic forces.

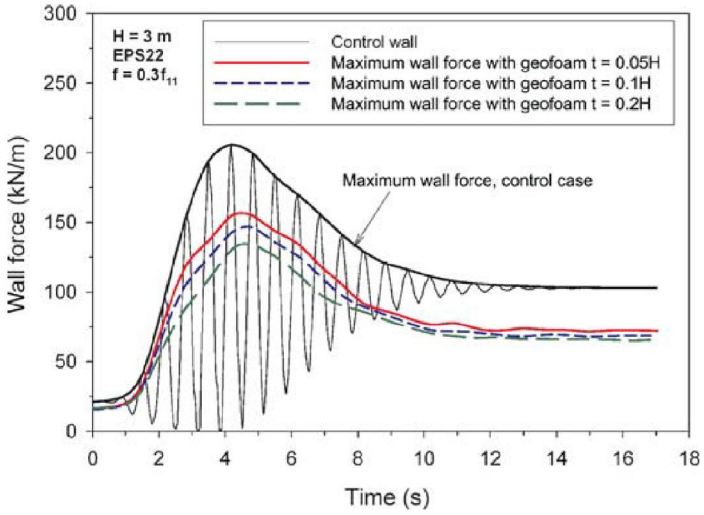

Figure 2-36 Evolution of wall thrust for 3 m high wall (Zarnani and Bathurst, 2009a)

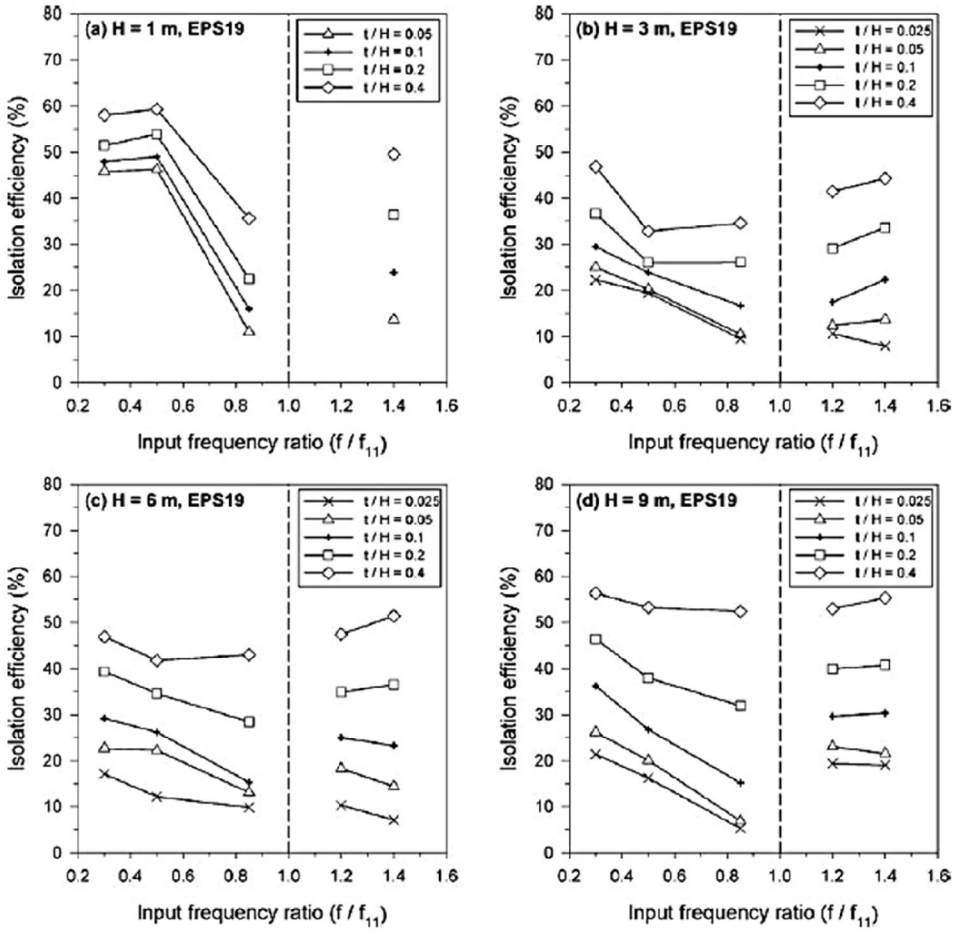

Figure 2-37 Isolation efficiency values for different predominant frequency of input motions (Zarnani and Bathurst, 2009a)

Trandafir et al. (2010b) performed finite element simulations for 9m high retaining wall with a deformable geofoam buffer of 0.6m thickness installed vertically against the wall (Figure 2-38). The purpose of the study was to address the reduction of lateral earth pressures acting on rigid non-yielding earth retaining walls. In their study, the cohesionless backfill was modeled as an elasto-plastic material designated with Mohr-Coulomb yield criterion. Properties of the buffer were selected based on the static and dynamic uniaxial tests performed by the authors. Analyses indicated that computed stresses in the backfill and the compressible inclusion remained in the elastic range for the investigated case. The results of their finite element analyses provided a framework for a laboratory study performed to investigate the dynamic properties of the EPS geofoam.

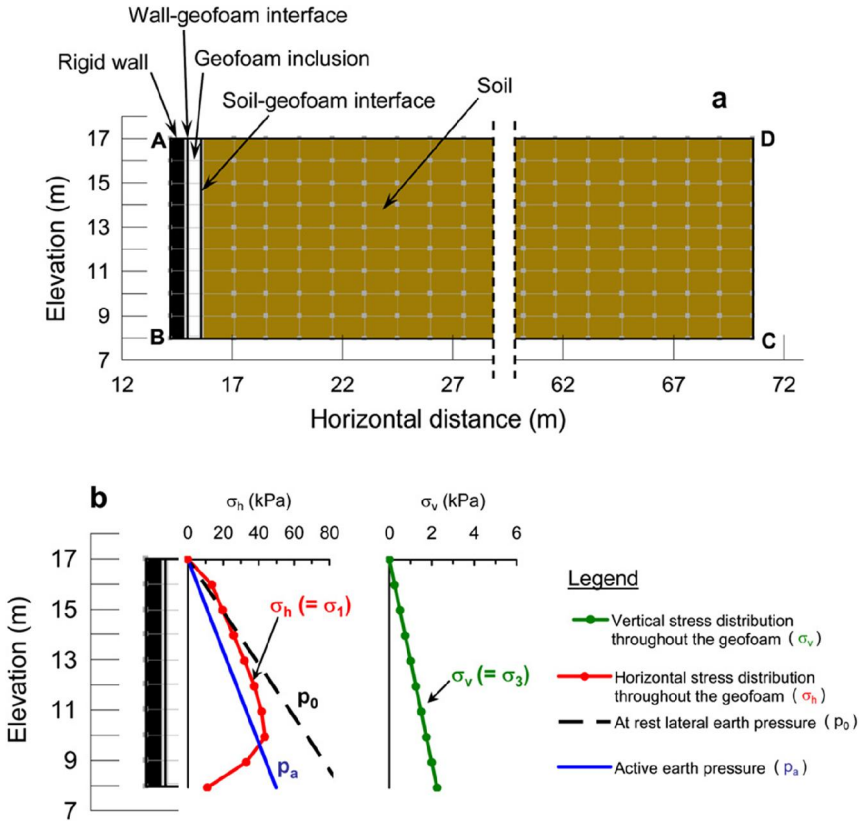

Figure 2-38 (a) Finite element model and (b) the comparison of the lateral stresses with theoretical values (Trandafir et al., 2010b)

2.7.3 Analytical studies related to performance of geofoam seismic buffers

The first analytical model proposed to estimate the thickness of the geofoam compressible inclusion for a certain type of wall height and backfill conditions was proposed by Partos and Kazaniwsky (1987). The current version of the equation for determining deformable buffer thickness (t_{ci}) was reported by Horvath (2008) as:

$$t_{ci} = \frac{E_{ci}.(\Delta_a/H)}{0.75.K_a.cos\ \delta.\gamma_t} \quad \text{2-17}$$

where E_{ci} = the Young's modulus of the geofoam, Δ_a = the amount of deformation necessary to mobilize the active stress conditions in the retained soil, H = wall height, K_a = coefficient of active earth pressures, δ = interface friction angle between the geofoam and soil and γ_t= total unit weight of the retained soil. This equation can be extended for determining the thickness of the required geofoam buffer (t_{cie}) for a seismic loading case such as:

$$t_{cie} = \frac{E_{ci}.(\Delta_a/H)}{0.75.K_{ae}.cos\ \delta.\gamma_t} \quad \text{2-18}$$

where K_{ae} is the seismic active earth pressure coefficient determined through Mononobe-Okabe Theory. Horvath (1997) modified a mathematical model proposed by Veletsos and Younan (1994b) to predict the seismic response of soil retaining walls with geofoam inclusions. The original mathematical model of Veletsos-Younan was based on elasticity theory and proposed for a seismic load application not involving any compressible inclusion behind the retaining walls. They considered the seismic response of a rigid, non-yielding gravity retaining wall that was free to rotate about its base. However, a restraining moment due to the resistance of underlying soil stratum was applied to the system. This moment was applied by means of a linear rotational spring of magnitude R_ϑ. Horvath (1997) extended this analytical approach to estimate the seismic pressures acting on the walls having geofoam cushions installed between the wall and the retained backfill. The authors suggested that Veletsos-Younan solution may be applied for the case of a rigid non-yielding wall with compressible inclusions by considering that the deformations in the retained soil were mobilized by the rotational

deflection of the geofoam located between the wall and the retained soil. The maximum horizontal displacement at the top of the retained soil and geofoam interface for a rotation of θ radian was given as:

$$\Delta_{ci} = H.\tan\theta = 1.56H\ (for\ one\ radian\ rotation) \qquad 2\text{-}19$$

where *H* is the wall height and θ is the angle of rotation (Figure 2-39). Designating the geofoam with a linear elastic material behavior such as $\sigma_{ci} = E_{ci}\varepsilon_{ci}$ where E_{ci} is the Young's modulus of the geofoam and ε_{ci} is the maximum horizontal normal strain occurring in the compressible inclusion:

$$\sigma_{ci} = \frac{1.56.H.E_{ci}}{t_{ci}} \qquad 2\text{-}20$$

where t_{ci} represents the thickness of the compressible inclusion.

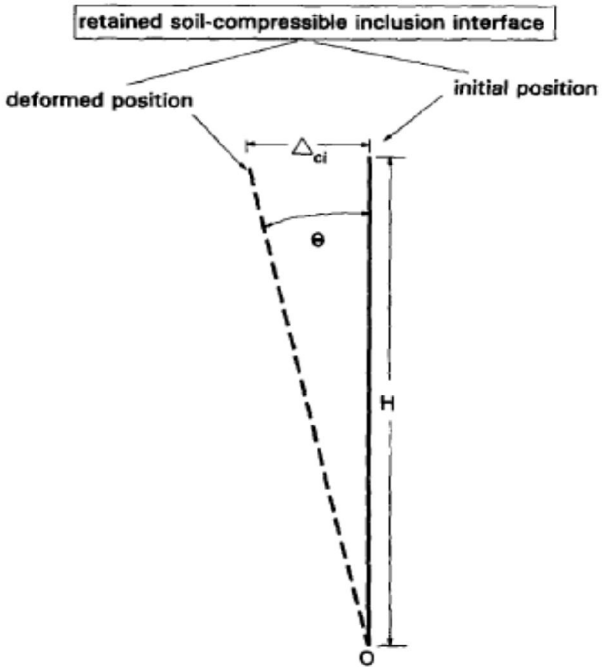

Figure 2-39 Rotation of the compressible inclusion (Horvath, 1997)

The resultant thrust per unit length of the wall was calculated through triangular distribution of the lateral force:

$$F_{ci} = \frac{0.78.H^2.E_{ci}}{t_{ci}} \qquad 2\text{-}21$$

Similarly, the resisting moment per unit length of the wall designated by $\mathrm{M_{ci}}$ was calculated as:

$$M_{ci} = \frac{0.52.H^3.E_{ci}}{t_{ci}} \qquad 2\text{-}22$$

Since M_{ci} was obtained for one radian rotation, it can be considered as the rotational spring stiffness per unit length of the wall designated as R_θ. Veletsos and Younan (1994b) described the relative soil-wall stiffness as:

$$d_\theta = \frac{G_s.H^2}{R_\theta} \qquad 2\text{-}23$$

where G_s is the shear modulus of the retained soil. Substitution of Eq. 2-22 into Eq. 2-23 results in:

$$d_\theta = \frac{1.92.G_s.t_{ci}}{H.E_{ci}} = \frac{0.96.E_s.t_{ci}}{(1+\vartheta_s).H.E_{ci}} \qquad 2\text{-}24$$

where ϑ_s is the Poisson's ratio and E_s is the Young's modulus of the soil retained. Author observed that d_θ value is simply the ratio of equivalent soil stiffness to the compressible inclusion stiffness. In a more recent study, Horvath (2008) slightly modified their previous equations as follows:

$$d_\theta = \frac{2.G_{av}}{\lambda.p_{atm}} \qquad 2\text{-}25$$

where λ is the ratio of ($H.E_{ci}$) to ($t_{ci}.p_{atm}$) and called as normalized compressible inclusion stiffness. Limiting values of the equation was obtained when λ =0 (perfectly compressible inclusion) and λ =infinite (perfectly rigid case). The author compared the results obtained through the analytical approach with the physical modeling test results of Bathurst et al. (2007a) and Bathurst et al. (2007b). Based on the data given in these papers, the author calculated d_θ values as 0.4, 2 and 5 for three different types of compressible geofoam buffers. The amount of load reduction estimated based on the relative values of d_θ and λ was consistent with the test results. The load reduction efficiency was also observed to be in

agreement with the results obtained through the graphs proposed by Veletsos and Younan (1994b).

In another study, Bathurst et al. (2007b) proposed a simple analytical displacement model to predict the seismic response of retaining walls with EPS geofoam buffers. In the proposed model, soil wedge was considered as a simple two dimensional rigid block as shown in Figure 2-40. It was assumed that only seismically induced horizontal motions occur in the wedge. Hence, horizontal acceleration time histories were prescribed to the base of the model. The soil wedge was considered to be in dynamic equilibrium under the system of forces acting on it. The forces acting on the analytical model was shown in Figure 2-41. The forces at the boundaries of the soil wedge were calculated by use of linear spring models.

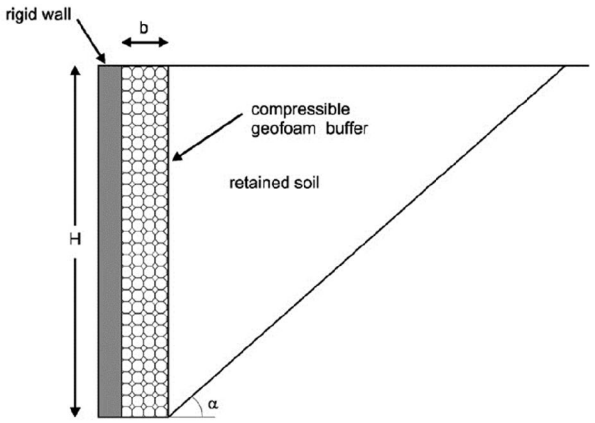

Figure 2-40 Sketch of the plane strain model (Bathurst et al. 2007b)

The normal forces were modeled with compression-only springs (k_N) whereas the forces forming the shear component was modeled through the use of stress dependent linear slip elements which can take into account of permanent sliding.

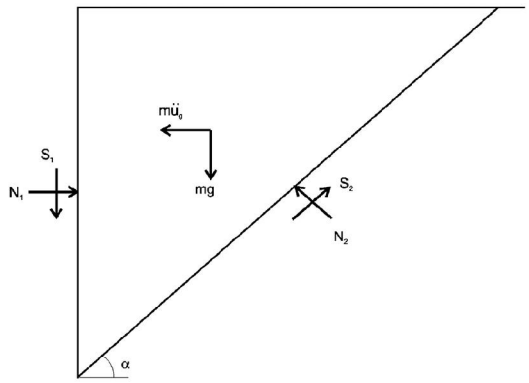

Figure 2-41 Forces acting on the soil wedge (Bathurst et al., 2007b)

An explicit, time marching finite difference approach was used as the solution scheme. The solution of the equations of motion for the block was performed at each time step which results in the forces acting to the wedge. The normal and shear forces occurring at the boundaries of the soil wedge were calculated according to the following force-displacement relationships:

$$(N_i)_{t+\Delta t} = (N_i)_t - \Delta n_i k_{N_i} \quad 2\text{-}26$$

$$(S_i)_{t+\Delta t} = (S_i)_t - \Delta s_i k_{S_i} \quad 2\text{-}27$$

where k_{N_i} and k_{S_i} are the normal and shear stiffness parameters and Δn_i and Δs_i are incremental normal and shear stiffness values, respectively. Using the outcomes of the incremental equations above, forces acting to the wedge depicted in Figure 2-41 were calculated as follows:

$$F_{hor} = \left(N_1 - m\ddot{u}_g - N_2 \sin\alpha + S_2 \cos\alpha - \beta m\dot{u}_1\right)_{t+\Delta t} \quad 2\text{-}28$$

$$F_{ver} = (-S_1 - mg - N_2 \cos\alpha + S_2 \sin\alpha - \beta m\dot{u}_2)_{t+\Delta t} \quad 2\text{-}29$$

where β is a mass damping factor and $\dot{u}_1$ and $\dot{u}_2$ are the velocity at the corresponding directions. The normal stiffness for the buffer-soil interface and the soil-soil interface were calculated as follows:

$$k_{N_1} = E_b \frac{H \times W}{b} \quad 2\text{-}30$$

$$k_{N_2} = E_s \frac{2W}{\cos\alpha \sin\alpha} \quad 2\text{-}31$$

where E_b and E_s are the modulus of elasticity of the buffer and soil, respectively, W is the unit width and α is the angle of inclination of the wedge. The stress dependent shear stiffness was calculated as:

$$k_{s_2} = \theta \sigma_N W = \theta N_2 \frac{\sin \alpha}{H} \qquad 2\text{-}32$$

where θ is the dimensionless stress factor and σ_N is the normal stress. The predictions of the analytical model were compared to the results of small scale shake table tests performed by Zarnani and Bathurst (2007). Peak compressive deformation of the geofoam was estimated through the procedure described above and compared to the results of physical tests as depicted in Figure 2-42.

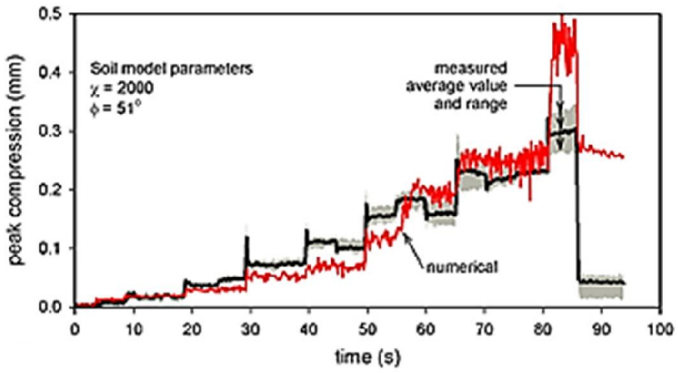

Figure 2-42 Deformation of the geofoam inclusion (Bathurst et al. 2007b)

According to the comparisons with actual physical models, the analytical approach was observed to give satisfactory results and may be used as a possible framework which can accommodate more complex material modeling and a wider range of problem geometry.

2.8 Failures in projects involving geofoam fills

Improper use of geofoam in some geotechnical applications inevitably caused failure. Horvath (2010) summarized the requirements of successful utilization of geofoam in geotechnical engineering field. According to the author, recent failures involving the block molded EPS geofoam occurred due to lack of understanding on basic rules regarding to stability of these structures. The stability of the

geotechnical constructions involving geofoam must be considered as internal stability, external stability, during-construction stability, and post-construction stability. Since the analysis and design of the geofoam applications are always strain based, they can be classified as small strain and large strain applications based on the operational strain level of the geofoam. In small-strain applications of EPS geofoam, it is common practice to limit the strain up to 1% which is a typical elastic strain limit for EPS. Beyond this strain level, excessive unrecoverable deformations occur due to the fracture in the cell structure of the EPS. Exposure to strains above the elastic limit of the material will increase the creep behavior of the EPS even it is applied for short durations. According to the author, once EPS blocks are damaged in any way, they can never be repaired or restored and stiffness properties deteriorate depending on time. Density is the most important parameter in regard to the determination the elastic limit and the stiffness of the material however, it should not be considered as the only measure of elastic limit stress. Production phase also plays an important role. Some geofoam manufacturers produce elasticized EPS geofoam which has a greater range of elastic behavior. According to the author, issues related to the internal stability of geofoam applications in the United States mainly resulted from overstressing the EPS blocks beyond the elastic limit stress. This common mistake leads to unexpected excessive compression of geofoam fills and differential settlements which increases in time due to creep effect. According to the severity of this failures, remedial actions are required such as the repaving the road, changing the EPS geofoam fill or even replace the geofoam fill with other geomaterials which will totally eliminate the advantage of using geofoam in the construction. Overstressing of the geofoam generally occurs by activity of heavy construction vehicles on the uncovered geofoam blocks. Since the effective load distribution is not provided without a cover layer, concentrated loads causes geofoam to be stressed beyond its elastic limit. The effect of overstressing may be observed after a short time after the end of the construction or the failures due to this mistake can substantially occur and get worse in time due to the creep of the geofoam. Issues related to the external stability of the geofoam fills rarely occur. Author reports one known failure of EPS lightweight fill. Floatation was observed in geofoam layers long years after the construction due to a rise in the ground water level. The portion of the highway was severely damaged. As a solution, entire fill was replaced by another geomaterial. This failure was considered as a result of poor design. There have been a few reported cases

about the failure of the EPS fills during construction. Failures were caused by unexpected movements of the geofoam fills as a block due to floods. In one of the cases reported, floatation combined with strong winds caused the EPS blocks to displace and cause a fatality of a worker due to a striking EPS block. There is not any reported post construction failure due to the material degradation of the EPS.

CHAPTER 3

PREVIOUS STUDIES ON THE STATIC AND DYNAMIC CHARACTERIZATION OF GEOFOAM

3.1 Introduction

Geofoam properties and testing methods performed to determine the characteristics of the geofoam materials were discussed in this chapter. Mostly used geofoam types are expanded polystyrene (EPS) and extruded polystyrene (XPS). According to ASTM D4439, geofoam is described as “block or planar rigid cellular foamed polymeric material used in geotechnical engineering applications”. For the production process of geofoam materials, ASTM D6817 dictates the following definition: “Rigid cellular polystyrene geofoam (RCPS) are formed by expansion of polystyrene resin beads or granules in a molding process (EPS) or by the expansion of polystyrene base resin in an extrusion process (XPS)”

RCPS’s are considered as organic materials and is considered as combustible. It should be stored away from heat sources and ignition agents. ASTM-D6817 designated the test methods of geofoam for qualification, acceptance or rejection. The ASTM-D6817 designations for various EPS and XPS geofoam were shown in Table 3-1 and Table 3-2 (ASTM, 2006).

3.2 Basic properties of geofoam and testing methods

According to Koerner (2005), basic properties of the geofoam can be classified in four categories, namely: physical, mechanical, thermal and endurance properties. Physical properties include dimensions, density, moisture absorption and oxygen index (minimum percentage of oxygen in site-specific gaseous environment required to support combustion).

Table 3-1 Physical property requirements for EPS geofoam (ASTM D6817)

Type	EPS12	EPS15	EPS19	EPS22	EPS29	EPS39
Density kg/m^3	11.2	14.4	18.4	21.6	28.8	38.4
Compressive resistance, min., kPa at 1%	15	25	40	50	75	103
Compressive resistance,min., kPa at 5%	35	55	90	115	170	241
Compressive resistance,min., kPa at 10%	40	70	110	135	200	276
Flexural strength, min., kPa	69	172	207	276	345	414
Oxygen index, min., volume %	24	24	24	24	24	24

Table 3-2 Physical property requirements for XPS geofoam (ASTM D6817)

Type	XPS20	XPS21	XPS26	XPS29	XPS36	XPS48
Density kg/m^3	19.2	20.8	25.6	28.8	35.2	48
Compressive resistance, min., kPa at 1%	20	35	75	105	160	280
Compressive resistance, min., kPa at 5%	85	110	185	235	335	535
Compressive resistance, min., kPa at 10%	104	104	173	276	414	690
Flexural strength, min., kPa	276	276	345	414	517	689
Oxygen index, min., volume %	24	24	24	24	24	24

3.2.1 Physical Properties of Geofoam

Density of geofoam is measured according to the specifications of ASTM-C578. Typical geofoam densities vary between 11kg/m^3 and 48kg/m^3 which are approximately 40 to 165 times smaller than the density of typical soils. Moisture absorption, which is also another important property of geofoam, plays a significant role in applications such as thermal insulation. The maximum value of absorption is reported as 0.3% according to ASTM C578. Oxygen index (*OI*) of geofoam is related to its combustibility and it is defined in ASTM-D2873 as the minimum percentage of oxygen in site-specific gaseous environment required to support combustion. For instance, geofoam having *OI* values smaller than 21% burn freely in air having 21% oxygen. Typical polystyrene has an *OI* value of 18%,

however EPS geofoam has a flame retardant attribute having a minimum *OI* value of 24%.

3.2.2 Mechanical Properties of Geofoam and Related Measurement Methods

Research indicates that geofoam materials should be considered as an elasto-viscoplastic material (Figure 3-1). For an elasto-viscoplastic material, the stress, after exceeding the yield stress, continues to increase beyond the initial yielding point.

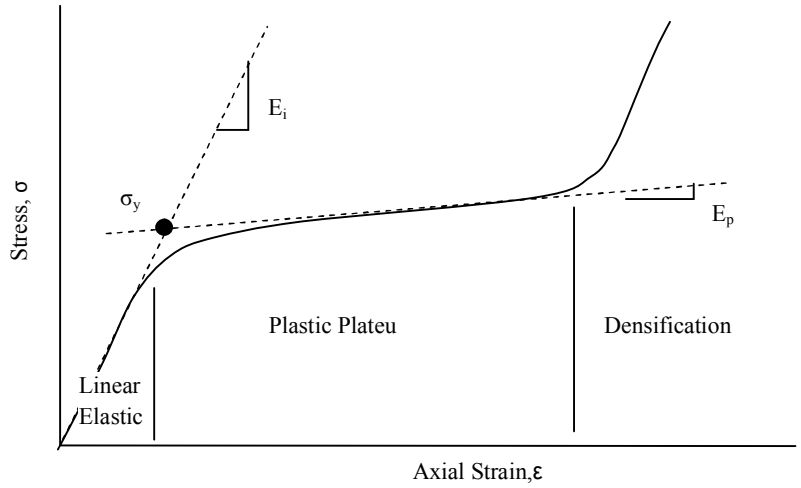

Figure 3-1 Typical stress-strain behavior of EPS geofoam (compression)

Mechanical behavior of EPS geofoam is mainly linear elastic characterized by Hooke's law up to axial strains of 1%. Beyond this limit strain level, bending and buckling in the cell structure cause significant decrease in initial stiffness (E_i) leading to plastic stiffness (E_p). The plastic strain accumulation occurs in a wide plateau of strain with limited hardening. High volumetric strains were observed in this stage. Plastic portion is observed to be approximately linear up to strain level of 70% which is followed by a densification of the geofoam due to modification of the material from cellular structure to stacks of polystyrene membranes. Due to the wide plastic zone under compression loading, large amount of energy is dissipated by EPS geofoam. According to Koerner (2005), mechanical properties of the geofoam can be classified as compression behavior, tension and flexural resistance, shear strength and compressional creep behavior. Compressive strength of geofoam is measured according to ASTM-C165, ASTM-D1621 or

German Code DIN-53421. Cubic samples of 50mm dimension are commonly used in compression testing. Measurements are taken at 1%, 5% and 10% strains for the specimens compressed under the strain rate of 10%/min. Size of the specimen may affect the mechanical behavior of the geofoam due to lateral confinement. Negussey (2001) reported discrepancies between the test results of small and large samples. In Figure 3-2, stress-strain response of EPS geofoam is depicted for various densities of the material tested according to the test procedure described in German Standard DIN-53421. The compressive strength of the material was taken as the axial stress at 10% axial strain since EPS does not show a well-defined yield behavior. A comparison of the stress-strain behavior of EPS and XPS type geofoam were depicted in Figure 3-3. According to the graphs, significant strain hardening is observed in EPS stress-strain curve, however stress increase after yield of XPS are not significant.

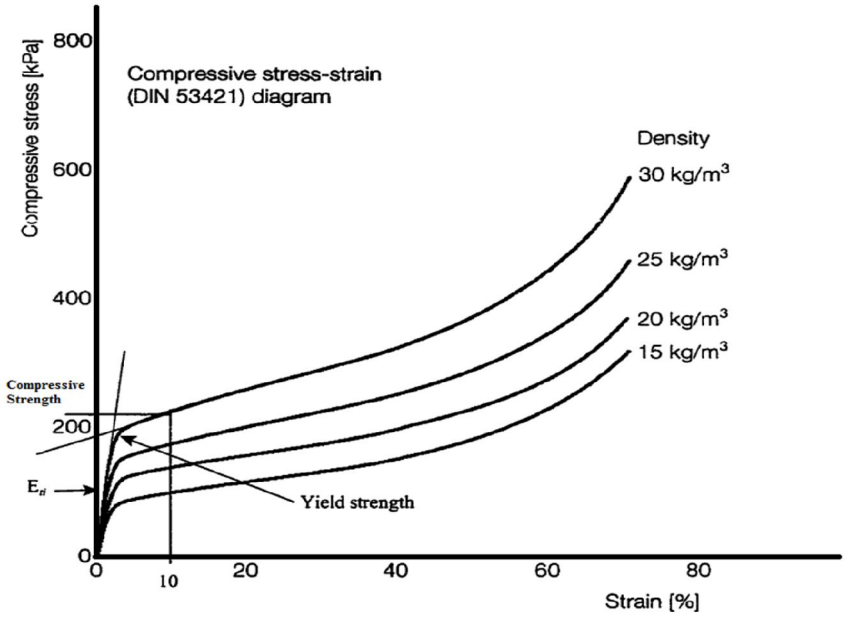

Figure 3-2 Stress-strain behavior of EPS under rapid monotonic unconfined compression testing according to DIN53421 (BASF, 1997)

Tensional strength of geofoam is determined through the procedure described in ASTM-C1623. In the test methodology, dumbbell shaped specimens were prepared which has a cross sectional area of 645mm^2 at the narrowest portion of the specimen. Strain rate of 5% were applied during tensile loading. Similarly, flexural strength is determined through ASTM-C203 procedure by preparing a geofoam beam of 250mm long by 150mm wide and applying 3-point loading.

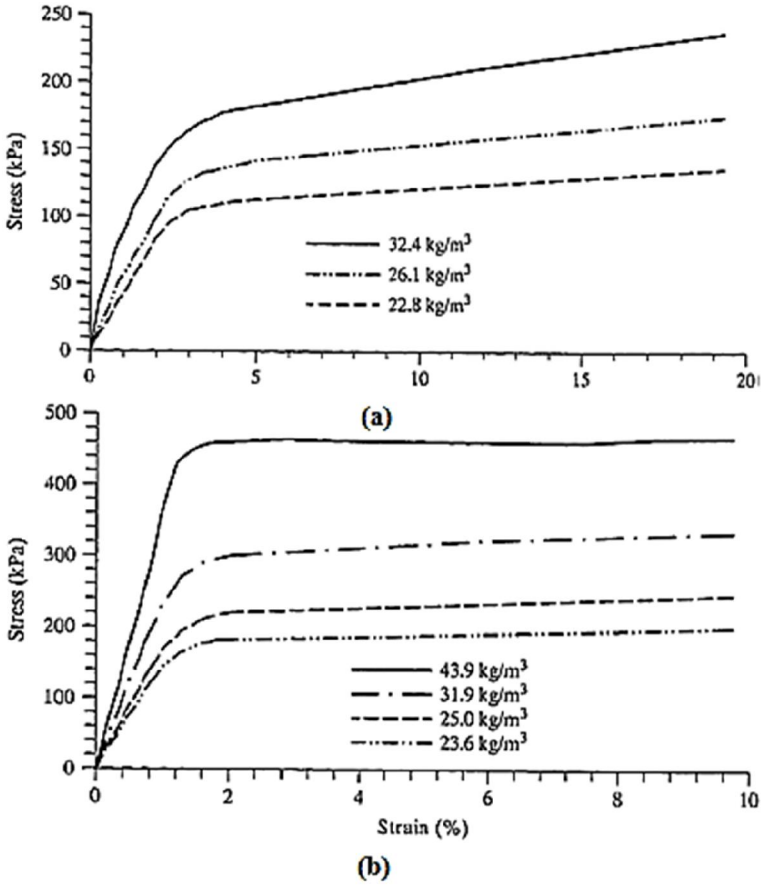

Figure 3-3 Stress-strain behavior of typical EPS and XPS geofoam (Koerner, 2005)

Shear strength of the geofoam may be discussed in several aspects. According to (Koerner, 2005), the external shear strength of geofoam-geofoam contacts and geofoam- soil or geofoam-structure contacts are under concern as well as internal shear strength of the geofoam materials. ASTM-C273 standard is applied to determine the internal shear strength of geofoam and this standard includes determination of the shear strength between geofoam blocks and also the contacts of geofoam with soil and other geosynthetics. Geofoam density has an important role of mechanical properties of geofoam. The overall mechanical properties of EPS geofoam for various densities were summarized in Figure 3-4 (BASF AG, 1991).

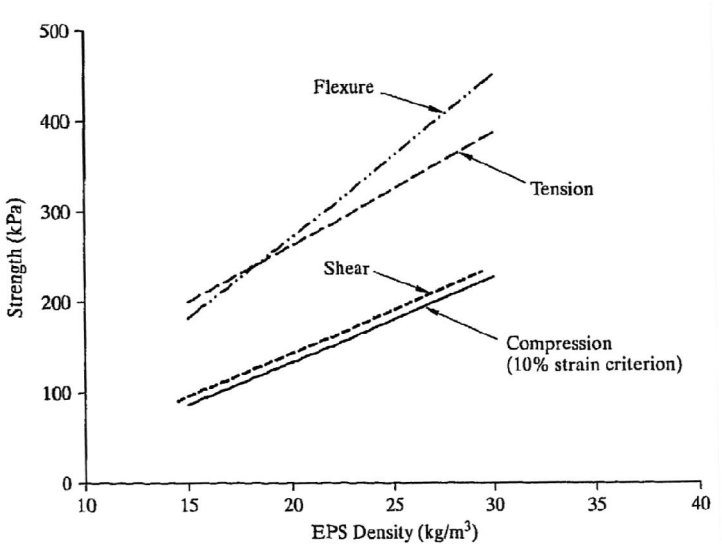

Figure 3-4 Overall strength characteristics of EPS geofoam for various densities (BASF AG, 1991)

Compressional creep behavior is measured under sustained compressive loadings applied on geofoam. The magnitude of the long-term load significantly affects the creep behavior. Negussey (1997) performed tests to investigate the long term behavior under various loads. Strain response of the EPS and XPS geofoam subjected to long-term loading is depicted in Figure 3-5.

3.2.3 Thermal Properties of Geofoam

Basic thermal properties of the geofoam can be grouped as thermal resistance and thermal cycling. Thermal resistance is measured according to ASTM-C578 and designated with *R*-values which are defined as the resistance of heat flow in a unit width of geofoam. The unit of *R* is m°C/W (Meter Celsius per Watts). The lower the *R* value the better insulation is provided. Thermal cycling provides information of fluctuations in *R* values due to temperature cycles.

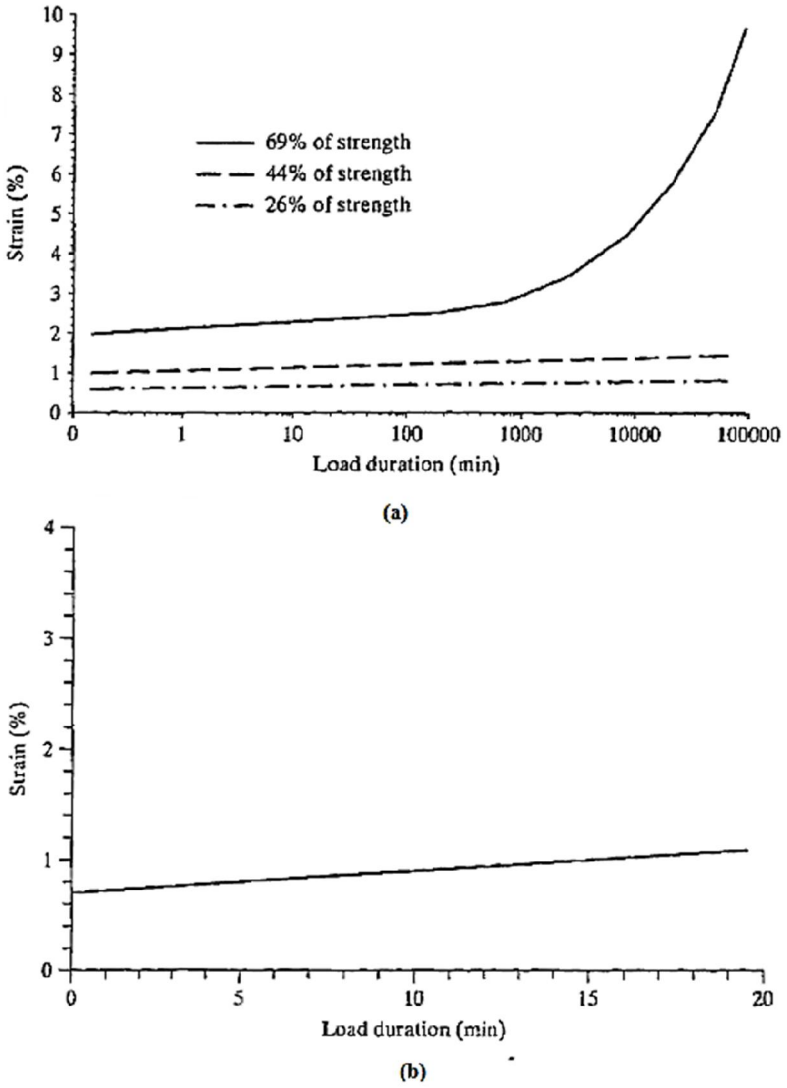

Figure 3-5 Creep behavior (a) EPS geofoam density=23.5 kg/m^3 (b) XPS geofoam density=30.9 kg/m^3 (Negussey, 1997)

3.2.4 Endurance Properties of Geofoam

According to Koerner (2005), chemical resistance, ultraviolet degradation, flammability, biological degradation and lifetime prediction are included in this group. Geofoam is a chemical which interacts with hydrocarbons and their vapors. Since the application field of geofoam is related to highways, airports, railroads etc., the risk of petrol spills are unavoidable. According to the application field of geofoam, the use of geotextiles for the purpose of covering and encapsulating the geofoam is required. The design of geotextile encapsulation should address the proper selection of the cover geotextile which will protect geofoam against

hydrocarbon attack. Ultraviolet degradation may result in geofoam which is exposed to long term sun light. Discoloration and powdering of the geofoam occur as a result of excessive UV light. Maximum exposure time depends on the specifications and site specific conditions.

Flammability of the geofoam is an important aspect of geofoam use in geotechnical field. Due to its oxygen index, geofoam produced from polystyrene is readily combustible. However, use of flame retardant agents decrease the flammability of the material. In any case, backfilling the geofoam as soon as possible is the most effective precaution since it is not subject to fire when it is embedded in soil.

Polystyrene does not contain any food source for insects, algae and fungi. Deterioration due to animal or plant activity is not observed however infestation by insects was observed in some cases. The lifetime expectancy of the geofoam is an important issue in designing with geofoam. Koerner (2005) reports presence of geotechnical applications involving geofoam which are successfully in use for more than fifty years.

3.3 Previous studies on static characterization of EPS geofoam

Negussey and Jahanandish (1993) performed constrained and unconfined compression tests on samples of two different densities to determine engineering behavior of EPS geofoam as an alternative geomaterial. For the constrained deformation tests, an oedometer which is instrumented to measure lateral stresses were utilized. Tests were also repeated for typical sand and clay materials for comparison purposes. The densities of EPS geofoam tested were 21kg/m^3 and 30.4kg/m^3. Test results indicated that density of the EPS acts similar as the overconsolidation effects in soils as observed in Figure 3-6. It the effect of initial density of the EPS geofoam on its mechanical behavior is found to be somewhat equivalent with the development of preconsolidation pressure in soils. The initial elastic modulus of the sand, clay, and EPS geofoam were determined as 25MPa, 30MPa and 4MPa, respectively. Coefficient of at-rest earth pressure was estimated as 0.55, 0.43 and 0.15 for sand, clay and EPS geofoam.

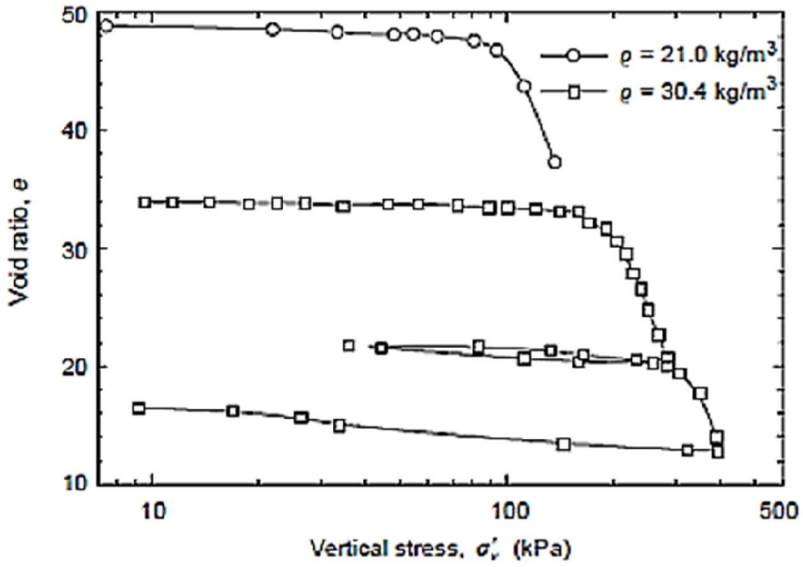

Figure 3-6 Behavior of EPS in one dimensional consolidation tests (Negussey and Jahanandish, 1993)

Based on their findings, it is concluded that stress-strain response and yield strength of EPS geofoam are well defined and similar to soils in many aspects. Young's modulus and yield strength was observed to be dependent on the initial density of the EPS and manufacturing process. The lateral stresses induced during the confined tests were observed to be very low indicating that EPS geofoam has low K_o and Poisson's ratio. Authors reported that geofoam having a density of 21kg/m^3 is equivalent to typical firm clay in regard to the compressive strength of the material. EPS with density of 30.4 kg/m^3 has a compressive strength similar to stiff, hard clays. Creep and time dependent behavior of EPS was observed to be significant if the stress levels were approaching the yield stress but this effect is quite small for stress values about half of the yield strength.

Preber et al. (1995) performed undrained triaxial tests with volume change measurements, punching shear and long term creep tests on EPS geofoam. An increase in the unit weight of the material resulted in higher elastic and plastic modulus. Effect of confining stress was somewhat different compared to soils. An increase in confining stress decreased the initial elastic modulus, however plastic modulus of the material increased. Based on the triaxial testing study, a constitutive model involving bi-linear stress-strain relationship was proposed. In the triaxial tests with volume change measurements, negative Poisson's ratio

values were obtained for EPS geofoam which are not common in natural geomaterials. Poisson's ratio remained at positive values for the smaller confining stresses however an increase in the confining stress leads to a decrease in Poisson's ratio and negative values were achieved for high confining stresses. Based on the limited data, the following relationship was proposed to estimate the Poisson's ratio of EPS:

$$\mu_{EPS} = 0.2 - 0.5\frac{\sigma_3}{62kPa}\ for\ 0 \le \sigma_3 \le 62\ kPa \quad \text{3-1}$$

where σ_3 is the confining stress in kPa. Creep tests were performed under a static deviator stress of 24kPa. Test results revealed a creep strain rate of 0.6% / year which is observed to be insensitive to material density. Repeated loading tests were performed under an axial loading of 72kPa for more than 300 load cycles of stress application. According to the tests, EPS geofoam can perform well under repeated loadings as long as the maximum stress was lower than the yield strength. Horvath (1995) proposed following relationships to determine the mechanical characteristics of EPS geofoam such as initial elastic modulus and Poisson's ratio:

$$E_{ti} = 0.45\rho - 3 \quad \text{3-2}$$

$$\mu = 0.0056\rho + 0.0024 \quad \text{3-3}$$

where E_{ti} is the initial tangent modulus in MPa, ρ is the density in kg/m^3 and μ is the Poisson's ratio. Duskov (1997) performed extensive laboratory tests to determine mechanical properties of EPS with bulk densities of 15kg/m^3 and 20kg/m^3. In the first group of tests, water absorption and hydro-thermal properties of EPS was investigated. It was observed that low temperatures as much as -15°C does not significantly affect the mechanical behavior and the results were observed to be similar with the test results obtained at room temperatures. Water absorption capacity of the EPS was observed to be between 1% and 1.5% in volume depending on the testing procedure. Cylindrical samples of 300mm height and 150mm diameter were tested. Maximum strain level was set as 10% which was considered as the stress level for the compressive strength values. Loading

speeds of 4, 20, 200 and 2000%/min were applied to investigate the effect of strain rate on mechanical behavior of EPS. Author indicated that EPS-15 and EPS-20 geofoam yield due to the plastic deformation of the EPS cell structure when the strain rate becomes greater than 1%. It was observed that, strain rate does not significantly affect the mechanical behavior of EPS geofoam within the strain range of 1%, however for strains greater than 1%; loading rate increases the stiffness of the material which was a frequently observed behavior in soils. Significant reduction was observed in secant modulus when loaded beyond the elastic limit. The decrease does not occur in a gradual manner. An abrupt decrease was noticed once the EPS cell structure is damaged. Author reports that the observed behavior implies the necessity of caution while handling the EPS material before and during the installation in the field. Trucks or other heavy construction vehicles running on EPS sub-base before the protective layers were placed on EPS, thus leading to lower dynamic modulus (E_{dyn}) values. Creep behavior of the EPS-20 geofoam was investigated in their study. Under a static stress of 20kPa, maximum creep was observed as 0.2% after one year period. Author investigated the variability of the results depending on the density of the EPS and proposed the following relationship:

$$E_{EPS} = 16.431 - 1.645\rho_{EPS} + 0.061\rho_{EPS}^2 \ (MPa) \qquad 3\text{-}4$$

where E_{EPS} is the Young's modulus of the elastic portion of stress-strain curve and ρ_{EPS} is the density of the geofoam in kg/m^3. Murphy (1997) conducted finite element analyses to investigate performance of a compressible inclusion installed between a rigid non-yielding retaining wall and backfill. Effect of the rapid loading and long period creep loading were investigated through a numerical modeling study. A real-scale retaining wall which was instrumented with pressure cells and extensometers (Partos and Kazaniwsky, 1987) was analyzed in finite element modeling studies (Figure 3-8). In the real scale model, the compressible geofoam inclusion was installed around the mid-height of the retaining wall.

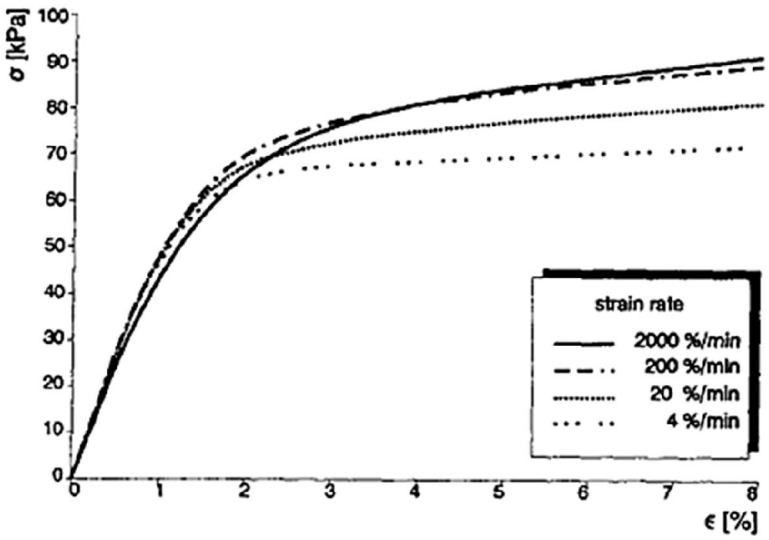

Figure 3-7 Stress-strain graphs for EPS15 at four different loading speeds (Duskov, 1997)

The presence of compressible inclusion was simulated in the numerical analyses. Based on the strain controlled uniaxial test results, the short-term elastic modulus of geofoam was determined for modeling of the rapid loading case, whereas unconfined uniaxial creep testing were performed to determine the creep loading modulus of the geofoam. The creep modulus was determined from the data of unconfined loading applied for duration of 1000 hours. Results of finite element analyses indicated decrease of lateral stresses in the portion of the wall where geofoam was present. The stresses were observed to be smaller than those calculated by Coulomb's theory. Stress profiles estimated through finite element modeling study indicated that arching was the main factor causing the decrease of lateral stresses in the vicinity of the compressible inclusion. The compression of the relatively softer material caused a deformation in the mid- portion of the retained backfill which resulted in a re-distribution of the lateral stresses. Arching caused the stresses to be transferred to the soil below and above the geofoam. Author indicated that this mechanism was identical with the 90° rotated version of the Terzaghi's well-known "Trap door" problem. The displacement profiles predicted by the finite element analyses were compared to the experimental data. It was observed that the predictions for the creep loading were overestimating the lateral displacements by up to 117%, however the predictions for the rapid loading case was in better agreement with the measurements. Author suggests that geofoam inclusion should be applied over the full height of the retaining wall for

achieving the maximum benefit of lateral force reduction. As a note for the design purposes with geofoam, it was indicated that bracketing the short and long term loading behavior of geofoam and carrying out the design process by considering the most conservative combination of results from the limiting values of the response was suggested.

According to Athanasopoulos et al. (1999), EPS geofoam can be characterized by its low unit weight which is approximately 1/100 of soils and very high void ratio values between 40% and 100%. For compressive strains greater than 1%, highly nonlinear behavior was observed accompanied with a decrease in tangent or secant Young's Modulus. According to the unconfined compression and triaxial compression test results, a decrease was observed in compressive stress of the EPS with increasing confining stress (Figure 3-9). Author indicated the important implications of this observation when designing EPS applications at great depths below the ground surface.

Elragi et al. (2000) presented results of laboratory tests on EPS blocks with different size and density to investigate the variation of the elastic parameters. Unconfined compression tests were performed on cubic and cylindrical specimens. Axial and lateral deformations were monitored to determine the Young's modulus and Poisson's ratio. 0.05m cubic samples were tested on a tabletop hydraulic loading system, whereas large cubic samples of 0.6m were tested by a free-standing hydraulic-servo loading apparatus. In the final group of tests, a stack of four 0.6m cubic specimens were loaded by a large high-capacity loading frame. All of the tests were carried out at the same strain level of 10% per minute. Tests results indicated that crushing and damage at the lower and upper portion of the EPS blocks causes vertical strains which were observed to be greater than the vertical strain at middle third of the specimen. The modulus of elasticity determined by using test data obtained from the middle third portion of the specimens was therefore, higher as compared to the upper and lower third portion of the EPS blocks.

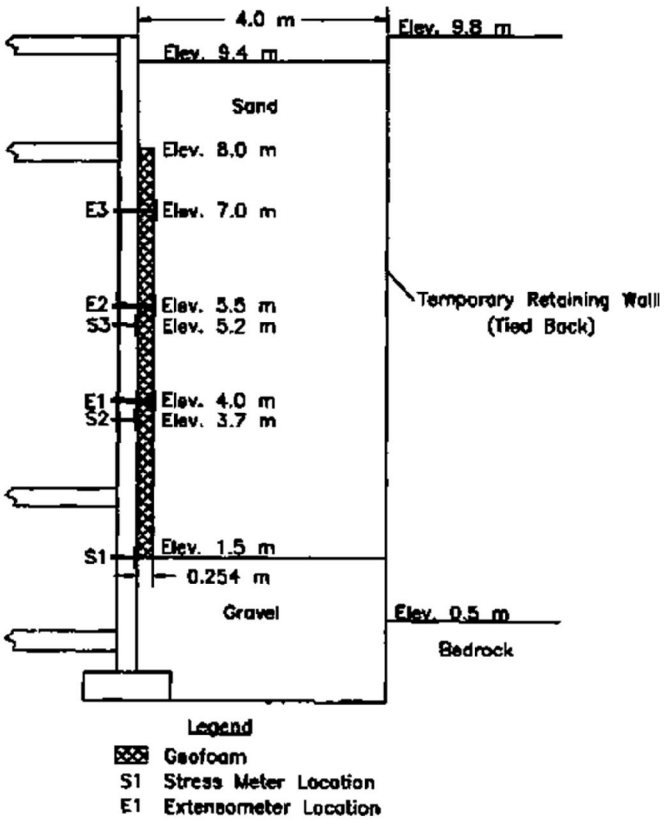

Figure 3-8 Geometry of the retaining wall- EPS-backfill system (Murphy, 1997)

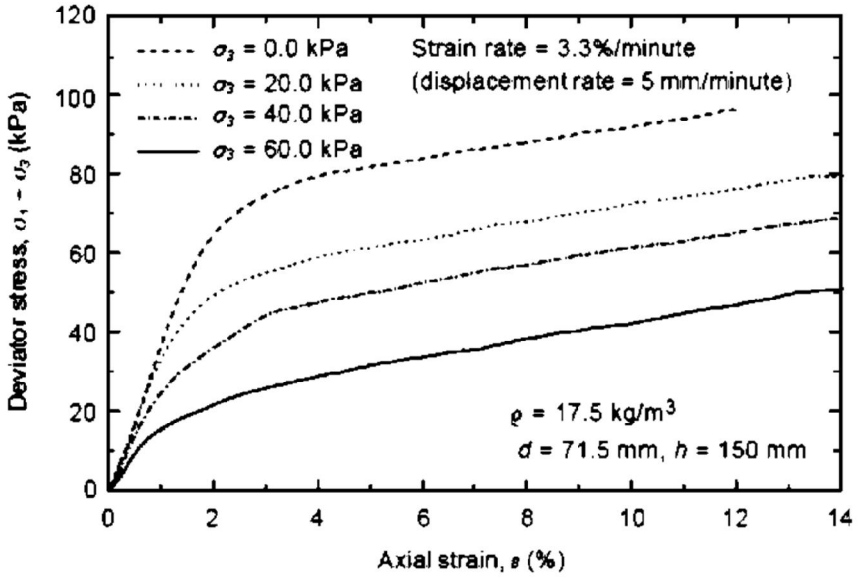

Figure 3-9 Stress-strain curves for rapid loading of EPS at different confining stresses (Athanasopoulos et al., 1999)

Similarly, Poisson's ratio observed at the mid-third was correspondingly higher than the values obtained for upper and lower boundaries of the specimen. It was reported that modulus values obtained from testing of 0.05m blocks were underestimating the Young's modulus values of the EPS geofoam. Authors indicated the inhomogeneity of stress and strains due to the crushing and damage of the geofoam near the end platens. Poisson's ratio determined for the larger samples were higher than the commonly assumed values which were proposed by Duskov (1997), Negussey and Sun (1996), Sanders (1996).

Beinbrech and Hohwiller (2000) indicated the need for a flat stress-strain curve with an extended elastic range in geotechnical applications. Generally, plastic deformations are avoided in the design of EPS geofoam structures. For this purpose, "elasticated" geofoam were produced by prestraining the ordinary geofoam to a strain of 60% and then releasing the applied pressure. It is observed that the plastic strains are significantly lower than the non-elasticated type EPS geofoam. The comparison of the stress-strain behaviors of elasticated and non-elasticated geofoam were depicted in Figure 3-10. Additionally, author performed creep tests on materials of different densities and presented the graphs in terms of loading time in days and buckling of the specimen in percent. Effect of creep deformations observed to be significant for higher stresses. An increase in geofoam density has a positive role in reducing creep deformations at the same stress levels.

Missirlis et al. (2004) performed long term compression tests in temperature and moisture controlled humidity chamber on EPS specimens of various densities (10 kg/m^3, 15 kg/m^3 , 20 kg/m^3 , 25 kg/m^3, 30 kg/m^3, 35 kg/m^3). Cylindrical samples of 100mm diameter and 200mm height were tested at 20°C, 30°C, 40°C and 50°C. For duration of three months, axial loads were applied to initiate axial strains of 0.25%, 0.50% and 0.75% which are covering the whole elastic range of the EPS material. The results of the compression creep tests at different temperatures yielded a master curve of creep behavior covering 100 years duration by the time-temperature superposition principle which was referred in ASTM Standard D6112 (ASTM, 1997). In this method, creep tests conducted in relatively short durations and different temperatures were shifted in the logarithmic scale to produce a master yield curve which may be used to determine the creep behavior of the tested material covering a long duration at a selected temperature. Author validated the applicability of this method to EPS by verifying against Arrhenius

equation. It was observed that creep behavior of the EPS geofoam is not dependent on the density of the material for the investigated density range. Based on the time shifted results, a constitutive model was proposed to determine the creep behavior of EPS describing the linear viscoelastic response of the investigated material for initial strains less than 0.5% and compressive stresses lower than the 30% of the compressive strength of the EPS material.

Gnip et al. (2005) proposed a regressive model to predict the stress-strain behavior of EPS on a strain range up to 35%. The effect of density on the stress-strain behavior was taken into account by a regression relationship. The relationships were obtained by using the data obtained from testing of 322 specimens. The density of the EPS material varied from 12 to 34 kg/m^3. The predictions made with these regression relationships provided results which are in agreement with the experimental data. Their model led to the prediction of the elastic modulus of the EPS and yield compressive stress.

Hazarika (2006) performed a series of unconfined compression tests on EPS specimens of different size and shapes. Author indicated that compressive testing on 50mm cubic samples of EPS was considered as a common practice to determine the mechanical characteristics of EPS. However, performance observations revealed that testing on small samples were underestimating the Young's modulus values of EPS geofoam. The authors points out the need of reliable correlations between the Young's modulus of small size specimens and full-size EPS blocks which are being used in the field. In For the experimental study, specimens were prepared from EPS blocks having nominal densities of 16 and 20 kg/m^3. Dimensions of the prismatic specimens were 100mm × 100mm × 100 mm , 50mm × 50mm × 50 mm, 100mm × 100mm × 50 mm, 50mm × 50mm × 100 mm and for the cylindrical samples Φ50mm × 100mm. The specimens were cut from full size EPS blocks by hot wire technique.

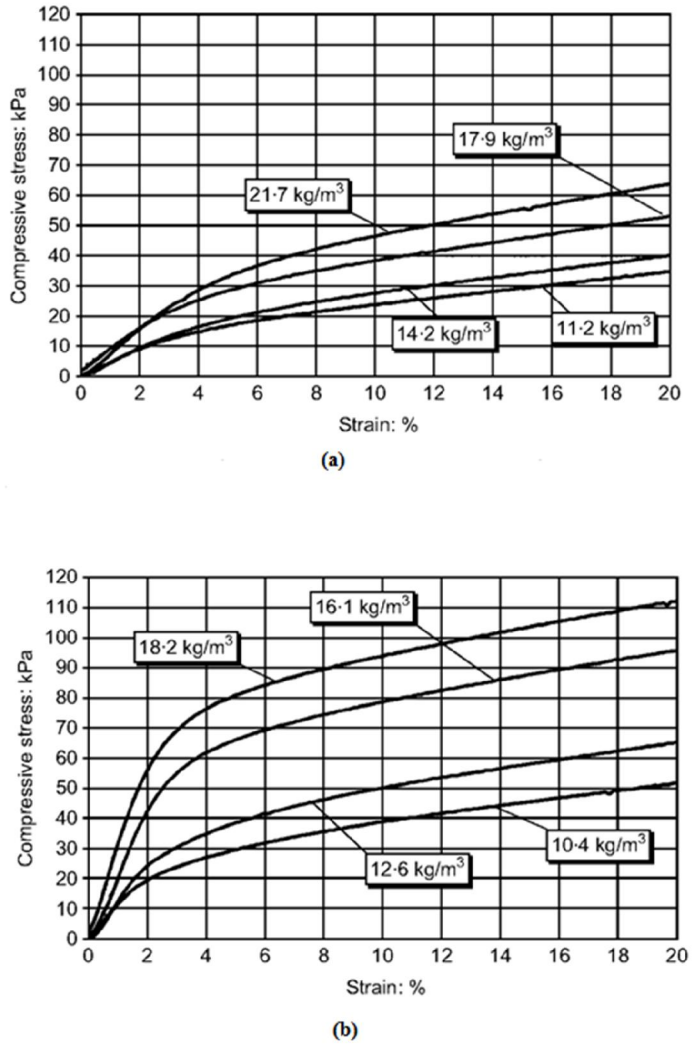

Figure 3-10 Stress-strain curves for the (a) elasticated and (b) non-elasticated geofoam for various densities (Beinbrech and Hohwiller, 2000)

Strain rate was taken as 9%/min which was a little smaller than 10%/min which is considered as a standard in worldwide applications. The stress-strain behavior of the tested EPS samples was observed to be highly non-linear with a small elastic range (Figure 3-11). Based on the tests performed at 9%/min strain rate, the following relationship on EPS modulus and density was proposed:

$$E_{EPS} = 0.41\rho_{EPS}\left(\frac{kg}{m^3}\right) - 2.8\ (MPa) \qquad 3\text{-}5$$

Gnip, et al. (2007) carried out experiments to determine tangent modulus of elasticity (E_t), ultimate strain (ε_{et}) and ultimate strength (σ_{mt}). Further tests were conducted to investigate the response of EPS geofoam when subjected to tensile forces (Figure 3-12). Leo, et al. (2008) performed true triaxial tests to determine stress-strain characteristics, volume change and yielding behavior of EPS geofoam. In the tests, prismatic EPS specimens of dimensions 70mm×70mm×140mm and density of 16 kg/m^3 were tested with the true triaxial apparatus which consists of four loading plates activated by hydraulic rams. The specimen encased in rubber membrane was located inside the plates which were instrumented by LVDT's. The overall system was located into a cell and the open faces of the specimen were stressed by the presence of cell pressure inside the chamber. This apparatus provides different combinations of major, intermediate and minor stresses. The friction developing between the loading plates and the rubber membrane was reduced by locating 0.01mm thick plastic sheets with thin layer of grease. Specimens were consolidated prior to the shearing under a confining pressure corresponding to a specific I_1 value (first invariant of stress). Consolidation process ended after allowing all the trapped air inside the specimen to escape. Following the consolidation phase, a controlled stress path loading was applied by increasing the major principal stress at a rate of 75kPa/min. The loading was applied by keeping the stress condition on the same deviatoric plane (I_1 is constant) by adjusting the deviatoric stresses, namely (σ_1-σ_3) and (σ_2-σ_3) while reducing the minor principal stress σ_3 at a prescribed stress level.

According to the results of the true triaxial tests, yield was observed at maximum axial strain of 4% which is less than the yield strain range of 1 to 2% obtained from standard triaxial compression testing by several researchers (Duskov, 1997),(Wong and Leo, 2006). Author concluded that EPS can be modeled as an elasto-plastic material; however the stiffness of the material decreases with increasing confining stress. Investigation of the volume change behavior indicates good accordance between the onset of volume change and the proportional limit of the material obtained from stress-strain response. Drucker-Prager Theory is found to be suitable to model the constitutive behavior of EPS geofoam.

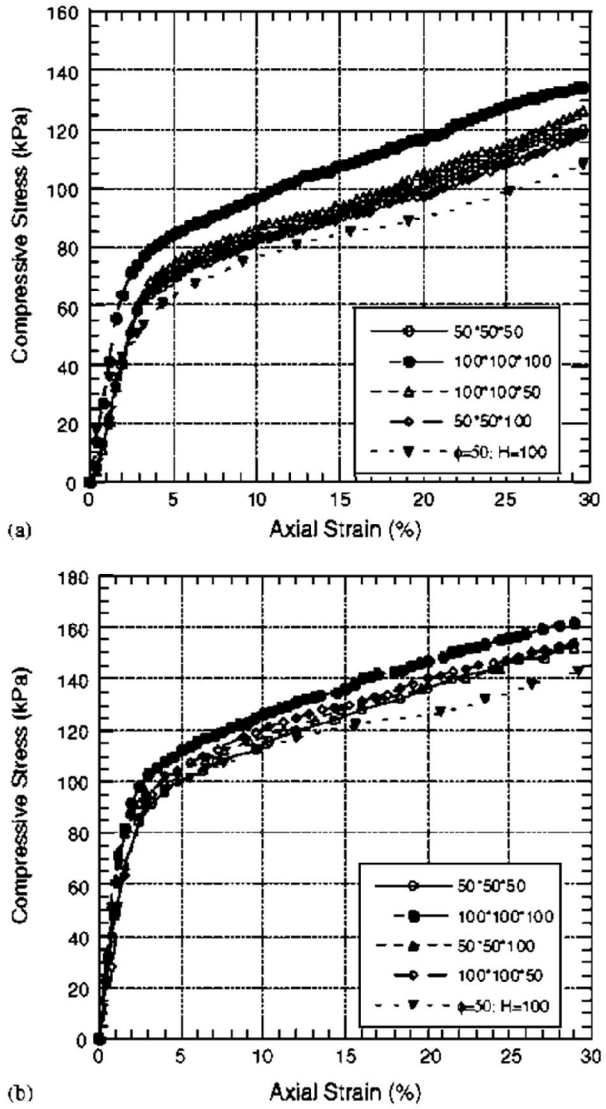

Figure 3-11 Stress-strain response (a) density of 16 kg/m^3 (b) density of 20 kg/m^3 (Hazarika, 2006)

Abdelrahman et al. (2008b) performed unconfined compression tests to investigate the rate dependency of EPS geofoam with densities of 19.3 kg/m^3 and 28.0kg/m^3. Specimens with 75mm diameter and 150mm height were tested under sustained loading and monotonic loading. It was observed that the strength of the material significantly increases with an increase in the strain rate and effect of strain rate becomes significant when the vertical strain becomes greater than 1%.

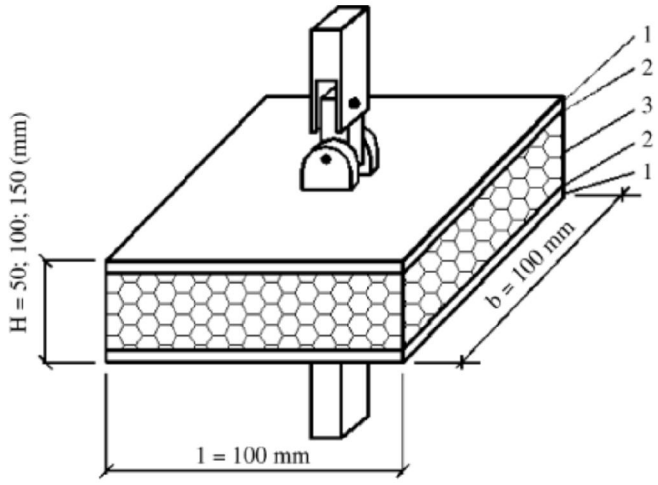

Figure 3-12 Schematic description of the apparatus for applying tensile force to EPS specimen 1: metal plate 2: adhesive 3: specimen (Gnip et al., 2007)

Significant inelastic deformation was observed after this strain limit. It was reported that the collapse of EPS bead structure and slippage at the interface of EPS cells are causing the large-scale yielding observed after the limiting strain value. The horizontal strains were observed to be lower than the vertical strain for small strains. After initialization of large-scale yielding, it was observed that specimen diameter decrease which indicates negative Poisson's ratio.

Ossa and Romo (2009) performed compressive loading tests on small and medium size specimens to investigate the micro and macro mechanical properties of the EPS geofoam. Small cubic samples (4mm dimension) were located in a load frame positioned with an electron microscope. Uniaxial compression was applied up to 60% strain. It was observed that there is not any significant change in the cellular structure of the specimen up to a strain level of 2.5%. When the strain reaches to 8%, flexure, buckling and tension in the specimen was observed. At this strain level, the reduction of the void spaces between the cells was significant. The geometry and internal cell arrangement were observed to change significantly at axial strain of 20%. Most of the void space was disappeared and full contact was observed between the individual cells. At strain level of 60%, the cell structure was completely deformed and microscopic observations showed that closed cells were collapsed into stacked polystyrene sheets. When the specimen was unloaded, 50% of the deformation was recovered however significant damage occurred in cell structure. Very small

lateral strains were observed in the small scale loading tests. This result was found to be compatible with the previous technical literature.

Macro scale tests were performed on samples with 10cm diameter and 17cm height. Effect of density (ρ), confining stress (σ_3) and displacement rate (*s*) were investigated through a series of uniaxial and triaxial compression tests. Tests were conducted on two different densities (17kg/m^3 and 30kg/m^3), three different confining stresses (0kPa, 30kPa and 60kPa) and three different strain rate (0.5 mm/min, 1.0 mm/min and 10 mm/min). Specimens were subjected to confining stress prior to axial compression. It was observed that displacement rate significantly affects the mechanical behavior of EPS geofoam. Increasing displacement rate resulted in higher compressive strength, initial tangent and plastic modulus. Confining stress was observed to be another important factor in mechanical behavior of the EPS. Increase in confining stress resulted in lower compressive strength and initial modulus as opposed to the general behavior of soils. However, an increase was observed in plastic modulus values with an increase of confining stress. Triaxial tests with measurement of lateral deformations revealed the auxetic behavior of the EPS geofoam. Auxetic foams have negative Poisson's ratio values when they are subjected to compression or tension. Based on the test data, author proposed relationships between the mechanical properties of the geofoam as follows:

$$E_i = -1.111 + 0.397\rho - 0.029\sigma_3 + 0.054s \quad \text{3-6}$$

$$E_p = -23.326 + 4.941\rho + 0.500\sigma_3 + 208.369s - 19.044s^2 \quad \text{3-7}$$

$$\sigma_y = 31.358 + 0.133\rho^2 - 0.620\sigma_3 + 1.137s \quad \text{3-8}$$

$$\vartheta = 0.475 - 0.0144\rho \quad \text{3-9}$$

where E_i is the initial tangent modulus (MPa), E_p is the plastic modulus (kPa), ρ is the density (kg/m^3), σ_3 is the confining stress in kPa and *s* is the strain rate in mm/min. In a recent study, Horvath (2010) summarized the behavior of EPS in rapid loading and creep loading. An investigation of Figure 3-13(a) indicates that EPS does not fail like the classical material failure sense. After the elastic range of the material is covered, a non-linear strain hardening occurs over a wide plateau of strain. During this phase, the void ratio of the EPS (approximately 98%

of the total volume) reduces. The material can be said to return its original solid polystyrene form. Poisson's ratio of EPS was observed to be zero or negative which means that the cross sectional area of the EPS was staying constant or decreasing in the perpendicular direction of the compressive loading. Based on these observations, it can be mentioned there is not a well-defined compressive strength of the EPS however stress level at 10% strain should be taken as the compressive strength. In Figure 3-13(b), small strain stress-strain behavior of the EPS was shown together with the creep loading behavior up to ten thousand hours of compressive loading.

3.4 Dynamic properties of geofoam and related testing methods

The use of EPS geofoam or other cellular rigid polystyrene materials as seismic deformable buffers for the earth retaining structures requires the determination of the dynamic properties of the geofoam since dynamic properties will be more important in seismic design of geotechnical structures involving geofoam.

3.4.1 Cyclic Stress-strain behavior and modulus degradation of geofoam

The dynamic modulus of the geofoam significantly depends on the range of stress applied and the density of the material. Similar to the soils, degradation in the shear modulus was observed when the stress level exceeds the yield strength of the material. According to Horvath (1995), modulus of elasticity significantly varies when the elastic limit was reached. Up to axial strain of 50%, reduction in the dynamic modulus continues.

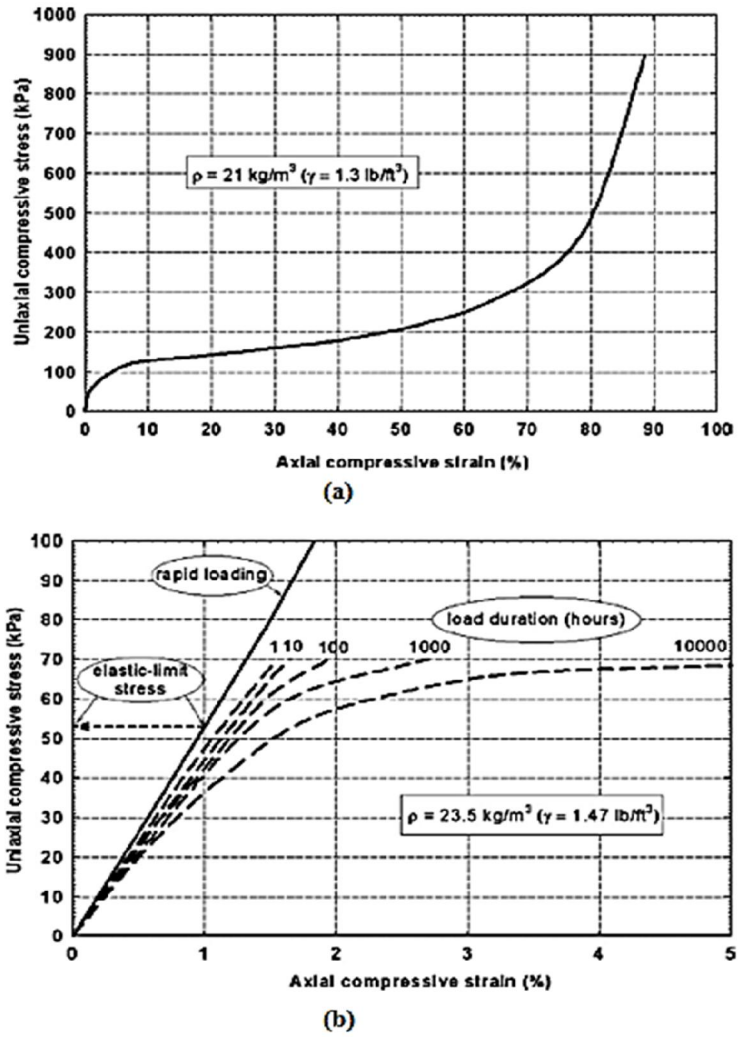

Figure 3-13 (a) Rapid loading of EPS (b) Small strain loading and creep behavior (Horvath, 2010)

After this threshold strain, significant strain hardening occurs causing the cyclic loading trace to make a sharp increase. Beyond this strain level, most of the voids in the EPS cellular structure were vanished and the cellular structure was transformed into two dimensional plates. At this point, geofoam should be considered as a solid plastic. Effect of cyclic loading on EPS dynamic modulus was presented in Table 3-3. The studies on the determination of the dynamic modulus values were summarized in detail in Section 3.5.

Table 3-3 Effect of cyclic loading on the dynamic modulus of the geofoam (Geotech Systems Corporation, 1999)

Stress Range(kPa)	Strain		Modulus (MPa) at		
	Initial	Residual	1st cycle	2nd cycle	100th cycle
9-17	0.0094	0.0094	1.5	1.5	1.5
18-35	0.0098	0.0097	2.6	2.6	2.9
26-58	0.016	0.023	2.4	2.4	2.3
44-85	0.028	0.097	2.3	1.8	1.9
68-128	0.043	0.19	2.2	1.9	2.0
88-172	0.057	0.21	2.3	1.8	2.4

3.4.2 Damping Characteristics of Geofoam

The damping ratio is a measure of the energy absorbed by the material during cyclic loading. As shown in Figure 3-14, typical cyclic hysteresis behavior was observed in the cyclic testing of the EPS geofoam. The area between the load-unload backbone curve makes an indication of the energy absorption behavior of the material. Straining causes shape changes in the spherical beads of the EPS geofoam. Compressive strain causes the cells to be flattened and unloading causes the shape of the cells to approach to their original shape; however the material cannot regain the original shape depending on the magnitude of compressive loading. This causes a reduction in the damping ratio of the EPS geofoam especially at strains above the elastic limit of the material. The measured damping ratios for the EPS geofoam of the same density under six different stress ranges were shown in Table 3-4.

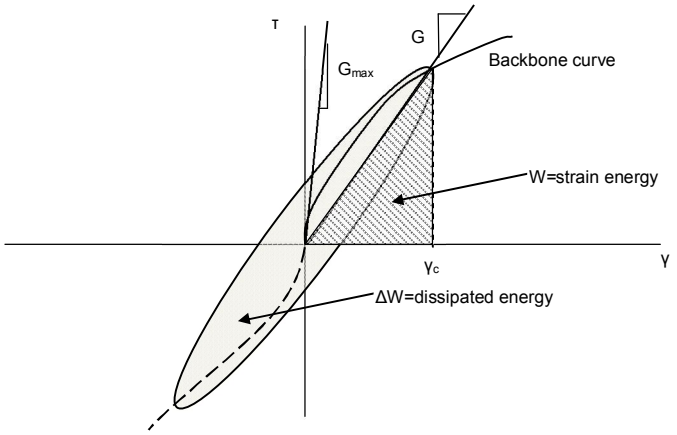

Figure 3-14 Typical hysteresis behavior of EPS geofoam

According to the Table 3-4, a reduction was observed on the damping ratio in all of the investigated cases in cyclic loading tests. The amount of decrease depends on the initial stress range on the EPS geofoam. After approximately 100 cycles, damping ratio observed to remain constant.

3.5 Previous studies on dynamic characterization of EPS geofoam

Utilization of advanced numerical modeling software and analytical techniques towards the modeling and design of EPS geofoam for the seismic isolation applications in geotechnical engineering field requires proper determination of dynamic mechanical properties of the geofoam as well as other geomaterials. In recent years, there is an increasing trend of the studies targeting the determination of cyclic loading characteristics of the geofoam products since limited data on the relationships between the dynamic modulus, damping, cyclic strain amplitude, and material density exist up to now.

As one of the first investigation on dynamic characterization of EPS geofoam, Horvath (1995) reported results of cyclic uniaxial tests on EPS samples with density of 13 kg/m^3. Gradually increased cyclic strains were applied to the specimen at various frequencies. Tangent Young's modulus at each cyclic strain phase was observed to be less than the initial static modulus of the material.

Table 3-4 Effect of cyclic loading on the damping ratio of the geofoam (Geotech Systems Corporation, 1999)

Stress Range (kPa)	Damping ratio	
	2^{nd} cycle	100^{th} cycle
9-17	0.047	0.023
18-35	0.055	0.022
26-58	0.11	0.040
44-85	0.27	0.082
68-128	0.36	0.082
88-172	0.30	0.074

In a following study, Duskov (1997) determined dynamic elastic modulus of the EPS geofoam by electro-magnetic method. In this test, ultrasonic waves were applied to the specimen and the arrival times of the waves were measured by a transmitter located at the opposite edge of the sample. The travel time of the waves were measured with an accuracy of 10^{-6} seconds. It was observed that the dynamic elastic modulus varies between 10MPa and 15MPa depending on the sample size. Samples smaller in length yielded larger elastic modulus values. This way of measuring the elastic modulus value of the EPS geofoam was considered as an ideal way to take into account the variations in density of the material. In the second group of tests, stress-controlled cyclic triaxial tests were carried out on cylindrical specimens (10cm diameter: 20cm height and 15cm diameter: 30cm height). The study of Duskov (1997) mainly focused on application of geofoam as lightweight fill under highway pavements. Hence, cyclic loading frequency of the tests was set between 3Hz and 6Hz which was considered as representative for the vehicle traffic loading on the pavements. Static deviatoric stress of 15kPa was applied to represent the typical dead weight of overlying protective soil layers located on EPS geofoam fill. Cyclic deviatoric stress amplitude varied between 10kPa and 50kPa which makes it possible to investigate plastic deformations as well as elastic ones. In each test series, specimens were subjected to 10000 loading cycles. Based on the test results, E_{dyn} values were observed to vary between 6.1MPa and 8.3MPa and Poisson's ratio, between 0.07 and 0.11. Permanent strains were not observed for 15kPa and 30kPa cyclic deviatoric stresses combined with a static deviatoric stress of 15kPa. Measured cyclic strain amplitudes were 0.17% and 0.34% for confining stresses of 15kPa and 30kPa. Permanent deformations were observed after cyclic

deviatoric stress of 50kPa under the corresponding cyclic strain of 0.62% at the beginning of the tests.

In another study, Athanasopoulos et al. (1999) carried out extensive research on the determination of dynamic characteristics of EPS geofoam through resonant column and cyclic triaxial tests. Dynamic stiffness and damping characteristics of EPS geofoam having two different densities (EPS-1:12.4kg/m^3 and EPS-2: 17.1kg/m^3) were measured. Resonant column tests provided small strain shear moduli for the cyclic shear strain amplitude range of 0.0005% to 1.6%. Tests yielded 2.1MPa and 4.9MPa for the low-amplitude shear moduli (G_0) of EPS-1 and EPS-2 specimen. Linear elastic behavior was observed to diminish after strains of 0.1% which is the 1/10 of the commonly used elastic limit of 1%. Resonant column tests indicated very small damping for strains up to 1% (Figure 3-15). To determine the dynamic properties in the strain range of 0.2% to 8%, cyclic dynamic compression tests were performed (Figure 3-16). In all the tests, no confining stress was applied. It was observed that test results based on shear strain measurements obtained from resonant column tests and axial strains from cyclic triaxial test data overlaps in a limited portion. Authors combined the data obtained from two different tests by converting the shear strains to axial strains by using relationships from elastic theory. Based on the combined data, modulus degradation and damping curves were established (Figure 3-17). Data obtained from low frequency cyclic triaxial compression tests were not used in the best line fit for the curves. Based on the test results, following set of equations were proposed to estimate the modulus reduction and damping curves:

$$\frac{G}{G_0} = \frac{1}{1+\frac{\gamma_C}{\gamma_{C_O}}} \qquad 3\text{-}10$$

where γ_{C_O} is constant having a value of 2.1% and γ_C is the cyclic shear strain (%)

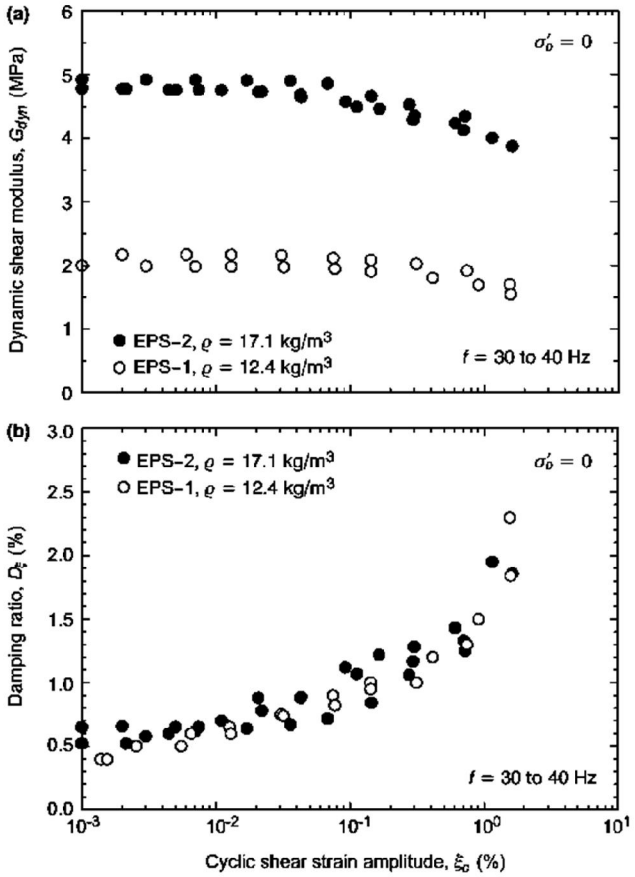

Figure 3-15 Resonant column test results (a) shear modulus (b) damping ratio for EPS-1 and EPS-2 geofoam (Athanasopoulos et al.,1999)

$$D_\gamma = 10 - \frac{10 - D_0}{1 + \frac{\gamma_C}{\gamma_{C_O}}} \qquad 3\text{-}11$$

where D_0 is the initial damping ratio which is equal to 0.55%. In Figure 3-18, experimentally obtained modulus degradation and damping curves for geofoam were superposed on the plots of Vucetic and Dobry (1991) proposed for soils with different plasticity index (*PI*). However, it should be noted that, the modulus reduction and damping curves were derived by testing EPS specimens at zero confining pressure (σ'). The effect of σ' on the dynamic behavior was not investigated in their study. According to the test results, damping ratio of EPS geofoam were smaller than 1.5% for strains up to 1%.

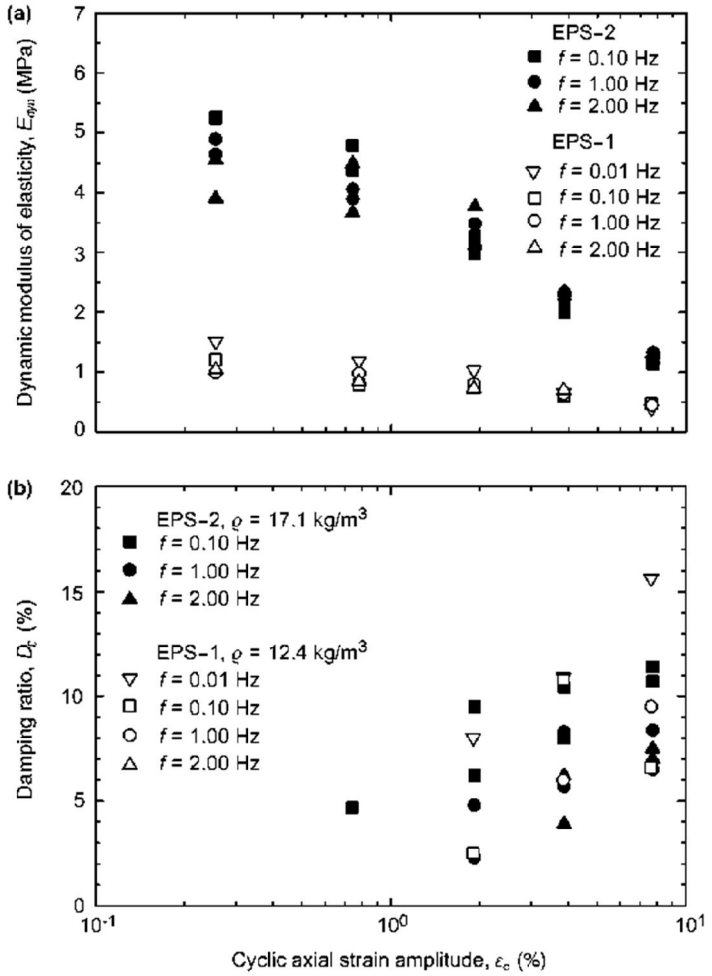

Figure 3-16 Cyclic triaxial test results (a) shear modulus (b) damping ratio for EPS-1 and EPS-2 (Athanasopoulos et al.,1999)

However, an increase in damping ratio was observed at higher strains, reaching to 10% for strain levels around 10%. Based on this finding, authors indicated that efficiency of EPS in reducing low strain vibrations is related with its low stiffness rather than the damping capacity. Another important finding was on the effect of EPS density on dynamic moduli of geofoam. E_{dyn} values increased for EPS geofoam with higher density. However, any clear relationship was not observed between the damping ratio and density. Cyclic loading rate did not significantly alter E_{dyn}, but slightly decreased the damping ratio for the investigated loading rate of 0.01Hz to 2Hz. cyclic strain ratio affected the dynamic modulus and damping ratio. Elastic modulus of the geofoam significantly decreased with increasing strain rate especially above strain level of 1% which may practically be considered as the end of the elastic behavior of the EPS geofoam.

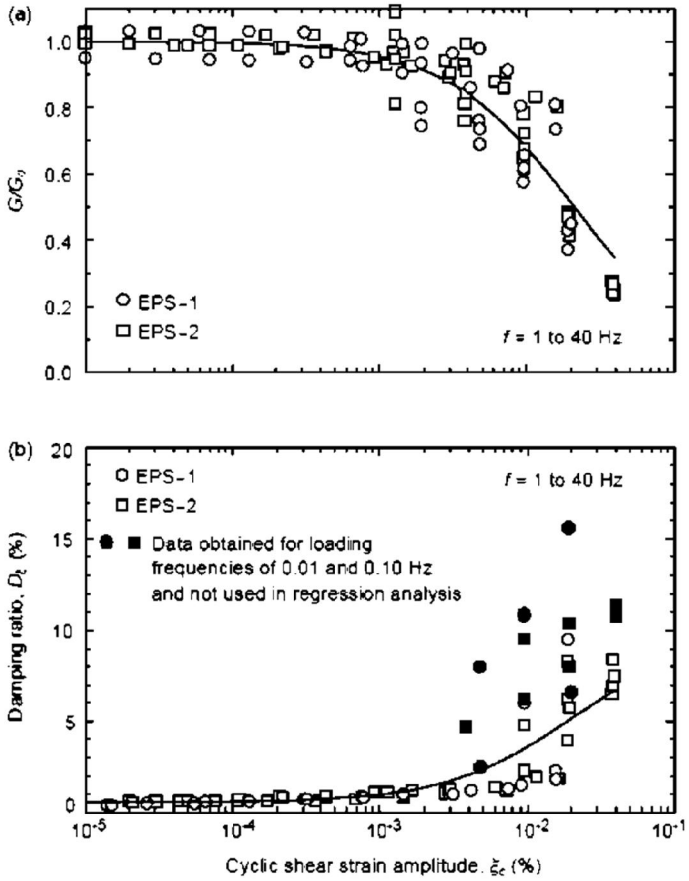

Figure 3-17 Shear modulus degradation and damping curves based on the combined test data (Athanasopoulos et al., 1999)

Contrary to the effect on the elastic modulus, increase is observed in damping ratio which may be as high as 15% for the maximum strain rate of the study (8%). This can be considered as a natural result of the extended plastic plateau observed in the stress-strain behavior. Authors indicated that a wide range of strain for the plastic hardening zone enables absorption of great amounts of energy during cyclic loading.

Trandafir et al. (2010b) performed stress-controlled cyclic uniaxial tests to investigate the dynamic properties of EPS geofoam. Non-elasticized EPS geofoam which is commonly used in geotechnical applications were tested in the laboratory environment. This type of geofoam is characterized by elastic stress-strain behavior up to the strain level of approximately 1%.

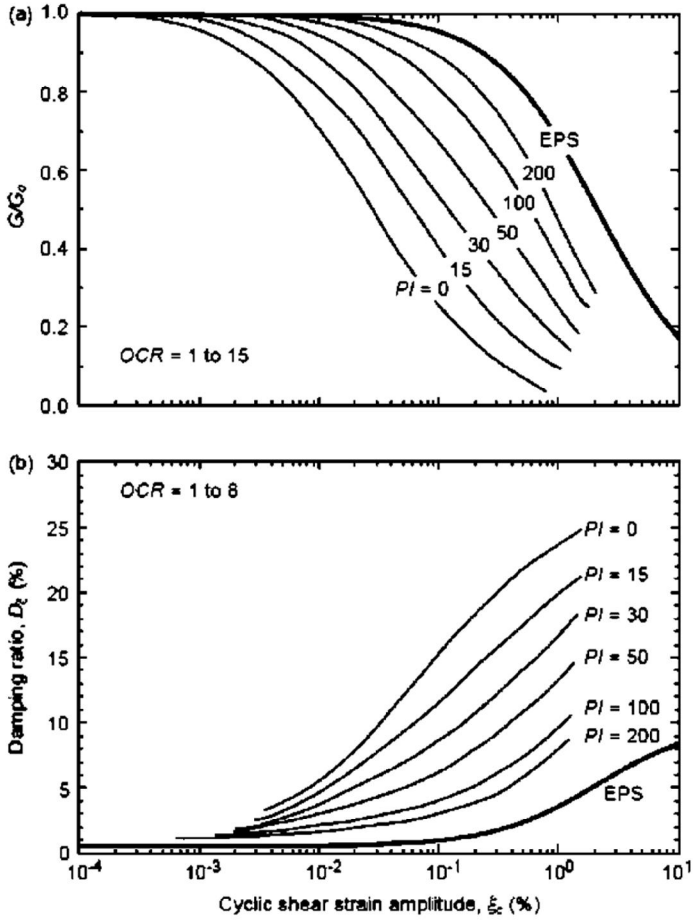

Figure 3-18 EPS (a) Modulus degradation and (b) damping ratio curves superposed on plots of Vucetic and Dobry (1991) (Athanasopoulos et al., 1999)

The density of the materials tested were 15 kg/m^3, 25 kg/m^3 and 32 kg/m^3 and the geofoam types were designated as EPS1, EPS2 and EPS3 throughout their study. All the tests were performed under zero confining stress. At the beginning of the testing, initial static deviator stress $(\sigma_a-\sigma_r)_{static}$ was applied to the specimen. (σ_a) and (σ_r) represent the major and minor principal stresses respectively where (σ_r) is always zero. Static deviator stresses were applied in the range of 15kPa to 60kPa. Cyclic deviatoric stress was applied after specimen has achieved equilibrium under the static deviatoric stress and creeping of the material was ceased. Magnitude of the cyclic deviator stress $(\sigma_a-\sigma_r)_{cyclic}$ were selected to keep the EPS specimen always in compression. Therefore, the tests should be considered as loading-unloading cycles rather than compression-extension cycles. All the tests were performed under 0.5Hz frequency and 20 cycles were applied in each test. In the tests where no plastic deformation was expected, five

cycles were considered as sufficient since any significant variation in response was not observed in the following cycles. The results of the tests were analyzed in terms of hysteresis loops at different *SSR* and *CDSR* where *SSR* represent the static stress ratio *($(\sigma_a-\sigma_r)_{static}/(\sigma_a-\sigma_r)_{yield}$)* and *CDSR* is the cyclic deviator stress ratio ($\Delta(\sigma_a-\sigma_r)_{cyclic}/(\sigma_a-\sigma_r)_{static}$). $(\sigma_a-\sigma_r)_{yield}$ was determined from monotonic uniaxial tests performed at 5%/min strain rate by using the method proposed by Magnan and Serratice (1989). In Figure 3-19, cyclic stress-strain response of EPS3 sample ($\rho=32kg/m^3$) were depicted. All the tests were initially subjected to a static deviator stress of 40kPa whereas the cyclic deviatoric component was set as 10kPa, 25kPa and 39kPa. Static stress ratio (*SSR*) was determined as 0.47 for this set of tests. It was observed that visco-elastic material behavior was dominant in the observed behavior of EPS geofoam. In the second set of tests, initial *SSR* was set as 0.70 and $(\sigma_a-\sigma_r)_{cyclic}$ was applied from this state of stress (Figure 3-20). Results indicated visco-elastic-plastic behavior with an increase in *CDSR* where major principal stress in yield of the material was being exceeded. The results of the cyclic uniaxial tests on EPS3 type specimen were further used in determination of the Young's Modulus and the damping ratio of the material in the cyclic axial strain range of 0.06% to 0.92%. In Figure 3-21, shear modulus ratio and damping data were plotted together with the upper and lower bounds determined based on the strain controlled cyclic tests compiled by Zarnani and Bathurst (2009b). The shear moduli obtained in this study is in fairly good agreement with the published data however the damping ratio values were not following the same trend with the published correlations. Authors explained the discrepancy between the damping ratios due to application method of cyclic load. Authors reported that most of the published data on the small strain damping behavior of EPS geofoam was based on the results of the torsional shear tests where the initial shear stress was zero however; in the cyclic tests performed in this study, there exists an initial static deviator stress at the beginning of the cyclic loading phase.

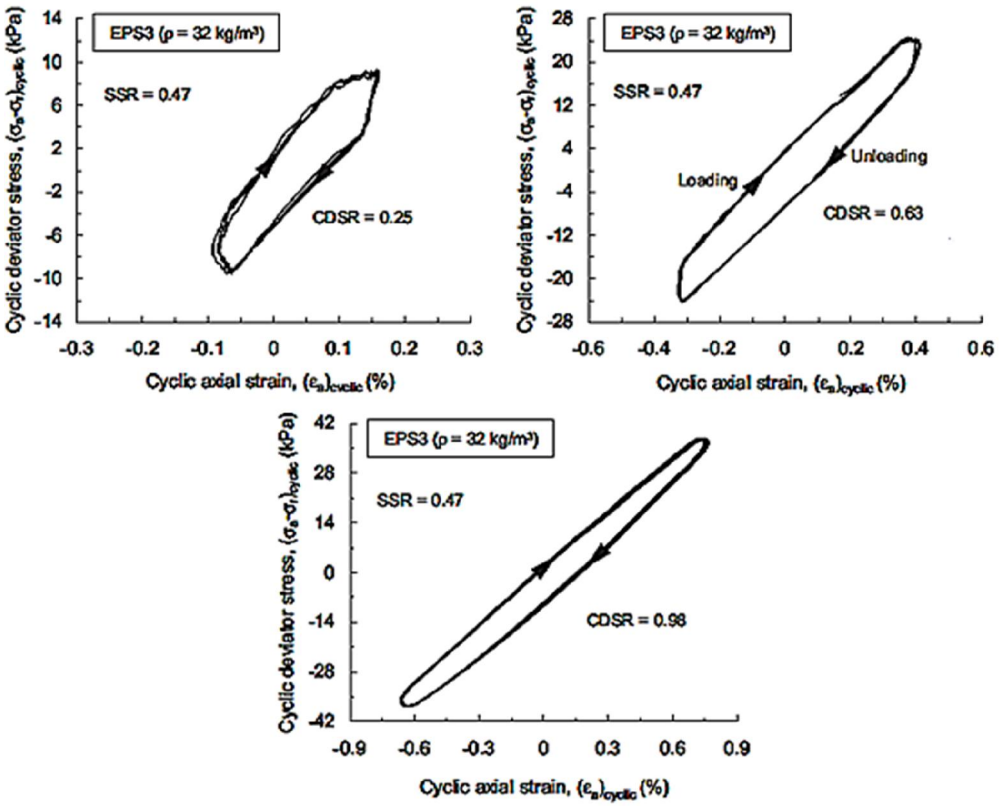

Figure 3-19 Results of cyclic uniaxial compression tests for SSR=0.47 (Trandafir et al., 2010b)

Based on their test results, authors proposed the following set of equations to estimate the shear modulus and the damping ratio of the EPS3 specimen:

$$\frac{G}{G_0} = 0.9967e^{-0.4603\gamma_c} \qquad 3\text{-}12$$

$$D(\%) = 4.7927 - 7.1213\,ln(\gamma_c) \qquad 3\text{-}13$$

where G and G_0 are in kPa and γ_c is in percents. Authors stated that in the previous studies on the dynamic response of EPS geofoam performed by Athanasopoulos et al. (1999), Ossa and Romo (2008), Young's modulus and damping ratios for cyclic strain amplitudes of up to 10% were provided by considering the non-elasticized EPS as a visco-elastic material in this strain range however; uniaxial compression tests indicated that the response of the material changes to visco-elastic-plastic after axial strain of about 1%.

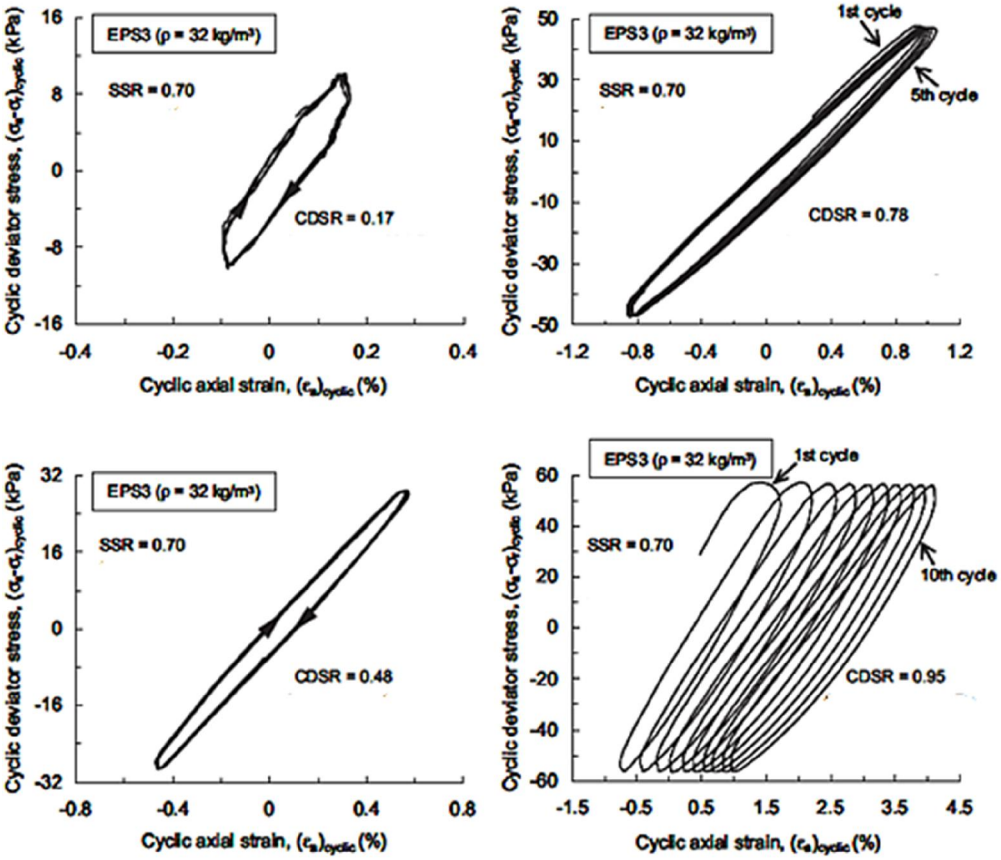

Figure 3-20 Results of cyclic uniaxial compression tests for SSR=0.70 (Trandafir et al., 2010b)

In the equivalent linear approach, investigated material should be considered as visco-elastic. Hence, shear modulus degradation and damping curves should be calculated from closed hysteresis loops. Authors showed the accumulations of plastic strains and formation on unclosed loops at certain combinations of static and cyclic deviator stresses. As a result, the equivalent linear approach for the EPS beyond the elastic strain level of 1% becomes invalid and should be avoided. Damping characteristics of the EPS play an important role in the cyclic isolation performance as a compressible inclusion. As a note, author indicated that the reduction of the lateral dynamic stresses acting on the retaining walls were mainly caused by the high compressibility of the geofoam rather than its damping characteristics since the volume of the geofoam was very small as compared to the retained backfill.

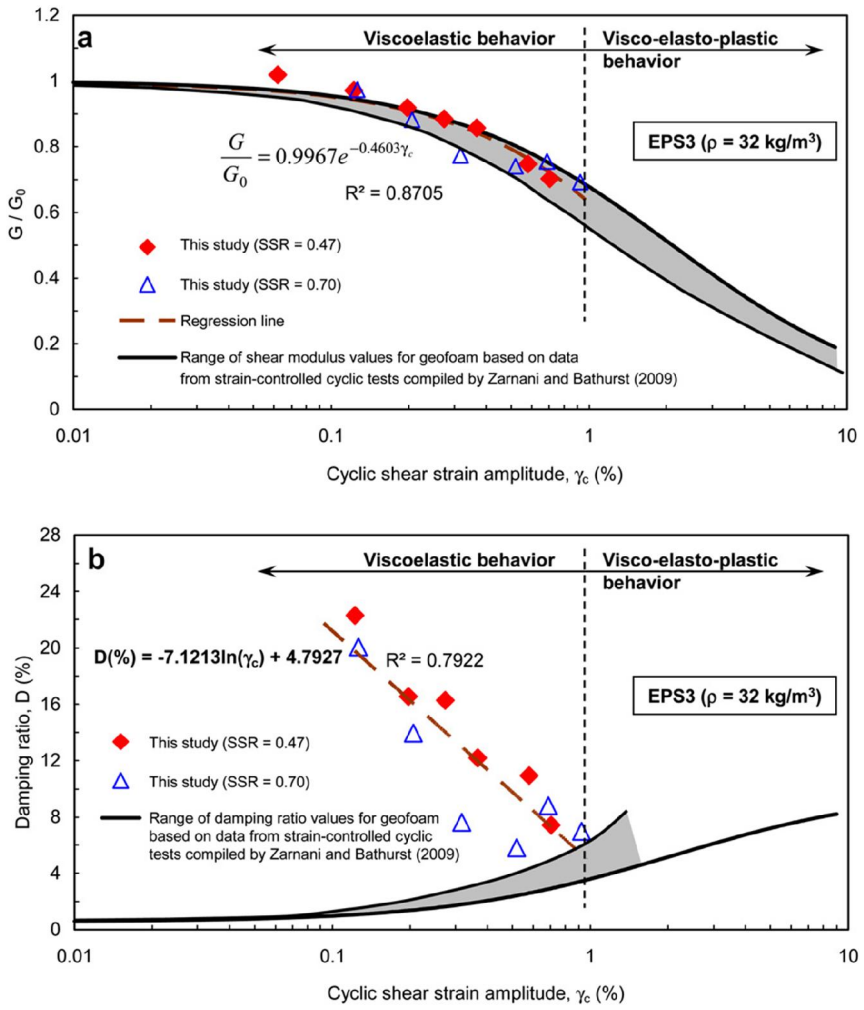

Figure 3-21 (a) Shear modulus versus cyclic shear strain (b) Damping ratio versus cyclic shear strain curves for EPS-3 geofoam (Trandafir et al., 2010b)

In a more recent study, Ossa and Romo (2010) conducted laboratory tests to investigate the dynamic response of EPS geofoam in detail. In this extensive study, effect of shear strain (γ), density (ρ) and confining stress (σ_3) on the shear modulus (G_0) and the damping ratio (λ) were investigated by resonant column tests as well as stress and strain controlled cyclic triaxial tests. Resonant column test results served to determine the dynamic properties at low shear strains (10^{-4}% to 10^{-2}%). Specimens of densities 24 kg/m^3, 30kg/m^3 and 32kg/m^3 with a diameter of 3.6cm and 8.9cm were cut by hotwire technique with computer controlled cutting machine. Specimens were tested under confining stresses of 0kPa, 30kPa and 60kPa. Tests were conducted by a fixed-free Drnevich type resonant column apparatus. Each test was repeated for three times to verify the consistency of the results. Strain-controlled cyclic triaxial tests served for the

estimation of shear moduli and damping values for strains above 10^{-2}%. In this type of tests, twenty cycles of displacement having amplitudes between 0.3mm to 2.0mm were applied at 1Hz loading frequency. Two or three tests were conducted to diminish the errors and inconsistency between the results. Shear moduli and damping ratios were estimated from the tenth cycle of the tests. Conversions between the G and E_{dyn} were performed by linear elastic theory. Stress-controlled cyclic triaxial tests served to determine the dependency of axial strain, ε_{max} and dynamic elastic modulus E_{dyn} to loading cycles. Tests were performed on specimens having densities of 25kg/m^3 and 30kg/m^3 under confining stresses (σ_3) of 30kPa and 60kPa. Initially, samples were loaded under a static deviator stress and 4000 load cycles were applied. Resonant column and cyclic triaxial tests provided shear strain and damping ratio for a strain range of 10^{-4}% to 30%. It was observed that a significant gap occurs between the results of the resonant column tests and cyclic triaxial tests. Similar problems were also reported by the previous researchers (Athanasopoulos et al., 2007) and (Abdelrahman et al., 2008a). These researchers observed that Poisson's ratio of the EPS geofoam was positive well below the elastic limit and approach to zero for axial strains approaching the elastic limit of the material. Beyond this strain level, negative values of Poisson's ratio were observed. Authors indicated that there has not yet been developed a methodology to relate the shear modulus and Young's modulus of the cellular EPS material. They proposed extension to the relationship based on the linear elastic theory. In their adopted relationship, an empirical factor estimated from the test results were multiplied with the classical shear modulus-Young's modulus relationship as follows:

$$G = \alpha \frac{E_{dyn}}{2(1+\mu)} \qquad \text{3-14}$$

where α is the empirical factor and μ is the Poisson's Ratio. α values were observed to vary between 1.5 and 2.2. The modified curves for the shear modulus and the damping ratio were shown in Figure 3-22. It was observed that shear modulus decreases and damping ratio increases for higher shear strains. In the shear strain range of 10^{-4} to 10^{-1}%, significant variation was not observed in shear moduli and damping ratios. Confining stress affects the shear modulus of the EPS geofoam under shear strains of 10^{-1}%. As opposed to the classical soil

behavior, increasing confining stress levels leads to a decrease in the stiffness of the EPS under cyclic loading. Authors stated the reason of the stiffness degradation as the deformation of the cellular structure of the geofoam. The re-arrangement of the beads and the auxeticity (lateral contraction under axial loads) of the material significantly affect the response of the material under triaxial loading conditions. Additionally, higher confining stresses may cause rupture in the bead connections leading a more deformable material under axial loads. Authors indicated that further research is required to fully understand the dynamic response of the material at different combinations of confining and axial stresses. The decrease in the shear modulus as the confining stress increases should be considered when designing geotechnical structures involving geofoam. It was reported that density of the EPS material contributes to the material's resistance against shear force as observed in Figure 3-22. However, any significant effect was not observed on the damping ratio values. Based on the database obtained from laboratory tests, authors proposed an empirical model for the estimation of shear modulus and damping ratio values. Following equations were formulated:

$$G = \frac{(G_{min} - G_{max})}{H_\gamma} + G_{max} \quad \text{3-15}$$

$$\lambda = \frac{(\lambda_{max} - \lambda_{min})}{H_\gamma} + \lambda_{min} \quad \text{3-16}$$

$$H_\gamma = \left[\frac{(\lambda/\lambda_r)^{2B}}{1 + (\lambda/\lambda_r)^{2B}}\right]^A \quad \text{3-17}$$

where λ_r is the reference strain corresponding to 50% of the maximum shear modulus, *A* and *B* are the dimensionless constants. *G*(MPa) and $\lambda\,(\%)$ are the shear modulus and damping ratio values at the required strain levels. The parameters in equations above were estimated through a multi-linear fitting procedure and formulated as follows:

$$A = -0.99\left(\frac{\sigma_3}{100}\right) + 0.65\left(\frac{\sigma_3}{100}\right) - 0.40\left(\frac{\rho}{10}\right)^2 + 0.22(\rho) - 1.92 \quad \text{3-18}$$

$$B = 0.26\left(\frac{\sigma_3}{100}\right)^2 - 0.07\left(\frac{\sigma_3}{100}\right) + 0.40\left(\frac{\rho}{10}\right)^2 - 0.22(\rho) + 3.61 \quad \text{3-19}$$

$$\gamma_r(\%) = 0.26\left(\frac{\sigma_3}{100}\right) + 0.40\left(\frac{\rho}{100}\right)^2 - 0.27(\rho) + 5.09 \quad \text{3-20}$$

$$G_{max} = -2.78\left(\frac{\sigma_3}{100}\right) + 9.62\left(\frac{\rho}{10}\right)^2 - 4.66(\rho) + 67.03 \quad \text{3-21}$$

$$\lambda_{min} = 0.36\left(\frac{\sigma_3}{100}\right) - 1.26\left(\frac{\rho}{10}\right)^2 + 0.69(\rho) - 8.64 \quad \text{3-22}$$

G_{min} and λ_{max} values should be determined in order to plot the shear modulus degradation and damping curves for the EPS geofoam. G_{min} were estimated from deviator stress-strain curves from monotonic compression tests. Authors indicated that in the absence of experimental data, deviator stress-strain curve can be estimated by using the previously proposed models (Chun, et al. (2004); Ossa and Romo (2009). λ_{max} can be taken as 12% based on the saturation of damping ratio values for shear strains greater than 1%. Additionally, authors also investigated the effect of the number of loading cycles on the dynamic behavior of EPS by interpreting the outcomes of stress-controlled triaxial compression tests. It was observed that E_{dyn} is not significantly affected by the number of cycles for stress levels (static plus cyclic) less than the yield stress. Considerable degradation in stiffness was observed when the applied stress overcomes the yield strength. The rate of degradation slows down after the tenth cycle of the loading.

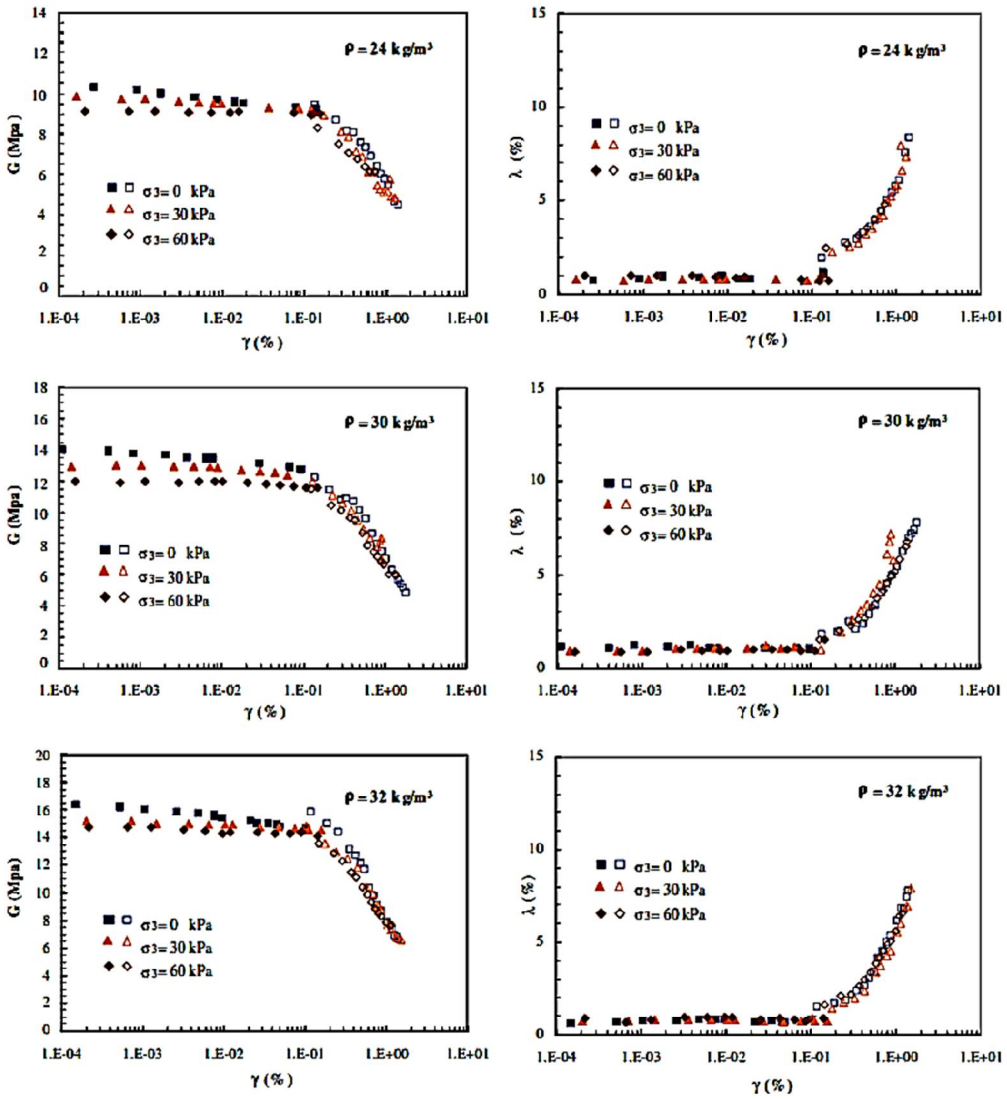

Figure 3-22 Shear modulus and damping ratio curves (Ossa and Romo, 2010)

3.6 Previous studies on constitutive modeling of EPS geofoam

Various models were proposed to describe the stress-strain behavior of the EPS geofoam material. These models should be categorized in two groups namely: time independent behavior and time dependent models involving creep effects.

3.6.1 Time-independent Preber Model (1995)

Preber et al. (1995) proposed a time-independent model to estimate the stress-strain relationships. Constitutive equations involved the initial modulus (E_i), plastic modulus (E_p), intersection of the axial stress axis and the plastic tangent line (I), axial stress value (Y_0) corresponding to strain X_0 which is the strain value at the

intersection of the initial and the plastic tangent lines. The following equations formulated by using the aforementioned parameters:

$$\sigma = \left(1 + E_p \epsilon\right)\left[1 - exp\left(-C\epsilon^2 - \frac{E_i \epsilon}{\left(1 + E_p X_0\right)}\right)\right] \quad 3\text{-}23$$

$$C = -\frac{E_i}{I X_0} - \frac{1}{{X_0}^2} ln\left[1 - \frac{Y_0}{\left(I + E_p X_0\right)}\right] \quad 3\text{-}24$$

where σ is the axial stress and ϵ is the axial strain. X_0 can be calculated analytically from E_i, E_p and I. Based on the experimental data, authors estimated E_i, E_p and I and Y_0 as follows:

$$E_i = (-4180 + 382.2\rho) + (-6.2 - 0.52\rho)\sigma_3 \quad 3\text{-}25$$

$$E_p = (104 + 4.3\rho) + (-3.6 + 1.5\rho)\sigma_3 \quad 3\text{-}26$$

$$I = (-107 + 8.9\rho) + (0.63 - 0.062\rho)\sigma_3 \quad 3\text{-}27$$

$$Y_0 = (1.4 + 8.7\rho) + (-1.1 + 0.04\rho)\sigma_3 \quad 3\text{-}28$$

Poisson's ratio (ν) was estimated as follows based of the limited test data:

$$\nu = 0.2 - 0.5\frac{\sigma_3}{62\ kPa}\ for\ 0 \le \sigma_3 \le 62\ kPa \quad 3\text{-}29$$

3.6.2 Time-dependent Findley and Chambers LCPC models

Horvath (1998) summarized the adaptation of the time dependent Findley model to estimate the time dependent stress-strain behavior and creep characteristics of EPS geofoam. Findley model was originally proposed to describe the creep behavior of polymers. To illustrate the correct use of Findley equation in geosynthetics field, author evaluated the results of laboratory creep tests for the EPS block geofoam. The tests were performed during 1987 to 1989 by the inventor company of EPS, BASF AG in Ludwigshafen, Germany. BASF tests extended for approximately 19000 hours (2.2 years) which are believed to be the

longest duration for the EPS creep tests. Up to that time, creep tests of longest duration lasted for 10000 hours (1.1 years). Test results were evaluated by general power-law equation (Findley and Khosla, 1956) shown below:

$$\varepsilon = \varepsilon_0 + mt^{n_F} \quad 3\text{-}30$$

$$\varepsilon_0 = f_{iF} sinh\left(\frac{t}{t_{iF}}\right) \quad 3\text{-}31$$

$$m = m_F sinh\left(\frac{t}{t_{mF}}\right) \quad 3\text{-}32$$

where *m* and *n* are dimensionless material parameters and ε_0 is the initial axial strain and *t* is the applied stress. t_{iF} and t_{mF} are Findley parameters in stress dimensions. m_F and n_F are dimensionless Findley parameters. Analysis of the equation 3.30 indicated that extrapolation of the results would be accurate for approximately 30 times the test duration. BASF Company was aiming to estimate the behavior of EPS geofoam for a 50-year design life. Therefore, minimum of 14600 hours of creep testing were required to achieve this goal. The actual test duration was 19000 hours which serves for obtaining the creep behavior for 65-year design life of the geofoam. The interpreted results were incorporated into the German national design manual for EPS geofoam lightweight fills (Forschungsgesellschaft für Straßen- und Verkehrswesen 1995). Following set of equations based on Findley model was developed by French Government Central Road Research Laboratory (LCPC) were utilized in estimation of EPS creep behavior:

$$f_i = \frac{t}{E_{ti}} + at^n \quad 3\text{-}33$$

$$a = 0.00209\left(\frac{t}{t_y}\right)^{2.47} \quad 3\text{-}34$$

$$n = -0.9log\left(1 - \frac{t}{t_y}\right) \quad 3\text{-}35$$

$$t_y = 6.41\rho - 35.2 \quad 3\text{-}36$$

$$E_{ti} = 479\rho - 2875 \quad 3\text{-}37$$

where E_{ti} is the initial tangent modulus (in kPa), t_y the yield strength of EPS (in kPa) and ρ the density of geofoam (in kg/m^3).

3.6.3 Time-independent Chun et al. model

(Chun et al. (2004) developed a hyperbolic model to estimate the time independent stress-strain behavior of the EPS based on triaxial test results. It was observed that the stress-strain behavior of the EPS was dependent on the density and confining stress. The following general constitutive model was proposed:

$$\sigma_1 = \frac{a[\varepsilon_1^b(\%)]}{c + [\varepsilon_1^b(\%)]} \quad 3\text{-}38$$

where σ_1 is the major principal stress in kPa, ε_1^b the major principal strain in percent and *a*, *b* and *c* are functions of the density of the geofoam and the confining stress:

$$a = -60.955 + 9.843\rho + 0.339\sigma_3 \quad 3\text{-}39$$

$$b = 1.135 + 0.042\rho - 0.008\sigma_3 \quad 3\text{-}40$$

$$c = -0.437 + 0.102\rho - 0.002\rho^2 + 0.011\sigma_3 - 0.00039\rho\sigma_3 \quad 3\text{-}41$$

where ρ is the density of EPS in kg/m^3 and σ_3 is the cell pressure in kPa.

3.6.4 Time-independent Wong et al. model

Wong and Leo (2006) proposed a simple elasto-plastic hardening model based on triaxial tests for confining pressures between 0kPa and 60kPa. The proposed model involved six parameters which should be calibrated by triaxial testing results. These constitutive constants were E and *v,* to define the isotropic elastic behavior, K_p and R_0 which define the first yield stress σ_{1y} , β to define the hardening rate and *K*, to define the flow rule and dilatancy behavior. The bilinear stress-strain behavior was shown in Figure 3-23.

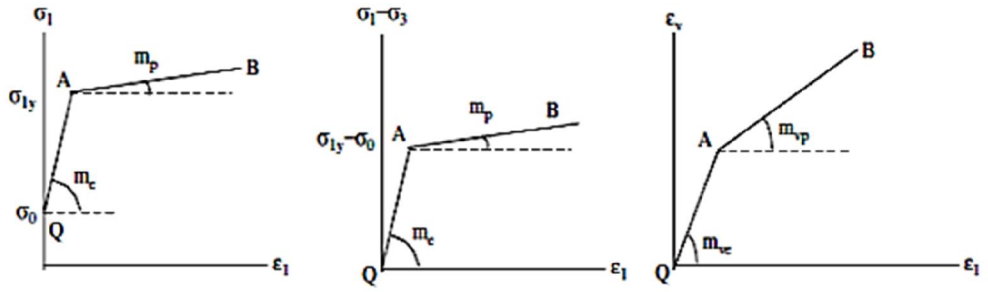

Figure 3-23 Bilinear stress-strain behavior predicted by the model

The elastic and plastic stiffness values, m_e and m_p as well as the volumetric deformation ratios m_{ve} and m_{pe} were determined as follows:

$$m_e = \left(\frac{\partial \sigma_1}{\partial \varepsilon_1}\right)_{QA} = \frac{\mu(3\lambda+2\mu)}{\lambda+\mu} = E \qquad 3\text{-}42$$

$$m_{ve} = \left(\frac{\partial \varepsilon_v}{\partial \varepsilon_1}\right)_{QA} = \frac{\mu}{\lambda+\mu} = 1-2\nu \qquad 3\text{-}43$$

$$\sigma_{1y} = K_p \sigma_0 + R_0 \qquad 3\text{-}44$$

$$m_p = \left(\frac{\partial \sigma_1}{\partial \varepsilon_1}\right)_{AB} = \frac{1}{\frac{1}{E}+\frac{2\sqrt{3}}{\beta(2+K)}} = \frac{1}{\frac{1}{E}+\frac{1}{H}} \qquad 3\text{-}45$$

$$m_{vp} = \left(\frac{\partial \varepsilon_v}{\partial \varepsilon_1}\right)_{AB} = \mu \frac{\sqrt{3}(2+K)\beta + 6(1-K)(3\lambda+2\mu)}{\sqrt{3}(2+K)\beta(\lambda+\mu) + 6\mu(3\lambda+2\mu)} \quad 3\text{-}46$$

$$K = \frac{d\varepsilon_V{}^P}{d\zeta} \quad 3\text{-}47$$

where μ and λ are classical Lame's constants, σ_{1y} is the yield strength of the material and $\zeta$is the positive plastic multiplier. The constants R_0 and K_p can be determined graphically by drawing the σ_{1y} and preconsolidation stress (σ_0). The constants R_0 and K_p are simply the slope and y-intercept in the graph, respectively. It was observed that constitutive model was able to estimate the stress-strain behavior of EPS under shearing.

3.6.5 Zarnani and Bathurst's study

Zarnani and Bathurst (2009b) performed a comparison of linear-elasto-plastic model with Mohr-Coulomb failure criterion and equivalent linear method incorporating hysteretic loading-unloading cycles using Masing type functions. Both of the compared models were utilized for the simulation of shaking table tests on the performance of EPS seismic buffers in shaking table tests performed by the same authors (Zarnani and Bathurst, 2007). In the equivalent linear approach, damping and shear modulus degradation were modeled with strain-dependent functions. In the linear elasto-plastic approach, 3% Rayleigh damping was taken into account as the frequency and mass dependent damping parameter. The loading and unloading regime of the material was shown in Figure 3-24. It was observed that hysteretic behavior occurs when the plasticity condition is reached. In the equivalent linear approach, Mohr-Coulomb failure criterion was used to determine the shear yield strength of the material. The linear-elasto plastic behavior and equivalent linear method were implemented in FLAC finite difference code to simulate the stress-strain behavior of EPS geofoam.

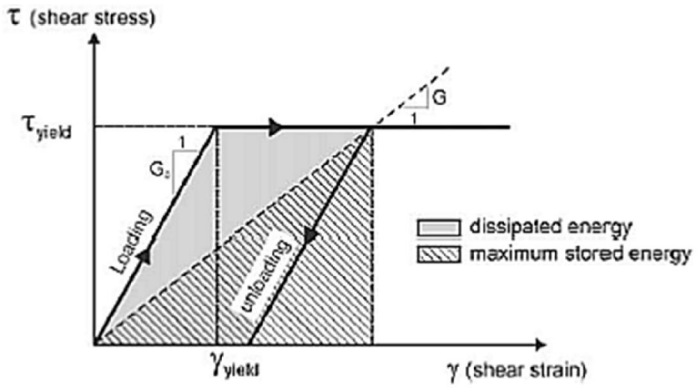

Figure 3-24 Cyclic loading in elastic perfectly plastic model obeying Mohr-Coulomb failure criterion (Zarnani and Bathurst, 2009b)

The hysteresis response implemented in FLAC code was fitted to the experimental results by using the following three-parameter sigmoidal function available in FLAC code:

$$M_{sec} = \frac{a}{1 + exp\left(-\frac{(log\gamma - x_0)}{b}\right)} \qquad 3\text{-}48$$

where *a, b* and x_o are the constants determined by fitting to the experimental data. Same function was utilized to estimate the damping ratio versus shear strain data. The comparison of the experimental data and the estimated curves were depicted in Figure 3-25. To estimate the hysteretic behavior of the sand used in the shake table tests, default modulus degradation function of sandy soils proposed by (Seed and Idriss, 1970). Investigation of Figure 3-26 revealed that lateral wall thrust estimated by elasto-plastic and equivalent linear approach were able to capture the measured load versus time histories. It was observed that analyses with equivalent linear approach yielded higher values of total peak wall forces especially at higher excitation levels. This approach was able to estimate the behavior of EPS buffers at greater accelerations, however simple elasto-plastic approach with Rayleigh damping was found to be sufficient in most cases.

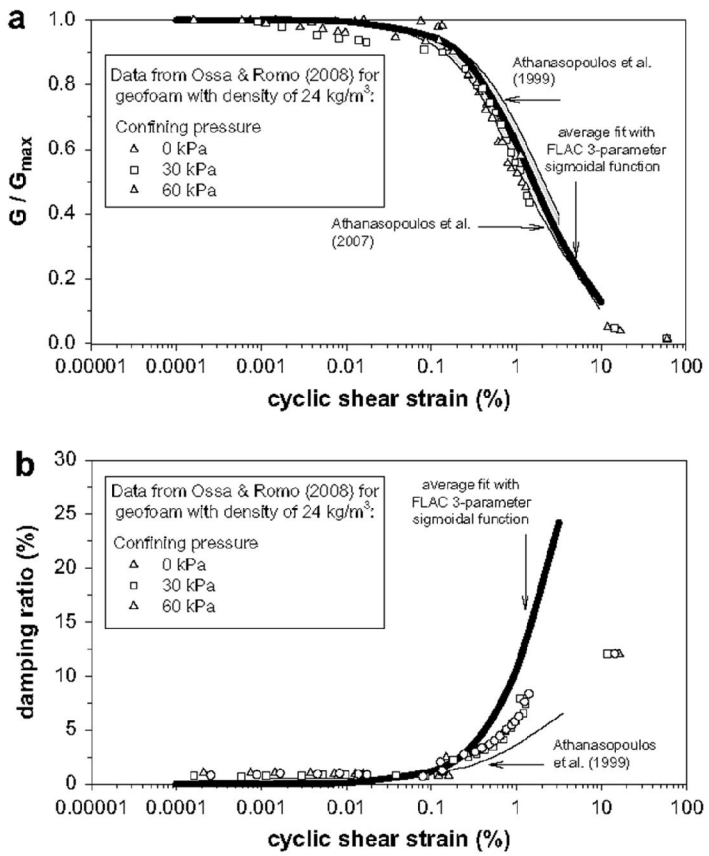

Figure 3-25 Comparison of the experimental data and the estimated curves by sigmoidal function (Zarnani and Bathurst, 2009b)

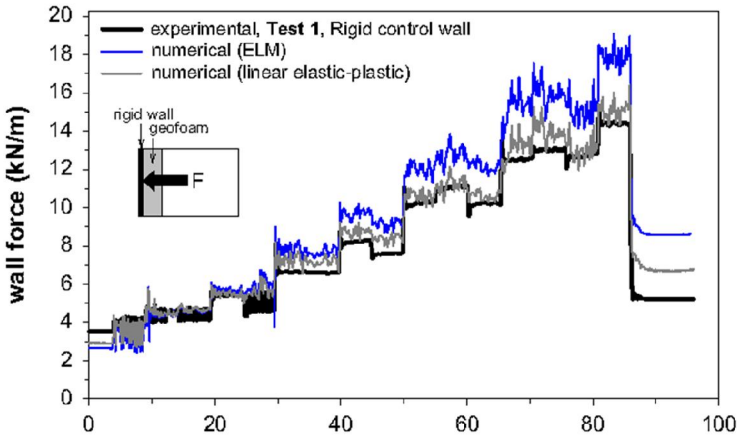

Figure 3-26 Comparison of wall thrust estimated using linear elasto-plastic and equivalent linear approach (Zarnani and Bathurst, 2009b)

CHAPTER 4

1-G PHYSICAL MODELING

4.1 Introduction

In this chapter, the procedure of the physical modeling study carried out on reduced scale cantilever wall models were explained in detail. The selection of physical attributes of the model walls based on dimensional modeling theory was discussed. The capabilities of the shake table system, the laminar container and the data acquisition system were presented. For a proper discussion of the results, the determination of the mechanical properties of the backfill material and the geofoam used in the study is required. Hence, an extensive laboratory testing was performed on model materials to determine the static and dynamic mechanical properties. A series of numerical analyses were performed to estimate the wall deflections and lateral earth pressures expected to occur in the model tests. Results of the numerical study presented in Chapter 6 served to plan the shake table testing program and to select dimensions of the wall models.

4.2 Fundamentals of physical modeling

Physical modeling is performed to investigate the behavior of a model structure which is considered as a representative of a prototype. Full-scale modeling is an example of physical tests where all the properties of the prototype structure are replicated with 1:1 scale in the laboratory. However, this is an expensive and time-consuming way of physical testing because actual dimensions of the model may be up to ten meters for a retaining structure or several hundred meters for an embankment dam. Hence, reduced-scale modeling is preferred in most cases since it is easier to obtain information about the investigated response more rapidly and with a closer control (Wood, 2004). In small scale modeling, a reduced

scale form (model) of a full size structure (prototype) is constructed. The scaled model is instrumented and tested to investigate the behavior of the prototype structure. Small-scale modeling is an inexpensive and efficient way of investigating the behavior of the prototype however it comes up with its own disadvantages. If the model is replicated in a reduced scale of the prototype, certain relationships are required to extrapolate the outcomes of the model behavior to prototype scale. At this point, theories of dimensional analysis lead to derivation of the required relationships. Dimensional analysis enables reduction in the number of variables that should be studied to understand the investigated problem. Dimensionally consistent equation sets are created which does not depend on the units of the measurement. Material behavior of the model and prototype is extremely important in dimensional analysis. If the expected behavior of the materials is entirely linear and material is homogeneous, the dimensional modeling may be a simple procedure. However, nonlinearity in the material behavior and interactions between materials having different responses will lead to several complications in dimensional modeling. According to Langhaar (1951), scale models can satisfy geometric, kinematic or dynamic similarity conditions. Geometric similarity means that scale model has homologous physical dimensions with the prototype. Kinematic similarity requires a model and prototype with homologous particles being at homologous points at homologous times. Dynamic similarity condition requires the presence of homologous net forces acting to the homologous points of the model and the prototype. According to Meymand (1998), all the requirements of the similitude may not be achieved in the model tests. For this reason, the degree of models in fulfilling the scaling relationships are indicated with a nomenclature such as “true”, “adequate” or “distorted” model. A true model will replicate all the physical aspects of the prototype in a scaled manner. Adequate models are also capable of simulating the primary features of the problem with minor deviations in fields which do not significantly affect the prediction equations. However, distorted models have also deviations in the main prediction equations.

4.3 Similitude and dimensional analysis

Dimensional analysis requires reduction of an engineering parameter into its fundamental system involving combinations of length (*L*), mass (*M*) and time (*T*) in most of the engineering problems. As an example, the elastic modulus of a

material is a measure of stress obtained as the ratio of the force to the area. The force may be indicated as a combination of *M, L* and *T* in the product form of MLT^{-2}. The stress then is represented by $ML^{-1}T^{-2}$. If the scale factor for mass is designated by η_M, the length η_L and time η_T, the relationship $\eta_M {\eta_L}^{-1} {\eta_T}^{-2}$ relates the elastic modulus of the model to the one of the prototype.

The key theorem in dimensional analysis is proposed by Buckingham (1915) and known as the Buckingham Pi Theorem. It states that if there is a physically meaningful equation involving *n* number of physical variables, and if these *n* variables can be represented by *k* independent physical quantities, the original physical equation may be expressed with a set of *n-k* dimensionless sets of parameters. However, Pi theorem only states the way of producing dimensionless sets and it does not guarantee the formation of physically meaningful sets. Buckingham's theorem states that it is possible to reduce a relationship into a set of completely dimensionless set of products if the main equation is dimensionally homogeneous. A set of dimensionless products of the variables describing a physical problem is assumed as complete if the product of variables in each set is independent from the others and all the other dimensionless products in each set are products of powers of dimensionless products in the set. Let the solution equation of a physical problem is as follows:

$$F(X_1, X_2, \dots, X_n) = 0 \qquad 4\text{-}1$$

Eq.4-1 can be expressed in terms of dimensionless π terms such as:

$$G(\pi_1, \pi_2, \dots, \pi_m) = 0 \qquad 4\text{-}2$$

where π terms represent the dimensionless products of physical parameters denoted by *X.* As stated in the theorem, the number of dimensionless π terms (*m*) is equal to the number of physical parameters (*n*) minus the number of the independent physical quantities. π terms are formed by grouping the physical *X* parameters into dimensionless subset of parameters, however it is important to group the physical parameters correctly to obtain meaningful sets of dimensionless parameters. After the formation of the π set of the governing physical equation, scaling relationships are determined between the prototype and the model to fulfill the following equation:

$$\pi_{i,m} = \pi_{i,p} \qquad 4\text{-}3$$

4.4 Application of scale model similitude in soil mechanics

Small-scale physical model tests in soil mechanics serve as a source of qualitative data on research areas where real scale prototype tests and case histories provide only limited data. Scale model tests are also utilized as quantitative calibration benchmarks for analytical and numerical methods which are used to predict response of the prototype. In order to make quantitative interpretation of the small scale test data, scaling relationships play a major role. As of our best knowledge, Rocha (1957) was the first to investigate the applicability of model tests to solve geotechnical problems. In his study, separate similitude relationships were derived for the total and effective stress conditions of soil. Rocha (1957) proposed linear scaling relationships between stress and strain behavior of the model and prototype to account for different stress regime occurring in 1-g physical tests. As shown in Figure 4-1, α and β parameters were defined to scale the stress and strain behavior of the model and prototype, respectively. In this graph, horizontal axis is the strain (ε_p : prototype strain and ε_m : model strain, Δp: displacement, L_p and L_m are prototype and model length, respectively) whereas the vertical axis indicates effective stresses for the prototype (σ'_p) and model (σ'_m) scale. The relationship was limited to elastic deformations and author indicated that the behavior gets extremely complicated when non-linear response is under concern. Roscoe (1968) extended Rocha's study and proposed the scaling relationships in the form of critical state soil mechanics. The difficulties of making scale models to replicate the prototype constitutive behavior of soils which are highly confining stress dependent were reported in his study. Roscoe (1968) proposed that the strain behavior of soil elements in the prototype and the model are identical when the elements were subjected to the same geometrical stress paths and their initial stress-strain position on the e-lnσ' plot is equidistant from the critical state line.

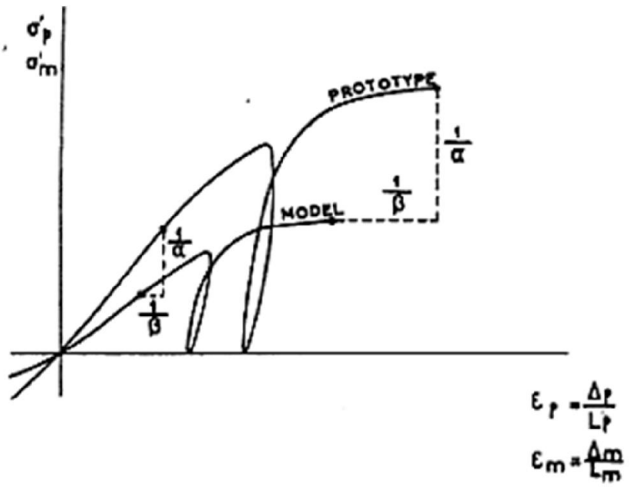

Figure 4-1 Scale modeling of the constitutive relationship of soil behavior (Rocha,1957)

Kagawa (1978); Kokusho and Iwatate (1979) investigated similitude of the non-linear dynamic response of ground by using Buckingham's π Theorem and obtained relationships limited to the shear deformations of soil structures. Iai (1989) indicated the need to extend previous studies to a more general form which may be used to interpret the results of dynamic model tests on saturated soil-structure and fluid systems. Based on the Rocha's work, Iai (1989) derived a detailed set of scaling relationships for the soil-structure-fluid system under dynamic loading. The entire problem was defined in terms of geometric, density and strain scaling factors. This method was validated by laboratory testing. However, author stated that his approach was limited to small-strain soil problems where soil particles do not lose contact. In a more recent study, Gibson (1996) investigated the scaling of constitutive material behavior under 1-g stress modeling conditions. Physical properties of the materials used in the model tests were modified to achieve a similar stress-strain behavior of the prototype. His work differs from the previous studies of Rocha (1957) and Iai (1989) which suggests modifying the constitutive relationship rather than the soil physical properties.

4.5 Scaling Relationships for 1-g Shake Table System

A "true" scaled model of the prototype is obtained by fulfilling all the governing similitude equations. However, in geotechnical engineering, it is not easy to

achieve a scaled model with a total fulfillment of the governing scaling equations. It is generally necessary to make an adequate model maintaining the first order similarity equations which will significantly affect the behavior and sacrificing the relationships with second order importance to the prototype behavior. The basic scaling factors play the major role in determining the advanced similarity equations. The primary scale relationship is the length scale factor (η_l) since the reduction of the geometrical dimension is the main target of reduced scale modeling:

$$\frac{(length)_{model}}{(length)_{prototype}} = \eta_l \qquad 4\text{-}4$$

The density scale factor (η_ρ) is provided as:

$$\frac{(density)_{model}}{(density)_{prototype}} = \eta_\rho \qquad 4\text{-}5$$

The density scale factor plays a major role in geotechnical modeling since second order density differences arise due to the confining stress dependency of the soil behavior even the same materials were used in the model and prototype scale. The gravitational acceleration scale factor (η_g) is represented as:

$$\frac{(acceleration)_{model}}{(acceleration)_{prototype}} = \eta_g \qquad 4\text{-}6$$

η_g is equal to one in 1-g model tests and will take some *n* times higher values in centrifuge modeling depending on the capacity of the geotechnical centrifuge. There exists an independent scale factor for the shear stiffness (η_G):

$$\frac{(stiffness)_{model}}{(stiffness)_{prototype}} = \eta_G \qquad 4\text{-}7$$

η_G is introduced as an independent scaling factor, however in geotechnical problems, the stiffness of the soil is dependent of several factors including the confining stress, strain rate and frequency of loading. The time scale (η_T) which is of interest in dynamic events, is formed by maintaining the similarity between the potential and kinematic energies in the model. The following relationships are derived for the similarity of time:

$$\eta_L.\left(\frac{\eta_\rho}{\eta_G}\right)^{1/2} = \eta_T \qquad 4\text{-}8$$

Similarly, for the frequency:

$$\frac{\left(\frac{\eta_G}{\eta_\rho}\right)^{1/2}}{\eta_L} = \eta_F \qquad 4\text{-}9$$

As of the special case of the applications of the similitude theory to dynamic geotechnical engineering problems, the scaling factors for the dynamic time and shear wave velocity is of utmost importance, since these properties directly affect the application of dynamic forces or displacements to the model and play and important role in the interpretation of the results taken from small scale model tests. The corresponding scaling relationship for shear wave velocity will be expressed by $\sqrt{\eta_G/\eta_\rho}$. A summary of the similitude relationships between prototype and model for the 1-g tests are summarized in Table 4-1.

Table 4-1 Summary of the similitude relationships for 1-g physical modeling

Physical quantity	Relationship	Physical quantity	Relationship	Physical quantity	Relationship
Mass	1	Acceleration	1	Length	$1/n$
Force	$(1/n)^3$	V_s	$\sqrt{1/n}$	Stress	$1/n$
Stiffness	$(1/n)^2$	Time	$\sqrt{1/n}$	Strain	1
Modulus	$1/n$	Frequency	$\sqrt{n}$	EI	$(1/n)^5$

4.6 Shaking table containers used in previous studies

Physical modeling of geotechnical problems requires a model container which does not impose any boundary conditions that do not exist in the prototype case. In other words, a successful shaking table container should deform under the seismic loading in a manner similar to the prototype free-field soil deposit by reducing the boundary forces. To fulfill this requisite, various soil containers were designed and used in dynamic geotechnical tests. To the best of the author, soil containers are classified mainly into three categories as:

- Rigid containers
- Flexible containers
- Laminar Container

4.6.1 Rigid containers

Rigid containers are the least expensive type since they don't have any moving parts and their maintenance costs are relatively low. However, rigid walls of the container significantly distort the boundary conditions of the prototype geometry by trapping the energy induced during dynamic excitations. Due to the wave reflections from the rigid boundaries, interference with the model behavior is unavoidable. Although they have several shortcomings, rigid wall shaking table containers are still widely used in modeling of bridge abutments, retaining walls and quay walls etc. In Table 4-2, some of the rigid containers used in the previous dynamic modeling studies were indicated.

Table 4-2 Rigid wall containers used in the previous research

Reference	Container dimension in mm's (W,H,L)	Backfill type	Structural model
Gohl and Finn (1987)	463, 463, 635	Dry Ottawa Sand	Single tubular pile
Valsangkar et al. (1991)	495,1016, variable height	Dry Ottawa Sand	Hollow aluminum pile
Zen et al. (1999)	3000, 3000, 1200	Saturated Niigata Sand	Retaining wall
Calisan (1999)	1000,1500,2000	Dry sand	Rigid retaining wall
Meneses et al. (2002)	1350,4500,2500	Saturated sand	Aluminum pile

4.6.2 Flexible containers

Flexible containers significantly improve the replication of free field soil deformations in the model. The reflected energy from the boundaries is reduced since the interaction between the model container and the soil is minimized by adjusting the stiffness and friction of the end walls to be similar with the adjacent soil column (Figure 4-2). However, the stiffness of the soil is dependent on several factors such as the void ratio and confining stress. Madabhushi (1994) indicates that it is not possible to assign variable stiffness to the end walls of flexible wall containers. Instead the end walls of the container are designed to match the stiffness of the soil layer at a specific void ratio and confining stress

and a specific range of shear strain. An example of flexible wall container in Cambridge University was depicted in Figure 4-3. The flexible wall containers are generally hinged-plate or equivalent linear beam type. Some of the studies with flexible wall containers are listed in Table 4-3.

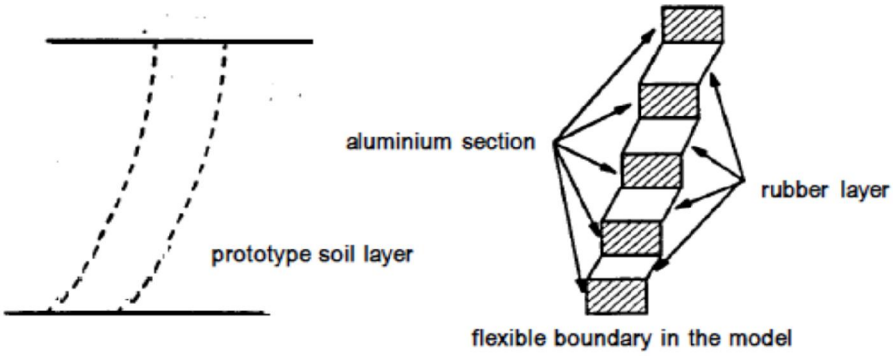

Figure 4-2 Representation of the free-field soil deformations by a flexible container wall

Meymand (1998) introduced a cylindrical flexible container with 2.3m diameter and 2.1m height (Figure 4-4). The top ring and the base plate were constructed from steel. The top ring is supported by steel pipes connected to universal joints thereby providing the soil model a full translational and rotational freedom while preventing the bending of the soil column. The side walls were produced from high strength kevlar material covered by 6.35mm neoprene rubber membrane. In Figure 4-5, a comparison of the free field accelerations was made for various container types (Meymand, 1998). It was observed that prototype behavior is modeled by the flexible wall container with a good accuracy.

Table 4-3 Flexible wall containers used in the previous research

Reference	Container dimension in mm's (W,H,L)	Backfill type	Structural model
Stanton et al.(1988)	Cylindirical,1219 diameter and 1219 height	Dry Ottawa Sand	Steel pipe
Richards et al. (1990)	Rectangular, 910,5500, 9000	Dry sand	Wooden shallow foundation
Meymand (1998)	Cylindrical, 2440 diameter and 2130 height	Kaolinite and bentonite mixture	Aluminum tubular pile group

Figure 4-3 A photograph of the Cambridge Equivalent Shear Beam Container (Madabhushi, 1994)

4.6.3 Laminar Box

Proper modeling of dynamic soil-structure interaction problems requires a container with ideal boundary conditions which would enable the model soil to make the same deformed shape with its prototype. Rigid and flexible walls have limitations in this aspect. Although, flexible containers provide reduced friction and stiffness at the side walls of the container, their affect is limited in most cases. The concept of stacked rings covered with low friction Teflon is proposed by Whitman et al. (1981). The individually moving stacks of aluminum frames (laminar frames) provided better boundary conditions which were close to the soil deformations. The sliding mechanism between the individual blocks can be linear bearings, ball bearings or a sliding mechanism made of Teflon.

Generally rectangular laminar boxes are common in the literature, even though cylindrical laminar containers are more suitable for bi-directional excitations. In Figure 4-6, cross section of a rectangular laminar box used by Taylor et al. (1995) is depicted. Laminar boxes can be classified according to their sizes. Table 4-4 depicts the typical dimensions of the laminar boxes. The weight of the laminar plates directly affects the behavior of the soil due to its inertia during dynamic excitation.

Figure 4-4 Flexible Wall Container (Meymand, 1998)

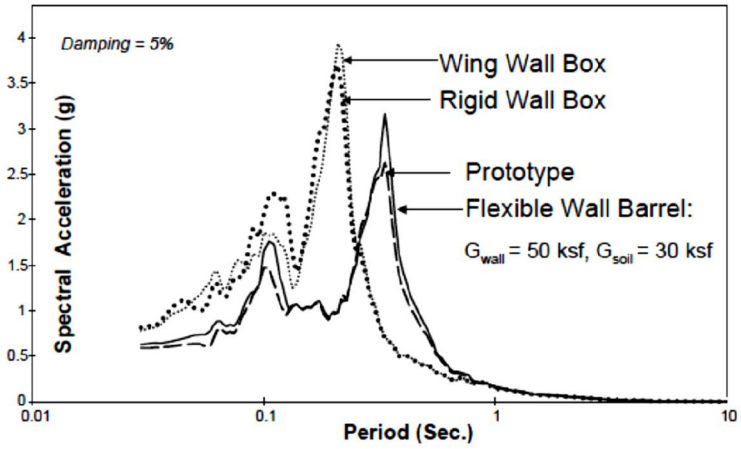

Figure 4-5 Comparison of the free field soil response of rigid and flexible wall model containers with the prototype conditions (Meymand, 1998)

In order to reduce the weight of the laminar frames, lightweight materials such as Styrofoam covered with vinyl chloride were used in a study carried out by Endo and Komanobe (1998). In Table 4-5, some of the laminar boxes used in previous geotechnical modeling studies were listed.

According to Prasad et al. (2004), an ideal soil container for dynamic studies should possess zero mass and the laminar frames and membrane should have zero stiffness against horizontal shearing. The friction between the side walls must not resist to vertical settlement of the soil. The dilation of the laminar frames

should be prevented. It was also recommended that the laminar plates should have a small height to increase the flexibility of the retained soil.

Table 4-4 Typical dimensions of various laminar containers used in shake table testing (Jakrapiyanun, 2002)

Characteristics	Small	Medium	Large
Scale	1/20	1-10 to 1/20	1/1 to 1/10
Container weight/Soil Weight (%)	18-22%	13-18%	9-13%
Height (m)	1	1-2	2
Length (m)	1.5	1.5-4	4

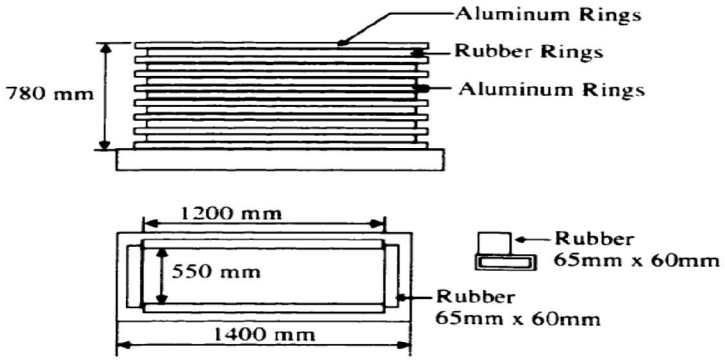

Figure 4-6 Laminar box cross section (Taylor et al., 1995)

The large scale 1-g laminar box located in Network for Earthquake Engineering Simulations (NEES) facility at the University of Buffalo has the capacity of carrying 80m^3 of model material. A soil deposit of up to six meters can be placed in the container which consists of 24 octagon shaped aluminum laminar stacks made of lightweight aluminum I-beams, each 0.25m wide and 0.30m deep, each of them weights 6.936kN without the soil model.

The friction coefficient between the ball bearings and the plates was reported to be less than 0.5%. The horizontal sliding capacity of each laminate is 36mm relative to the adjacent laminate. This amount of deflection in each laminate provides 15% maximum shear strain in the soil backfilled in the container. The ratio of ring weight to saturated weight of the soil inside the ring was reported to be 11% which is satisfactory in reducing inertia effects induced due to the weight of the container (Thevanayagam et al. 2009). The dimensions of the container are 5.0m by 2.75m (length by width) and the height is about 6.2m when all of the

laminar stacks are installed. The laminar container and the excitation system have the capability of simulating bi-axial excitation by two servo high speed actuators supported by a rigid reaction wall. The shaking system is designed to provide maximum horizontal shaking intensity of 0.3g. Real earthquake ground motions or any synthetic motion can be applied to the base of the laminar box accurately. The base of the whole system sits on a strong floor in order to withstand the total weight of the system and the model (Figure 4-7). For the backfilling purposes, a hydraulic filling system is present for underwater sand placement. For modeling sloping ground conditions, the base of the laminar container has the ability to incline in the longitudinal direction.

Table 4-5 Laminar containers used in the previous research

Reference	Container dimension in mm's (W,H,L)	Backfill type	Structural model
Sakajo et al. (1995)	Rectangular, 16 frames,800,1200,100	Loose saturated silicon sand	25 mm-Plastic pipe for 6X6 pile group
Taylor et al. (1995)	Rectangular, 8 aluminum frames, 550, 1200, 780	Dry Leighton Buzzard Sand D_r=90%	No structure
Ishimura et al. (1992)	Rectangular, 18 aluminum frames with ball bearings, 1500, 2000, 980	Toyoura Sand D_r=98%	Shallow Foundation
Kagawa et al. (1995)	Rectangular, 2000,2000,1000	Loose saturated Kasumugara sand D_r=40%	Steel plate
Taylor et al. (1997)	Rectangular aluminum frames, 1000, 5000, 1150	Dry sand	No structure
Endo and Komanobe (1995)	Cylindrical, 30 frames of styrofoam rings covered in vinyl chloride, mechanical ball bearings, inner diameter 1400	Saturated Quartz Sand Dr=50%	No structure

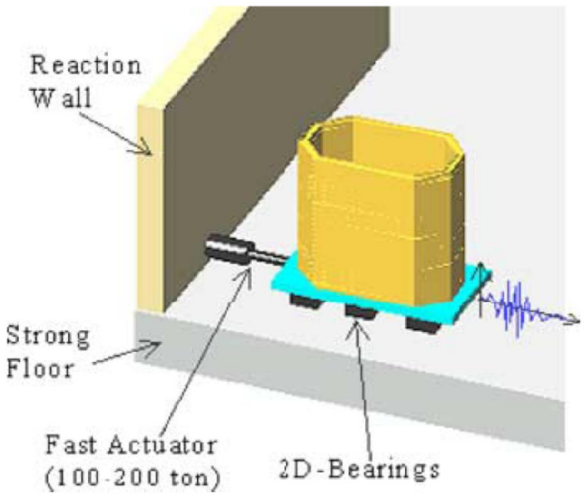

Figure 4-7 Three dimensional view of the laminar container system (Thevanayagam et al., 2009)

The laminar container in University of Western Ontario has dimensions of 1.22m by 1.22m which is excited by hydraulic actuators controlled with a digital control module (Turan et al., 2009). Various types of dynamic excitations may be applied to the soil container including harmonic spectrums and earthquake records. The shaking table operates in the range of 1Hz-150Hz with maximum displacement amplitude of 12mm in both directions. The laminar box installed on the shaking table consists of 24 horizontal laminates supported by linear bearings and steel guide rods connected to an external frame (Figure 4-8). The overall height of the laminar container is 807mm when all the laminar frames are used. In plan, the dimensions are 900mm by 450mm. The clearance between each laminar plate is 2mm which ensures the independent movement of the frames without any friction. The linear bearings provide a single direction movement parallel to the longitudinal direction of the containers.

4.7 Shaking table and laminar container of the current study

In this section, recent modifications on the actuator system and the soil container of the shaking table system which was built as a part of a previous Ph.D. thesis study (Calisan, 1999) were explained.

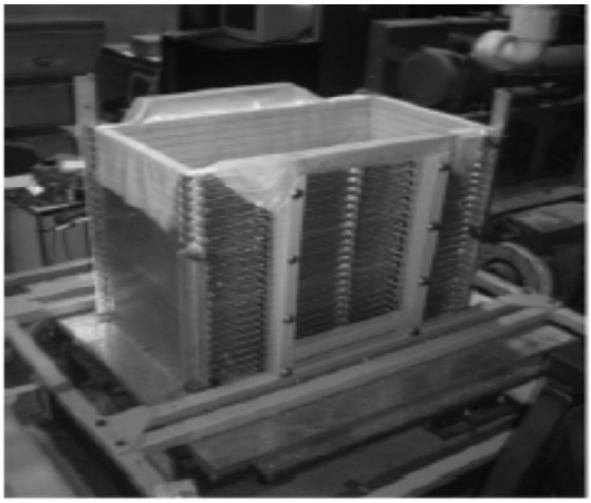

Figure 4-8 (a) Laminar box covered with latex membrane (Turan et al., 2009)

4.7.1 Previous shaking table system

Previous shaking table system consisted of two rigid steel frames equipped with a gear box and electric motor. The main frame of the shaking table had dimensions of 3.5m by 1.0m in plan and was manufactured by welding steel U profiles. This frame serves as a skeleton of the shaking table system on which all the remaining parts were built. A reinforced concrete foundation with dimensions of 2.5m × 4.0m × 0.8m had been constructed to provide as a rigid base for the main frame. 30cm×30cm steel anchor plates were left in the reinforced concrete and the main frame had been welded to the anchor plates. The second frame which forms the rigid platform for the soil container had been built by welding U beams and attached to the main frame by four rubber bearings located at each corner. The steel base of the soil container had been rigidly installed on this sliding frame that was connected to a rigid transmission shaft which in turn was connected to a circular disc. The circular motion of the electric motor is converted to harmonic horizontal motion by providing eccentricity between two discs. The shift of the axis of rotations of each of the rotating discs ends up with a harmonic translational motion in the transmission shaft. However, this mechanism leads to a combination of vertical and horizontal displacements in the shaft. To eliminate the vertical motion, both ends of the transmission shaft are pin connected so that the vertical displacements of the discs are not transmitted to the shaking table platform. The AC electric motor of the system has an operating frequency of 50Hz which is reduced to 2Hz by means of a built in gearbox. The designed excitation system provides a sinusoidal harmonic motion which can be represented as:

$$x = x_0 \sin \omega t \qquad 4\text{-}10$$

where x is the displacement at time (t), x_0, the displacement amplitude and ω is the angular frequency of the motion. A gear with a diameter of 21.9mm had been connected to the axis of the rotation and the motion generated due the eccentricity of the two discs was transferred by means of a steel rod (Figure 4-9). The frequency of the excitations was adjusted by using various combinations of gears however, only a limited number of motions were achieved by using this gear system (Table 4-6).

Table 4-6 Available frequencies of the previously used gear box mechanism

Gear No	Frequency of the shaking table (Hz)
1	3.03
2	3.23
3	3.75
4	4.6

In the previous studies Calisan (1999) and Yunatci (2003), a rigid soil container having dimensions of 2m×1m×1m had been used in the shaking table tests. The side and bottom walls of the soil container were made from 3mm thick steel plates. The bottom and sides of the test box were covered with emery paper (Calisan, 1999). In these studies, response of laterally braced sheet pile walls had been investigated as well as gravity retaining walls. The surcharge effects and wall flexibility on the dynamic response of the lateral earth pressures had been studied by Cilingir (2005) by using the rigid container.

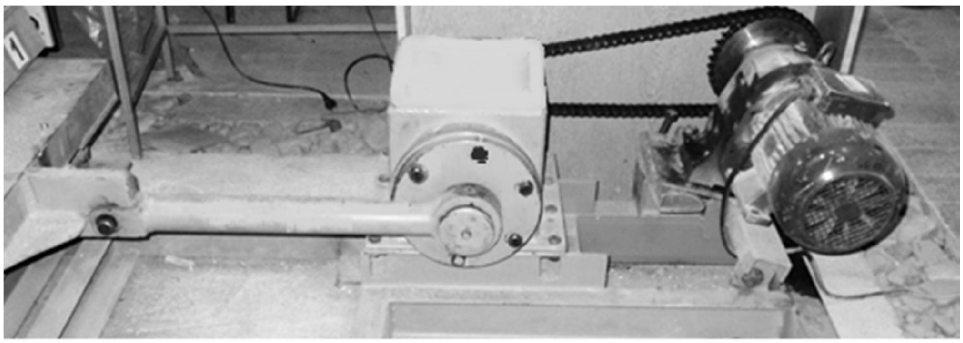

Figure 4-9 Transmission mechanism of the shaking table

4.7.2 The modifications on the excitation system for the current study

During the current Ph.D. study, the frequency adjustment mechanism of the excitation system has been replaced by a digital frequency inverter shown in Figure 4-10. This device enables adjustment of the output frequency of the electric motor more accurately in a wider range therefore preventing the frequency limitations of the previous mechanism. The renovated system can transmit excitations with 8mm displacement amplitude and up to 11Hz frequency to the base platform of the soil container. The displacements are limited with this value due to the displacement capacity of the rubber bearings installed under the container frame. Peak ground acceleration achieved on the table is measured as 1.2g.

4.7.3 Design of a laminar container for the current study

It is difficult to design an all-purpose container since the requirements of each model problem are different. Modeling of a deep foundation or a pile group requires a deeper container compared to the retaining wall or shallow foundation models due to the boundary interactions between the container and the model. It is certain that larger containers which allow for preparation of larger models provide more reliable results. However, the size of the container is strongly dependent to the capacity of the excitation system.

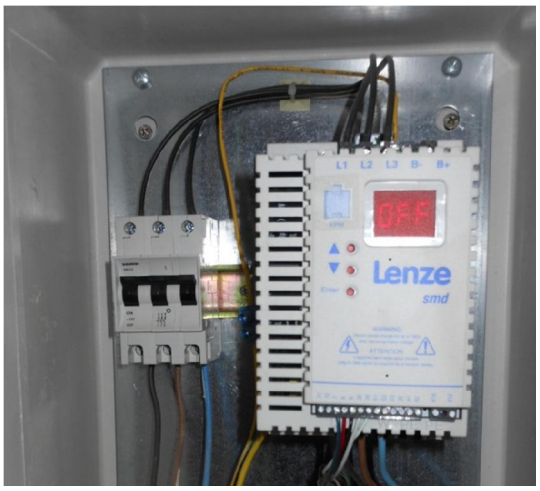

Figure 4-10 Lenze SMD153 frequency inverter connected to the AC electric motor in order to adjust frequency of the output motion

Another important factor on the design of the container for a dynamic soil structure interaction study is the natural frequencies of the container itself and the

model structure. The natural frequency of the investigated model must not coincide with the natural frequency of the laminar container since interference may occur in the expected behavior of the model structure. In the current study, the behavior of a cantilever retaining wall model is under concern. The behavior of the retaining walls strongly depends on the properties of the backfill retained by the wall. Analytical solutions are mainly based on the formation of a failure wedge in the backfill. To make reliable comparisons with the results of the analytical solution methods, plane strain assumption and the formation of a full failure wedge behind the retaining wall should be provided. Hence physical dimensions of the container should be selected by taking into account the limitations mentioned above. Additionally, following requisites suggested by Prasad et al. (2004) were taken into account for the design of the laminar container:

1. Laminar container should allow free movement of soil along the excitation axis.
2. It should have the ability to retain soil without leakage.
3. Laminar frames and the membrane should have minimum resistance to horizontal shear.
4. The container should offer little resistance to vertical settlement of soil.
5. Height of each layer should be as small as possible in order to decrease the resistance to the free soil movement

Considering the aforementioned limitations and requirements, a rectangular laminar container with uni-axial excitation capability was designed (Figure 4-11). Jafarzadeh (2004) states that laminar containers having a circular cross section are more suitable for multi-axial excitation purposes owing to the symmetry of the container since stress concentrations are inevitable at the sides of the square or rectangular containers. However, laminar box of the current study is uni-axial type and influence of the stress concentrations at the sides may not be as pronounced as the systems having multi-axial excitation capability. The main components of the designed container are:

a) Steel laminar frames
b) Low friction linear bearings
c) Rotational bearings
d) Guide walls and rails
e) Internal rubber membrane

The laminar container of the current study is composed of individual laminar frames which are shown in Figure 4-12. The dimensions of each laminar frame are 1.004m × 1.507m × 0.100m (Length × width × height). All the elements are made of steel plates having 11mm thickness. The short sides of the laminar frames except the uppermost one are connected to the long sides by rotational bearings to provide the rotational movement of the plates during the excitation. Linear ball bearings were installed on four sides of the laminar frames to enable the horizontal displacement while reducing the friction as much as possible. The weight of each laminar plate is approximately 42.9kg. There exist nine frames which constitute the laminar container shown in Figure 4-13. The total weight of the container is 386kg when all the frames are in place. The linear bearings of the laminar frames were attached to guide walls made from 15mm thick steel. The guide walls at each side of the container were rigidly bolted to the strong ground. Rigid guide walls prevent the out-of-plane motions of the container. The entire weight of the container is supported by the guide walls rigidly bolted to the strong ground. A total of 36 linear bearings and bearing support units were installed for carrying the weight of the laminar stacks.

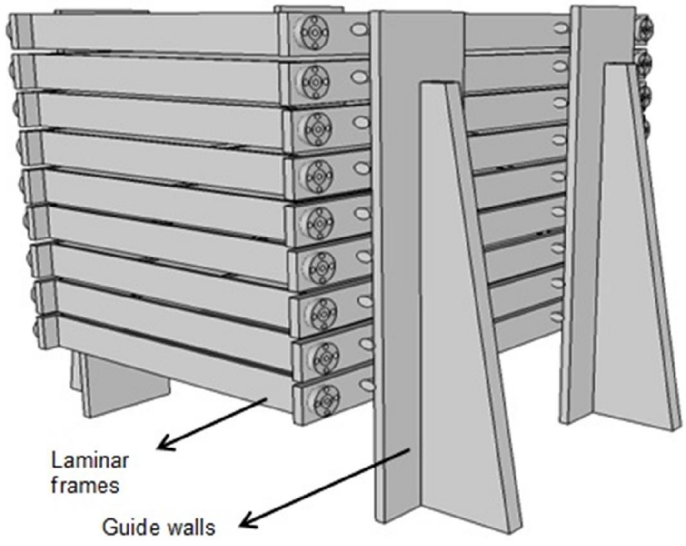

Figure 4-11 Perspective view of the laminar container used in the current study

Precise installation of the linear bearings is required to prevent jamming of the bearings during the base excitation. The frames were positioned with approximately 5mm vertical clearance to prevent any interface contact between

the adjacent laminar frames during horizontal sliding. Each laminate has a sliding capacity of ±95 mm from its original position. In Figure 4-14, perspective view of the laminar container installed on the shaking table was depicted.

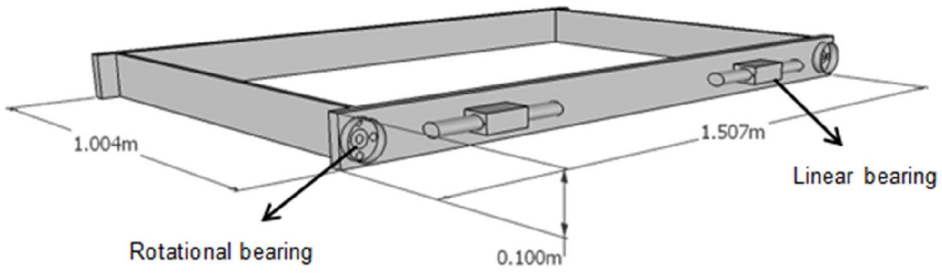

Figure 4-12 Perspective view of laminar frames

4.7.3.1 Calibration of the laminar box

Prasad et al. (2004) classifies the factors which may affect the performance of the laminar containers as follows:

a) Inertia effect
b) Friction effect
c) Membrane effect
d) Wall effect

For this study, the effect of these parameters on the performance of the laminar container was investigated to increase the quality of the test data. It was observed that the most important factor affecting the response of the soil inside the container is the inertia effect. The ratio of the weight of the laminates to the weight of the soil is determined as 17.1%. According to Prasad et al. (2004), the measured acceleration magnitudes will be less than the actual due to the inertia of the laminar container. To account this effect, a simple correction factor was proposed as follows:

$$a_s = \frac{(m_1 + m_2)}{m_1} a \qquad 4\text{-}11$$

where m_1 and m_2 are the mass of soil within a laminate and the self-weight of the laminate, respectively. In the current case, the mass of each laminate is the same, an overall correction factor, a_s is calculated as 1.17. Prasad et al. (2004)

reports that inertia factors in different tests ranged between 1.4 and 1.5 depending on the density of the soil. Tests were carried out in order to determine the static and dynamic resistance of each individual frame against sliding. A load cell was mounted on each laminar frame and forces were applied until movement occurs. It was observed that the linear bearing system successfully reduced the frictional resistance induced during the operation of the laminates. In Appendix A, the detailed results of frictional resistance measurements were presented. It was observed that static resistance of the frames was higher compared to the kinetic resistance. In Table 4-7, the summary of peak static and average dynamic resistance of the laminates was provided. The maximum static resistance of each individual laminar plate against sliding measured in the tests varied between 25N and 30N. There is not an increase in frictional forces for the lower laminates contrary to the findings of Prasad, et al. (2004) since weight of each frame is carried independently by the linear bearings hence there is not an accumulation of weight on the lower laminar frames. By assigning a low friction factor of 0.5 for the soil and taking the unit weight of the soil as 16.5kN/m^3, the frictional force of the soil in the uppermost frame will be approximately 1200N, which is significantly higher than the self-friction of the laminates. The ratio of the self-friction of the laminar frames to the soil friction is even smaller for the lower laminar elements since the friction of the soil is higher due to the increased vertical stresses. The dynamic frictional forces induced by the laminar frames are lower than the static values. This decrease will further reduce the effect of the frictional forces on the model test results. To prevent pouring of the model sand form the openings between the laminar frames, a membrane should be installed inside the container. Different types of synthetic EPDM rubber (ethylene propylene diene Monomer) membranes are tested for this purpose and the most suitable ones for the physical modeling study were selected. EPDM membranes are originally produced for water proofing purposes and they have a good resistance to abrasion, burst and tear. The thickness of the membranes varied between 2mm and 6mm. Average tensile strength of the 3mm thick EPDM membrane was reported as 15MPa and elastic modulus value for 100% elongation is 9.2MPa according to manufacturer's catalogue.

Piece of membranes were glued and tightened on a plywood box to form a waterproof membrane having the same dimensions with the container. The tests were conducted to observe the effect of the membrane thickness on the response

of soil present in the container. Sinusoidal base excitations in the frequency range of 4.25Hz to 10Hz were applied to the laminar container base. The response of the soil column in the laminar container was compared for membranes having 2mm and 4mm thicknesses.It was observed that membrane thickness does not have a pronounced effect on the amplification of the motion within the container. A comparison of the FFT amplitudes for the base excitation (f=4.25Hz), acceleration time history recorded by uppermost acceleration transducer and estimation of the amplified acceleration time history by Shake-91 (Schnabel et al.,1972) are depicted in Figure 4-15. A slight amplification of the excitation occurs at the top of the soil column however it is not too pronounced due to the limited height of the test-setup.

Table 4-7 Frictional forces induced by laminar frames

# of the laminar frame (from base)	Static Frictional Force (N)	Kinetic Frictional Force (N)
1	24.80	18.40
2	31.00	17.80
3	28.60	24.05
4	29.90	18.97
5	26.20	20.55
6	24.90	19.23
7	29.30	24.80
8	28.50	22.70
9	25.06	20.55

4.7.4 Previous data acquisition system

The data acquisition system which was used in previous dynamic modeling studies at METU Civil Engineering Department consists of an analog to digital data acquisition card, eight signal conditioning boards, DOS based data acquisition software and several transducers including displacement and acceleration transducers and load cells. Operation procedure of the data acquisition system is as follows: The analog data transmitted by the transducers first arrives to the signal conditioning boards as small voltage differences. These low voltage analog signals are amplified by Advantech PCLD-770 type amplifier units. The amplified and filtered signals are sent to the data acquisition card. The data acquisition card is ADVANTECH® PCL-818 HD A/D plug-in type lab card which supports 8 differential or 16 single ended inputs at 100kHz sampling

frequency. PCL-818 HD has a 12-bit resolution which means that the voltage input is divided in 2^{12} grids and sampled accordingly.

(a)

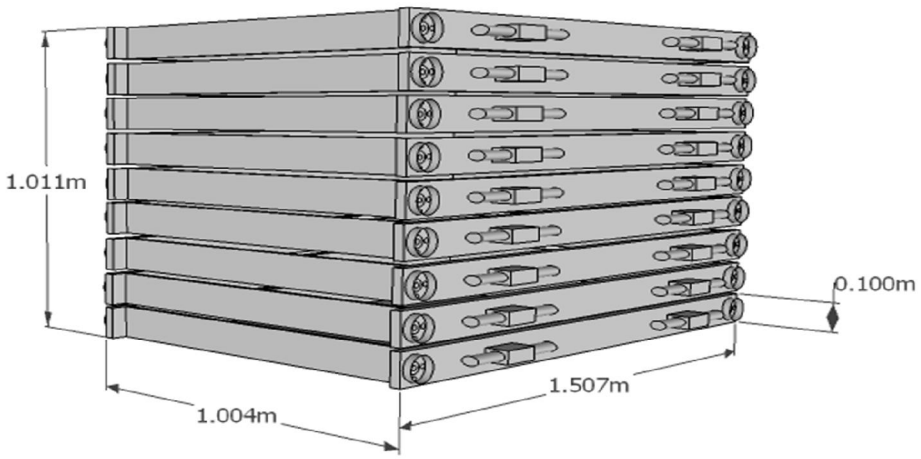

(b)

Figure 4-13 (a) Physical dimensions of the container (b) A photo of the laminar container

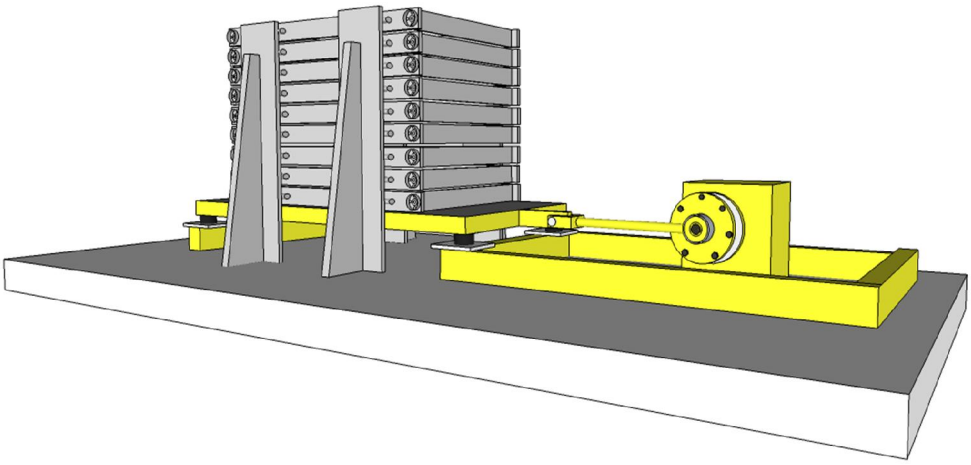

Figure 4-14 Perspective view of the laminar container and the excitation system

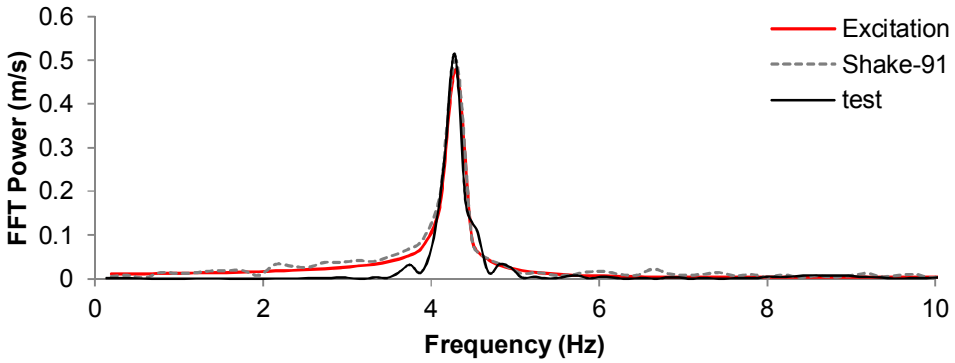

Figure 4-15 Comparison of the soil response with predictions made with Shake-91

4.7.4.1 Recent modifications in the data acquisition system for the current study

For the current study, eight additional amplifiers, (Advantech ADAM-3016 strain gage type input modules) were purchased and integrated with the previously built signal conditioning system. This current modification increased the capacity of the data acquisition twice by enabling the use of additional eight channels which may receive signals from strain gage type sensors. All of the signal conditioning modules possess electrical input range between ±10mV and ±100 mV and gives an output potential difference between 0V and 10 V. ADVANTECH® PCL-818 HD A/D plug-in data acquisition card was used for tracking the analog signals received from signal conditioning boards. The lab card was connected to a PC and controlled by software programmed specifically for this study in MATLAB environment. The software operates on an ethernet based Windows system with

MATLAB XPC Target module and provides real time monitoring of the test data. The M-File for programming the data acquisition card is provided in Appendix A. The graphical user interface of the software is depicted in Figure 4-16.

The data sampling frequency of the card is 100kHz for single channel. Use of additional channels reduces the sampling frequency reserved for each channel. However, the data acquisition rate strongly affects the quality of the recorded waveforms in dynamic tests. As depicted in Figure 4-17, there exist significant variations in the recorded waveforms if the sampling frequency is less than two times the Nyquist frequency which is considered as the maximum frequency present in the analog signal registered by the sensors (Lynn and Fuerst, 1989). Use of 16 channels simultaneously in the current data acquisition system will reserve 6.25kHz sampling frequency for each channel which is enough for capturing the response of the investigated model where input excitation frequency varies between 2Hz to 10Hz.

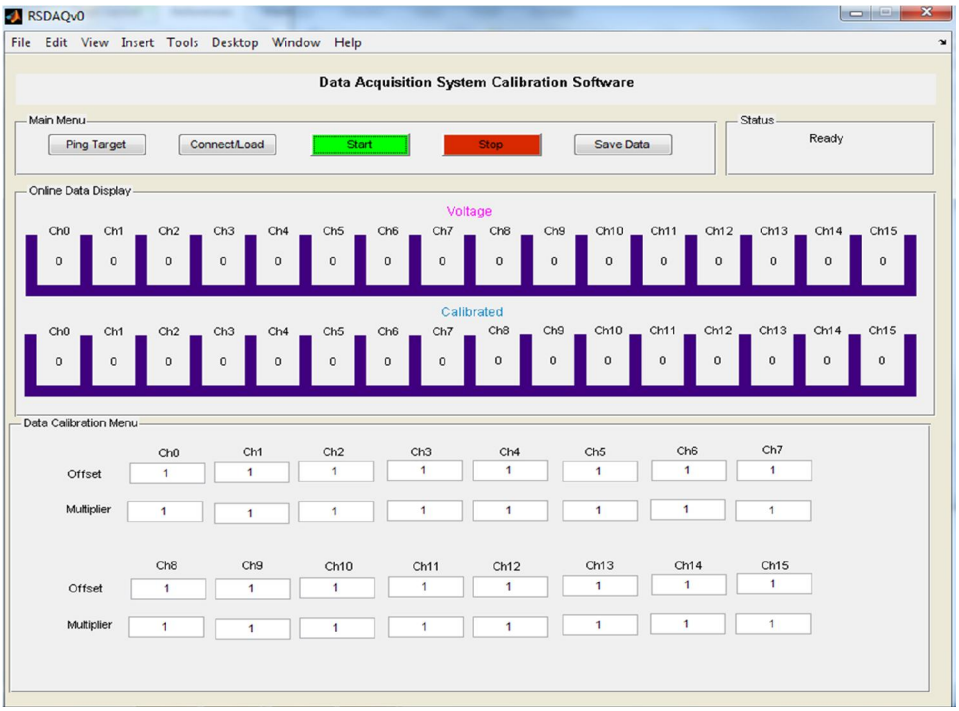

Figure 4-16 Graphical user interface programmed in MATLAB environment

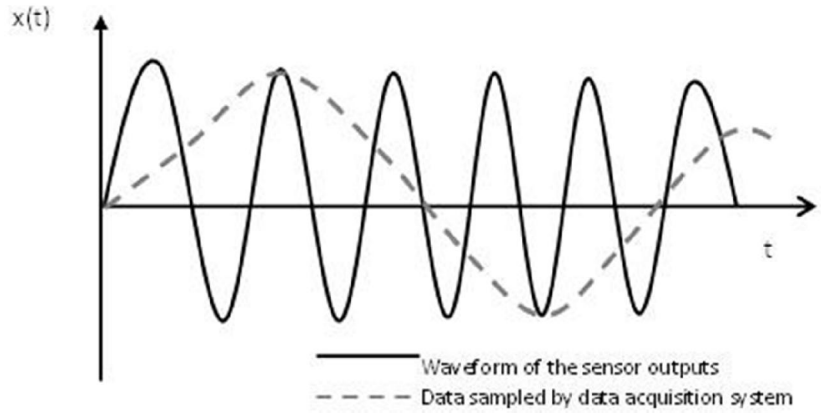

Figure 4-17 Sampling below two times under the Nyquist frequency (Lynn & Fuerst, 1989)

4.7.5 Dry Sieving Mechanism

It is generally necessary to test samples at various states and densities under laboratory conditions. For this purpose, various reconstitution methods have been developed for preparing soil samples. It is possible to group these methods into two categories, namely, those where density is adjusted after deposition and those where density is adjusted during deposition (Butterfield and Andrawes, 1970). Shoveling, tamping and vibrating are considered to be in the first group whereas pluviation and spreading techniques are examples for the second group.

Dry pluviation or “raining of sand through the air” is a commonly used method used for preparing sand samples which are representative of some initial state (Okamoto, 2006). For the current study, a steel shutter and diffuser screen of the same width and length with the laminar box was manufactured in Ostim, Ankara (Figure 4-18). Manufactured shutters are depicted in Figure 4-19. Hole spacing of the shutter screen is 60mm and the openings are in a triangular manner as suggested by (Okamoto,2006). The diffuser sieve size was 2.36mm. According to Okamoto (2006), various relative densities are achieved by simple combinations of hole spacing and sizes. Diffuser sieve placed on top of the laminar box is shown in Figure 4-20.

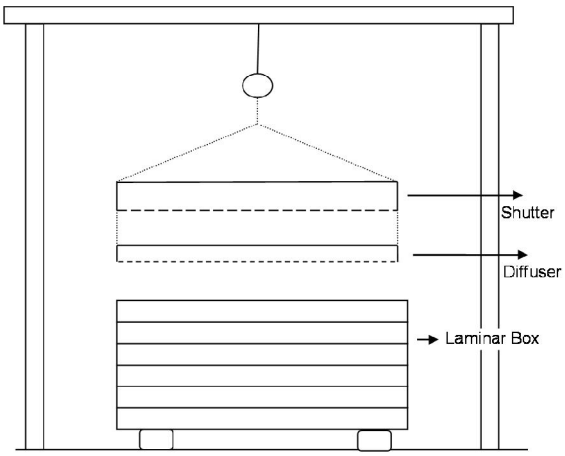

Figure 4-18 Cross Sectional View of Raining Mechanism

4.8 Physical modeling Study

The physical modeling study focuses on the static and dynamic response of cantilever earth retaining wall models with compressible geofoam buffers placed between the wall and the cohesionless backfill.

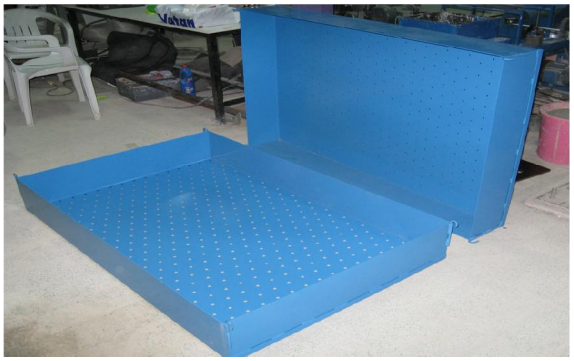

Figure 4-19 Shutters with openings of 6mm and 15 mm

Figure 4-20 Diffuser with 2.36mm sieve size placed on top of the laminar box

In the tests, static and dynamic lateral deflection of the wall stems, lateral earth pressures at several elevations along the wall height, accelerations on the wall foundation, the wall stem and at various locations inside the backfill were measured under dynamic base excitations. The detailed testing program was provided in Appendix B. The attributes of the materials used in the physical modeling study and the testing procedure were explained in detail in the following sections.

4.8.1 Selection of structural properties of the wall models

Cantilever retaining walls are generally considered as geotechnical structures under plane strain conditions. Required outputs from the physical modeling of flexible cantilever walls are typically the bending moments occurring along the wall stem and the wall deflections which are related to the stress distribution acting on the wall. According to Wood (2004), the following dimensionless similarity condition should be maintained for the dimensional modeling purposes of the cantilever retaining walls:

$$\varphi = \frac{EI/b}{GH^3} \qquad 4\text{-}12$$

where *EI* is the flexural rigidity of the wall stem which influences the moment distribution, *b* is the width of the retaining wall, *G*, the shear modulus of the backfill and *H*, the height of the wall stem. Since the plane strain assumption is considered, the bending moment should be normalized by the width (*b*) and the structural parameter controlling bending moment acting on the wall will be the flexural rigidity per unit width (i.e. *EI/b*). If the scale factors for the Young's

Modulus, shear modulus and the second moment of inertia is denoted as η_E, η_G and η_I, respectively, the following relationship is deduced:

$$\eta_E \eta_I = \eta_G {\eta_l}^3 \quad \text{4-13}$$

The quantity of *b* is considered as a notional value representing the unit width of the model and does not show up in scaling relationships. In Eq. 4-13, η_G represents the scale factor for shear stiffness of the geomaterial previously defined in Eq. 4-7. In most cases, the shear stiffness of the soil is not an independent factor since the deformation properties of the soils are strongly dependent on parameters such as confining stress and strain level (i.e., small strain or large strain problems). In problems involving dynamic response and wave propagation, the behavior of the soil is generally in the small-strain range. According to Wood (2004), small-strain stiffness of the soil is dependent on the effective stress level with an exponential parameter *α* according to the following relationship:

$$G \propto \sigma^{\alpha} \quad \text{4-14}$$

Experiments indicate that value of *α* is approximately 0.5 for sands and 1 for the clays. A value of zero indicates that material is independent of the confining stress level. Rewriting the Eq. 4-13 by taking η_I as 1/n, and η_G, $1/n^{\alpha}$, where 1/*n* is the scale factor for length, the following equation is obtained:

$$\eta_E \eta_I = 1/n^{\ 3+\alpha} \quad \text{4-15}$$

for 1-g physical testing case. By taking α as 0.5, Eq. 4-16 is obtained:

$$\frac{\frac{1}{12} E_m {t_m}^3}{\frac{1}{12} E_p {t_p}^3} = 1/n^{\ 3.5} \quad \text{4-16}$$

Eq. 4-16 may be rewritten to obtain the thickness of the model wall stem as follows:

$$t_m = t_p \left(\frac{E_p}{E_m} \frac{1}{n^{3.5}} \right)^{1/3} \quad \text{4-17}$$

The required thickness and the material properties for the wall stem can be calculated by Eq.4-17. The material of the prototype wall model was considered as reinforced concrete with Young's Modulus of E_p=20GPa and wall stem thickness was taken as 0.5m which is typical according to the design specifications of the United States Army Corps of Engineers (Figure 4-21). In Table 4-8, the thickness of the model wall stem required to satisfy similitude equation for the 0.5m thick prototype wall made of reinforced concrete with E=20GPa was indicated. Although micro concrete may be considered as more suitable to replicate the interface conditions occurring in the prototype scale, steel is selected as the model wall material considering the flexibility demands and the ease of model production since the construction of the concrete wall having approximately 12mm thickness would not be feasible. The thicknesses satisfying the similitude equation for various prototype stem thicknesses were indicated in

Table 4-9.

Table 4-8 Thickness of the model walls satisfying dimensional similitude (η=30)

Material	E_{model} (GPa)	t_{model} (mm)
Steel	210	4.4
Aluminum	70	6.3
Micro concrete	10	12.1
Polypropylene	0.9	27.0

Table 4-9 Thickness of the steel model walls satisfying dimensional similitude for various $t_{prototype}$ values (η=30)

$t_{prototype}$ (m)	t_{model} (mm)
0.2	1.8
0.3	2.6
0.4	3.5
0.5	4.4
0.6	5.3
0.7	6.1
0.8	7.0
0.9	7.9
1.0	8.8

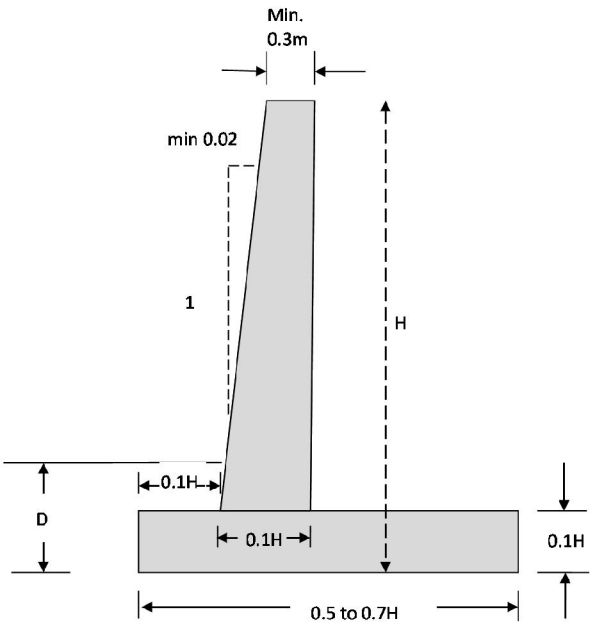

Figure 4-21 Typical proportioning of a cantilever retaining walls according to US. Army Corps. of Engineers

Another important factor relating to the selection of the material type and the thickness of the wall stem is the relative flexibility of the wall compared to the retained backfill material. According to Younan and Veletsos (2000), relative flexibility (d_w) is considered as the primary parameter affecting the response of the system and defined as:

$$d_w = \frac{GH^3}{D_w} \qquad 4\text{-}18$$

where *G* is the shear modulus of the backfill, *H* is the wall height and D_w is the flexural rigidity of the wall given by the following equation:

$$D_w = \frac{E_w {t_w}^3}{12(1-{\nu_w}^2)} \qquad 4\text{-}19$$

where E_w is the Young's Modulus value of the wall, t_w is the wall thickness and ν_w denotes the Poisson's ratio of the wall material. Combining Eq.s 4-18 and 4-19, the relative flexibility (d_w) of the wall is calculated as follows:

$$d_w = 12(1-\nu_w{}^2)\frac{G}{E_w}\left(\frac{H}{t_w}\right) \qquad 4\text{-}20$$

For a prototype wall made from concrete (E_w=21 GPa, ν_w=0.17 and H/t_w=30) which is retaining a backfill with a density of 1600 kg/m^3, d_w is obtained as 87.65 for V_s = to 61 m/s and 779.10 for V_s= 183 m/s. The dimensions of the laminar box which will be used in the physical modeling study are a limitation for selecting the model wall geometry. The presence of a 200mm thick foundation layer under the wall base limits the wall height to a maximum of 800mm. In Table 4-10, d_w values are indicated for two different model heights and various wall thicknesses between 2mm to 12mm. In this study, the effect of wall flexibility on the dynamically induced lateral forces and displacements are mainly under concern. For this reason, the model wall thicknesses were selected to cover a wide range of d_w values for typical prototype walls. The availability of the steel products constitutes an important limitation for the selection of wall parameters. Taking into account of these parameters, the model wall height was selected as 700mm and the thickness of the model wall varied between 2mm and 8mm. Models were manufactured from St-37 type carbon steel with elastic modulus of approximately 210GPa.

Table 4-10 d_w values for $H_{prototype}$=5m

H_{model}=300mm			H_{model}=700mm		
t_w (mm)	D_w (kN.m)	d_w	t_w (mm)	D_w (kN.m)	d_w
2	0.141	645.31	2	0.141	8197.828
4	1.131	80.66	4	1.131	1024.729
5	2.210	41.30	5	2.210	524.661
6	3.818	23.90	6	3.818	303.6233
8	9.051	10.08	8	9.051	128.0911
10	17.678	5.16	10	17.678	65.58263
12	30.547	2.99	12	30.547	37.95291

4.8.1.1 Wall geometry

The model walls were comprised of steel with dimensions of 700×980×(2,4,5,8) (height×length×thickness in mm's) rigidly welded to a steel base of 980×500×8 (length×width×thickness in mm's). Dimensions of the wall stem and wall foundation are depicted in Figure 4-22. The connections of the stem and

foundation parts were attained by continuous welding. Width of the wall is 980mm hence there remains 10mm clearance at each side of the wall when it is placed in the laminar container. To prevent sand seeping from the sides of the wall stem, rubber strips were glued to the sides of the wall. The base width of the wall was chosen as 50cm by taking into account the sliding and overturning stability calculations explained in Section 4.8.1.2. Wall base was completely covered with emery paper to increase the friction between the backfill and the wall base to increase the resistance against sliding. A cross section of the test setup and the position of the transducers are depicted in Figure 4-23. Pressure transducers were mounted into small recesses machined into the inboard face of the wall stem to ensure that the sensing surfaces of the transducers will be flushed with the face of the wall. Four of the pressure sensors were installed along the wall at 200mm spacing from one another. Two soil pressure gages (Tokyo Sokki TML KDE-200kPa) were mounted at two different positions on the toe and heel of the model wall base to record the base pressures. Displacement transducers (Tokyo Sokki SDP-C) were used to measure horizontal displacements at the top and mid height of the wall model as shown in Figure 4-23. Wall stem thicknesses varied as 2mm, 4mm, 5mm and 8mm according to the dimensional modeling calculations explained in section 4.8.1.

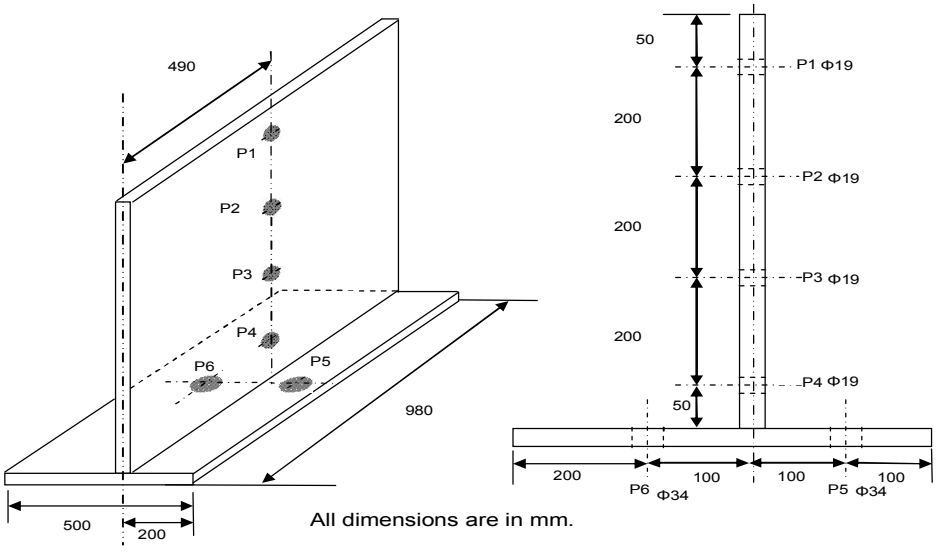

Figure 4-22 Wall dimensions and positions of the transducers

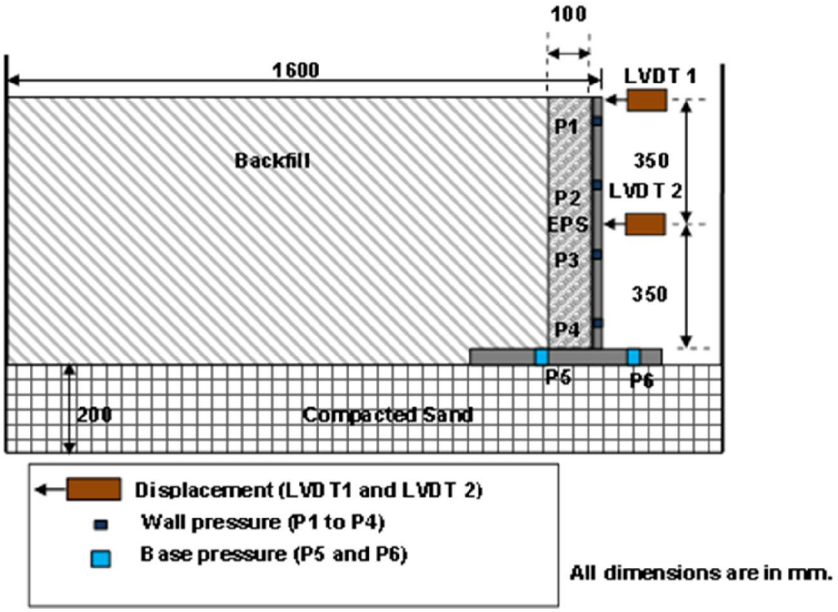

Figure 4-23 Cross section of the test setup and positions of the transducers

4.8.1.2 Sliding and overturning stability of the model walls

The stability of the model walls against sliding and overturning were controlled according to the procedure indicated by Bowles (1996). Factor of safety of the model walls against sliding and overturning are given in Table 4-11. Detailed calculations were provided in Appendix D.

Table 4-11 Factor of Safety of the models walls against sliding and overturning

t_w (mm)	$FS_{sliding}$	$FS_{overturning}$
2	1.68	3.12
4	1.73	3.19
5	1.76	3.23
8	1.84	3.33

4.8.2 Potential active failure mechanism for the model wall

Orientation of the expected static and dynamic active failure wedges was determined through theoretical methods. The orientation of the seismic active wedge according to Mononobe Okabe's theory for the backfill material with $\Phi_{backfil}$ =43.5° was calculated for k_h=0 and k_h=0.5 cases where $a_h=k_hg$. The vertical component of the acceleration was set to zero since any vertical motion was not applied in the tests. According to Zarrabi and Kashani (1979), the critical failure

surface for Mononobe-Okabe analysis can be calculated through Eq.4-21 to Eq.4-23. The parameters in the equation set are defined in Figure 4-24.

$$\alpha_{AE} = \phi - \psi + tan^{-1}\left[\frac{-tan(\phi - \psi - \beta) + C_{1E}}{C_{2E}}\right] \quad 4\text{-}21$$

where

$$C_{1E} = \sqrt{tan(\phi - \psi - \beta)[tan(\phi - \psi - \beta) + cot(\phi - \psi - \beta)]}\,[1 + tan(\delta + \psi + \theta)\,cot(\phi - \psi - \theta)] \quad 4\text{-}22$$

$$C_{2E} = 1 + \langle tan(\delta + \psi + \theta)[tan(\phi - \psi - \theta) + cot(\phi - \psi - \theta)]\rangle \quad 4\text{-}23$$

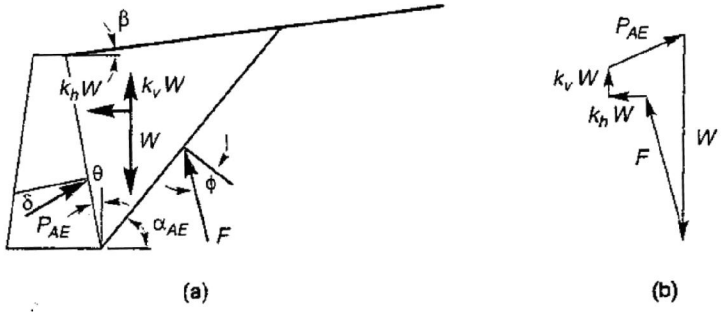

Figure 4-24 Forces acting on the active wedge in Mononobe-Okabe analysis (b) Force polygon acting for the equilibrium of active wedge

The orientation of the failure wedge for k_h=0 case is identical with the result obtained from original Coulomb's theory of lateral earth pressure. In the physical modeling study, the model wall should be placed far enough from the boundary of the laminar container to avoid intersection of the critical failure wedge with the limits of the laminar container. The critical angles of the failure wedge which were calculated according to Eq. 4-21 are depicted in Figure 4-25. As shown in the figure, inclination of the critical wedge for the dynamic case is significantly smaller than the slope of the wedge for the static case. The horizontal surface length of the wedge for k_h=0.5 is calculated as 1.91m. There is not a potential intersection problem for the static failure wedge; however critical wedge for k_h=0.5 case intersects with the container boundary due to limited dimensions of the test container.

4.8.3 Characterization of the backfill material

Cohesionless material used in the physical modeling represents a drainable soil with a high friction angle as recommended by the current design guidelines and specifications. Air-dried clean sand collected from the banks of Cine River in Turkey was used as both backfill and foundation soil in the physical model tests. Microscopic examinations revealed that the sand grains are highly angular. Approximately 3000kg of sand was transported to the Department of Civil Engineering. The material was already cleaned and air-dried. In the following sections, the physical characteristics of the sand from various laboratory tests are presented.

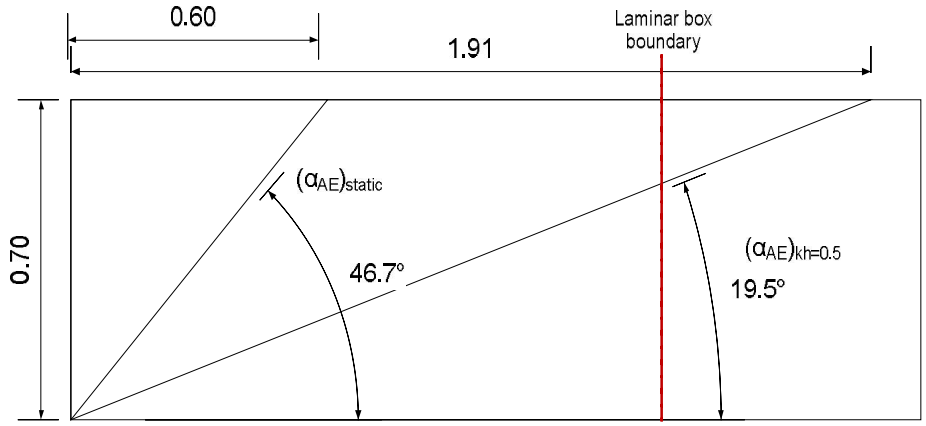

Figure 4-25 Limits of the failure wedge calculated according to Mononobe-Okabe wedge analysis (Dimensions are in meters).

4.8.3.1 Soil classification

The physical characteristics of the cohesionless material were determined through laboratory tests. Various index properties of the material are summarized in Table 4-12. The grain size distribution of the Cine Sand (Figure 4-26) was determined by dry sieving procedure described by Head (1992). The model sand has 1.15% fines (silt and clay). C_c and C_u was determined as 0.80 and 3.31, respectively. According to the Unified Classification system, material was classified as poorly graded sand (*SP*).

Table 4-12 Index Properties of Cine Sand

Average Unit Weight (kN/m^3)	16.50
Maximum Void Ratio (e_{max})	0.745
Minimum Void Ratio (e_{min})	0.436
Void ratio achieved in model tests (e)	0.523
Specific Gravity	2.66
C_c (coefficient of curvature)	0.80
C_u (coefficient of uniformity)	3.31
Percent finer than #200 sieve	1.14

Maximum and minimum void ratios of the soil were determined as 0.745 and 0.436, respectively by the procedure described by (Head, 1992). Specific gravity (G_s) was determined in accordance with ASTM D854-83 procedures.

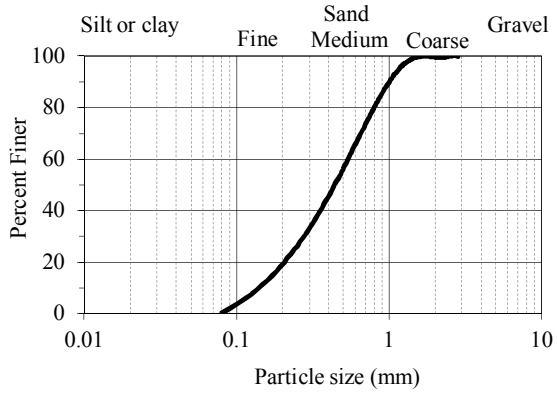

Figure 4-26 Grain size distribution of Cine Sand

4.8.3.2 Static stress-strain behavior of cohesionless backfill material

Series of triaxial tests were performed by the state-of-the-art triaxial testing device at the Department of Geology and Geophysics in University of Utah. The confining stress level in the model tests is relatively low due to the limited height of the model wall. It is well known that the behavior of sands is heavily dependent on the level of confining stress. High internal angle of friction values are generally observed due to the dilatancy of the sand during shearing under low confining stresses (Lambe and Whitman, 1969). Tests were carried on the samples with a relative density of 70% for three different confining stresses with the loading rate

set to 0.1mm/min. Based on CD test results, internal friction angle of the material was determined as 43.5°. The dilatancy angle of the Cine Sand was determined as 22.57° from volumetric strain measurements. Direct shear test results indicated a friction angle of around 50°. Due to low confining stresses applied in the tests, the accuracy of the applied normal stress in direct shear test is not as controllable as the triaxial testing. Data obtained from direct shear and triaxial testing was provided in Appendix C.

4.8.3.3 Dynamic characterization of the cohesionless backfill material

Stress controlled cyclic triaxial tests were performed on the fully-automated equipment in the Department of Geology and Geophysics in University of Utah. This equipment can be employed to carry out both static and cyclic triaxial tests on cylindrical specimens (Figure 4-27). Cyclic triaxial device consists of a LoadTrac-II load frame, two FlowTrac-II flow pumps for controlling cell and sample volume and pressure, a hydraulic pump, a servo valve with a hydraulic cylinder, an external signal conditioning unit and a computer for data acquisition purposes (Figure 4-28). The cyclic triaxial system runs all of the phases automatically once the specimen to be tested is placed in the triaxial device and the test conditions were selected. Test data is stored in a file for subsequent reduction and plotting needs.

To determine dynamic modulus of elasticity (E_{dyn}) and maximum axial strains (ε_{max}), confining stresses and additional cyclic deviator stresses were applied to specimens having *h:d* ratio of 2:1 where *h* is the specimen height (100mm) and *d* is the diameter of the specimen. In all of the cyclic tests, cyclic component of the stress remained below the static confining stresses; hence the specimen was always subject to compression. Samples having relative density (R_d) of 75% were tested by applying the static confining stress first and proceeding with the cyclic component of the stress (Figure 4-29). Tests were repeated for various cyclic deviator stresses. In Figure 4-30, representative hysteresis loops which were taken to calculate the stiffness and the damping ratio of the model sand were depicted. Shear moduli and damping ratio of model sand were determined based on the test data (Table 4-13).

Due to lack of small strain test data (resonant column test, bender element test etc.), empirical formulas which are available in the literature may be used to estimate small-strain stiffness of the soils.

Figure 4-27 Cyclic triaxial testing device in the Soil Mechanics Laboratory, Department of Geology and Geophysics, University of Utah

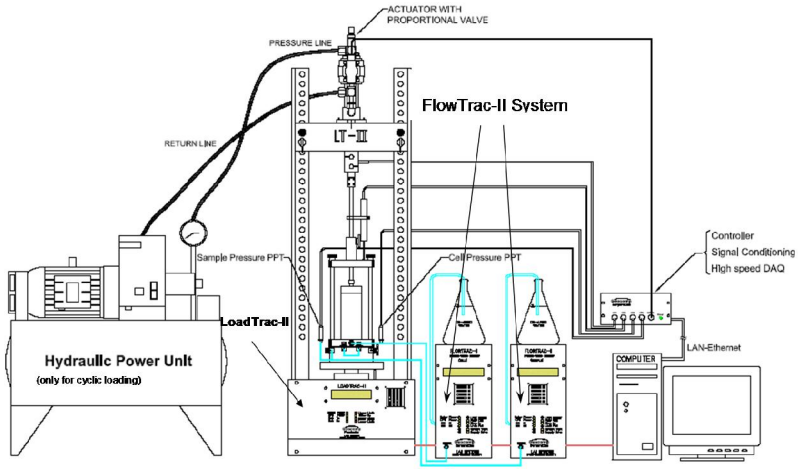

Figure 4-28 Set-up of the cyclic triaxial equipment (Geocomp Corporation, 2006)

The small-strain dynamic modulus value of the model sand in this study was calculated by the following empirical formula for angular grained sands (Chang and Makarechi, 1982):

$$G_{max} = 1230\frac{(2.973-e)^2}{1+e}\sigma_m^{0.5} \qquad 4\text{-}24$$

The G_{max} value for e=0.523 is determined as 11650kPa with Eq.4-24. Taking $\upsilon = 0.33$, small strain E_{dyn} is estimated as 30990kPa.

Table 4-13 Summary of damping ratio and dynamic modulus calculations

$(\sigma_d)_{cyclic}$ (kPa)	$(\varepsilon_a)_{max}$	ζ (%)	E_{secant} (kPa)	G_{sec} (kPa)	γ_c (%)	G/G_{max}
10	0.019	3.17	16767	6303	0.025327	0.54103
20	0.04	2.37	20278	7623	0.05332	0.654335
30	0.04	2.93	20523	7715	0.05332	0.662232
40	0.05	3.05	18884	7099	0.06665	0.609356

4.9 Characterization of the compressible inclusion used in the tests

In the shake table tests, Teknopanel brand EPS and Izocam XPS were used as compressible inclusions behind model retaining walls. In this section, static and dynamic properties of the EPS and XPS geofoam used in the model tests were discussed in detail. The density of the EPS material supplied for the tests was determined as 15.2kg/m^3. A geofoam product having low density was selected since the stresses acting on the compressible inclusions are relatively low due to low confining stresses in the physical modeling study. However, in field applications of the geofoam, higher density materials are preferred since the field stresses acting on the geofoam inclusions are significantly higher than those for small-scale model tests.

According to ASTM Standard C578-05 (Table 4-14), EPS geofoam used in the tests were classified as TYPE I. In Table 4-15, technical specifications of the EPS-15 are indicated according to the manufacturer´s catalogue data. The density of the XPS material was measured as 22kg/m^3 and classified as TYPE-X according to ASTM Standard C578-05 (Table 4-16). In Table 4-17, technical specifications of the XPS-22 are provided according to the manufacturer´s catalogue data. The static and cyclic triaxial tests were carried out on EPS and XPS samples to determine mechanical properties of the materials in more detail. The specimens having *h:d* ratio of 2:1 where *h* is the specimen height (100mm) and *d* is the diameter of the specimen were extracted from EPS and XPS panels by computer controlled laser cutters in ACH Foam Company of Salt Lake City, Utah (Figure 4-31).

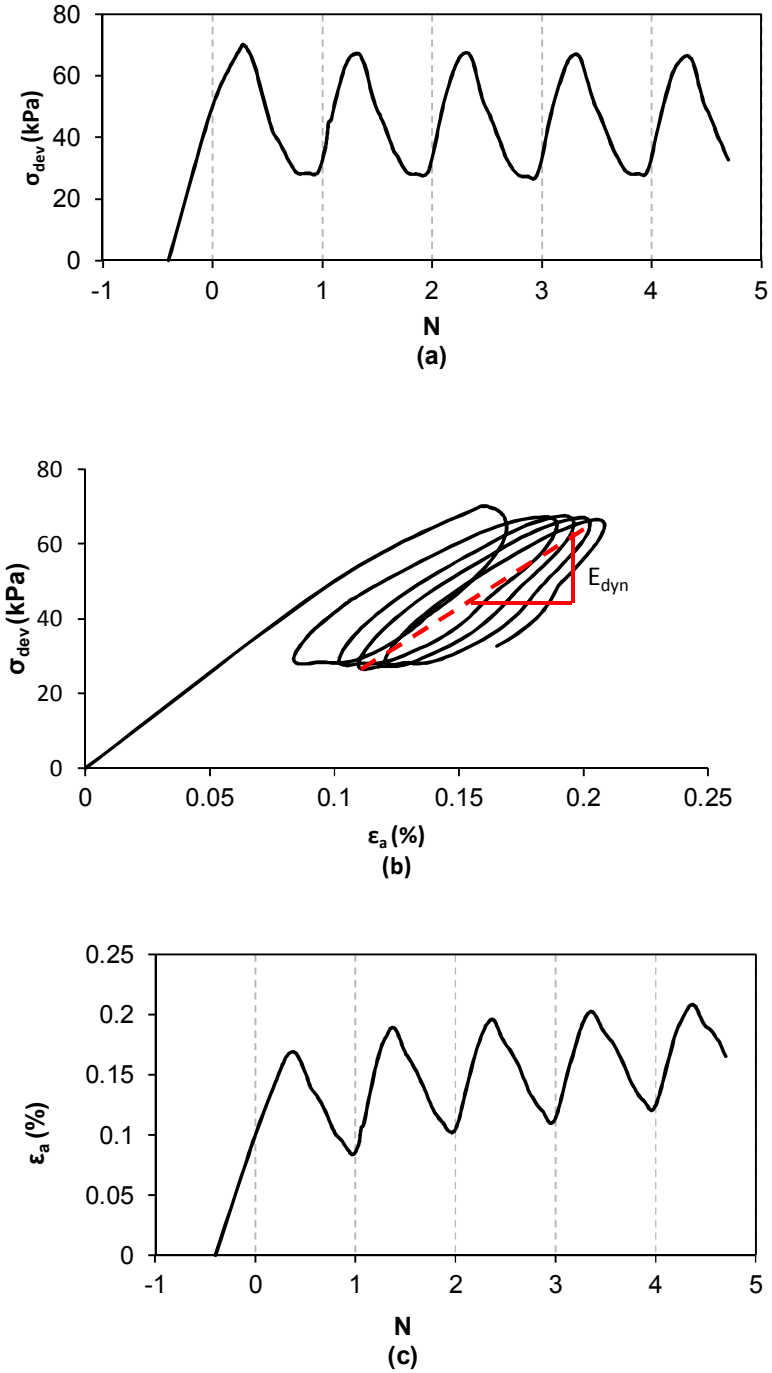

Figure 4-29 Stress controlled cyclic triaxial tests on cohesionless material for $(\sigma_a-\sigma_r)_{static}$= 50kPa and $\Delta(\sigma_a-\sigma_r)_{cyclic}$= 20kPa

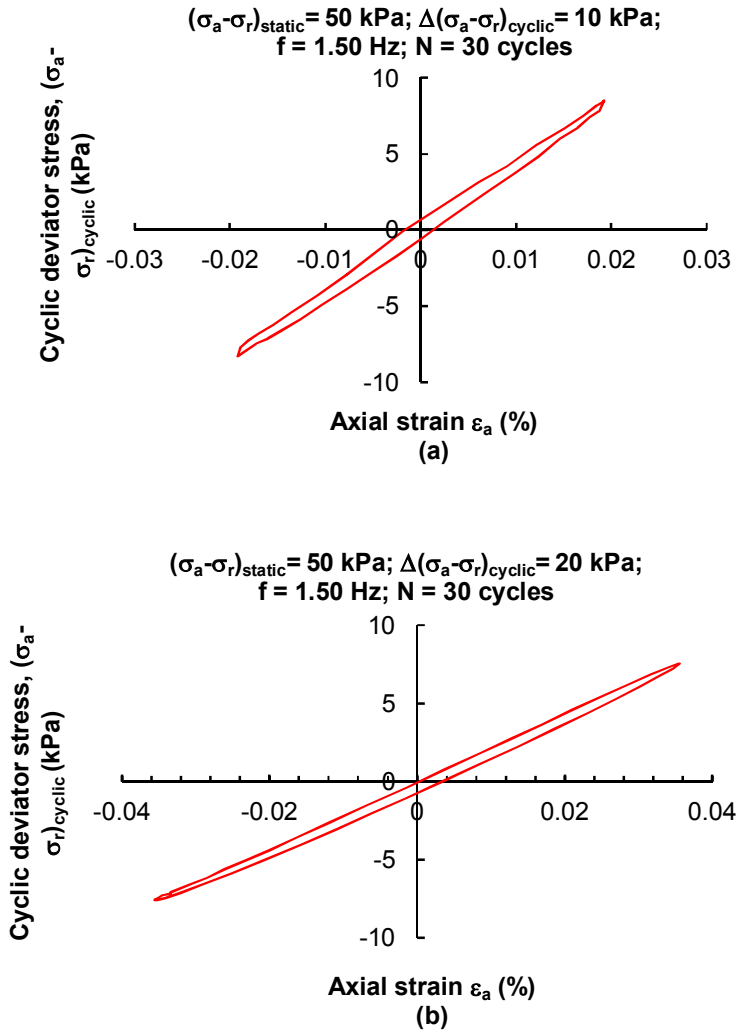

Figure 4-30 Typical hysteresis loops for Cine sand (a) $(\sigma_a-\sigma_r)_{static}$= 50kPa; $\Delta(\sigma_a-\sigma_r)_{cyclic}$= 10kPa (b) $(\sigma_a-\sigma_r)_{static}$= 50kPa; $\Delta(\sigma_a-\sigma_r)_{cyclic}$= 20kPa

Table 4-14 ASTM-C 578-05 classification for standard EPS densities

Material TYPE (ASTM DESIGNATION)	Nominal Density (kg/m^3)	Minimum Density (kg/m^3)
XI	12	11
I	16	15
VIII	20	18
II	24	22
IX	32	29

Table 4-15 Technical specifications of EPS-15 geofoam according to manufacturer´s data

TECHNICAL SPECIFICATIONS		RELATED STANDARDS	UNITS	EPS-15
DENSITY		DIN 53420	Kg/m^3	15
BUILDING MATERIAL CLASSIFICATION		DIN 4102	-	B1*
Thermal conductivity	**LABOR VALUE**	DIN 52612	W / mK	0,036-0,038
	ACCOUNT VALUE	DIN 4108	W / mK	0,04
Deformation Resistance at 10% strain		DIN 53421	N/mm^2	0,07-0,12
Deformation Resistance at strains smaller than 2%		-	N/mm^2	0,012-0,025
Shear strength		DIN 53427	N/mm^2	0,09-0,12
Bending strength		DIN 53423	N/mm^2	0,16-0,21
Tensile strength		DIN 53430	N/mm^2	0,15-0,23
Modulus of Elasticity		-	N/mm^2	0,6-1,25
Temperature Resistance	**SHORT-TERM**	DIN 53424	°C	100
	LONG-TERM 5000 N /m^2	DIN 53424	°C	80-85
	LONG-TERM 20,000 N/m^2	DIN 18164	°C	75-80
Thermal expansivity		-	1/K	$5\text{-}7.10^{-5}$
SPECIFIC HEAT CAPACITY		DIN 4108	J / (Kg.k)	1500
WATER ABSORBING CAPACITY	**7 DAYS**	DIN 53428	VOLUME, %	3
	1 YEAR		VOLUME, %	5

*not easily combustable

Table 4-16 ASTM-C 578-05 classification for standard XPS densities

Material TYPE XPS (ASTM DESIGNATION)	Nominal Density (kg/m^3)	Minimum Density (kg/m^3)
X	22	21
IV	27	26
VI	31	29
VII	38	35
V	50	48

4.9.1 Determination of the static stress-strain behavior of EPS-15

The stress-strain response from uniaxial compression testing of the EPS-15 geofoam is depicted in Figure 4-32. In this figure, (σ_a-σ_r) represents the deviator stress (where σ_a and σ_r denote the axial and radial stress, respectively). The uniaxial monotonic loading test was carried out at an axial strain rate of 0.01% strain/min that is consistent with the loading rate of the EPS geofoam panel during

the backfilling process of the 700mm high retaining wall model depicted in Figure 4-23.

Table 4-17 Technical specifications of XPS-22 geofoam according to manufacturer´s data

TECHNICAL SPECIFICATIONS		**RELATED STANDARDS**	**UNITS**	**XPS-22**
DENSITY		DIN 53420	Kg/m^3	22 kg/m^3
Deformation Resistance	**%10 deformation**	DIN 53121	N/mm^2	0,15
			Kg/cm^2	1,5
	<%2 deformation		N/mm^2	0,060
			Kg/cm^2	0,6
WATER ABSORBING CAPACITY		DIN53428	VOLUME %	0,1
VAPOR Diffusion Resistance Coefficient (μ)		DIN 52615	1	80/150
BUILDING MATERIAL CLASSIFICATION		DIN 4102	B1 or	B1
			B2	

Based on the uniaxial compression test results (Figure 4-32), the yield strength of the material is obtained as 38kPa according to the procedure developed by Magnan and Serratice (1989). The Young's modulus describing the linear-elastic portion of the stress-strain curve is determined as 1500kPa.

Triaxial tests were performed on samples with *h:d* ratio of 2:1 under three different radial stress values (i.e. 10kPa, 20kPa and 30kPa). It was observed that increase in radial stress causes a decrease in the compressive strength of the EPS-15 as opposed to the general behavior of soils (Figure 4-33). However, an increase in the strain rate leads to higher compressive strength of the material. An approximately bilinear stress-strain response was observed in all the tests. Material behaved linearly elastic up to axial strains of 2%.

Initial tangent modulus (E_{ti}) and Poisson's ratio (ν) that were calculated according to the empirical relationships given in Section 3.3 are summarized in Table 4-18. The initial tangent modulus derived from the uniaxial testing of EPS-15 samples used in this study are significantly lower than the values calculated by the proposed relationships for EPS geofoams since the EPS sample used in this study is not specifically manufactured for geotechnical applications. However, the

low modulus of the EPS material was considered as an advantage in the small-scale model tests since the stresses acting on the compressible inclusion located behind the retaining wall model are significantly low and required amount of compressive deformations for active stress conditions may not be achieved if high modulus EPS geofoams with higher elastic modulus would be used in the physical modeling study.

Figure 4-31 Cylindrical EPS and XPS samples prepared for the triaxial compression tests

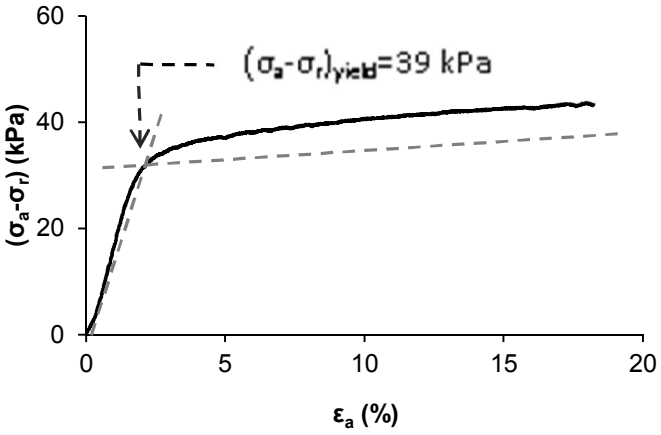

Figure 4-32 Results of uni-axial tests on EPS-15 under strain rate of 0.01%/min

Table 4-18 E_{ti} and v values of EPS-15 estimated with empirical equations

E_{ti} (kPa)	v
3750 (Eq. 3-2)	0.2 (Eq.3-1)
5481 (Eq.3-4)	0.0864 (Eq.3-3)
3350 (Eq.3-5)	0.259 (Eq.3-8)
4900 (Eq.3-6)	

4.9.2 Determination of the static stress-strain behavior of XPS-22

Based on the uniaxial compression test results depicted in Figure 4-34, the yield strength of the material was observed as 131.5kPa. Young's modulus describing the linear-elastic portion of the stress-strain curve is determined as 5580kPa (Confining pressure (σ_r)=0kPa). To the author's best knowledge, there does not exist any empirical relationship to predict the initial tangent modulus of the XPS geofoam to make comparisons with the measured values.

Triaxial tests (Figure 4-35a, b) were performed on samples with *h:d* ratio of 2:1 under three different radial stress values (i.e. 10kPa, 20kPa and 30kPa). Effect of slow and rapid loading conditions (0.01%/min and 8.5%/min) was investigated. Similar to the behavior of EPS geofoam behavior, increase in radial stress causes a decrease in the compressive strength of the XPS-22 as opposed to the general behavior of soils. However, an increase in the strain rate leads to higher compressive strength of the material. Stress-strain behavior of the material is more similar with that of soils with a linear elastic behavior up to axial strains of 1.5%. A comparison of the stress-strain behavior for cohesionless material (Cine Sand), XPS-22 and EPS-15 were depicted in Figure 4-36. It was observed that there is a significant difference in compressive yield strength of the materials. The stress-strain behavior of the EPS-15 shows approximately bilinear behavior contrary to the nonlinear trend observed for Cine Sand and the XPS-22 material.

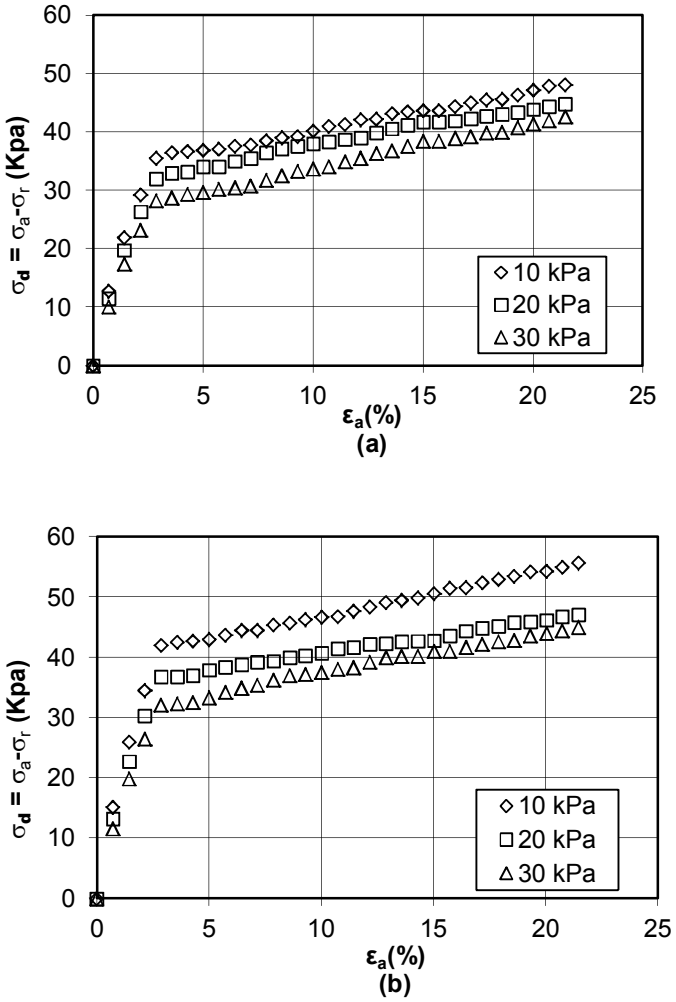

Figure 4-33 Stress-strain behavior of EPS-15 for various confining stresses under (a) strain rate of 0.01%/min (b)strain rate of 8.5%/min

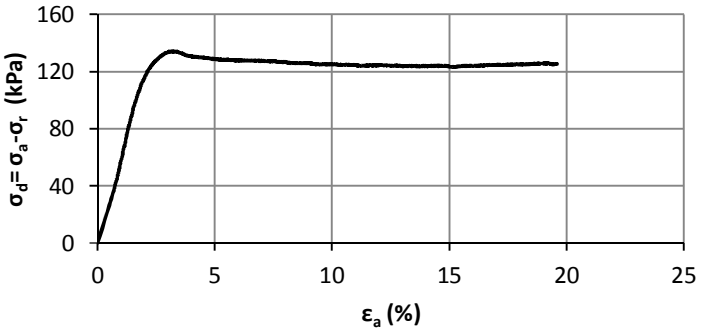

Figure 4-34 Results of uni-axial tests on XPS-22 under strain rate of 0.01%/min

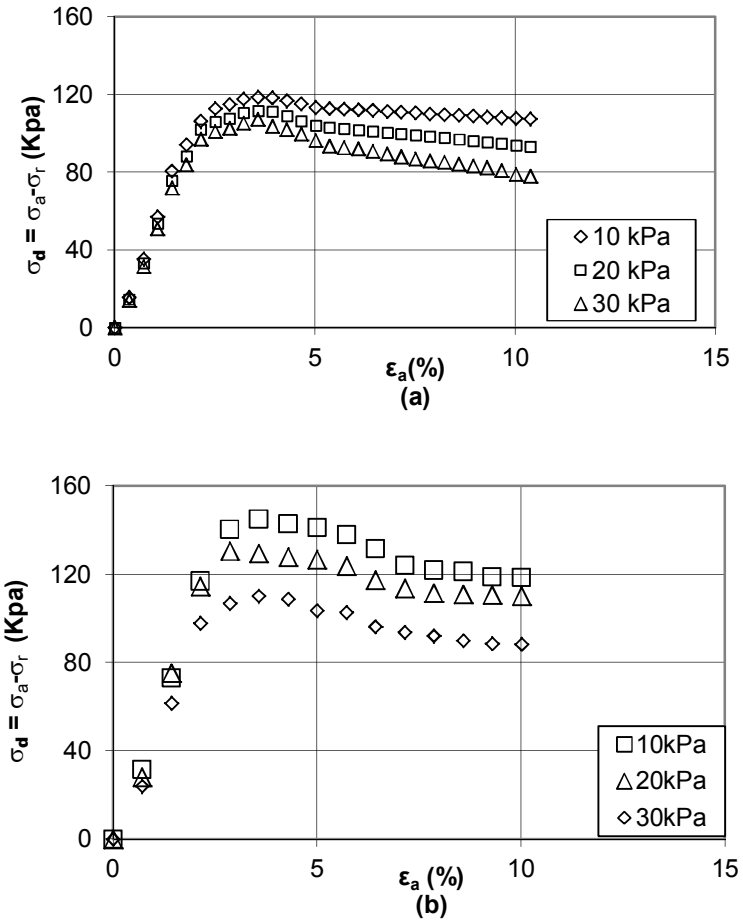

Figure 4-35 Triaxial testing on XPS-22 for various confining stresses under (a) strain rate of 0.01%/min (b) strain rate of 8.5%/min

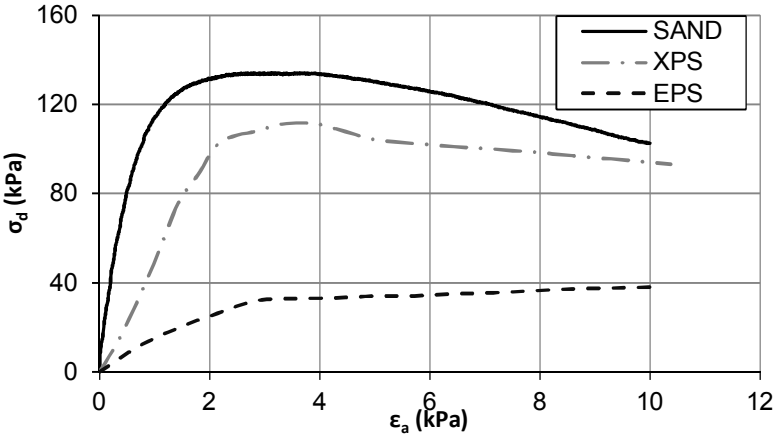

Figure 4-36 Comparison of stress-strain behavior of sand, XPS-22 and EPS-15 for σ_r=20kPa

4.9.3 Dynamic characterization of the EPS-15 and XPS-22 geofoam

Stress controlled cyclic triaxial tests on EPS-15 and XPS-22 samples having *h:d* ratio of 2:1 were performed to determine dynamic modulus of elasticity (E_{dyn}) and maximum axial strains (ε_{max}). The cyclic component of the stress remained below the static confining stresses, hence the specimen was always under compression. In Figure 4-37, representative hysteresis loops selected for calculating the stiffness and the damping ratio of the EPS and XPS samples were depicted. Shear moduli and damping ratio of EPS-15 were determined based on the triaxial test data (Table 4-19). E_{secant} and $(\varepsilon_a)_{max}$ values indicated in Table 4-19 were converted to shear modulus (G) and shear strain (γ_c) by:

$$G = \frac{E}{2(1+\nu)} \quad 4\text{-}25$$

$$\gamma_C = (1+\nu)\varepsilon_a \quad 4\text{-}26$$

Due to lack of small-strain test data (resonant column test, bender element test etc.), the small-strain dynamic shear modulus value and Poisson's ratio of the EPS-15 was estimated as 3400kPa and 0.2695 using the following empirical formulas proposed by Athanasopoulos et al. (2007) based on resonant column test data:

$$G_0 = 0.32\rho - 1.40 \; for \; \sigma_3 = 0 \quad 4\text{-}27$$

$$\nu_0 = 0.22 + 0.0033\rho \; for \; \sigma_3 = 0 \quad 4\text{-}28$$

However, experimental results indicated that confining stress applied to the specimen reduces G_0 and ν_0 values. The relationships proposed by Athanasopoulos et al. (2007):

$$\frac{G_{0(\sigma_3)}}{G_{0(\sigma_3=0)}} = 1.02 + 0.599\frac{\sigma_3}{\sigma_c} - 1.41\left(\frac{\sigma_3}{\sigma_c}\right) \quad 4\text{-}29$$

$$\nu_{0(\sigma_3)} = 0.25 - 0.33\left(\frac{\sigma_3}{\sigma_c}\right) \quad 4\text{-}30$$

where σ_c is the compressive strength of EPS samples with h:d ratio of 2 may be used to estimate the dynamic shear modulus and the Poisson's ratio for various confining stresses. By using Eq.s 4-29 and 4-30, G_0 and ν_0 for EPS-15 were estimated as 2379kPa and 0.120, respectively for σ_3=15kPa. Similarly, the small-strain dynamic shear modulus value (for σ_3=0kPa) and Poisson's ratio of the XPS-22 were estimated as 5640kPa and 0.292 by Eq.s 4-27 and 4-28. To include the effect of confining stress on the stress-strain behavior, Equations 4-29 and 4-30 were applied. G_0 and ν_0 were estimated as 5231kPa and 0.212, respectively for σ_3=15kPa. The summary of the dynamic properties of XPS-22 determined through cyclic triaxial tests is depicted in Table 4-20.

Table 4-19 Summary of damping ratio and dynamic modulus calculations for EPS-15

$(\sigma_d)_{cyclic}$ (kPa)	$(\varepsilon_a)_{max}$ (%)	ζ (%)	E_{secant} (kPa)	G_{sec} (kPa)	γ_c (%)	G/G_{max}
3	0.093725	2.549	3434	1533	0.10497	0.46725
6	0.15838	3.295	4429	1428	0.17739	0.43541
9	0.278915	4.211	2670	1191	0.31238	0.36329
12	0.3533	4.573	2532	1253	0.39569	0.34451
14	0.43225	5.185	2178	972	0.48412	0.29635

Table 4-20 Summary of damping ratio and dynamic modulus calculations for XPS-22

$(\sigma_d)_{cyclic}$ (kPa)	$(\varepsilon_a)_{max}$	ζ(%)	E_{secant} (kPa)	G_{sec} (kPa)	γ_c (%)	G/G_{max}
3	0.00814	2.413	8756	3621	0.009841	0.698934
6	0.02458	2.519	8359	3456	0.029717	0.667244
9	0.10114	2.6458	7345	3037	0.122278	0.586303
12	0.16824	2.9135	5317	2198	0.203402	0.424421
14	0.20475	4.9705	4599	1901	0.247543	0.367108

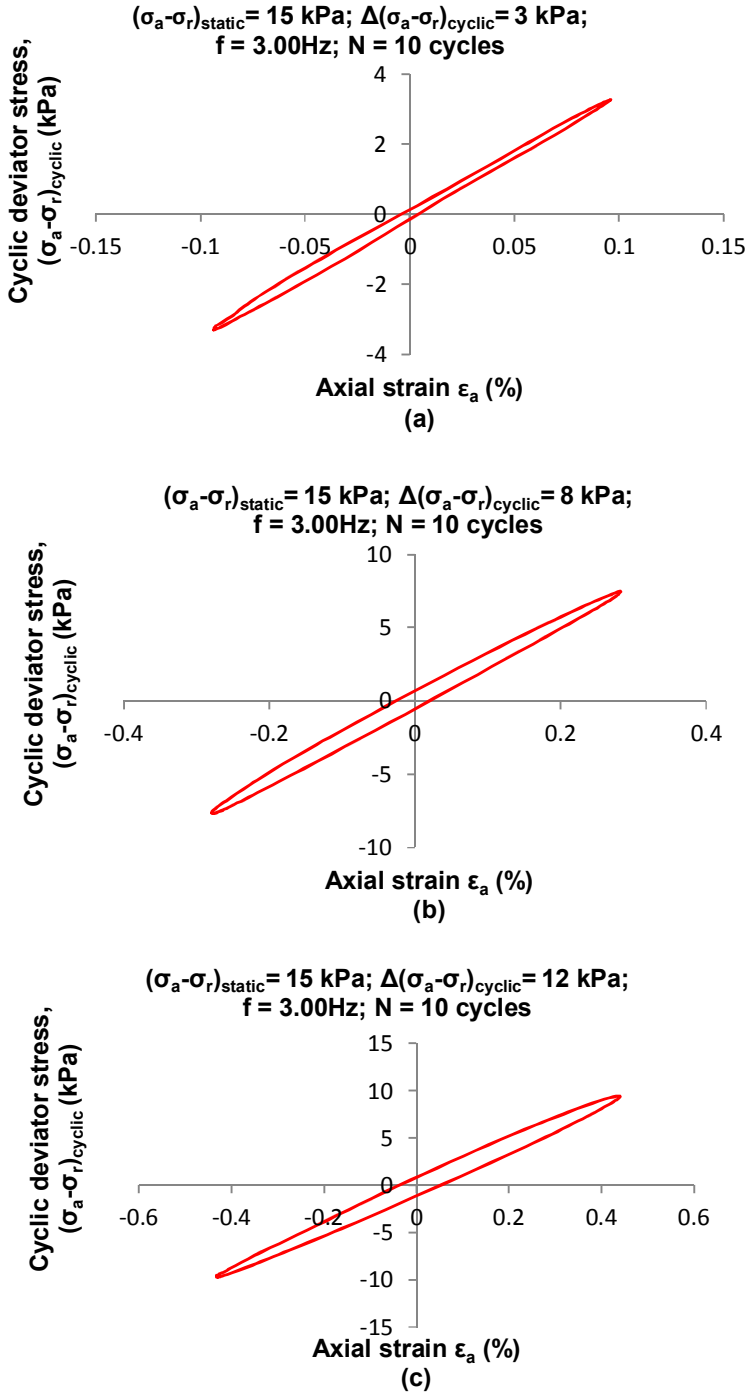

Figure 4-37 Typical hysteresis loops for EPS-15 (a) $\Delta(\sigma_a-\sigma_r)_{cyclic}$= 3kPa (b) $\Delta(\sigma_a-\sigma_r)_{cyclic}$= 6kPa (c) $\Delta(\sigma_a-\sigma_r)_{cyclic}$= 12kPa

4.10 Physical modeling test program

Three groups of tests were performed in the physical modeling study. In the first group (control tests), compressible buffer was not present between the retaining wall model and the backfill (Table 4-21). In the second and third sets, EPS-15 and XPS-22 buffers of different thicknesses were installed between the model walls and the backfill (Table 4-22). Effect of the excitation amplitude was investigated for acceleration amplitude range between 0.06g and 0.7g. Similarly, the range of frequency for the input harmonic motion varied between 4.25 and 10 Hz.

The results of control test series served to make comparisons on the response of cantilevered retaining walls for different wall flexibilities, excitation amplitudes, and frequencies. Efficiency of various type of compressible geofoam buffers were investigated by making comparisons with control test results. The tests were repeated for two different buffer thickness (t/H=0.07 and t/H=0.14 where t is the thickness of the buffer and H denotes the wall height) and various wall thicknesses (t_w=2mm, 4mm, 5mm and 8mm).

Table 4-21 Test group 1 (No compressible inclusion)

Wall thickness (mm)	Peak Base Acceleration Amplitude (g)	Excitation Frequency (Hz)	Geofoam Buffer
2-4-5-8	0.1	5.2	CONTROL TESTS (NO GEOFOAM COMPRESSIBLE INCLUSION)
2-4-5-8	0.2	5.2	
2-4-5-8	0.4	5.2	
2-4-5-8	0.6	5.2	
2-4-5-8	0.7	5.2	
2-4-5-8	0.3	4.25	
2-4-5-8	0.3	5.2	
2-4-5-8	0.3	6.4	
2-4-5-8	0.3	7.7	
2-4-5-8	0.3	10	

Table 4-22 Test group 2 (EPS-15 buffer) and 3 (XPS-22 buffer)

Wall thickness (mm)	Peak Base Acceleration Amplitude (g)	Excitation Frequency (Hz)	Geofoam Buffer	Inclusion Thickness (*t/H*)
2-4-5-8	0.1	5.2	EPS-15-XPS22	0.07-0.14
2-4-5-8	0.2	5.2	EPS-15-XPS22	0.07-0.14
2-4-5-8	0.4	5.2	EPS-15-XPS22	0.07-0.14
2-4-5-8	0.6	5.2	EPS-15-XPS22	0.07-0.14
2-4-5-8	0.7	5.2	EPS-15-XPS22	0.07-0.14
2-4-5-8	0.3	4.25	EPS-15-XPS22	0.07-0.14
2-4-5-8	0.3	5.2	EPS-15-XPS22	0.07-0.14
2-4-5-8	0.3	6.4	EPS-15-XPS22	0.07-0.14
2-4-5-8	0.3	7.7	EPS-15-XPS22	0.07-0.14
2-4-5-8	0.3	10	EPS-15-XPS22	0.07-0.14

4.11 Test Methodology

In this section, the preparation of the test set-up, and procedure followed for the static and dynamic testing phases were explained in detail.

The test procedure for a typical test is as follows:

1. The laminar container is filled with air-dried sand up to a height of 30cm above its bottom and vibro-compacted to achieve the maximum dry density of the sand (Figure 4-38).
2. Emery paper was glued on the surfaces of the model wall which are in contact with the backfill to provide friction between the wall and the cohesionless material (Figure 4-39).
3. To investigate the static and seismic response of the cantilever retaining wall models, the displacements of the wall stem, lateral earth pressures, wall base pressures and the acceleration values at various locations on the wall and in the backfill should be monitored during the test series. Hence, instrumentation of the wall stem and the wall base were carried out prior to placing the wall model in the laminar container.

Figure 4-38 Vibro-compaction of the foundation sand layer

Pressure transducers are mounted into small recesses machined into the inboard face of the wall stem to ensure that the sensing surfaces of the transducers will be flushed with the face of the wall. Four of the Honeywell brand pressure sensors were installed along the wall at 200mm center to center spacing. Two load cell type soil pressure gages were mounted on the toe and heel side of the model wall base to record the base pressures. Two acceleration transducers were rigidly mounted on the wall stem to register vertical and horizontal accelerations of the wall base. The locations of the pressure transducers installed on the retaining wall model are shown in Figure 4-40. The acceleration and pressure transducers were positioned along the centerline of the soil container to reduce the influence of the side friction between the soil and the container as much as possible.

4. The wall model shown in Figure 4-41 was placed on the compacted layer in the sand tank by slowly positioning it with the help of the stationary crane. The thin gaps between the sides of the model wall and the container were sealed using greased rubber strips in order to ensure deflection of the wall with minimum resistance between the container and the wall. A mechanical jack placed between the short side of the sand container and the free face of the cantilever wall model prevented any lateral wall deflection during the preparation of the backfill. Displacement transducers were installed on a stationary rigid steel frame bolted on the ground to measure horizontal displacements at the top and mid height of the wall model. (Figure 4-42).

Figure 4-39 Retaining wall models covered with emery paper

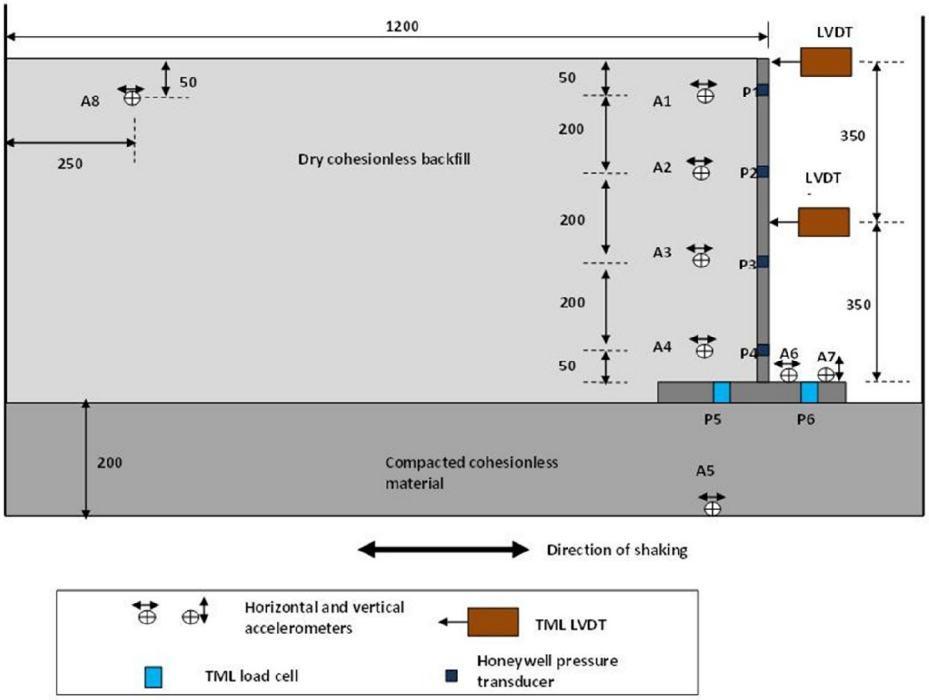

Figure 4-40 Locations of the transducers used in the physical models

5. Physical tests were initially planned to be carried out for loose and dense backfills. A loose state of the backfill (D_r=72%) was achieved by pluviation of the air-dried sand from a fixed height of 50cm (Figure 4-43). Initially, it

was planned to achieve a relative density of 95% by the raining procedure described by Okamoto (2006), however it was observed that relative densities higher than 75% may not be achieved by the raining procedure. As an alternative, the backfill was laid in 10cm lifts and compacted with the vibro-compactor to obtain relative densities between 90% and 95%. It was observed that vibro-compaction of the backfill induced significant additional stresses in the vicinity of the wall and geofoam panels and disturbs the alignment of the pressure sensors, therefore interfering with the proper operation of the data acquisition system. Given the small dimensions of the model and the magnitude of associated lateral stresses acting on the wall, compaction induced stresses represent a significant source of uncertainty in the measurements thus complicating the interpretation of the data. Hence, the test results for the dense backfills are not included in this study.

6. During the pluviation of the granular backfill material, cylindrical shaped containers placed on top of each layer were used to monitor the soil density achieved in each lift. Void ratio achieved in the model tests by raining was found as 0.523 corresponding to a relative density of 71.8%. Graduated tapes were placed at six different locations on the side walls of the laminar container to monitor the settlements during the excitations. The test set-up after completion of the pluviation stage is depicted in Figure 4-44.
7. Following the preparation of backfill, data acquisition system was activated to monitor wall pressures. During the measurements, mechanical jack between the wall stem and container was kept locked to prevent lateral sliding or deflection. In the next step of data acquisition, horizontal fixity of the wall was slowly removed by unloading the mechanical jack located between the wall model and short side of the soil container. Wall pressures and deflections were measured until no further wall deflection and pressure redistribution occur. During the removal of lateral fixity, sliding and rotation of the retaining wall were not observed. Hence, measured displacements were considered as pure flexural deflections of the wall model.
8. Following the data acquisition for the static phase, the preparations for the dynamic phase started. Before the activation of the excitation generator, data acquisition started and data is collected for duration of 30 seconds to

observe probable fluctuations in the initial readings of the transducers. Full amplitude base excitations were applied to the laminar container for a duration of 7 seconds.

(a)

(b) (c)

Figure 4-41 (a) Positioning the wall by mini crane (b, c) Placement of the model wall in the laminar container

9. The tests involving compressible geofoam inclusions were carried out by following the same procedure, however, EPS and XPS geofoam inclusions were installed between the wall model and the backfill prior to the pluviation of backfill material (Figure 4-44). All faces of the EPS panel used in the retaining wall model tests were covered with duct tape to

minimize the interface friction at the geofoam contact with the wall and the backfill. Direct shear tests were performed to determine the friction coefficient between the backfill material and EPS geofoam covered with duct tape. Friction coefficient was found as 0.13 for the stress range of the model tests.

Figure 4-42 Placement of upper and lower displacement transducers

4.12 Properties of the applied base accelerations

The models were excited by harmonic displacements to match a target sinusoidal accelogram with various frequencies within a range of 4.25 Hz to 10 Hz (Figure 4-46). The amplitude of the accelogram varied between 0.06g to 0.7g. Gradually increasing and decreasing type excitations were applied at the beginning and the end of the base motion to prevent the impact type loading effect on the retaining wall models. Application of a simple harmonic base excitation allows all of the retaining wall models to be excited in the same controlled way which enables more accurate comparisons to be made about the effect of variables investigated in this study. The application of random earthquake excitations is generally considered more realistic however Bathurst and Hatami (1998) and Matsuo et al. (1998) indicated that the simple harmonic base excitation is more aggressive compared to a real earthquake excitation with similar predominant frequency and amplitude.

(a) (b)

Figure 4-43 (a) Positioning the sieve on the laminar container (b) Pluviation of air-dried sand by raining method

Figure 4-44 View of the test setup after pluviation of the backfill material

(a) (b)

Figure 4-45 (a) Installation of the geofoam compressible inclusions between retaining wall model and backfill (b) View of the test setup prior to testing

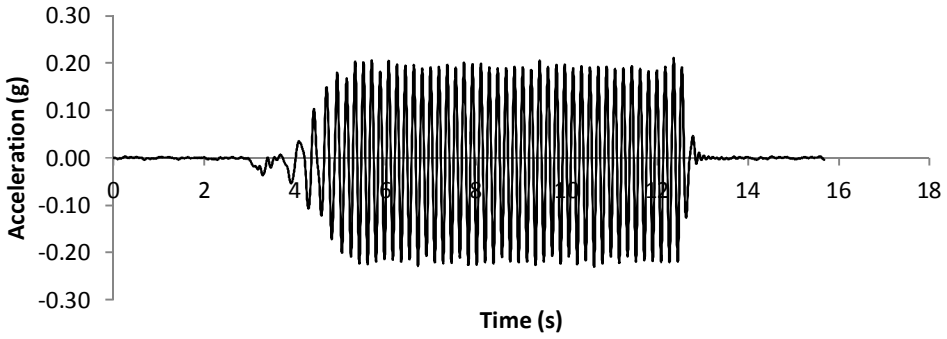

Figure 4-46 A sample acceleration record applied to the base of laminar container (a_{max}=0.2g, f=6.5Hz)

Based on the scaling relationships proposed by Iai (1989), base excitations having a frequency range between 5Hz and 10Hz at 1/10 model scale corresponds to 1.58Hz and 3.16Hz in the prototype scale. According to Bathurst and Hatami (1998), frequencies in the range of 2Hz-3Hz are considered as representative of predominant frequency content of medium to high frequency earthquakes.

CHAPTER 5

TEST RESULTS

5.1 General

In the static phase of the tests, the lateral earth pressures at four different elevations along the wall stem, the wall displacements at the mid-height and top of the wall were monitored. Data acquisition was activated while horizontal wall supports were in place and continued for 20 seconds. This phase of the tests simulates the stress conditions acting on a non-yielding and rigid wall model. In the next phase of static test stage, horizontal fixity along the wall stem was slowly removed by unloading the mechanical jack located between the wall model and sides of the strong box. Lateral earth pressures and deflections were measured until no further wall deflection and pressure redistribution occur. Sliding and rotation of the retaining wall model were not observed in the static phase of the tests.

5.2 Test results

The evolution of the lateral stresses at various elevations on the wall with and without EPS-15 compressible inclusion were depicted in Figure 5-1(a) and (b) for the model wall with t_w=5mm. It was observed that there is a significant decrease in the initial lateral stresses for the presence of EPS-15 compressible inclusion. Unloading of the mechanical jack causes flexural deflections of the wall stem. The wall deflections provide further reduction in the stresses by mobilizing greater portion of soil shear strength. In Figure 5-2, lateral thrust acting on the model walls were depicted for various relative wall flexibility (d_w) and deformable buffer types. Lateral earth forces acting on the walls were calculated by the integration of the lateral stresses recorded at different elevations over the wall height by

using numerical trapezoidal rule. EPS-15 buffer type provides significant contribution on the reduction of lateral earth forces. Wall thrust in this case was observed to be even lower than active earth thrust determined by Rankine's Theory, however contribution of the XPS-22 type buffers are fairly low since the stiffness of this material is lower compared to EPS-15 type geofoam buffer. Presence of a thicker buffer between the wall and the backfill (i.e. *t/H*=0.14 where *t* is the wall thickness and *H* is the wall height) further reduces earth thrust.

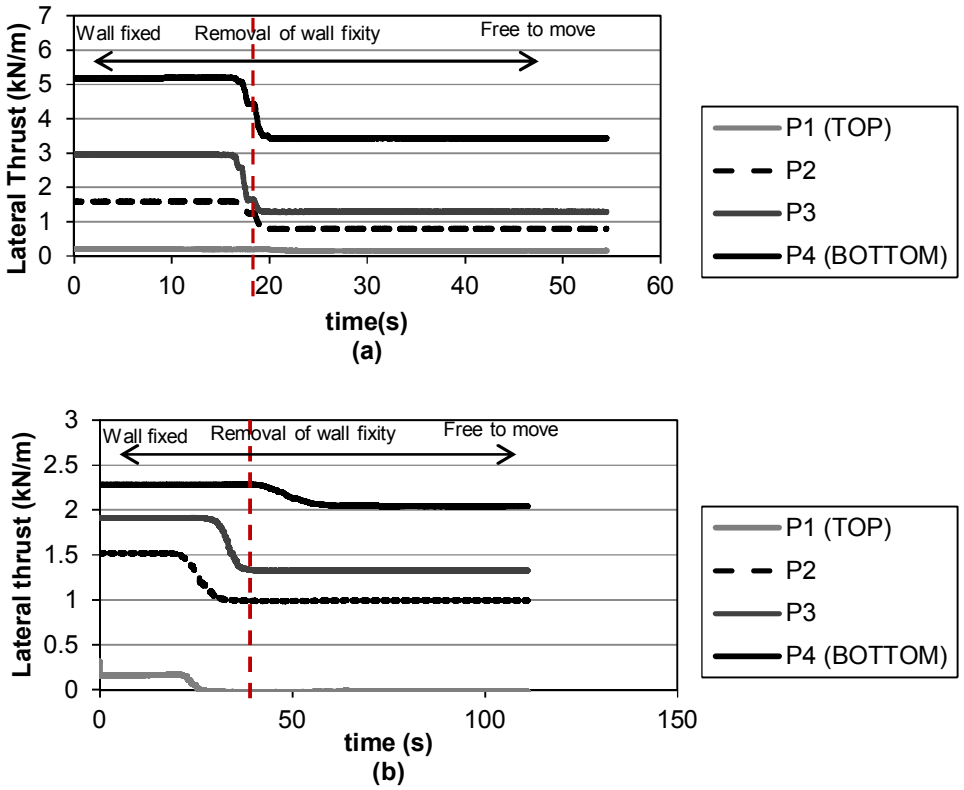

Figure 5-1 Evolution of lateral stresses before and after the removal of wall supports (a) NO EPS case for t_w=5mm (b) EPS-15 cushion *t/H*=0.07, t_w=5mm

The isolation efficiency (i_p) of various compressible buffers in terms of total lateral force was calculated according to Equation 5-1:

$$i_p = \frac{(P_o - P)}{P_o} \times 100 = \frac{(K_0)_{exp} - (K)_{exp}}{(K_0)_{exp}} \times 100 \qquad 5\text{-}1$$

where P_o indicates lateral wall thrust in absence of compressible inclusion and *P* indicates the reduced thrust due to the presence of the compressible layer. This equation may also be expressed in terms of lateral earth pressure coefficients where $(K_0)_{exp}$ and $(K)_{exp}$ represent the earth pressure coefficients in the absence

of compressible buffer and the value in the presence of the buffer, respectively. In Figure 5-3, efficiency of geofoam buffers were compared for various d_w values. Approximately 65% reduction was observed in the lateral thrust for the presence of EPS-15 inclusion (t/H=0.14) when it is installed against the non-yielding and rigid wall model. The efficiency (i_p) decreases as the relative wall flexibility (d_w) increases since a portion of the backfill deformations were already achieved by the flexural wall deflections. The presence of the XPS-22 does not prominently affect the lateral earth force on the wall. Since the elastic modulus of the XPS-22 material is found to be 3.72 times higher than the modulus of EPS-15, smaller compressive strains occur in the XPS-22 buffer under the same lateral forces due to retained backfill. Although, XPS geofoam used in this physical modeling study is one of the products having the lowest density and the strength available in the market, the lateral static stresses generated in the backfill are not sufficient enough to produce required compressive strains in the geofoam buffer.

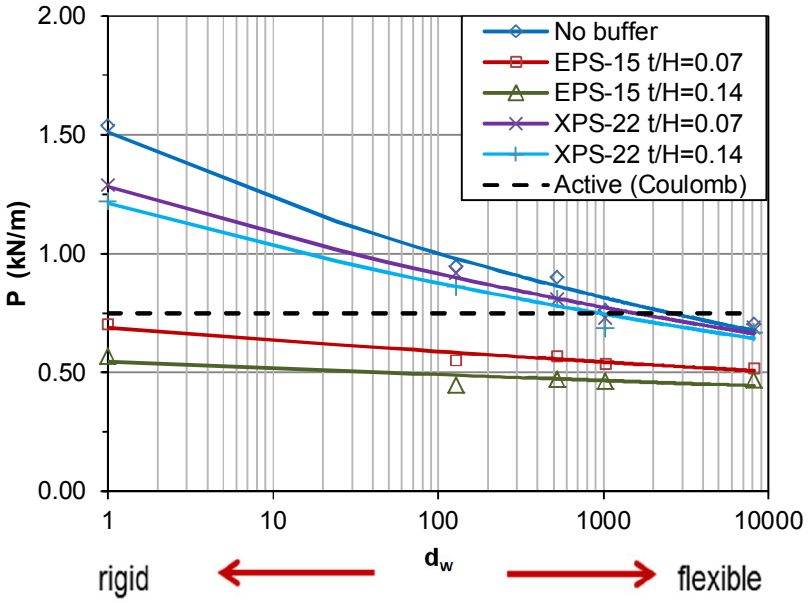

Figure 5-2 Lateral earth force vs. relative flexibility (d_w)

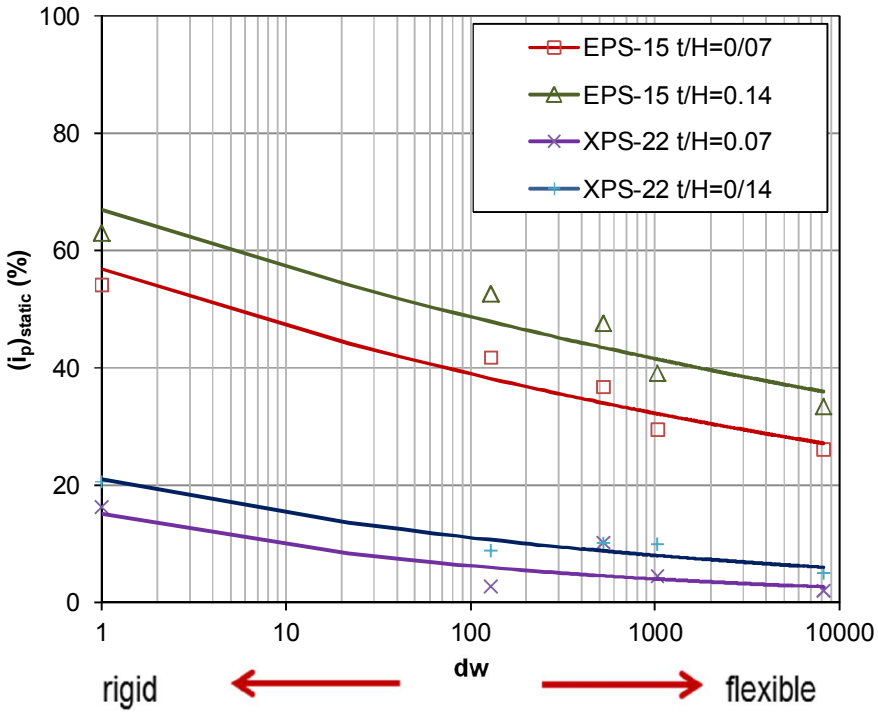

Figure 5-3 Lateral load reduction efficiency (i_p) vs. relative flexibility (d_w)

5.2.1 Determination of the lateral earth pressure coefficients (K_{exp})

Lateral earth pressure coefficient obtained from physical tests (K_{exp}) was back calculated according to the following formula:

$$K_{exp} = \frac{2}{\gamma H^2} \int_0^H \sigma_x \, dz \qquad 5\text{-}2$$

where γ, H and σ_x represent the unit weight of backfill, wall height and lateral earth pressure, respectively. The back-calculated K_{exp} values were normalized by the coefficient of lateral active pressure (K_a) calculated by Coulomb's theory. According to Figure 5-4, presence of geofoam buffer has a positive impact on the magnitude of static lateral earth pressure coefficients depending on the buffer type and relative wall flexibility.

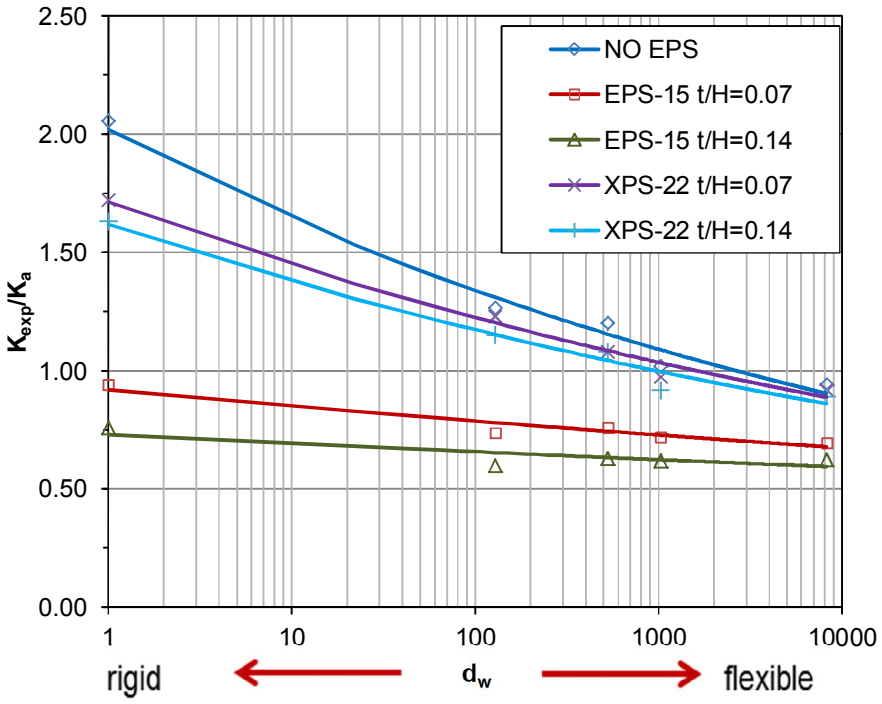

Figure 5-4 Normalized earth pressure coefficients vs. relative flexibility (d_w)

5.2.2 Lateral wall deformations

The lateral wall pressures and deflections were continuously monitored until they achieved steady values. In none of the static tests, the retaining wall models experienced significant base sliding and rotation. Hence, the measured lateral displacements were considered as flexural deflections of the wall model. Test results indicate that increasing relative flexibility leads to higher wall deflections as expected. Presence of geofoam compressible inclusions provides reduction in wall deflections in varying amounts. Figure 5-5 demonstrates the influence of buffer characteristics and relative wall flexibility (d_w) on the wall deflections.

5.2.3 Point of application of static wall thrust

The point of application of the static wall thrust varied between 0.24*H* and 0.33*H* (measured from the base) depending on the wall flexibility and deformable buffer type. It was observed that increasing wall flexibility causes total wall thrust act at a higher elevation. Placing a compressible buffer between the wall and the backfill slightly increases the location of the application point.

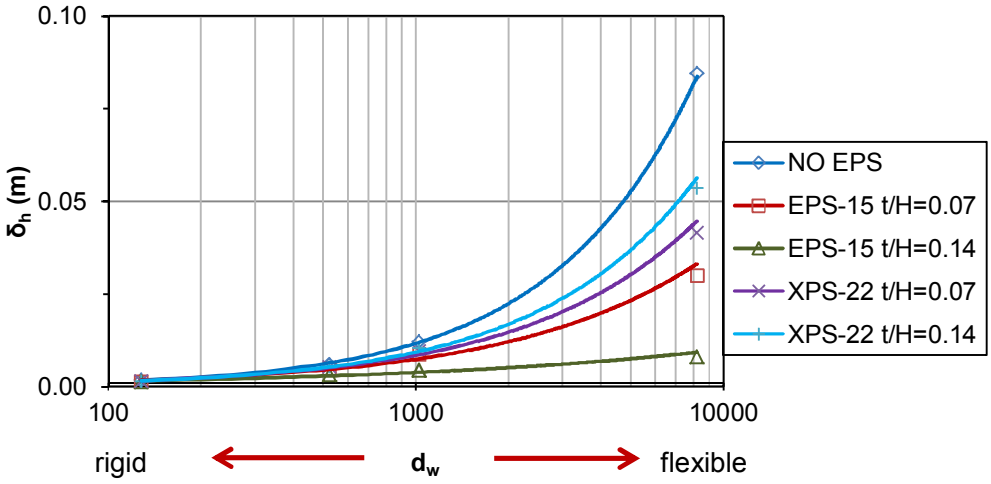

Figure 5-5 Static wall deflections for various (d_w) relative flexibility values

Table 5-1 Point of application of static wall thrust

d_w	*Point of application of total thrust (from wall base)*				
	No geofoam	*EPS-15 t/H=0.14*	*EPS-15 t/H=0.28*	*XPS-22 t/H=0.14*	*XPS-22 t/H=0.28*
128	0.26H	0.31H	0.34H	0.30H	0.31H
524	0.25H	0.32H	0.32H	0.31H	0.30H
1028	0.32H	0.33H	0.35H	0.32H	0.29H
8200	0.33H	0.31H	0.33H	0.33H	0.32H

5.3 Dynamic test results

In addition to the physical quantities monitored in the static tests, horizontal accelerations at various elevations in the backfill and on the wall were monitored in the dynamic phase of the tests. The general format of the presentation of the data related to physical parameters will be in the form of the Figure 5-6. The use of “maximum”, ‘’minimum’’ and ‘’residual’’ key words indicate that the reference of the physical quantity is origin, however the values are referenced according to initial static value if used with ‘’dynamic’’ word before. In the absence of a keyword such as minimum or maximum (i.e. dynamic wall thrust), it will refer to a value at a particular time instance.

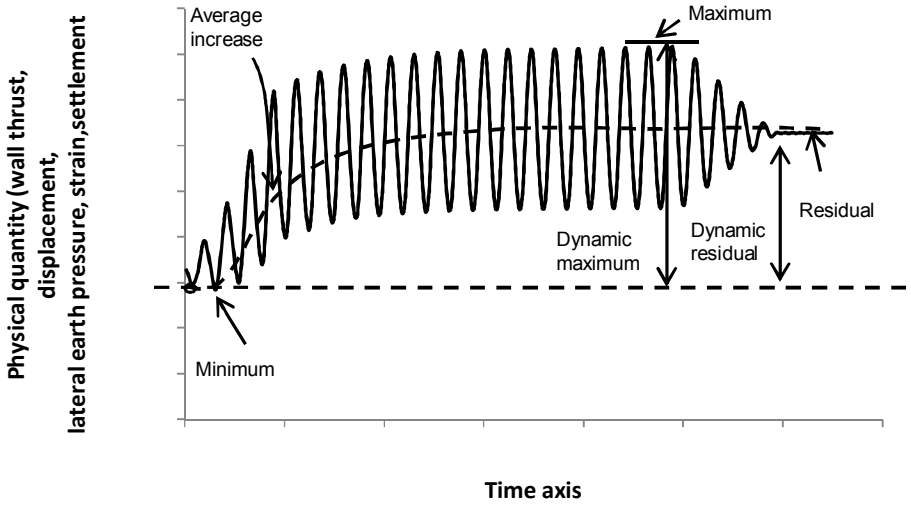

Figure 5-6 General presentation format of the various dynamic response parameters

5.3.1 Filtering of the data

Raw data acquired in the dynamic phase contains various amounts of noise depending on the type of the transducers. The types of noise in the data may be classified as electrical noise, mechanical noise and digital noise. The electrical noise occurs as a result of electrical interference generated in the transducers, power supplies, and transmission cables between the transducers and the data acquisition card. The mechanical noise is originated due to the vibrations of the experimental system components. Digital noise occurs during the process of analog to digital conversion which is incorporated with various amounts of truncation errors generated during the data acquisition, signal conditioning, filtering and data evaluation. The factors listed above cause non-systematic errors in the evaluation of test results. Generally the sources of these kinds of errors are difficult to identify and their effect cannot be evaluated in terms of deterministic approaches. In this study, the electrical noise was minimized by shielding the data acquisition cards, signal conditioning boards and the transmission cables with proper electromagnetic cable coatings. External power sources and alternating currents were kept away from the low voltage components of the data acquisition system. However, it was observed that noise was still present and use of filtering technique was unavoidable before interpreting the results. Investigation of the raw data shows that the outputs of the accelerometers and pressure transducers incorporate more noise compared to those of linear variable displacement

transducers and load cells. Filtering technique may be helpful to reduce the level of noise in the data. For this purpose, information contained in the specific frequency band should be extracted from the measured data by designing suitable filters. Investigation of the power spectrum of the unfiltered data depicted in Figure 5-9(a) indicates that noise in the measurements is mainly associated with the frequencies greater than 25Hz. Based on this observation, a low-pass analog filter was designed in MATLAB environment to remove the frequency components greater than 25Hz. The design of the filter was made according to the theory of linear filters (Newton, 1988). The filtered version of a time series $\tilde{m}(t)$ is defined as:

$$\tilde{m}(t) = \sum_{j=-\infty}^{\infty} \beta_j m(t-j) \qquad 5\text{-}3$$

where $m(t)$ is the unfiltered time series and β_j denote filter coefficients. The purpose of the filter design is to determine filtering coefficients β_j so that the filtered time series possess the required spectral characteristics. The filter should be designed to remove the frequency components containing noise without modifying the components having meaningful data. A low pass filter should satisfy the following equation:

$$f_{\tilde{m}}(\omega_k) = \begin{cases} f_m(\omega_k) & for\ 0 > \omega_k > \omega_b\ and\ (1-\omega_b) > \omega_k > 1 \\ 0 & for\ \omega_b > \omega_k > (1-\omega_b) \end{cases} \qquad 5\text{-}4$$

where $f_{\tilde{m}}(\omega_k)$ is the power spectral density function of the conditioned time series, $f_m(\omega_k)$ is the power spectral density function of the raw time series and ω_b is the filter cut-off frequency. The satisfaction of this equation provides that the filter has the ability to reduce the amplitudes of the components in the noise frequencies while preserving the required components. ω_b is calculated as:

$$\omega_b = \frac{\omega_h}{\omega_s} \qquad 5\text{-}5$$

where ω_h is the frequency limit where the higher components will be filtered and ω_s is the sampling frequency of the data acquisition system. Based on this theory, a low pass Butterworth filter of fourth order was designed in MATLAB environment to filter the raw time series in order to reduce the frequency components greater than 25Hz. For the majority of applications, use of the Butterworth filter type provides a maximally flat response in the pass-band (i.e. practically no deviation from unity) sacrificing the roll-off steepness (in comparison

to a Chebyshev filter of the same order). However, this can be easily overcome by the use of a higher order filter. The behavior of the filter is depicted in Figure 5-7. In Figure 5-8(a) and (b), a window of the raw data and filtered data of the base acceleration transducer were depicted. The power spectra for the unfiltered and filtered data was provided in Figure 5-9 for comparison purposed.

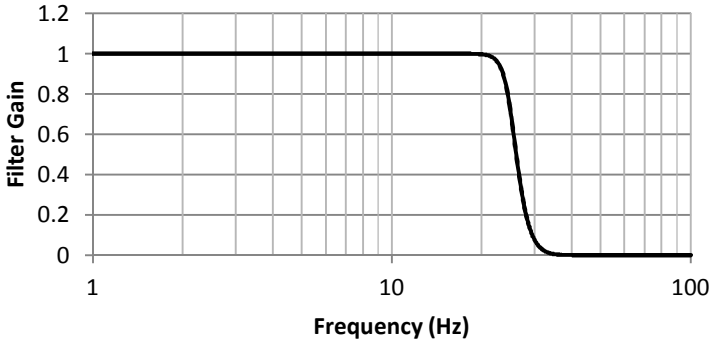

Figure 5-7 Filter gain for the fourth order Butterworth filter

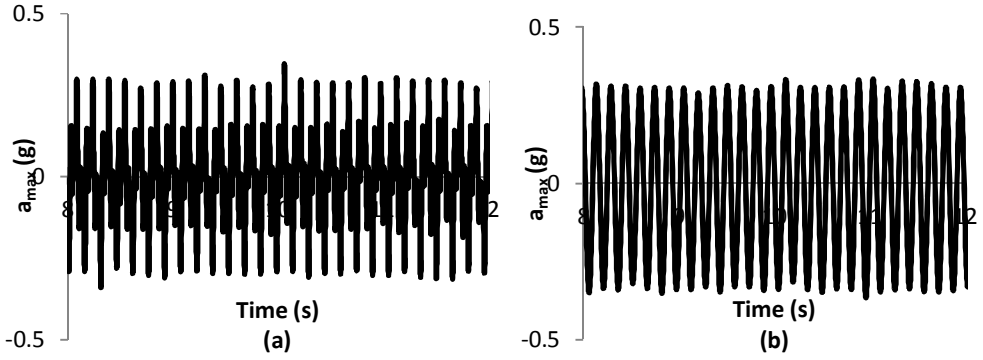

Figure 5-8 (a) Unfiltered and (b) Filtered horizontal acceleration time histories

5.3.2 Dynamic wall deflections

Dynamic wall deflections at the wall tip, mid-height of the wall, base of the wall and the shake table surface were compared for different base excitation characteristics, relative wall flexibility values and compressible buffer types.

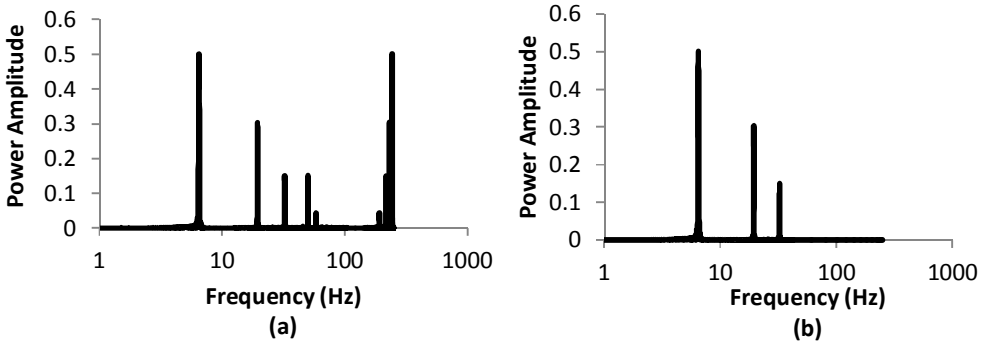

Figure 5-9 Power spectrum for (a) unfiltered (b) filtered acceleration time history

While the deflections at the wall top and wall mid-height were directly measured by displacement transducers installed on the wall stem at these elevations, those of the wall base and shake table were calculated by integration of the acceleration time histories recorded by the acceleration transducers placed on wall base and shake table surface. In Figure 5-10(a), unfiltered displacement time histories for CW-C7 test (no geofoam buffer, 0.7g@5Hz excitation) were depicted. The processed data by the low-pass filtering procedure were plotted in Figure 5-10(b). The maximum displacements recorded by the displacement transducer at the wall tip and mid-height were approximately 6.20cm and 2.47cm, respectively. The maximum translational movement of the wall base was observed as 0.8cm. Hence, flexural deflection of the wall tip is found as 5.40cm. In most of the tests, any translational movement of the wall base was not observed (Refer to Appendix E). A comparison of the time histories for the most flexible wall (type CW-A8) and most rigid (CW-D8) wall type are made in Figure 5-11(a) and Figure 5-11(b) for the applied base motion having amplitude of 0.3g at 4.25Hz frequency. The residual deflections of the CW-A8 model wall are significantly high compared to CW-D8 due to high flexibility of the wall. It was observed that sliding of the wall is very low compared to the flexural deflections of the wall models. In CW-D8 test, the maximum displacements of the wall tip and wall mid-height are approximately same, since the wall model behaves as a rigid body, however for CW-A8 type, there is approximately 55% difference between wall tip and wall mid-height deflections. In Figure 5-12, the displacement time-histories of CW-C8 (wall without geofoam buffer) and CW-CE8 (wall with EPS-15 compressible geofoam buffer having a *t/H* ratio of 0.07) are compared. The residual lateral deflection of the wall top at the end of CW-C8 test (no geofoam case) was observed as 6.9cm, whereas 4.61cm lateral deflection was measured at the end of CW-CE8 test.

A summary of the results regarding to the maximum dynamic wall deflections were provided in Figure 5-13 and Figure 5-14. The effect of wall flexibility on the wall deflections were depicted in Figure 5-13. Wall flexibility significantly affects the performance of the geofoam seismic buffers. An increasing trend was observed in flexural deflections when relative wall flexibility (d_w) increases which means higher amount of horizontal displacements occur in the backfill. The evaluation of the dynamic lateral wall pressures are investigated in conjunction with the wall movements for a more detailed understanding of the backfill-geofoam-structure interaction (Refer to Section 5.3.4).

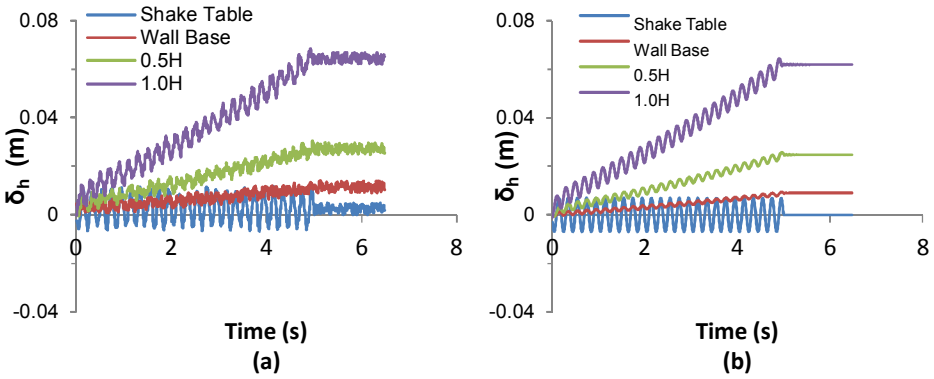

Figure 5-10 Dynamic displacement-time history for CW-C7 test (a) Unfiltered graph (b) Filtered graph

Decrease in flexural wall deflections may reach up to 65% for the type-D wall (most rigid wall, d_w=128) for buffer thickness of t/H=0.14 however only 20% reduction was observed for type-A wall (most flexible wall, d_w=8197).In Figure 5-14(a), the effect of excitation frequency on the displacement response of the model wall CW-C is depicted.

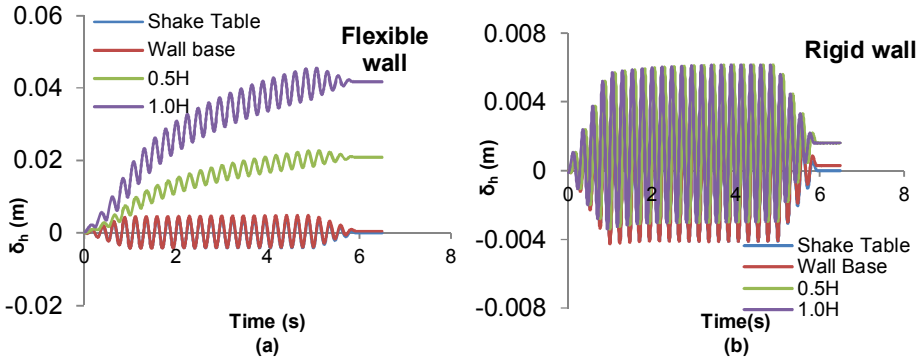

Figure 5-11 Dynamic displacement-time history for (a) CW-A8 test (b) CW-D8

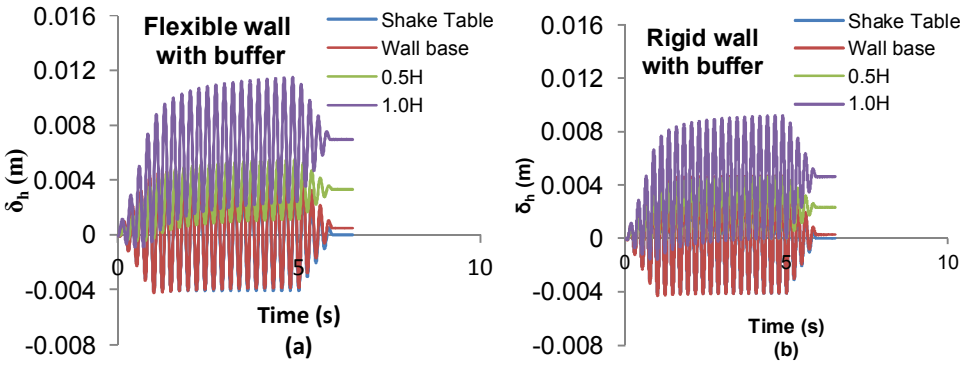

Figure 5-12 Dynamic displacement-time history for (a) CW-C8 test (b) CW-CE8

In this graph, frequency of the base excitation (*f*) is normalized by the natural frequency of the wall-backfill system (f_n) calculated in Section 5.3.3.1. Observed wall displacements tend to increase for higher excitation frequencies. However, with the presence of geofoam buffer, flexural deflections decrease depending on the stiffness and thickness of the buffer. EPS-15 type buffers were found to be more effective in reducing flexural deflections as compared to the XPS-22 type buffers. The effect of excitation amplitude on wall deflections (Figure 5-14-b) was presented in a similar fashion. As expected, lateral deformations increase while excitation amplitude increases. Amount of decrease in wall deflection varies between 10% and 35% depending on the amplitude. Geofoam buffers provide reductions in the wall deflections depending on the amplitude of the base excitation and the physical characteristics of the geofoam buffer. As compared with no geofoam case, 13.6% reduction occurs in maximum wall deflection for the presence of EPS-15 inclusion having *t/H* ratio of 0.14.

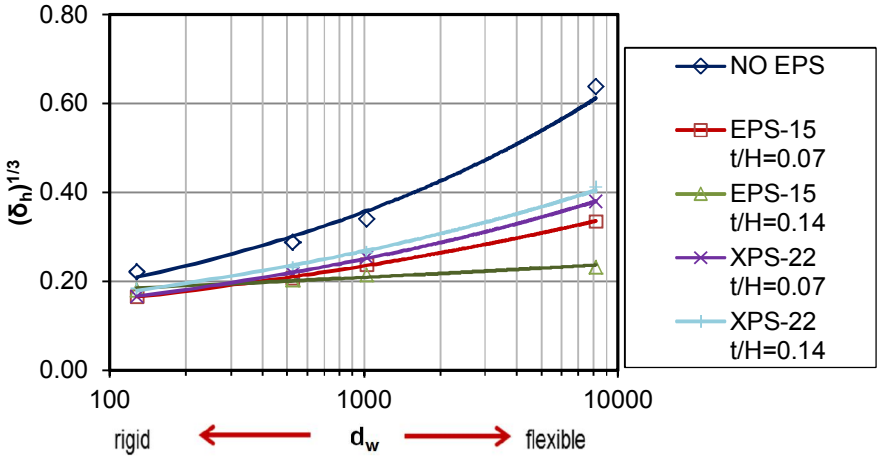

Figure 5-13 Flexural deflection (power of 1/3) versus d_w

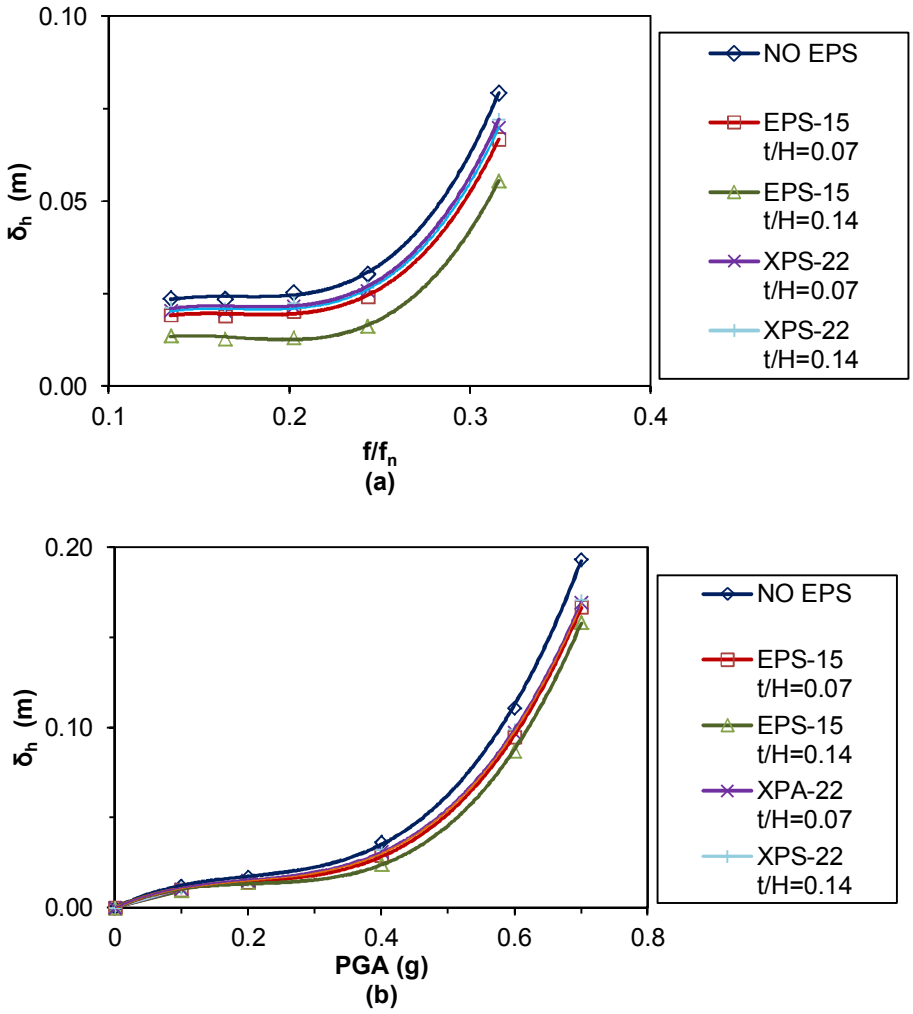

Figure 5-14 Lateral wall deflection vs. (a) f/f_n (b) PGA for d_w=1024

5.3.3 Amplification of base motion through the backfill

Horizontal accelerations were monitored by the acceleration transducers placed at various locations in the model (Figure 5-15). Amplification of the base acceleration was investigated by converting time history data into frequency domain by Fast Fourier Transform (FFT). In Figure 5-16, Fourier spectra of the acceleration time histories recorded on the shake table (A5), wall tip (A1) and far end of the backfill (A8) in CW-C10 and CW-CE10 tests were plotted. Amplification factor (η) is defined as:

$$\eta = \frac{(A_{fft})_{h=1.0h}}{(A_{fft})_{h=0h}} \qquad 5\text{-}6$$

where$(\mathrm{A_{fft}})_{\mathrm{h=1.0h}}$ is the FFT amplitude of the acceleration time history recorded at the wall top and $(\mathrm{A_{fft}})_{\mathrm{h=0h}}$ is the FFT amplitude of the applied base motion. The amplification characteristics observed in the vicinity of the wall and far-end of the backfill shows slight variations. Higher amplification factors were observed at the wall vicinity.

Amplification behavior in relation to the wall flexibility was depicted in Figure 5-17. In most of the cases, the amplification was observed to be higher in the wall vicinity compared to the far-end. The discrepancy between amplification behaviors observed in the wall vicinity and in the far-field increases with increasing relative flexibility (d_w). Presence of EPS-15 seismic buffer against the wall leads to a significant increase in the amplification. Influence of XPS-22 seismic buffer is not as pronounced as those of EPS-15 type buffer.

Amplification response in relation to the peak base acceleration amplitude is depicted in Figure 5-18. In most of the tests, η values for the wall side and laminar container boundary side are similar, however for the presence of EPS-15 (t/H=0.07) compressible buffer, amplification in the vicinity of the wall are slightly higher than those near the laminar container boundary. The discrepancy diminishes for increasing PGA values.

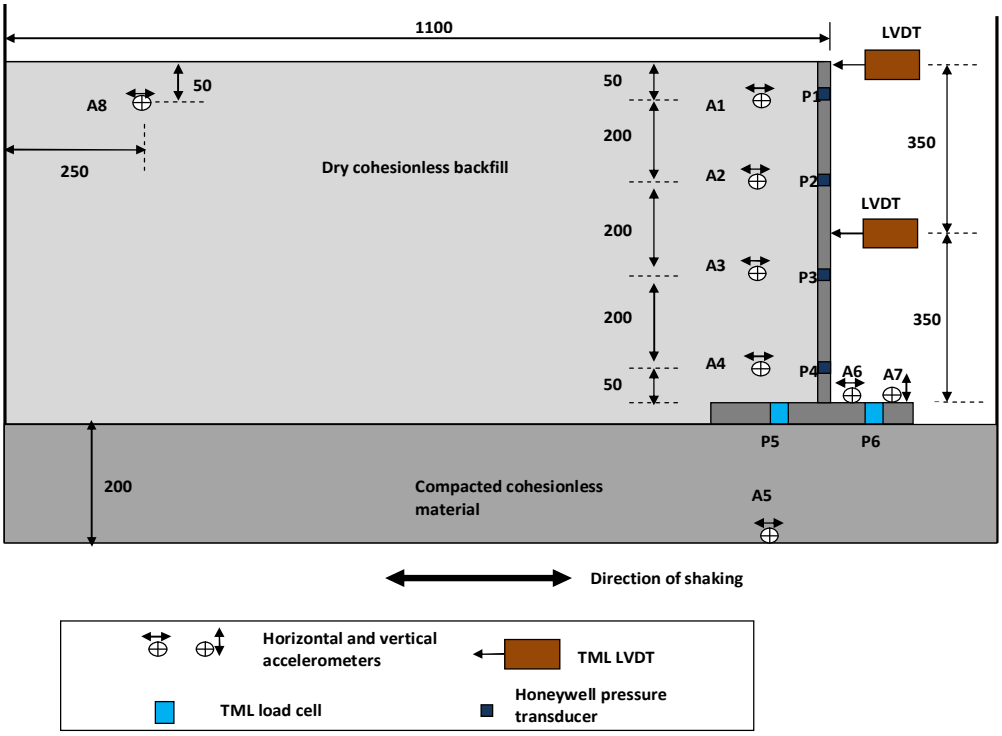

Figure 5-15 Positions of the transducers used in model tests

In Figure 5-19, amplification behavior in relation to the frequency of excitation was depicted. Due to the limitations of the shaking table, the maximum frequency of the applied base motion is approximately 30% of the fundamental frequency of idealized wall-backfill system. It was observed that amplification response tends to increase as f/f_n ratio approaches to unity. A discrepancy was observed in the amplification factors in vicinity of the wall side and boundary side, especially at higher frequency ratios. Amplification of base motion may reach up to 2.6 for f/f_n=0.30 at the wall side whereas slightly smaller values were observed at the boundary side (far-field).

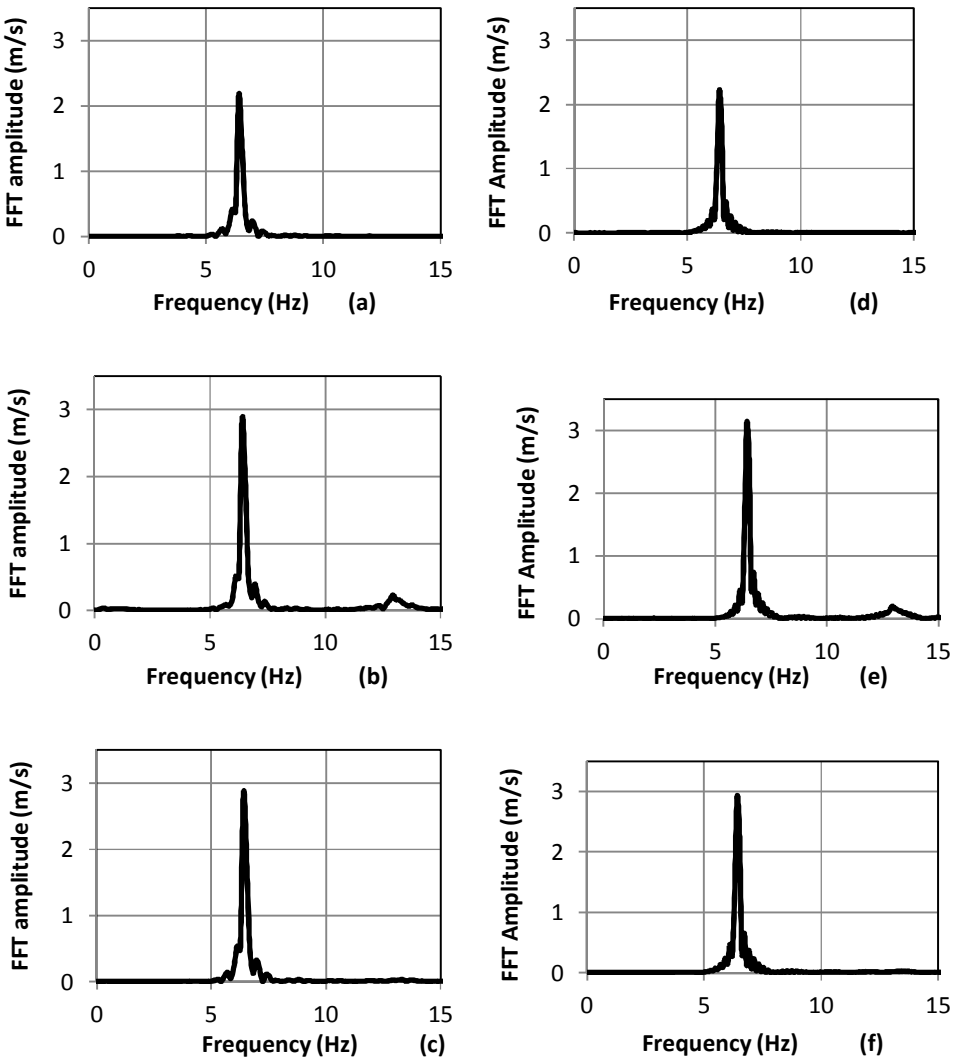

Figure 5-16 Fourier spectra for (a) CW-C10 Base excitation (b) CW-C10 at 1.0H in the vicinity of the wall (c) CW-C10 at 1.0H far-field (d) CW-CE10 Base excitation (e) CW-CE10 at 1.0H in the vicinity of the wall (f) CW-CE10 at 1.0H far-field

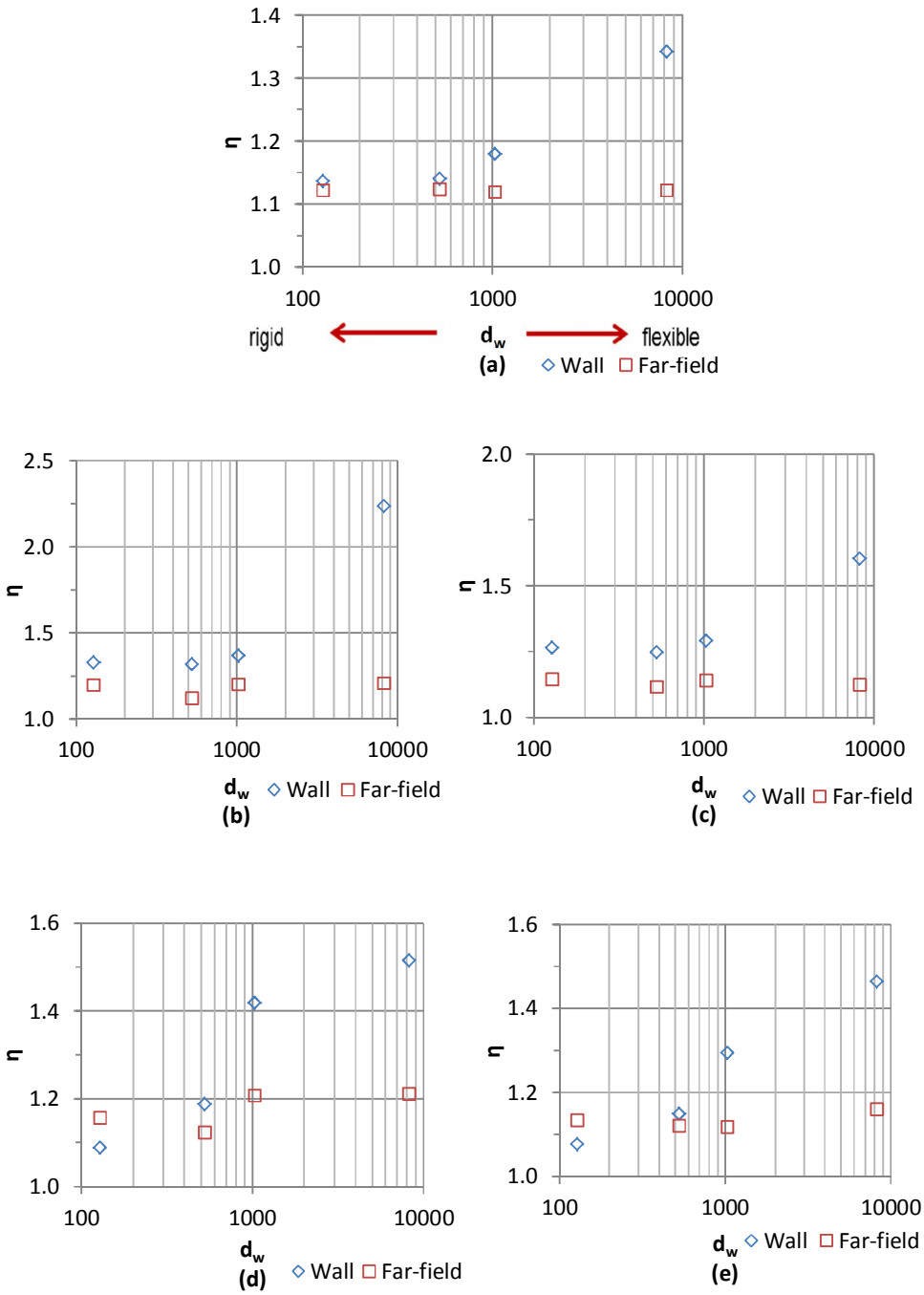

Figure 5-17 Amplification response for various wall flexibilities (a) No geofoam buffer (b) with EPS-15 and t/H=0.07 (c) with EPS-15 and t/H=0.14 (d) with XPS-22 and t/H=0.07 (e) with XPS-22 and t/H=0.14

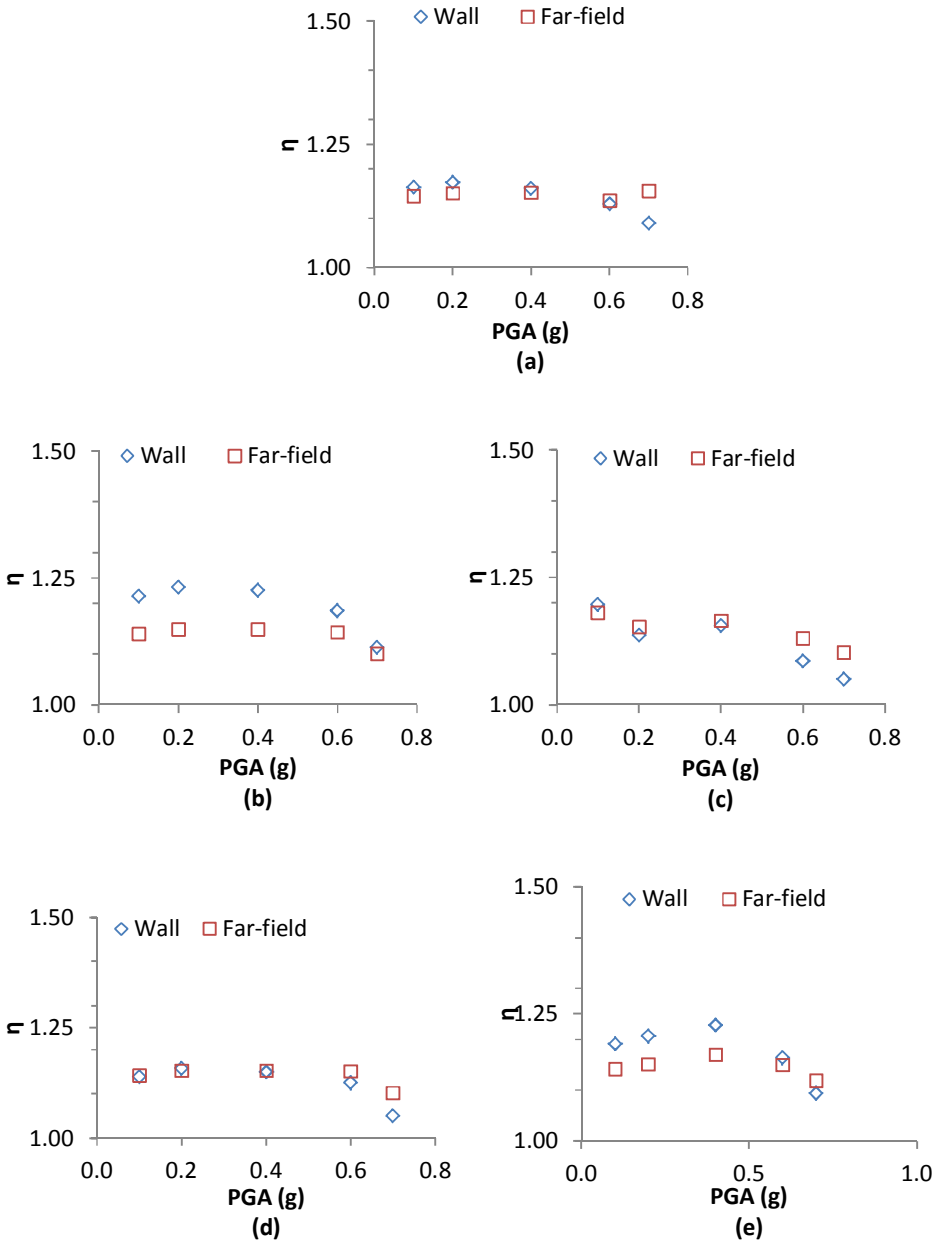

Figure 5-18 Amplification response for various excitation amplitudes (a)No geofoam buffer (b) with EPS-15 and t/H=0.07 (c) with EPS-15 and t/H=0.14 (d) with XPS-22 and t/H=0.07 (e) with XPS-22 and t/H=0.14

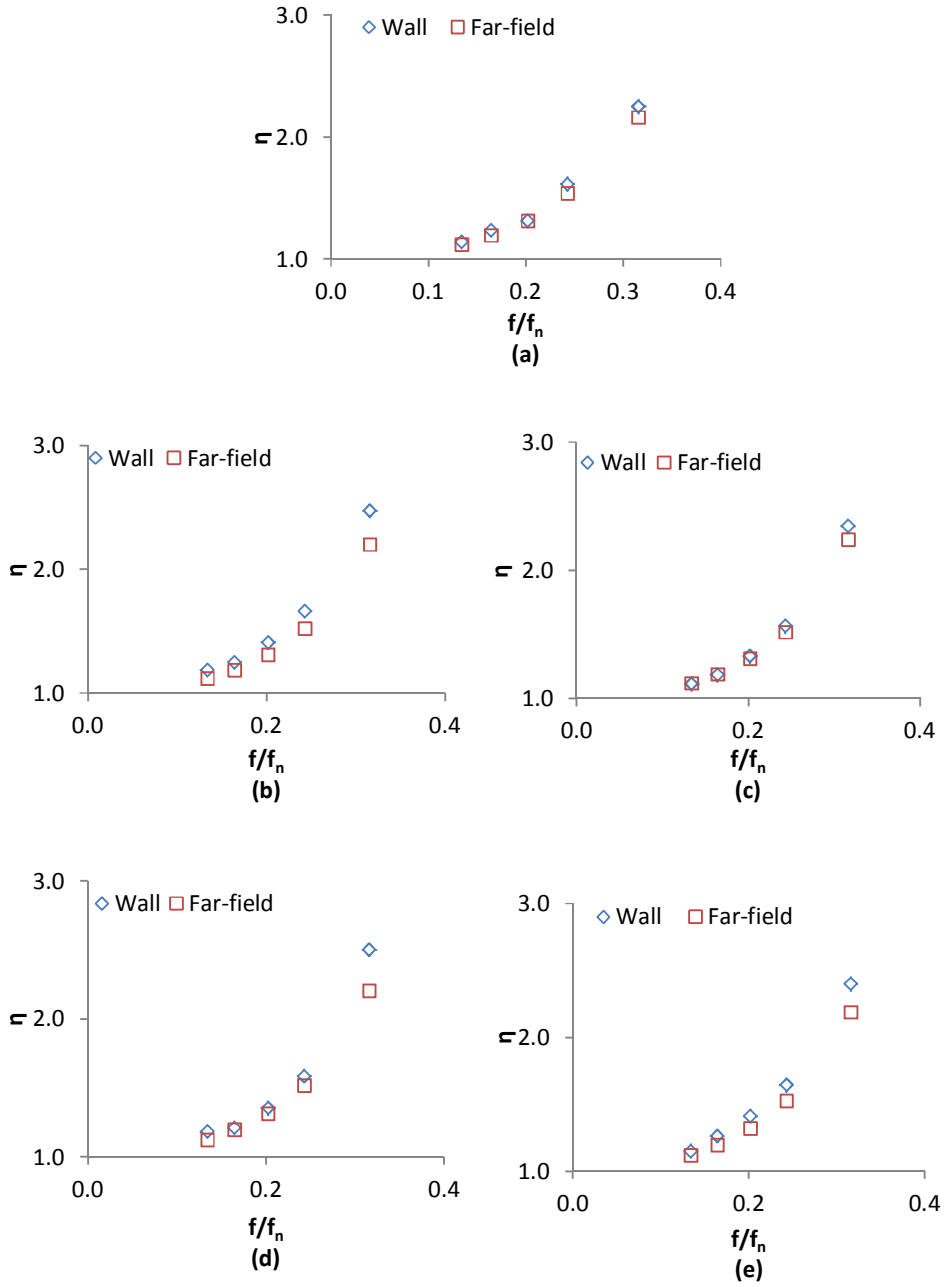

Figure 5-19 Amplification response vs f/f_n (a) No geofoam buffer (b) with EPS-15 and t/H=0.07 (c) with EPS-15 and t/H=0.14 (d) with XPS-22 and t/H=0.07 (e) with XPS-22 and t/H=0.14

5.3.3.1 Natural frequency of the wall-backfill system

The fundamental frequency of the backfill material was estimated using theoretical and numerical methods. The first fundamental frequency of an equivalent one-dimensional and linear elastic soil column is calculated for a known height (*h*), shear modulus (*G*) and material density (*ρ*). The equation is as follows:

$$f_1 = \frac{1}{4h}\sqrt{G/\rho} \qquad 5\text{-}7$$

In a recent study, Bathurst and Hatami (1998) showed that the fundamental frequency of plane strain retaining wall models can be approximated by the shape factors introduced by Wu (1994). The shape factor adds the capability of taking into account of the height (*h*) and width (*b*) of the two dimensional model involving a retaining wall. The closed form solution will be in the form of:

$$f_1^{*} = S.f_1 \qquad 5\text{-}8$$

$$S = \sqrt{1 + \left(\frac{1}{2-\upsilon}\right)\left(\frac{h}{b}\right)^2} \qquad 5\text{-}9$$

Fundamental frequency of the wall-backfill system was calculated as 31.65Hz with Eq. 5-8. The calculations were performed considering h=0.7m, ρ=1.65t/m^3, G=11850kPa, b=1.4 and υ=0.3. In order to estimate first fundamental frequency of a cantilevered beam, the following closed form solution should be used:

$$\omega_1 = (1.875)^2\sqrt{EI/mH^4} \qquad 5\text{-}10$$

where *E*, *I* and *m* are the Young's modulus, moment of inertia and mass per unit length of the beam, respectively. By using eq. 5-10, natural frequency of the wall itself is estimated as 378 Hz, which is quite high compared to the natural frequency of the wall-backfill system estimated by Eq. 5-8.

5.3.4 Dynamic earth pressures

In the following sections, the influence of various parameters on the dynamic earth pressures and forces was investigated. These parameters include:

a. Relative flexibility of the wall (d_w)
b. Thickness and stiffness of the seismic buffer
c. Base excitation characteristics (Frequency, PGA)

5.3.4.1 Effect of relative wall flexibility (d_w) on the dynamic earth pressures (p_{dyn})

Relative wall flexibility (d_w) is an important factor on the evolution of the dynamic lateral forces since it directly affects the amount of soil displacements. It was observed that dynamic earth stresses on flexible walls are significantly lower than those acting to the rigid and non-yielding walls since wall flexibility leads to displacements in the retained medium which leads to mobilization of higher portion of the soil shear strength.

In Figure 5-20, evolution of dynamic thrust (P_{dyn}) on Type-A, B, C and D walls which were excited with same base motions were depicted. It was observed that amplitude of dynamic thrust is significantly high for the least flexible wall (d_w=128). At the end of dynamic phase, a residual lateral force remained on the wall due to the densification of the soil during the excitation. The relative density of the backfill at the end of dynamic phase was observed to be in the range of 80% to 85%. The amount of residual lateral force ($\Delta P_{residual}$) is approximately same in all cases. In Figure 5-21, evolution of the dynamic thrust on wall model with seismic buffer (EPS-15, t/H=0.14) were depicted. It was observed that seismic buffers provide prominent contribution on reduction of dynamic earth thrust. Peak to peak amplitude of the maximum dynamic thrust increment of type-D wall (stiffest wall) is 0.672kN/m without geofoam inclusion, whereas this values decreases to 0.320kN//m under the presence of EPS-15 seismic buffer. For type-A wall without buffer (the most flexible wall model), maximum P_{dyn} occurred as 0.214kN/m. It decreased to 0.083kN/m when EPS-15 type geofoam buffer is present. A comparison of lateral earth pressure profiles are provided in Figure 5-22 and Figure 5-23. In these figures, initial static and total dynamic pressure profiles leading to maximum dynamic thrust are depicted. The theoretical active pressure distribution was calculated according to Rankine's theory and included for comparison purposes. It was observed that wall flexibility has a significant impact on static and dynamic stress distributions. Initial static earth pressure profiles are generally in good agreement with theoretical pressure distributions. The static stress distribution of flexible walls is close to active earth pressure profiles

calculated according to Rankine's theory. The presence of deformable buffer provides decrease in both initial static and total dynamic earth pressures. The dynamic pressures observed in the physical tests were compared with the pressure distribution calculated using Steedman- Zeng (S-Z) Method (Steedman and Zeng, 1991). It should be expressed that pressure distrubutions obtained from S-Z solutions are in good aggrement with test results and provide an upper bound for the dynamic wall stresses in all the cases. Comparison of Figure 5-22 and Figure 5-23 exhibits the significant contribution of compressible inclusions on reduction of static and dynamic earth pressures. Effect of relative wall flexibility (d_w) on the dynamic thrust and base moments for the model walls with and without compressible geofoam inclusions are depicted Figure 5-24 (a) and (b). Presence of a compressible layer provides a decrease in P_{dyn} especially for greater d_w values. The effect of inclusion stiffness is more pronounced for less stiff walls.

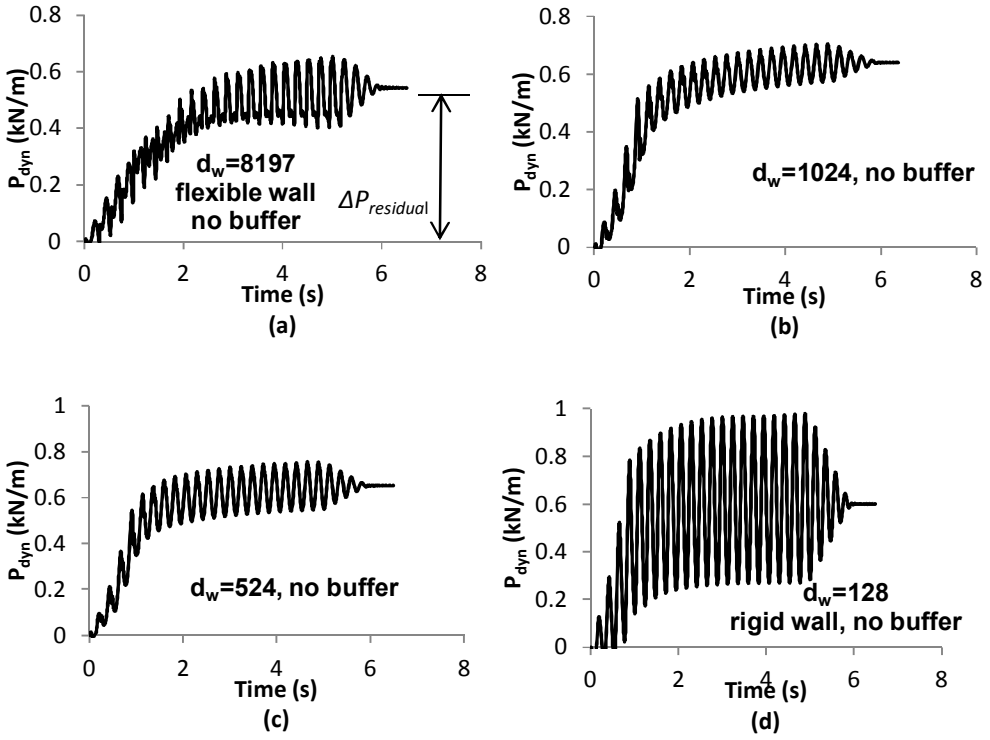

Figure 5-20 Evolution of the dynamic forces for various d_w values

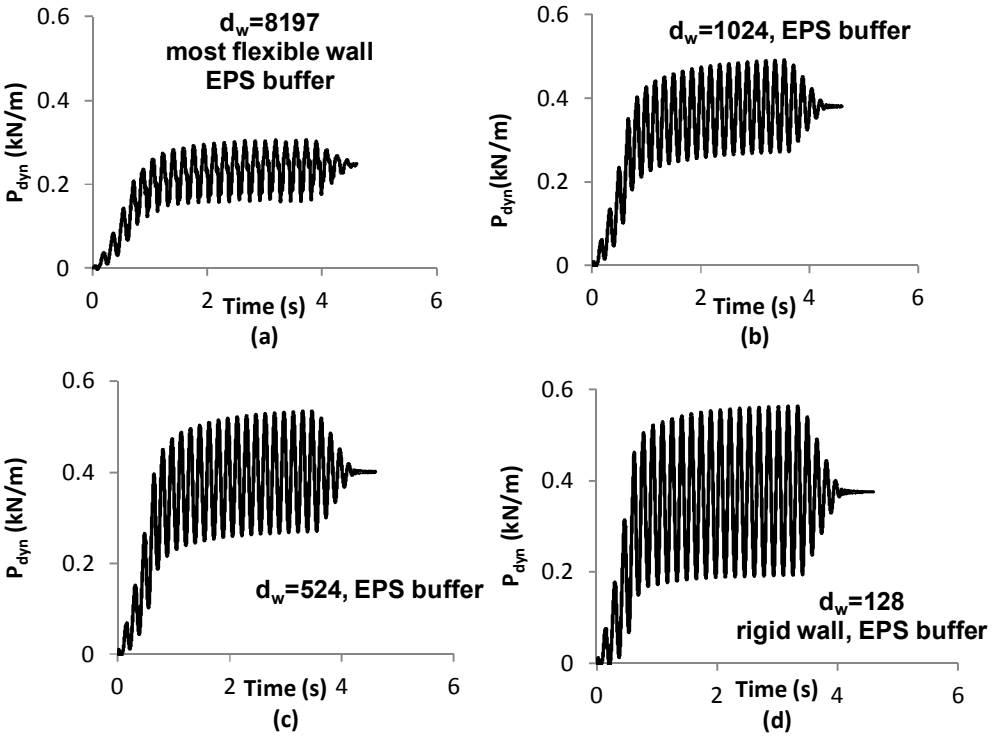

Figure 5-21 Evolution of the dynamic forces for various wall and buffer combinations

5.3.4.2 Incremental seismic thrust

Buffer stiffness and thickness has an important role on the maximum dynamic thrust (*ΔP)*. The performance of various geofoam inclusions for different d_w values are evaluated by calculating dynamic earth thrust reduction efficiency ($i_{\Delta p}$)

$$\mathrm{i}_{\Delta p} = \frac{\Delta P_{w/o\ inc} - \Delta P_{w/inc}}{\Delta P_{w/o\ inc}} \qquad 5\text{-}11$$

where $\Delta P_{w/o\ inc}$the dynamic increment of the wall thrust without geofoam buffer and $\Delta P_{w/inc}$ is the value of *ΔP* for the presence of seismic buffers. In Figure 5-25, dynamic force reduction efficiency of various geofoam buffers is depicted. The positive contribution of the geofoam buffers on reducing dynamic earth forces decrease when relative wall flexibility increases.

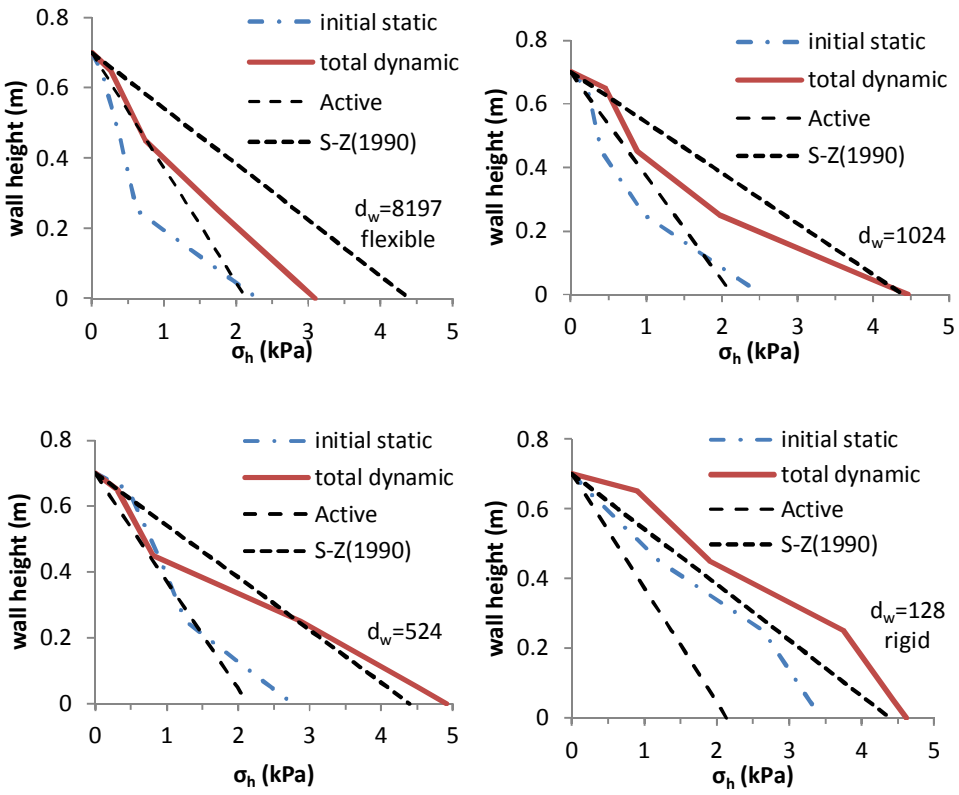

Figure 5-22 Total pressure profiles leading to peak dynamic wall thrust (no seismic buffer)

5.3.4.3 Effect of peak ground acceleration (*PGA*) on the dynamic earth pressures

In this section, performance of seismic buffers in relation to the peak acceleration amplitude was discussed. In Figure 5-26, lateral dynamic earth pressure profiles on type-C wall model for base motion having PGA=0.6g and f_{exc}=5Hz is depicted. Test data were compared with the pressure profile estimated using Steedman and Zeng Approach (1991). The initial static earth pressure distributions are provided for comparison purposes. It was observed that the dynamic earth pressures (p_{ae}) in the absence of compressible inclusions are significantly higher than those observed when geofoam material is present. In all the cases, stress profiles estimated using Steedman-Zeng Approach are higher than stresses observed in the physical tests. Comparison of maximum lateral dynamic earth thrust (P_{ae}) and bending moment (M_{ae}) calculated by the integration of the lateral stresses are depicted in Figure 5-27(a) and (b).

An increasing trend was observed in all the tests. Presence of geofoam provides various amounts of reduction in dynamic earth thrust depending on the thickness and relative stiffness of the inclusion. Best performance in reducing the lateral dynamic force is exhibited by EPS-15 inclusion with t/H=0.14 since the E_{inc}/t_{inc} ratio is smallest for this inclusion type (E_{inc} *is the elastic modulus and* t_{inc} *is the thickness of the buffer)*. Dynamic earth stresses and the dynamic thrust reduction efficiency ($i_{\Delta p}$) are provided in Figure 5-28(a) and (b). EPS-15 inclusions reduce the dynamic thrust between 20% and 60% depending on magnitude of base motion. The discrepancy between $i_{\Delta p}$ values are not more than 10% for twofold increase in buffer thickness. This discrepancy is even negligible for XPS-22 inclusion type which exhibits the poorest performance in reducing Δp_{dyn} values.

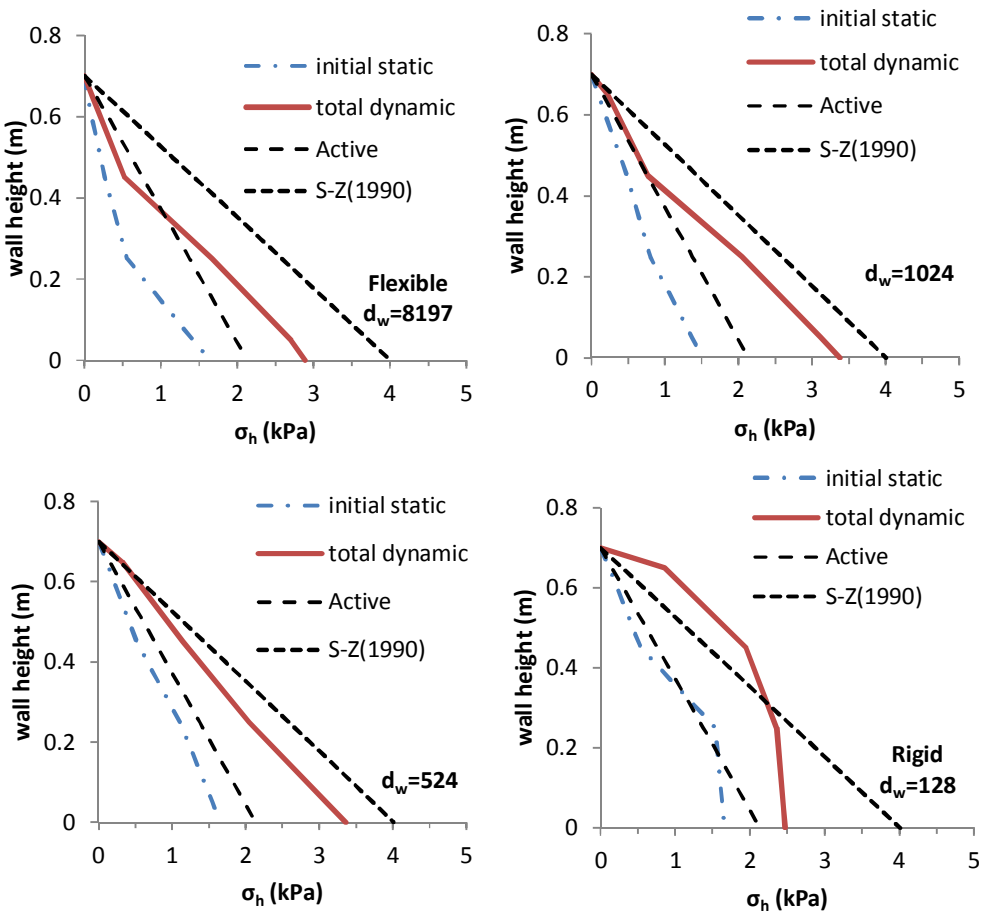

Figure 5-23 Total pressure profiles leading to peak dynamic wall thrust (EPS-15, t/H=0.07)

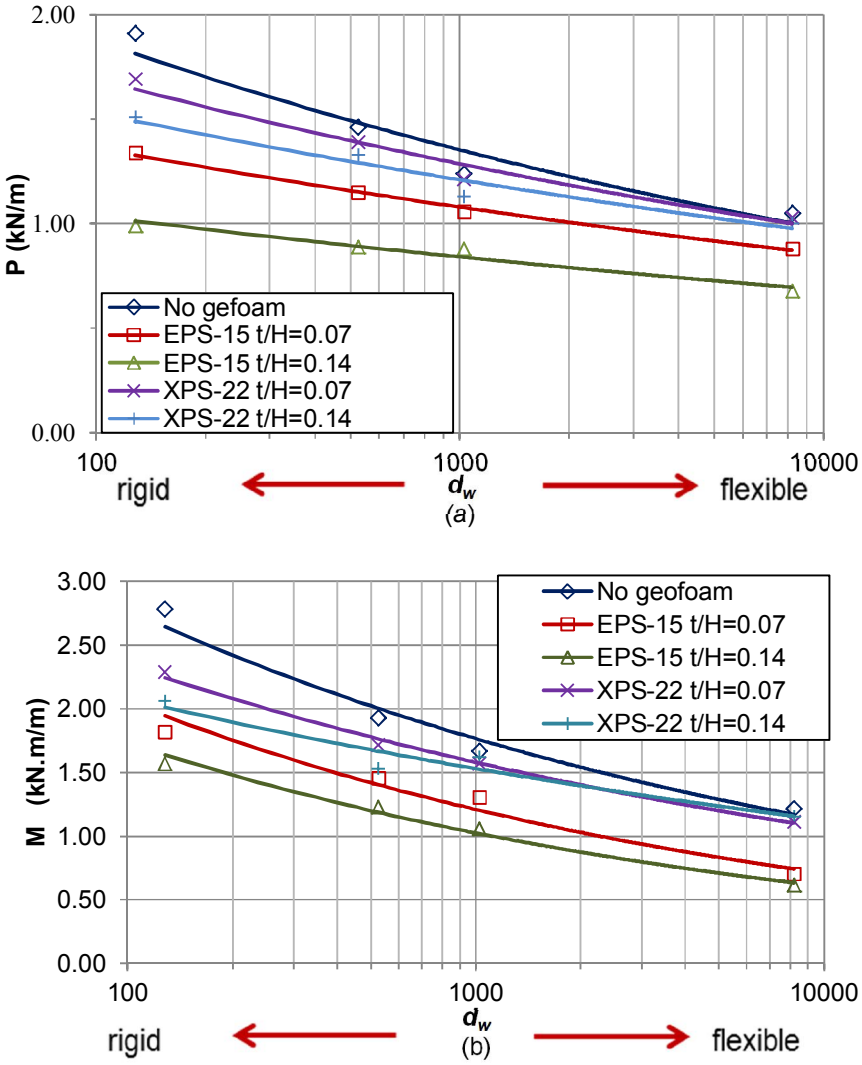

Figure 5-24 (a) Dynamic wall thrust (b) Bending moments in relation to d_w

5.3.4.4 Effect of f/f_n on the dynamic earth pressures

In this section, the effect of the excitation frequency on the dynamic stresses on the wall models was discussed. The frequency ratios (f/f_n) varied between 0.13 and 0.32 where f is the base excitation frequency and f_n is the first fundamental frequency of the wall-backfill system estimated in Section 5.3.3.1. Total dynamic earth pressure profiles on type-C wall model excited with PGA=0.3g and f_{exc}=7.7Hz are depicted in Figure 5-29. For this PGA and f_{exc} combination, dynamic lateral stresses (p_{ae}) obtained in the tests are in good agreement with estimations of Steedman-Zeng approach for walls without buffer. Presence of buffer reduces

p_{ae} values as expected. Comparison of the maximum total dynamic earth thrust (P_{ae}) and bending moment at base level (M_{ae}) are depicted in Figure 5-30(a) and (b). A nonlinearly increasing trend in P_{ae} and M_{ae} is observed with increasing f/f_n ratio. Dynamic thrust reduction efficiency ($i_{\Delta p}$) for various buffer types are provided in Figure 5-31. Positive effect of XPS-22 buffers is not more than 5% for the investigated f/f_n range since the stiffness of this type geofoam is relatively higher than the stiffness of EPS-15 geofoam. The effect of thickness is more pronounced for EPS-15 buffers. Positive contribution of two fold increase in thickness of EPS-15 type geofoam buffer may reach up to 20%.

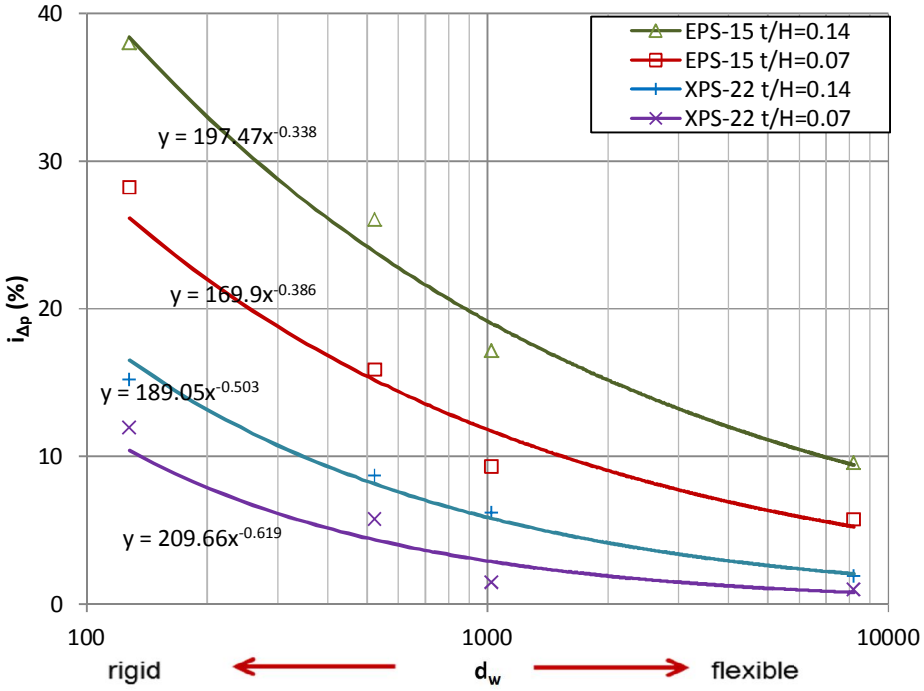

Figure 5-25 Dynamic load isolation efficiency vs. wall flexibility (d_w)

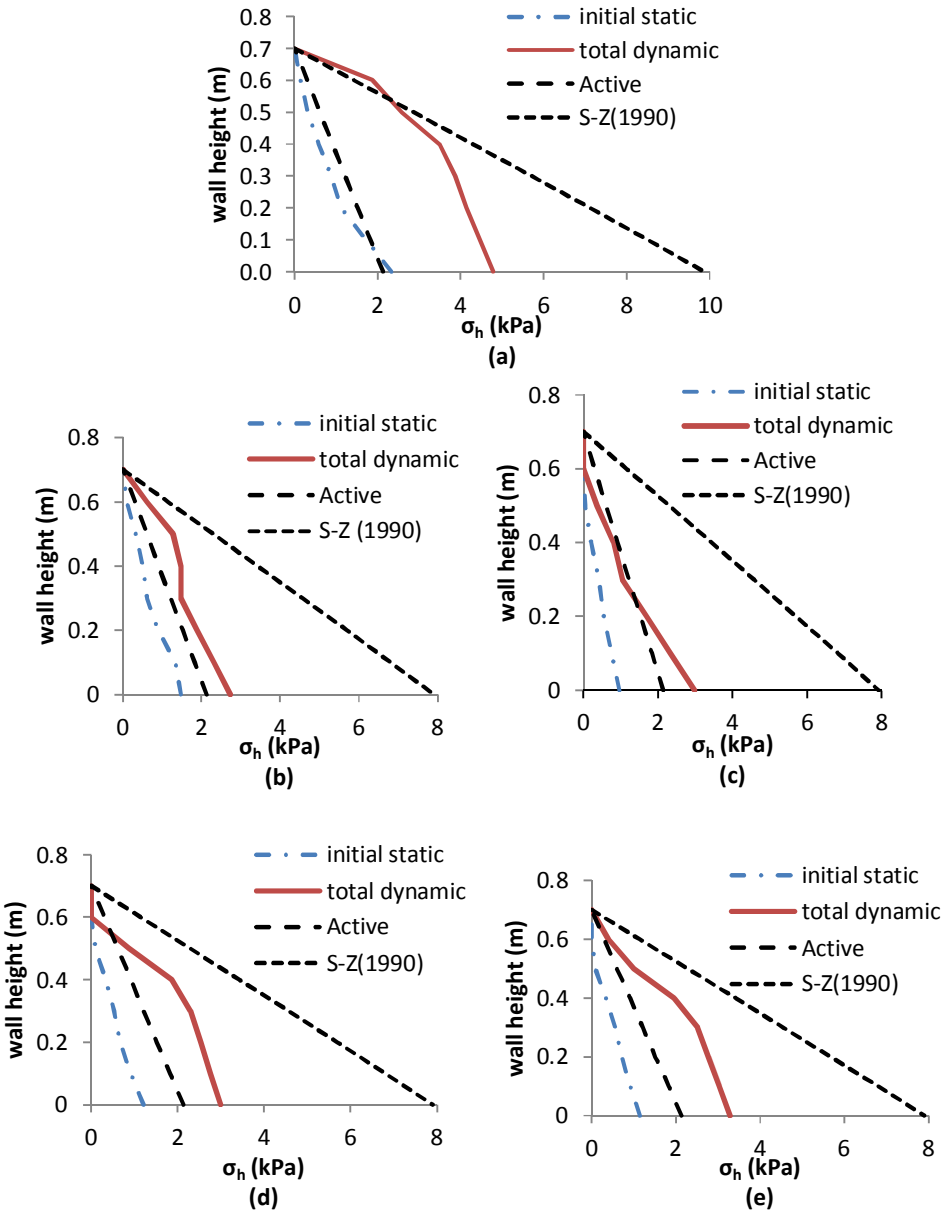

Figure 5-26 Pressure profiles leading to peak dynamic wall thrust for various deformable buffer types (PGA=0.6g, f_{exc}=5Hz) (a) No geofoam (b) EPS-15 t/H=0.07 (c) EPS-15 t/H=0.14 (d) XPS-22 t/H=0.07 (e) XPS-22 t/H=0.14

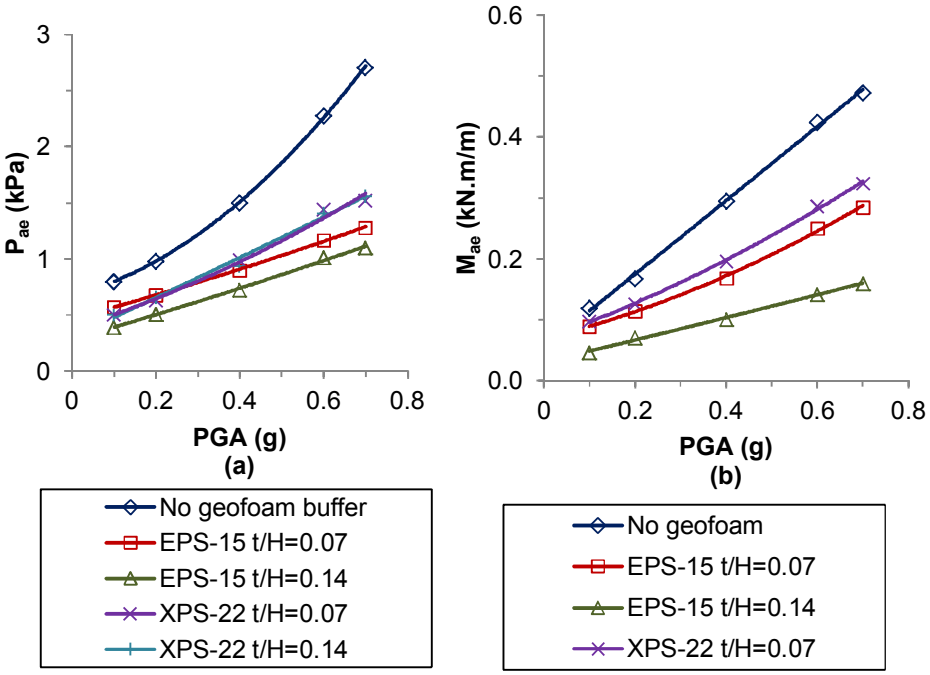

Figure 5-27 (a) Dynamic wall thrust (b) Bending moments

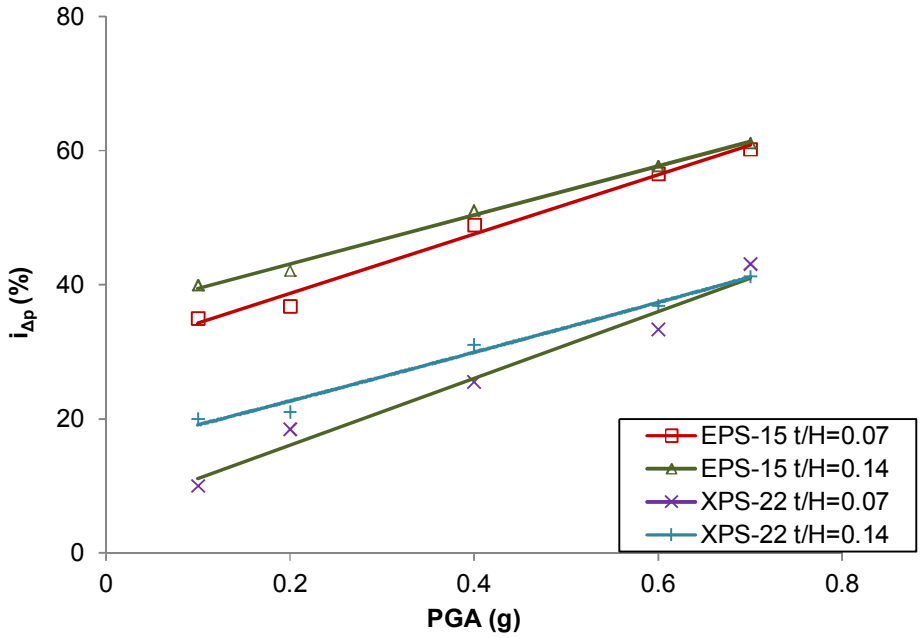

Figure 5-28 Dynamic force reduction efficiency vs. PGA

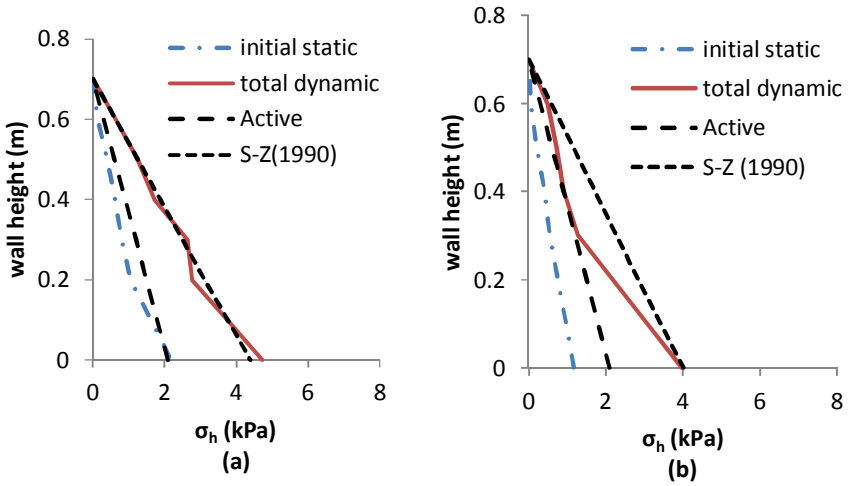

Figure 5-29 Pressure profiles leading to peak dynamic wall thrust for various compressible inclusion types (*PGA*=0.3g, *f*=7.7Hz) (a) No geofoam (b) EPS-15 *t/H*=0.14

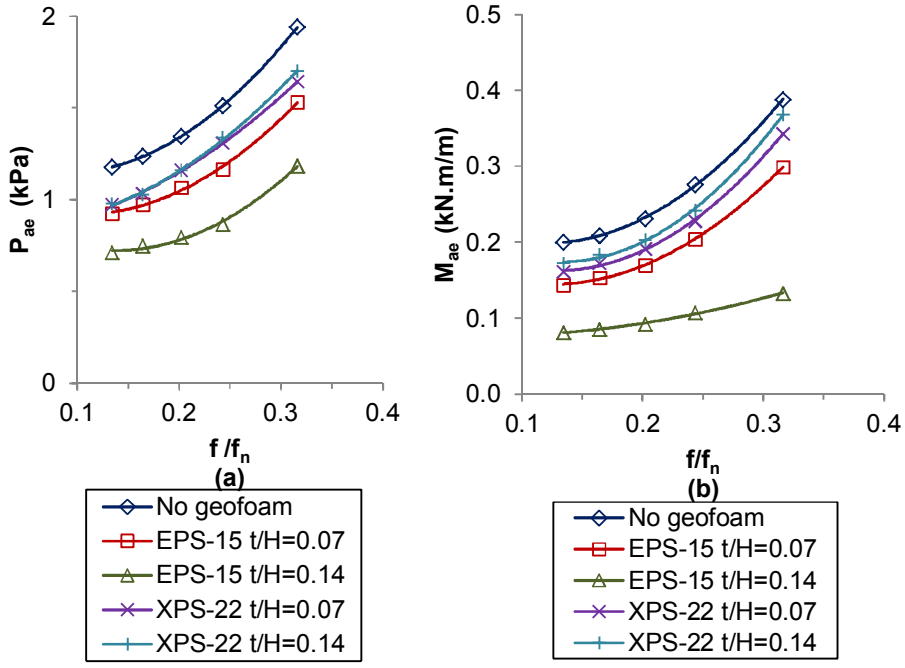

Figure 5-30 (a) Total dynamic wall thrust vs f/f_n (b) Bending moments vs f/f_n

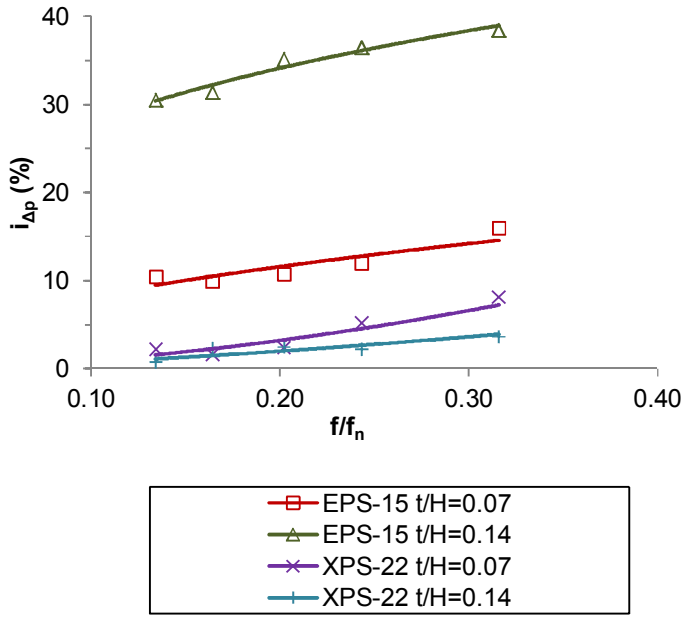

Figure 5-31 Dynamic force reduction efficiency vs f/f_n

5.3.5 Seismic earth pressure coefficients (K_{ae})

Seismic lateral earth pressure coefficients $(K_{ae})_{exp}$ were back-calculated based on lateral stresses measured during physical tests. The lateral seismic earth pressure coefficients $(K_{ae})_{exp}$ are calculated by Eq.5-12:

$$(K_{ae})_{exp} = \frac{2}{\gamma H^2}\int_0^H \sigma_x dz \qquad 5\text{-}12$$

where H is the wall height, γ is the backfill unit weight and σ_x is the lateral earth pressure (total) at depth (z). Variation of back-calculated K_{ae} values in relation to PGA was depicted in Figure 5-32. Increasing excitation amplitude causes an approximately linear increase in the seismic earth pressure coefficients. A comparison of $(K_{ae})_{exp}$ values with those calculated from Mononobe-Okabe and Steedman-Zeng methods indicated that back calculated values are found to be lower compared to the estimations made using analytical methods. Presence of deformable buffers lead to further decrease in $(K_{ae})_{exp}$ depending on the relative buffer stiffness.

Further comparisons were made between back-calculated K_{ae} values and estimations of analytical methods for various frequency ratios (f/f_n) and relative flexibility values of the wall(d_w). For the investigated f/f_n range, the contribution of

the geofoam buffer in reducing earth pressure coefficients was clearly exhibited (Figure 5-33). The influence of wall flexibility on K_{ae} values were depicted in Figure 5-34. EPS-15 type buffer with t/H=0.14 provides the lowest values of $(K_{ae})_{exp}$ due to the low relative stiffness of the buffer. The effect of the presence of geofoam buffer is more prominent for stiffer walls (lower d_w), however this trend is less pronounced as the wall flexibility increases. Approximately 50% decrease was observed in $(K_{ae})_{exp}$ values by using an EPS-15 type buffer (t/H=0.14) for the wall model with d_w=128. The same geofoam buffer provides 33% decrease in $(K_{ae})_{exp}$ for the wall model with d_w=8197.

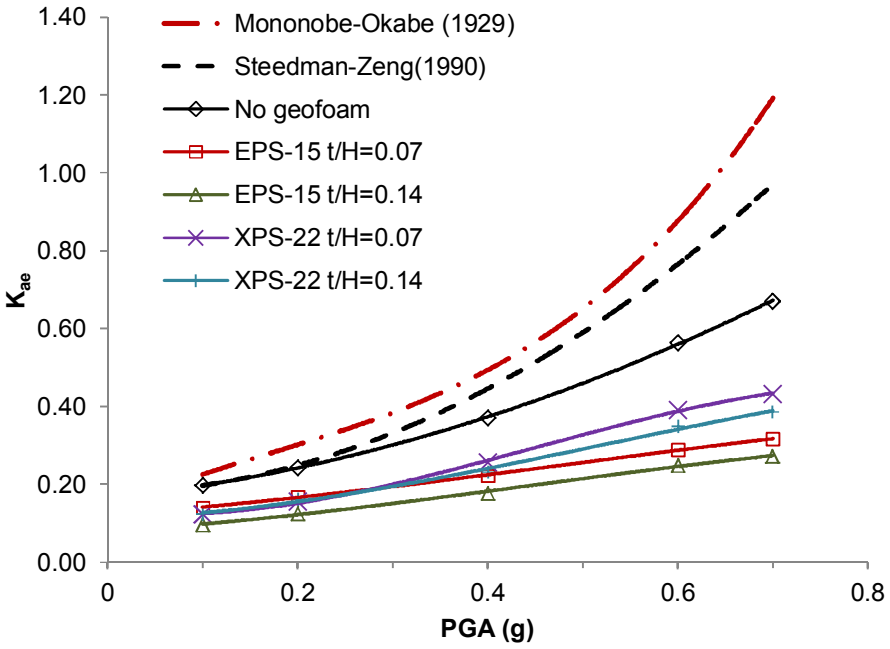

Figure 5-32 Variation of dynamic earth pressure coefficient (K_{ae}) with PGA (f=4.25Hz)

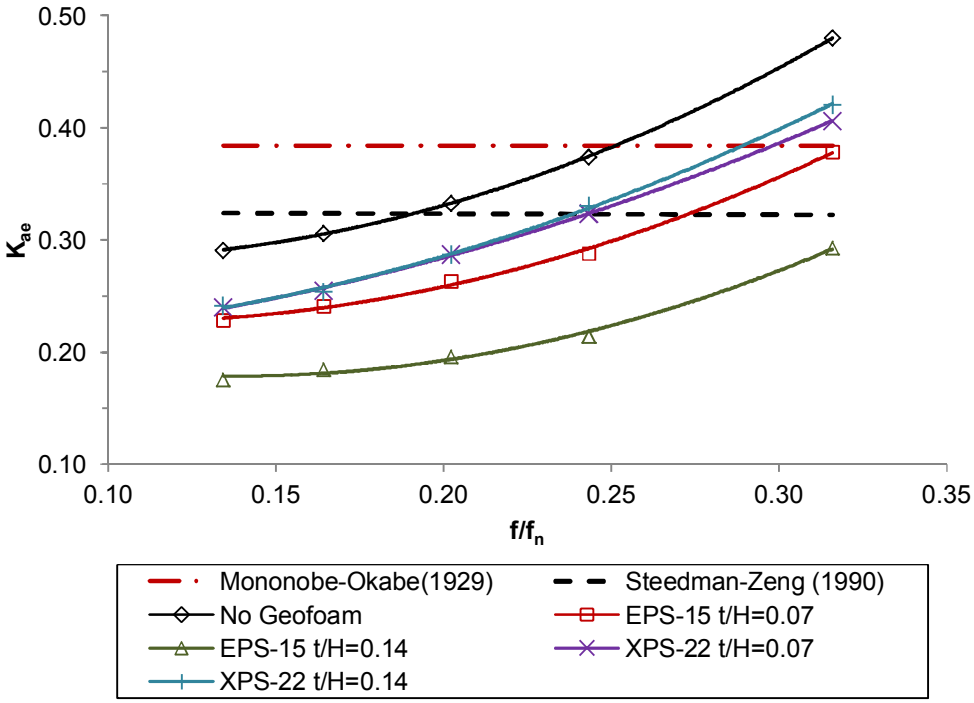

Figure 5-33 Variation of dynamic earth pressure coefficient (K_{ae}) with f/f_n (PGA=0.3g)

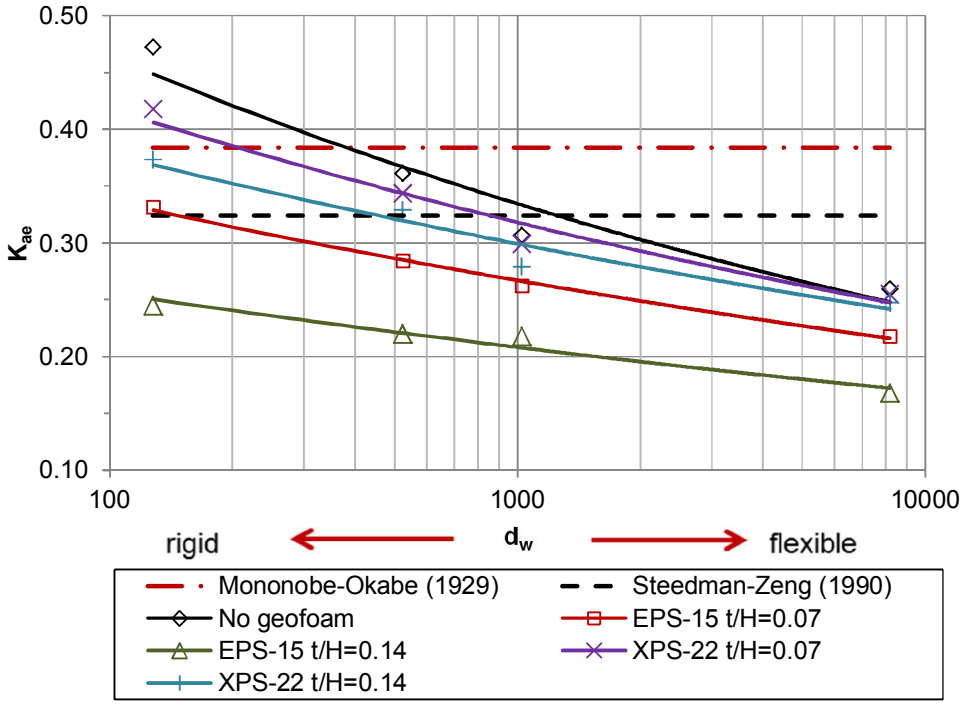

Figure 5-34 Variation of dynamic earth pressure coefficient (K_{ae}) with d_w (for base motion f=4.25Hz, PGA=0.3g)

5.3.6 Application point of the seismic thrust

The position of the application point (h_d) for the maximum total thrust does not show significant variation. The value of h_d is observed to be between 0.40*H* to 0.60*H* *(measured from the base)* depending on the excitation amplitude, frequency, and type of geofoam buffers. In Figure 5-35, variation of h_d/H ratio is depicted for different excitation characteristics and seismic buffer types. A slight increase occurs in the position of the application point with increasing frequency ratio and excitation amplitude. For the investigated acceleration amplitude range, values calculated by M-O Method are in good agreement with test results and they capture the general trend observed in the tests; however this method does not take into consideration of the influence of excitation frequency on the response of the retaining walls. Steedman-Zeng approach provides more reasonable estimates of the behavior for different excitation frequencies. The estimations of the analytical methods are generally satisfactory. However, attention should be paid to the limitations of the analytical approaches.

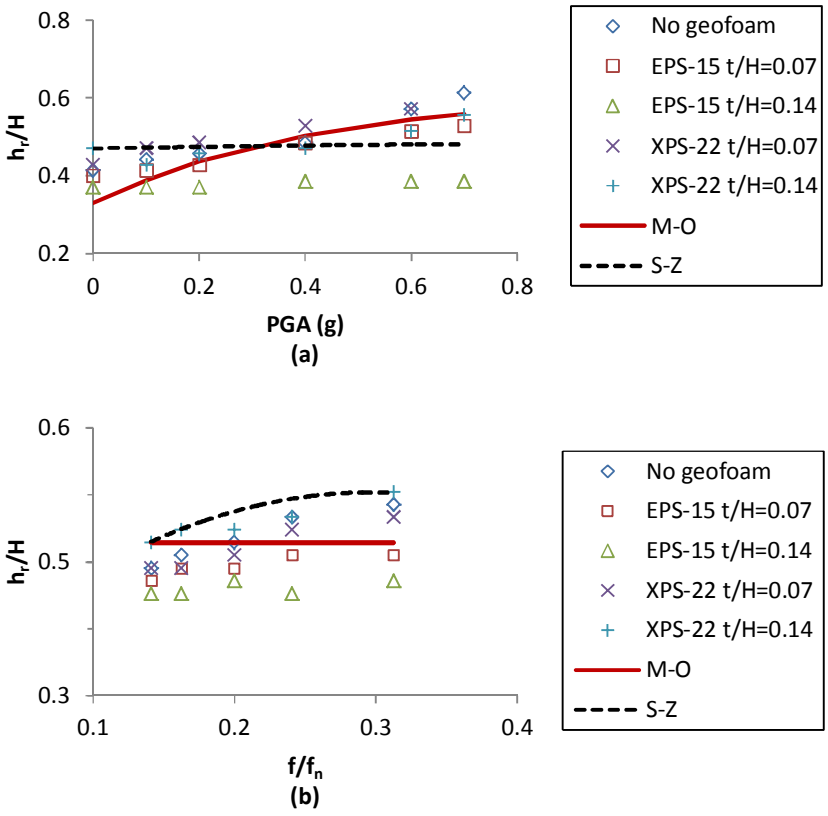

Figure 5-35 Location of maximum thrust (a) in relation to *PGA (for f=4.25Hz)* (b) in relation to frequency ratio (f/f_n) (for *PGA*=0.3g)

5.3.7 Base pressures

Base pressures were monitored by load cells mounted at the toe and heel side of the steel wall base. The evolution of the base pressures were observed simultaneously for the toe and heel side during the dynamic phase of the tests. Maximum vertical pressure occurs at the toe side while minimum base pressure develops under the heel at the same instant during the dynamic phase.

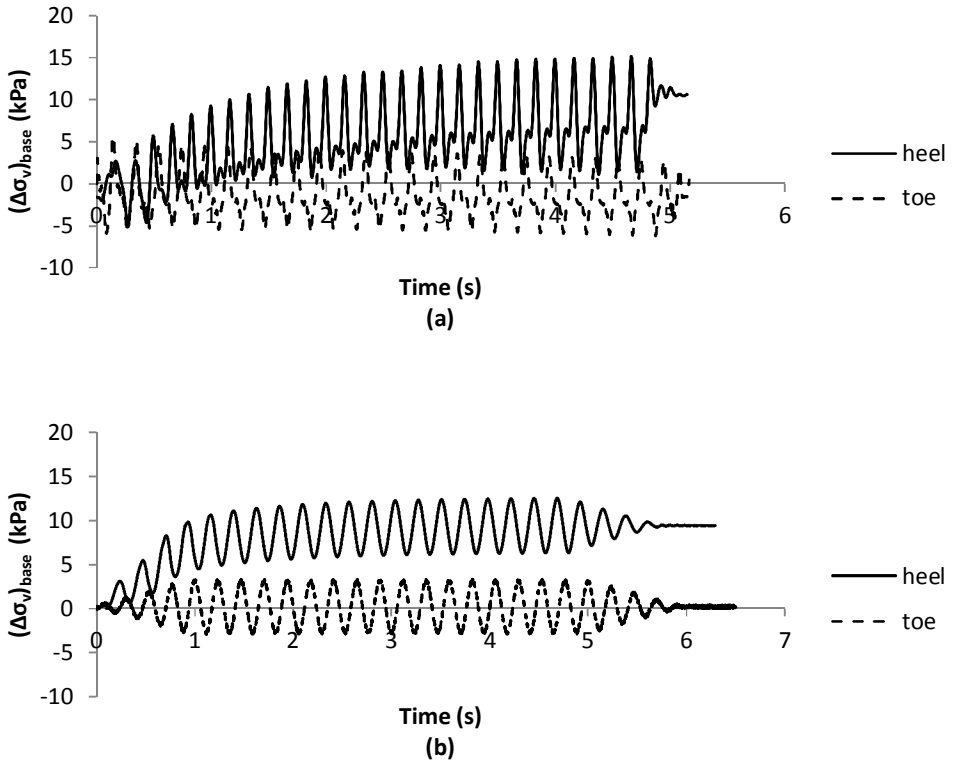

Figure 5-36 (a) Evolution of base pressure for CW-C8 test (No geofoam inclusion) (b) CW-CED8 test (EPS-15 t/H=0.14)

The flexibility of the wall has a significant effect on the observed base pressures. Dynamic excitations of the most flexible (Type-A) wall model (d_w=*8192*) caused the lowest incremental dynamic stresses at the wall base (Figure 5-37). In all the tests, $(\Delta\sigma_v)_{base}$ at the heel of the wall base was comparatively higher than those observed at the toe of the wall base. Presence of geofoam buffers provided reductions in the base pressures at varying amounts depending on the stiffness and the thickness of the inclusion (Figure 5-38). Geofoam seismic buffers having the lowest E_{inc}/t_{inc} ratio provide the highest reduction in the dynamic base pressures. At the end of dynamic phase, permanent vertical pressures

accumulate at the toe side (Figure 5-36). The amount of stress accumulation depends on the magnitude of the base excitation.

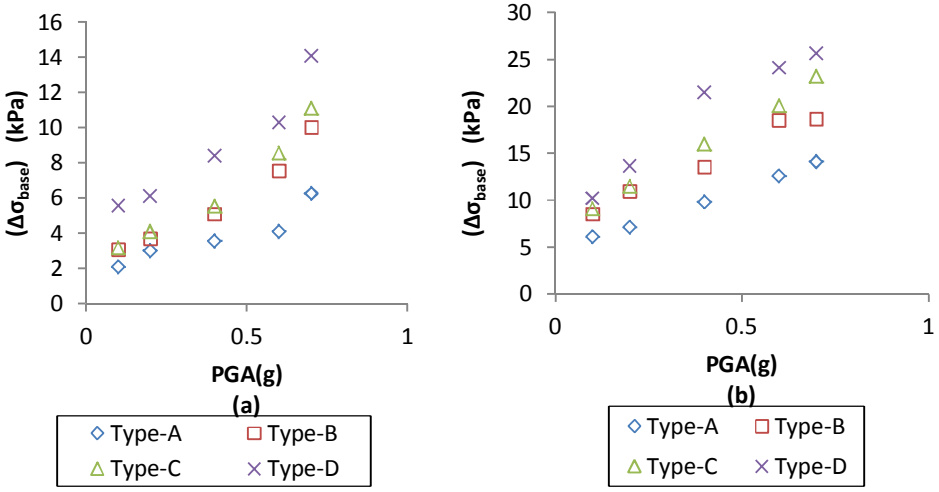

Figure 5-37 Dynamic incremental base pressures for wall models without geofoam inclusions (a) Toe pressures (b) Heel pressures

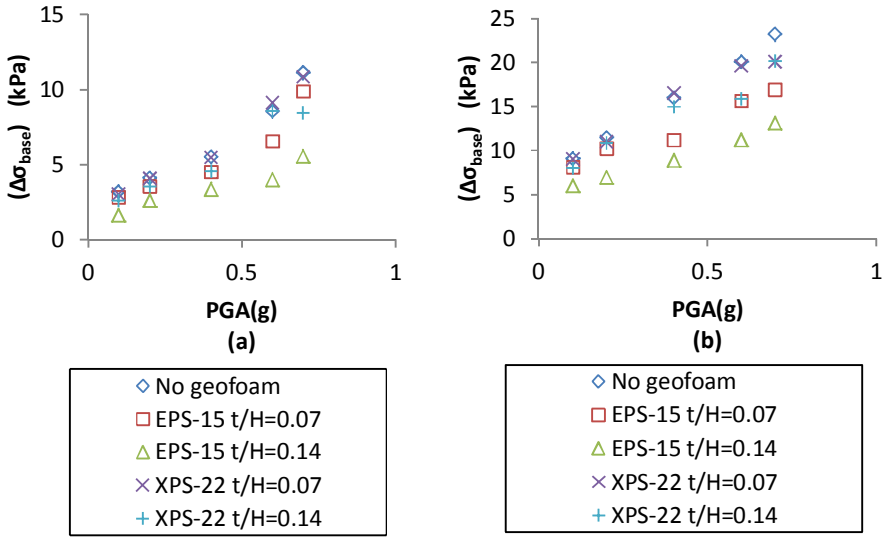

Figure 5-38 Dynamic incremental base pressures for wall models with geofoam inclusions (a) Toe pressures (b) Heel pressures

5.3.8 Backfill settlements

Settlements were observed in the backfill at the end of each test due to vibrational densification (Figure 5-39). Amount of settlement was measured at the end of

each test by using rulers placed at various positions of the test container. Magnitude and frequency of the applied base excitations as well as flexibility of the wall affected settlements through the backfill. Maximum settlements of approximately 60mm were observed in tests where Type-A walls were subjected to base excitations having 0.3g amplitude with 10Hz frequency.

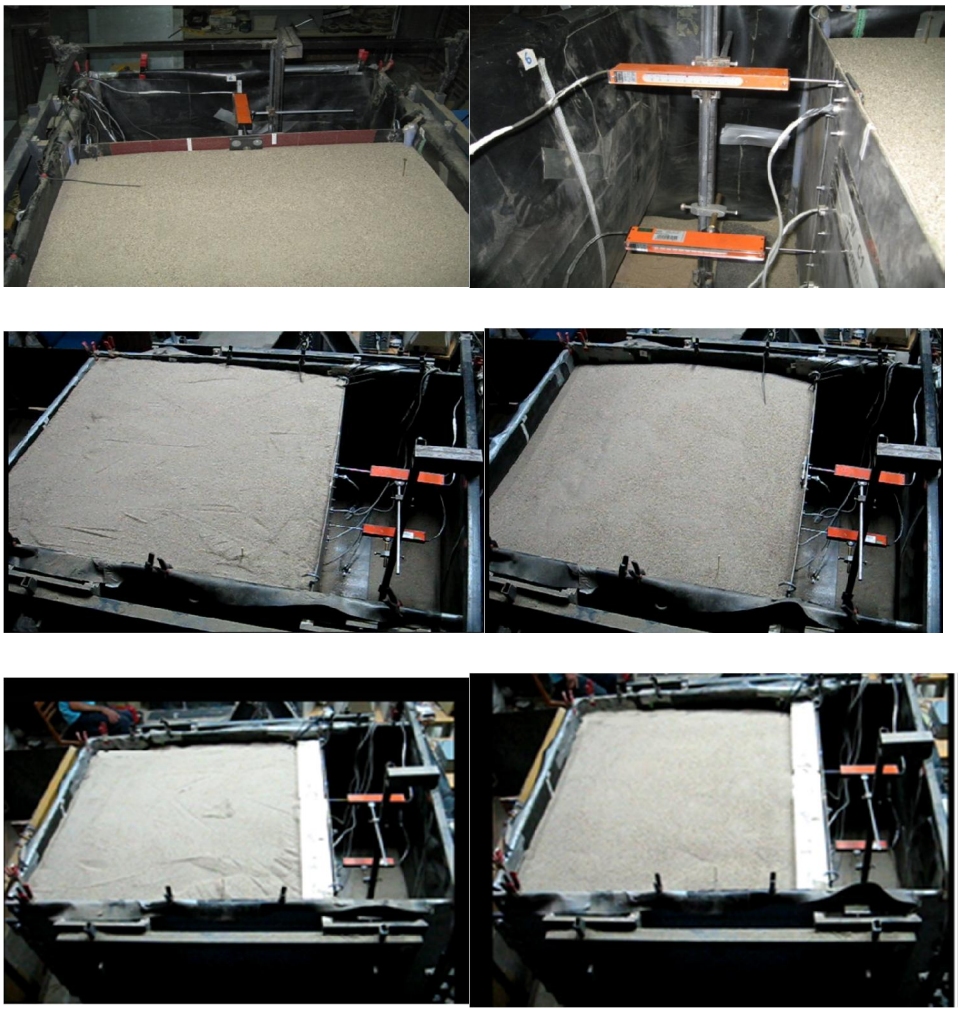

Figure 5-39 Settlements in the backfill at the end of dynamic excitations (a) CW-C8 (No geofoam inclusion) (b) Another view of CW-C8 test set-up (No geofoam inclusion) (c) CW-CED8 test set-up

CHAPTER 6

NUMERICAL MODELING

6.1 General

The physical model tests with shake table demonstrate the behavior of the small scale system with good accuracy. However it replicates a limited portion of the investigated problem. Various boundary conditions and dimensions may result in significant differences in the observed response. On the other hand, numerical modeling technique attempts to replicate the physical system and interactions with mathematical relationships. Use of numerical simulation techniques in conjunction with experimental modeling provides valuable insight towards a better understanding of the interaction mechanism between the retaining structure, compressible geofoam inclusion, and retained backfill for this study. Initiated on this motive, a series of numerical simulations were performed using the general finite difference method software named FLAC 2D v6.0 (Fast Lagrangian Analysis of Continua) (Itasca, 2008). The outcomes provided insight regarding the influence of parameters such as buffer stiffness and thickness on the static and dynamic response of retaining walls.

In the numerical analyses, significant emphasis is given to make an insight into the behavior of wall-buffer-backfill system and magnitude of the wall displacements, earth pressures and accelerations. Development and implementation of advanced constitutive models for the soil and geofoam is not within the scope of this study.

6.2 Fundamentals of FLAC

FLAC 6.0 is a two dimensional explicit finite difference code used for simulating static and dynamic behavior of geotechnical structures composed of soil, rock, concrete and other geomaterials. FLAC uses an explicit, time-marching method to

solve algebraic equations. Stresses and forces acting on a finite difference grid are used with the equation of motion to determine velocities and displacements in a circular fashion.

In the finite difference method, every derivate which occurs in the governing equation is replaced by an algebraic equation written in terms of field variables such as stress and displacement at discrete points in the space. Contrary to the implicit, matrix oriented methods such as finite element method; global stiffness matrices are not created or updated in the finite difference algorithms. The general calculation procedure of FLAC is illustrated in Figure 6-1 (Itasca, 2008). In the first step, equations of motion are invoked to derive new velocities and displacements from stresses and forces. As the second phase, the strain rates are derived from velocities and new stresses from the strain rates. One time step is taken for every cycle around the loop. In each box depicted in Figure 6-1, all the grid variables are updated from their known values while the control of the numerical algorithm is in that box. Each cycle occurs in short time increments which prevents any physical disturbance to be transmitted from one element to the other during the cycle. This provides stability to the finite difference scheme even for physically unstable structures. There are several advantages of explicit numerical methods. No iterations are required when computing stresses in elements, even non-linear constitutive models are implemented to the numerical scheme. However, in implicit methods such as finite element method, every element communicates with each other during each time step. Several iterations are required to satisfy compatibility and equilibrium equations depending on the non-linearity of the constitute model. The global stiffness matrices are formed and updated at each time step. However, FLAC uses Lagrangian Analysis where global stiffness matrix is not needed. Explicit methods are more efficient in modeling nonlinear problems involving large strain and physical instability conditions.

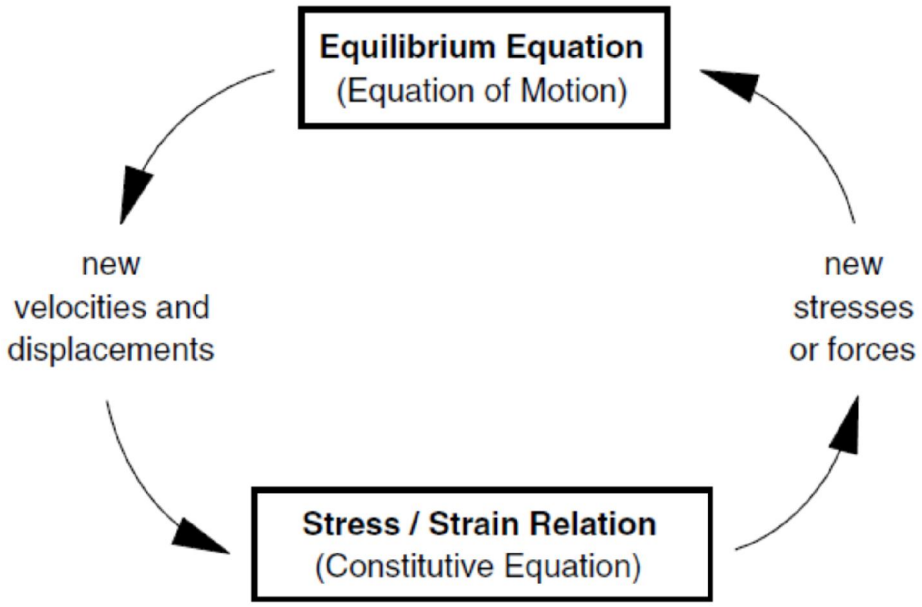

Figure 6-1 Calculation cycle of FLAC (Itasca, 2008)

6.3 Model development and description of the wall-geofoam-soil system

In the finite difference method, grid is considered as the basis of the numerical model since the number of nodes used to simulate the physical system is determined by the grid. Density of grid increases the accuracy of the finite difference calculations however increasing grid density leads to increasing computational effort. Considering these factors, sensitivity analyses were performed to investigate the effect of grid density on the static and dynamic response of the retaining wall model. The grid density was selected to achieve sufficient accuracy and affordable calculation time.

In numerical modeling of the static and dynamic response of the model retaining wall, several assumptions and idealizations were made. The assumptions of the numerical model are as follows:

1. Two dimensional plane strain model is established.
2. Backfill material behaves elasto-plastic and yield condition is modeled with Mohr-Coulomb failure criterion
3. Geofoam buffer behaves linear elastic since expected stresses acting on the geofoam buffer are lower than the yield strength of the geofoam types used in the physical modeling study (Refer to Section 4.9).

4. Retaining wall is idealized with beam elements characterized by linear elastic model.
5. Elastic parameters of the geo-materials were calculated based on static and cyclic triaxial test results. (Refer to Sections 4.8.3 and 4.9)
6. Base excitations were applied as a velocity time history at the base of the whole model.
7. Absorbent boundary conditions were defined at the left and right boundaries of the geometry to reduce the influence of wave reflections in the observed response.

Finite difference model of the physical test set-up (Figure 6-2) consisted of 0.7m high wall-backfill system and 0.2m thick underlying foundation soil layer. The basic grid for the soil was composed of 100mm square cells. To represent the 2.0m long by and 0.9m high geometry, twenty horizontal and nine vertical cells were used. The model consists of four subgrids:

a. The backfill
b. The geofoam buffer
c. The foundation soil layer
d. The left side subgrid (required to apply absorbent boundary conditions to the lateral edge of the model because these boundary types cannot be applied across the interface of two grids.)

Each of the subgrids was attached at their contact surfaces. In addition to the subgrids mentioned above, cantilever wall stem and base is defined by beam elements characterized by linear elastic material behavior.

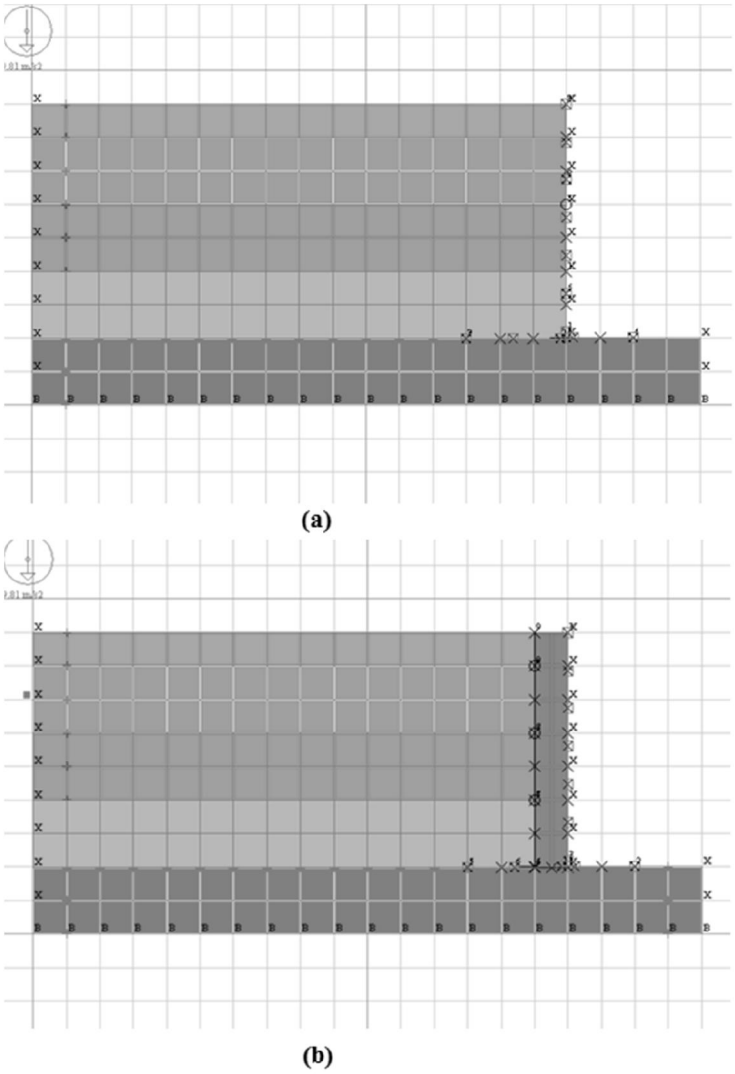

Figure 6-2 FLAC grid for the model retaining wall (a) No geofoam buffer (b) With geofoam buffer (t/H=0.07)

To avoid numerical distortion of the propagating waves and enable accurate calculation of the model response, proper dimensioning of the finite difference zones are required. Itasca (2008) recommends use of elements having length smaller than one tenth to one eight of the wavelength associated with the highest frequency component of the input motion:

$$\Delta l \leq {}^{\lambda}/_{10} \quad \text{6-1}$$

$$\lambda = {}^{v_s}/_{f} \quad \text{6-2}$$

$$f_{max} \leq {v_s}/{10.\Delta l} \quad \text{6-3}$$

where v_s is the shear wave velocity, λ is the wavelength, f_{max} is the highest frequency component of the input motion and Δl is the element length. Considering the v_s of the cohesionless material as 100m/s, current finite difference model should adequately propagate shear waves with frequencies of up to 100Hz according to Eq.6-3.

6.3.1 Interfaces

Without use of interfaces, the adjacent finite difference cells do not possess the ability to slip and separate since any cells with a common contact will always touch along their face. Hence, interfaces are placed at the contacts of structural elements and the geomaterials. In the analyses, zero thickness slip and separation interfaces were placed between the contact surfaces. A friction angle was defined whereas the cohesion was set close to zero to enable separation of the two subgrids. A friction angle of 15° was taken which is consistent with the results of direct shear tests performed to determine the friction angle between the geofoam and cohesionless backfill. The normal and shear modulus values of the interface were taken as ten times of the adjacent soil stiffness which is consistent with the recommendations of FLAC (Itasca, 2008). The elastic material properties do not possess any physical meaning for the interface modeling, however proper values should be taken to provide numerical stability in the finite difference calculations.

The analyses consisted of incremental placement of the backfill where geostatic pressure conditions are achieved while the static displacements or deflections occur in the wall stem (Figure 6-3). This phase is followed by dynamic analysis wherein the identical base motions of the physical model tests were applied at the base of the finite difference model.

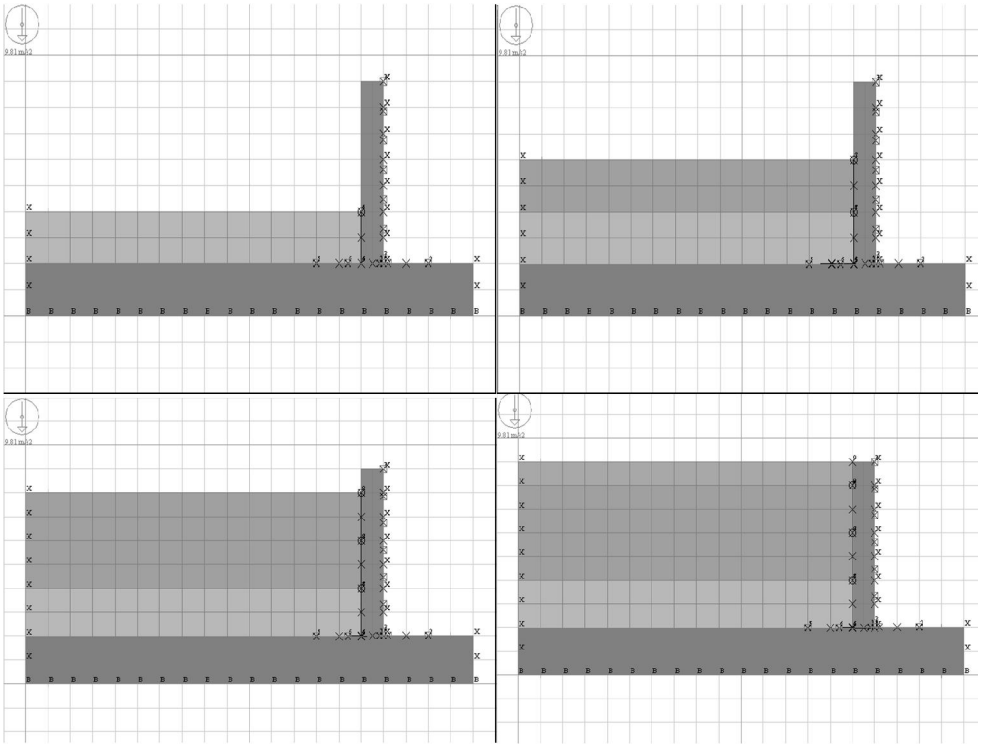

Figure 6-3 Simulation of the backfilling sequence

6.3.2 Boundary conditions for the static case

For the static phase of the simulation, the boundary conditions involve restrained horizontal and vertical displacements along the bottom horizontal boundary and restrained horizontal displacement along the vertical boundary on the backfill side. In the first four stages of the static phase where the backfilling process were simulated, the retaining wall was kept fixed in the horizontal direction. In the fifth stage of the static phase, the horizontal fixity on the wall stem was removed to simulate the yielding of the wall due to lateral earth forces.

6.3.3 Boundary conditions for the dynamic phase

In FLAC, the dynamic input can be applied in one of the following ways:

(a) An acceleration time history;

(b) A velocity time history;

(c) A stress (or pressure) time history; or

(d) A force time history.

Due to the numerical scheme of FLAC, velocity time history provided a repeatable method to achieve a given acceleration time history (Gaskin 2000). To replicate the acceleration time history of the base motion applied in the physical tests, a harmonic velocity time history with constant amplitude and frequency was defined as an input for the finite difference model. Gradually increasing and decreasing type motions were applied to avoid the effect of high frequency components of the motion during the initiation of the dynamic phase. A fish function was written to create this velocity time history which would be applied to the base of the model (Appendix F).

In dynamic problems, ordinary static boundary conditions cause reflection of the outward propagating waves back into the geometry. However, absorption of the energy is required to simulate the free-field conditions. The use of a larger model may solve the problem since most of the reflection waves are absorbed by the material damping, however computational time significantly increases. The viscous boundaries developed by Lysmer and Kuhlmeyer (1969) are utilized in FLAC to absorb radiation energy. Silent viscous boundaries operate in the time domain and based on the use of independent dashpots in the normal and shear directions applied at the model boundaries. The normal and tangential dashpots forming the viscous boundaries are characterized by Eq.s 6-4 and 6-5.

$$t_n = -\rho C_p V_n \quad \text{6-4}$$

$$t_s = -\rho C_s V_s \quad \text{6-5}$$

Where ρ is material density, C_p and C_s are the compression and shear wave velocities, V_n and V_s are the velocities in the normal and the tangential directions at the boundary. FLAC manual (Itasca 2008) states that a silent boundary is effective in absorbing the propagating waves arriving at angles of incidence larger than 30°. Silent boundaries were invoked along the left and right boundaries prior to the application of dynamic excitation.

In FLAC, size of the time step is governed by the frequency content of the loading and the stiffness of the materials involved in the analyses. Frequency content of the motion should be limited to lower frequencies and sudden displacements and high frequency vibrations should be avoided (Gaskin 2000). In FLAC, maximum stable timestep for dynamic analysis is determined by the largest material stiffness. The stiffness of the elements in a finite difference model can show wide

variations if stiff structural elements such as reinforced concrete walls, piles, reinforced concrete foundations etc. are involved in the analyses. Even though the major portion of the model involves geomaterials which have lower stiffness compared to structural elements, a few zones with high stiffness may determine the critical time step of the analyses. To overcome this problem, a procedure known as dynamic multi-stepping was introduced in FLAC. This procedure reduces the computational time required for the dynamic computations by classifying the zones and grid points having similar critical time steps. Each zone is calculated at its specific time step and information is transferred between adjacent zones. This procedure was also applied in the current numerical study to reduce the runtimes.

6.3.4 Model parameters

In the numerical analyses, cohesionless backfill and foundation layer were treated as isotropic elasto-plastic materials characterized by Mohr-Coulomb yield function, which behaves elastic below the yield surface and plastic for states of stress above the yield surface. The internal angle of friction (Φ) and dilatancy angle (ψ) were selected based on the triaxial compression test results aforementioned in Sections 4.8.3 and 4.9. The static secant modulus (E_{50}) corresponding to the 50% of the deviator stress at yield was determined as 5200kPa for the cohesionless backfill. The observed value of the secant modulus is very low due to small confining stress. The geofoam and the wall model were treated as linear-elastic considering the stress range of the model tests. Since the stress levels in the model tests are lower than the yield stress of the geofoam used in this study, linear elastic assumption should provide a sufficient approximation of the material behavior. The Young's moduli describing the linear elastic portion of the EPS-15 and XPS-22 geofoam were taken as 1500kPa and 5000kPa respectively. A summary of the model parameters for the geomaterials were indicated in Table 6-1. Cantilever wall stem and base is defined by beam elements characterized by linear elastic material behavior with properties indicated in Table 6-2. Dynamic properties of the geomaterials were calculated based on the cyclic triaxial test results. The average E_{sec} for the backfill was taken as 19500kPa according to Table 4-13. Similarly, E_{sec} values were taken as 3000kPa and 6875kPa for EPS-15 and XPS-22 geofoam, respectively (Refer to Table 4-19 and Table 4-20).

Table 6-1 Constitutive model properties for the geomaterials for the static phase of finite difference modeling

Parameter	*Backfill*	*Foundation*	*EPS-15*	*XPS-22*
Model	M-Coulomb	M-Coulomb	Linear Elastic	Linear Elastic
Unit Weight (γ)	16.50	17.50	0.15	0.22
Young's	5200	5500	1500	5000
Poisson's Ratio	0.33	0.33	0.01	0.01
Cohesion (c)	0	0	---	---
Friction angle	43.5	45.0	---	---
Dilatancy Angle	22.5	22.5	---	---

Table 6-2 Elastic properties for the flexible wall

Property	*Wall Stem*	*Wall Base*
Unit Weight (γ) [kN/ m^3]	78	78
Thickness (t_w) [mm]	5	8
Young's Modulus (E) [kPa]	1.61×10^{8}	1.61×10^{8}
Moment of Inertia (I) [m^4]	1.041×10^{-8}	4.266×10^{-8}

6.4 Damping

The use of elasto-plastic constitutive model in conjunction with Mohr-Coulomb failure criterion introduces the following hysteretic damping into the system (Itasca, 2008) :

$$D = \frac{2}{\pi}\left[1 - \frac{G}{G_{max}}\right] \qquad 6\text{-}6$$

where D is the hysteretic damping, G is the secant shear modulus and G_{max} is the small strain value of the shear modulus. According to this formula, plastic deformation of the elasto-plastic material introduces hysteretic damping to the system up to $D=2/\pi$. However, damping is zero when shear strain of the material is not exceeded.

The sudden change of material stiffness as discussed previously causes distortions in the response of model. These fluctuations are generally reduced by introducing Rayleigh damping to the system. Although, contribution of the hysteretic damping is sufficient to take into account of the material damping, it is common to apply additional Rayleigh damping to the system (Finn, 1988).

In this study, damping of the geomaterials was taken into account by frequency dependent Rayleigh damping explained in FLAC manual (Itasca, 2008). Rayleigh damping (c) has two components as shown in Eq.6-7:

$$C = \alpha M + \beta K \qquad 6\text{-}7$$

where α and β are the mass-proportional and stiffness-proportional damping constants, respectively, M is the mass matrix and K is the stiffness matrix. FLAC (Itasca 2008) lets users to define the mass and stiffness dependent constants individually or as a sum of the both components. Frequency dependent component is more dominant at lower frequencies whereas mass proportional coefficient provides damping at higher frequencies of the system. By a proper selection of α and β coefficients, a frequency dependent damping response is provided in a limited frequency range around the natural frequency of the finite difference model. Based on the cyclic triaxial tests, the average damping ratio is taken as approximately 4% for EPS-15, 3% for XPS-22 and 2.9% for the backfill material. Rayleigh damping parameters corresponding to these damping ratios were calculated and defined as an input in FLAC code with the central frequency of the Rayleigh damping set to the fundamental frequency of the wall-backfill system. The lowest natural frequency for this model may be estimated by running the FLAC model without introducing damping. A plot of velocity history depicted in Figure 6-4 shows that dominant natural frequency of the finite difference model is approximately 12Hz. It was observed that Rayleigh damping acts as a filter for high frequency waves occurring during the analyses. However; utilization of Rayleigh damping in the FLAC code drastically reduces the time step. As a consequent, solution time increases. The calculation time for the simulation of the dynamic test phase is approximately six hours with the Intel i7 Processor.

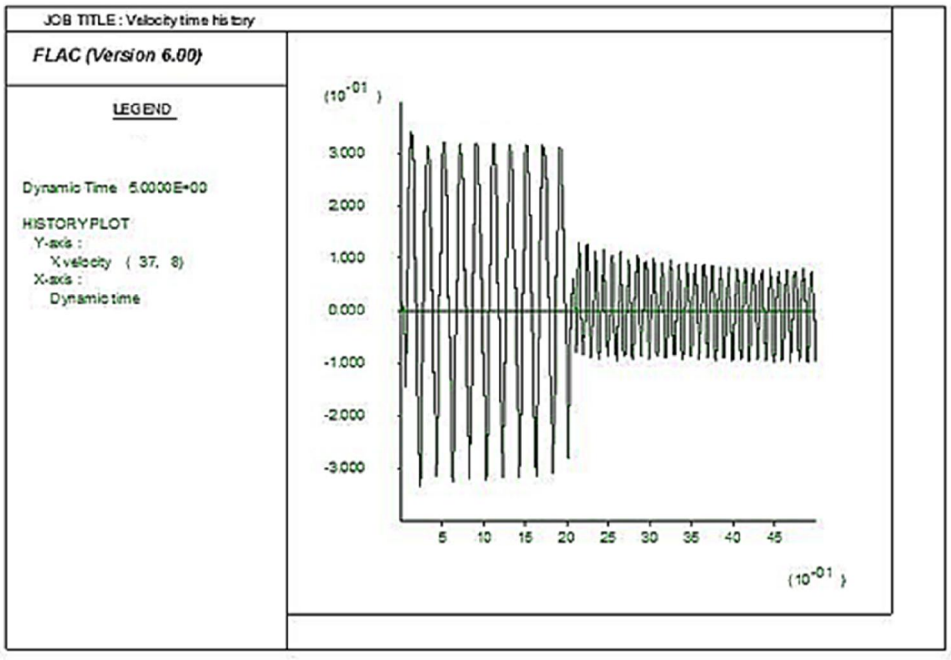

Figure 6-4 Velocity history output used to estimate lowest natural frequency of the wall-backfill system

Several parameters were collected at every 1000 steps of FLAC analyses. The sampling rate corresponds to approximately 600Hz considering the typical timestep as 1.7×10^{-5}s. This value is considered to be sufficient for the accurate determination of any response frequency for an applied signal of 25Hz (Lynn and Fuerst, 1990). The response parameters collected for the dynamic phase of the FLAC analyses include horizontal accelerations and displacements at various nodes in the finite difference grid, lateral earth pressures, relative wall displacements as well as shear force and bending moment profiles of the wall stem. The time history of the unbalanced force occurring during the dynamic phase is also collected since this parameter is an important indicator for tracking the overall stability of the FLAC finite difference model. This value is defined as the summation of the unbalanced forces acting on all the nodes at a specific time step. An excessive unbalanced force may be an indication of excessive grid distortion and instability problems.

6.5 Wall displacements

The deformed grids and displacement vectors for pre-excitation and post-excitation phase for wall model without geofoam buffer (CW-C8) and wall with EPS geofoam buffer (CW-CE8) were depicted in Figure 6-5. It was observed that presence of deformable buffer between the wall model and backfill provides lateral deformations concentrated at the lower half of the retained backfill. Flexural deflections of the wall incorporated with the compression of the geofoam buffer causes reduction in the overall deflection of the wall stem. Comparison of lateral displacement contours prior to the removal of the lateral wall fixity were made in Figure 6-6. As seen in this figure, a well-defined failure surface is not observed in the backfill. On the other hand, the presence of the vertical geofoam panel behind the wall causes lateral backfill displacements within the lower half of the retained soil mass. The displacements concentrated at the lower half of the backfill cause stress redistribution (Figure 6-7) in retained soil known which is similar to soil arching proposed by Terzaghi (1943) as the “trap door” problem. The lateral arching effect induced in the retained soil due to the lateral compression of the geofoam inclusion has a positive effect, by absorbing a portion of the total unbalanced lateral force exerted by the backfill and thus causing a reduction in the lateral wall thrust compared to control case (no geofoam buffer). Backfill displacements occur in a wider zone especially for the presence of thicker geofoam buffers (Figure 6-6b). This leads to the mobilization of the soil shear strength on a greater wedge. In Figure 6-8, displacement contours after the removal of the wall fixity were shown. It was observed that additional displacements occurred in the upper half of the wall stem due to effect of the wall flexibility. In the simulations with geofoam compressible buffers, there is a decrease in lateral wall displacements which is in agreement with the physical test results. It was observed that presence of geofoam buffers with various thicknesses contributes to the reduction of the pre-excitation and post-excitation deflections of the wall stem (Figure 6-9 and Figure 6-10). Wall deflections predicted by the finite difference method is in fairly good agreement with the test data.

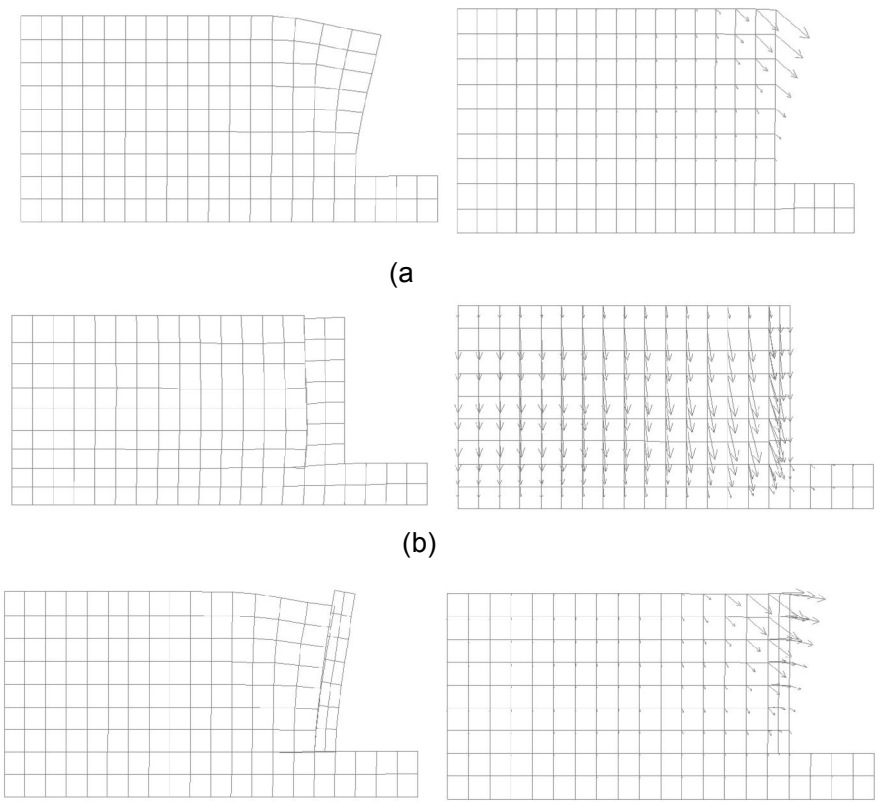

Figure 6-5 Deformed grids and deformation vectors for (a) CW-C8 (no geofoam buffer) post-excitation phase (b) CW-CE8 (EPS-15 geofoam buffer with t/H=0.07) pre-excitation phase (c) CW-CE8 (EPS-15 geofoam buffer with t/H=0.07) post-excitation phase

Results of the numerical modeling study indicated that compressive strain levels in the geofoam inclusion were below 1% which is smaller than the compressive strain at yield obtained from uniaxial tests on geofoam thus validating the linear elastic assumption. It was observed that the positive effect of XPS-22 type buffer on reducing wall movements is not as pronounced as the less stiff EPS-15 buffer type. Shear strain distribution in the backfill at the end of dynamic phase was depicted in Figure 6-11. Comparison of the contours for no-geofoam case and geofoam case presents the formation of soil wedge in a wider zone.

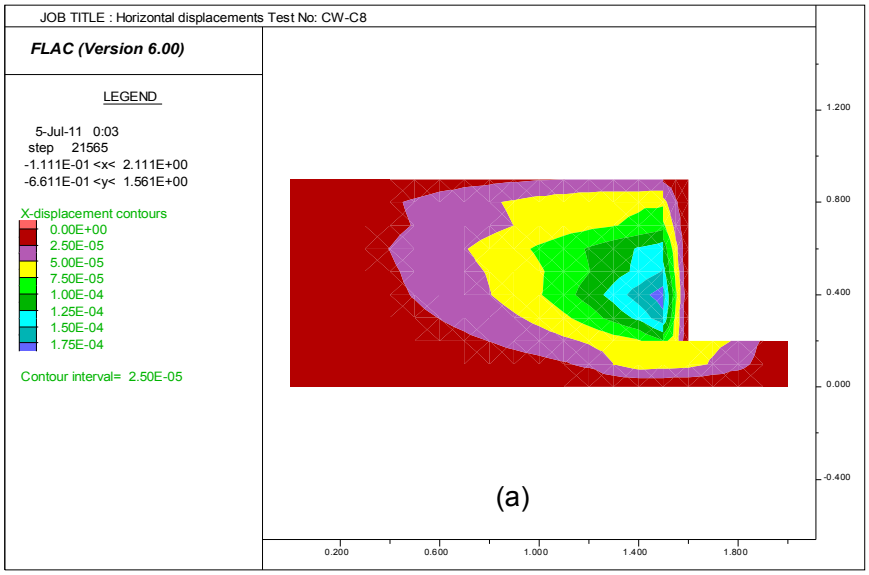

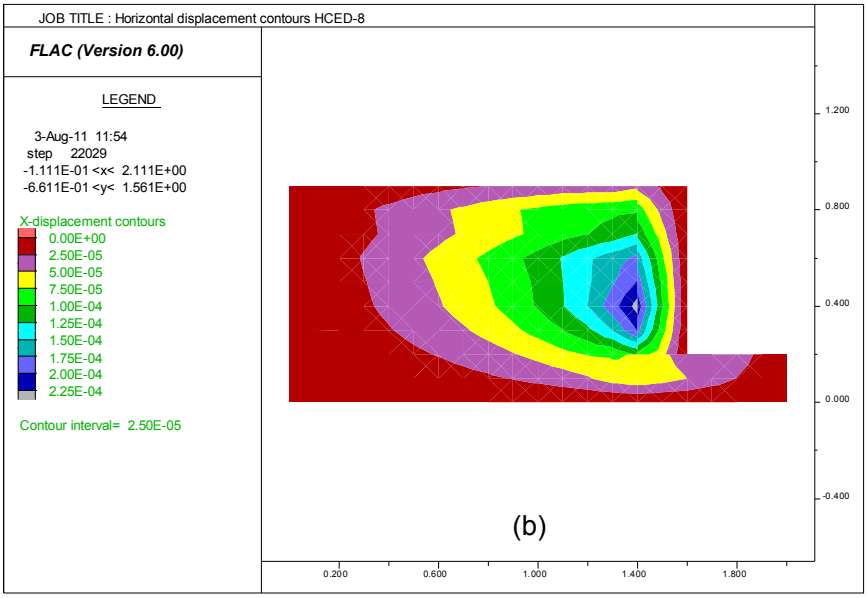

Figure 6-6 Lateral displacement contours prior to the removal of horizontal wall fixities (a) CW-CE8 (t/H=0.07) (b) CW-CED8 (t/H=0.14)

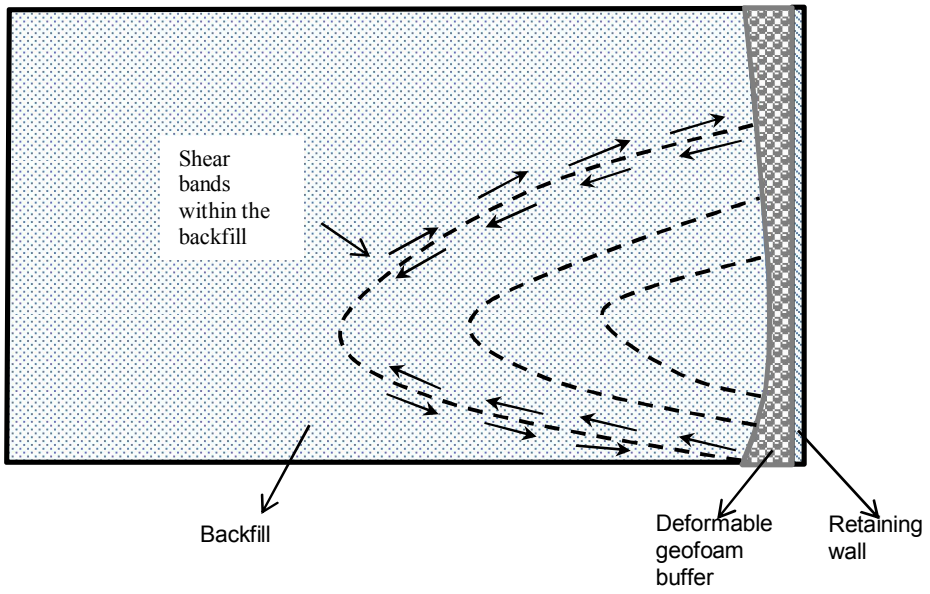

Figure 6-7 Stress redistribution acting on the wall stem due to lateral soil arching

6.6 Lateral stresses

Lateral stresses at various nodes were tracked during the static and dynamic phase of the FLAC simulations. In Figure 6-13, lateral stress contours in the backfill were depicted for walls with and without geofoam buffers prior to the dynamic phase. It was observed that geofoam buffers provide reductions in the lateral stress distribution through the backfill compared to those without seismic buffers. The evolution of lateral stresses at the vicinity of the wall base during the dynamic phase of CW-C7 (no buffer) and CW-CE7 (EPS-15 type buffer) simulations was plotted in Figure 6-12. The comparison of the earth pressure profiles at the instant of peak dynamic thrust was provided in Figure 6-14. Predictions obtained by numerical analyses are in quite good agreement with physical test data throughout the overall height of the wall except the vicinity of the wall base. Pressure profile determined from test data has a parabolic shape and generally higher compared to those of FLAC analyses. The difference between measured and finite-element predicted stresses in the vicinity of the wall base may be a result of the interface friction occurring at the wall base-backfill and wall base-geofoam interfaces.

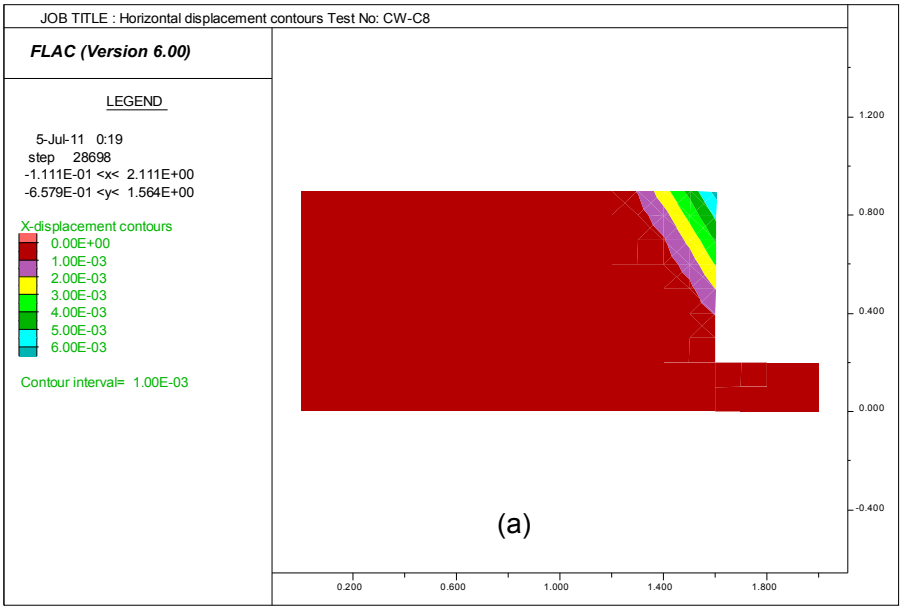

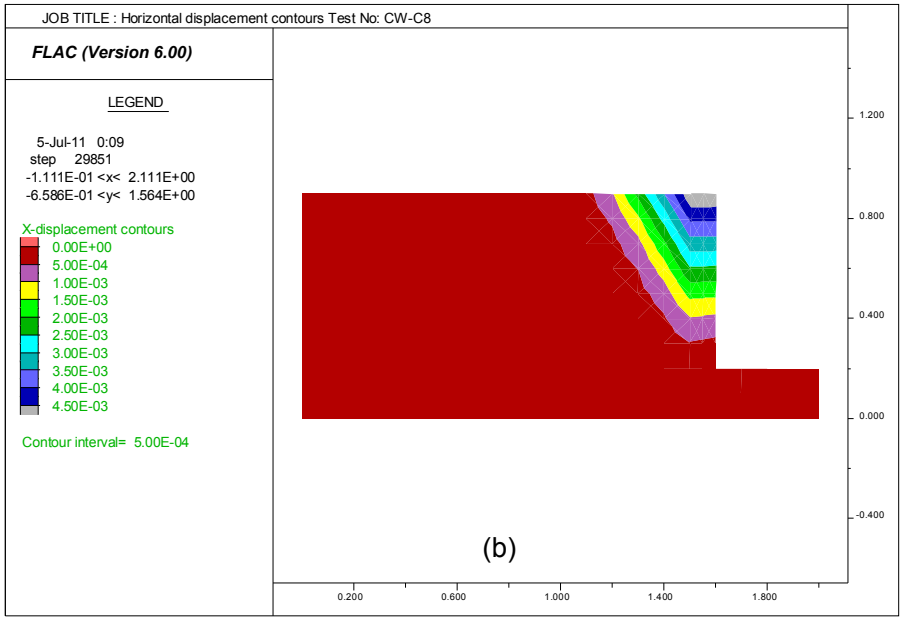

Figure 6-8 Lateral displacement contours after removal of lateral wall fixities (a) CW-C8 (b) CW-CE8

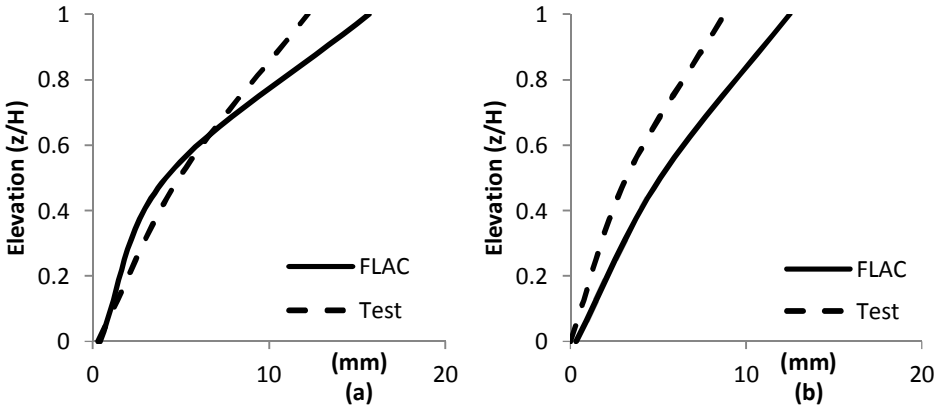

Figure 6-9 Comparison of static (pre-excitation) wall displacements for Type-C wall model (a) No geofoam buffer (b) EPS-15 geofoam buffer with t/H=0.07

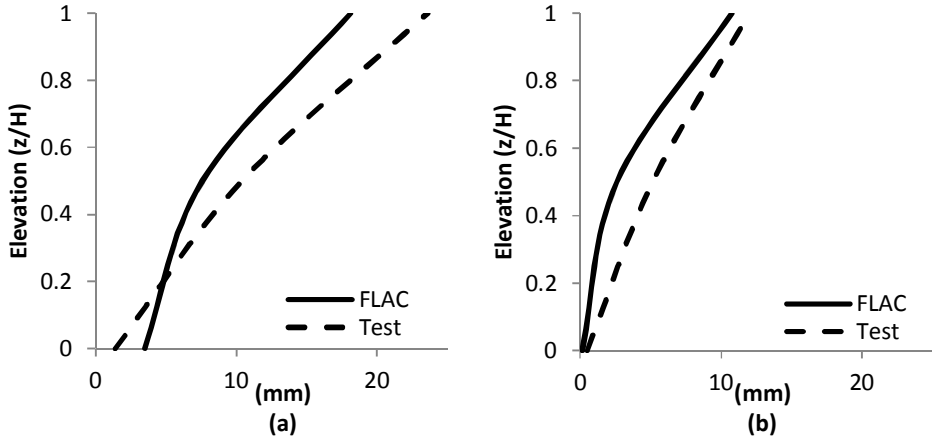

Figure 6-10 Comparison of post-excitation wall displacements for Type-C wall model (a) No geofoam buffer (b) EPS-15 geofoam buffer with t/H=0.07

Using lower friction values along the wall base in order to get a better estimate of stresses at this location significantly alters the predicted distribution of lateral stresses observed in the lower mid-height of the wall. Therefore, interface parameters at the wall base were calibrated to better fit the experimental data in the greater portion of the wall height thus sacrificing the agreement of the results around the small portion in the vicinity of wall base.

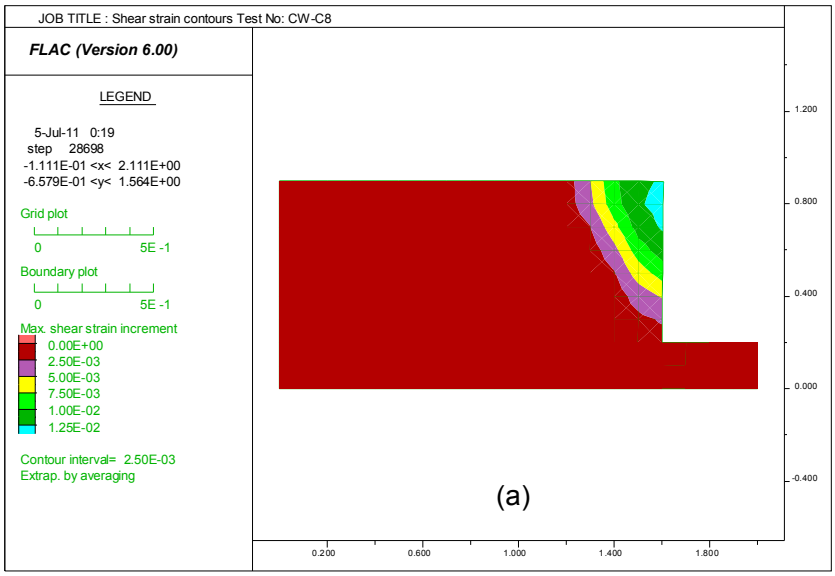

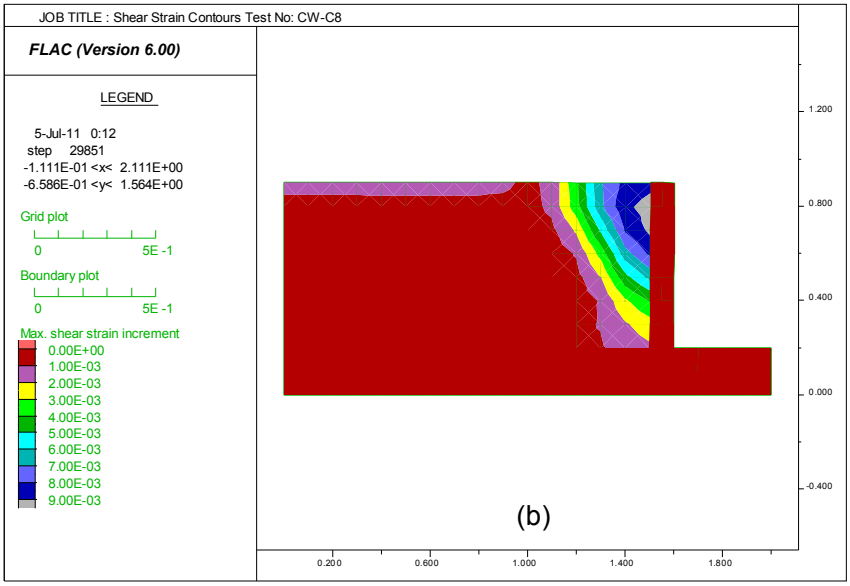

Figure 6-11 Shear strain contours at the end of dynamic phase

Total dynamic pressure profiles leading to maximum and minimum thrust are compared for the least flexible wall in Figure 6-15 (CW-D8, d_w=128) and Figure 6-16 (CW-DED8, d_w=128, EPS-15 having t/H=0.14). The horizontal accelerations in the backfill at the instance of maximum and minimum thrust are provided in the same figures. Presence of geofoam buffer leads to significant decrease in earth pressures.

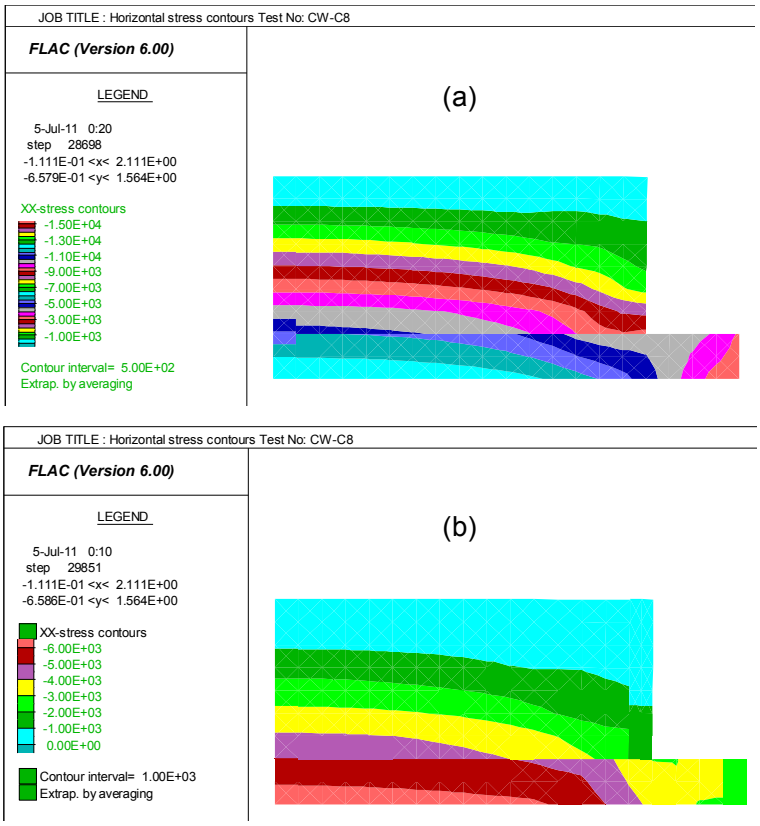

Figure 6-12 Lateral stresses (a) No geofoam buffer (b) EPS-15 geofoam buffer (t/H=0.07)

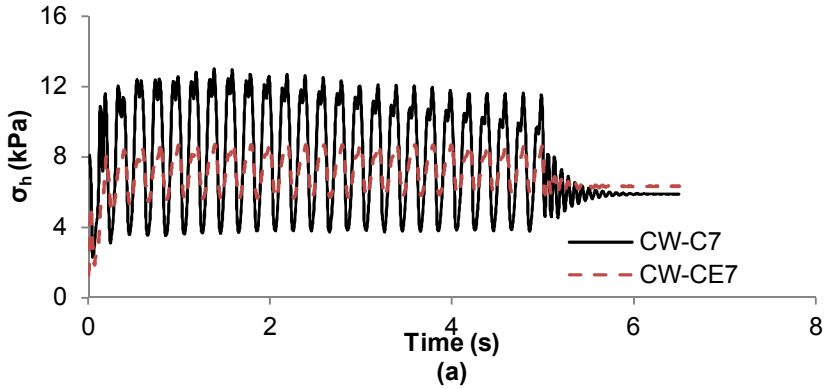

Figure 6-13 Comparison of lateral dynamic earth pressures at z=0 for C7 (no buffer) and CE7 (EPS buffer with t/H=0.07)

Similarly, pressure and acceleration profiles for the most flexible type model wall are depicted in Figure 6-17 (CW-A8, d_w=8192) and Figure 6-18 (CW-AED8, d_w=8192, EPS-15 having t/H=0.14). Presence of geofoam buffer reduces lateral stresses; however this decrease was not as pronounced as the reduction

occurring for the non-yielding and rigid wall model. In Figure 6-19, back calculated dynamic earth pressure coefficients (K_{ae}) based on numerical analyses were compared to those obtained from physical modeling study. K_{ae} values were calculated according to Eq.6-8:

$$K_{ae} = \frac{2}{\gamma H^2} \int_O^H \sigma_h(z)_{dyn} dz \qquad 6\text{-}8$$

where $\sigma_h(z)_{dyn}$ is the total dynamic earth pressure at depth (z) from wall top. It was observed that predictions made from finite difference analyses were relatively lower than those of the physical modeling tests. However, both of the predictions are successful in determining the general trend for the wall models having various relative wall flexibilities.

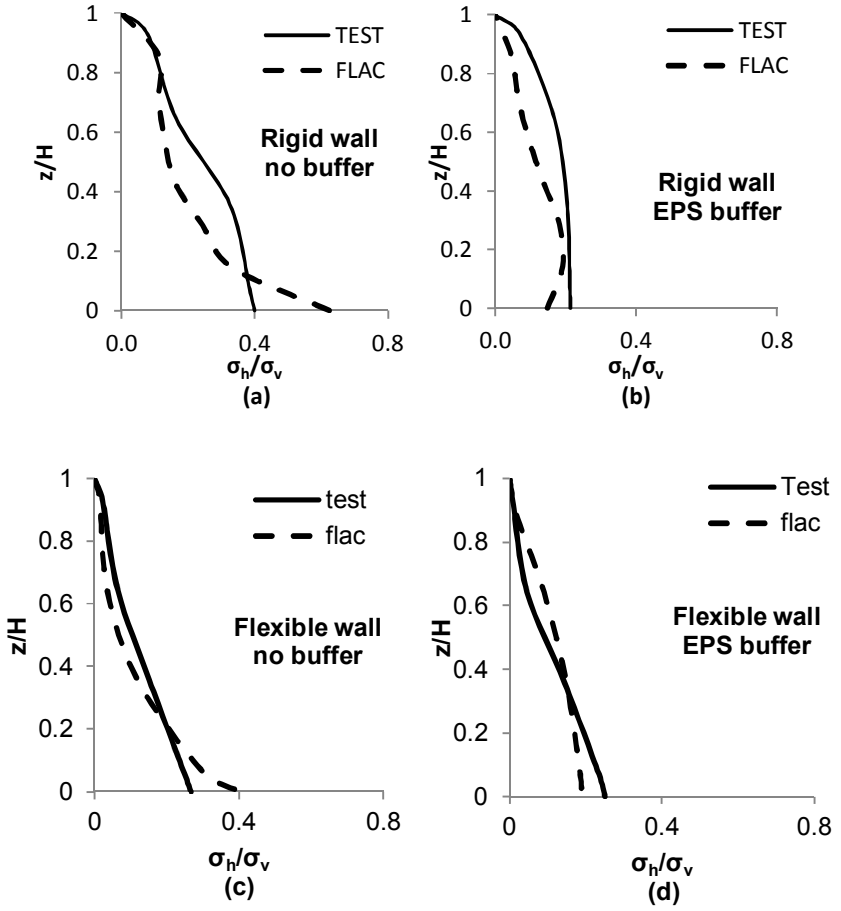

Figure 6-14 Comparison of experimental and numerically calculated total earth pressure profiles leading to peak dynamic thrust (a)CW-D8 (most rigid wall, d_w=128) (b) CW-DE8 (most rigid wall, d_w=128 with EPS buffer) (c)CW-A8 (most flexible wall, d_w=8197) (d) CW-DE8 (most flexible wall, d_w=8197 with EPS buffer)

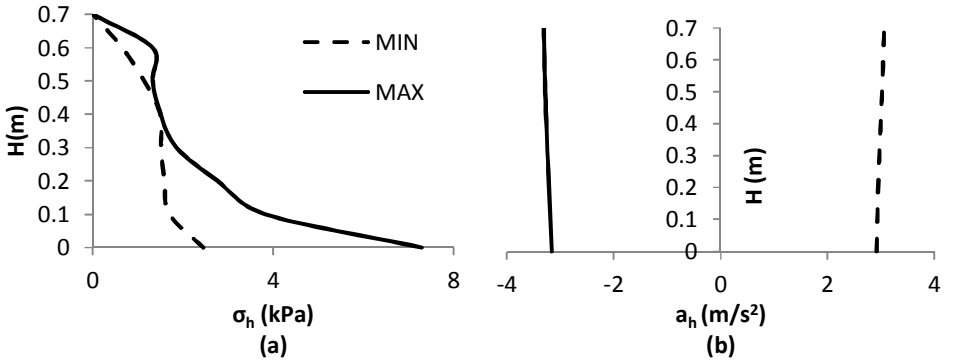

Figure 6-15 (a)Earth pressure profile (b) Horizontal acceleration distribution at the instant of maximum and minimum dynamic thrust (CW-D8)

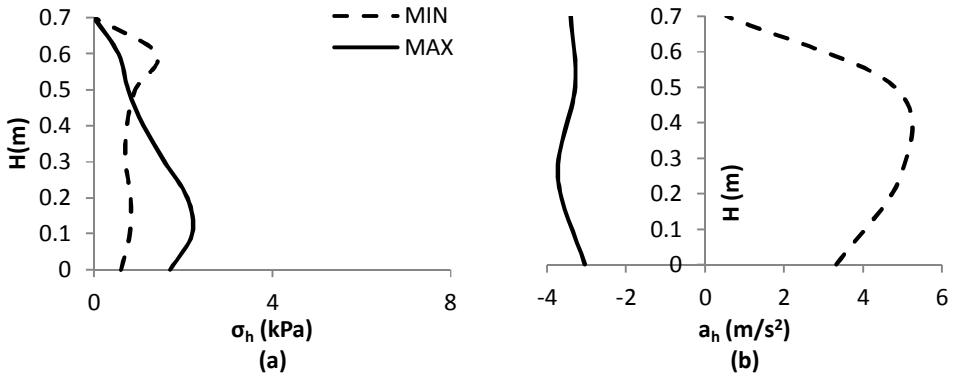

Figure 6-16 (a) Earth pressure profile (b) Horizontal acceleration distribution at the instant of maximum and minimum dynamic thrust (CW-DED8)

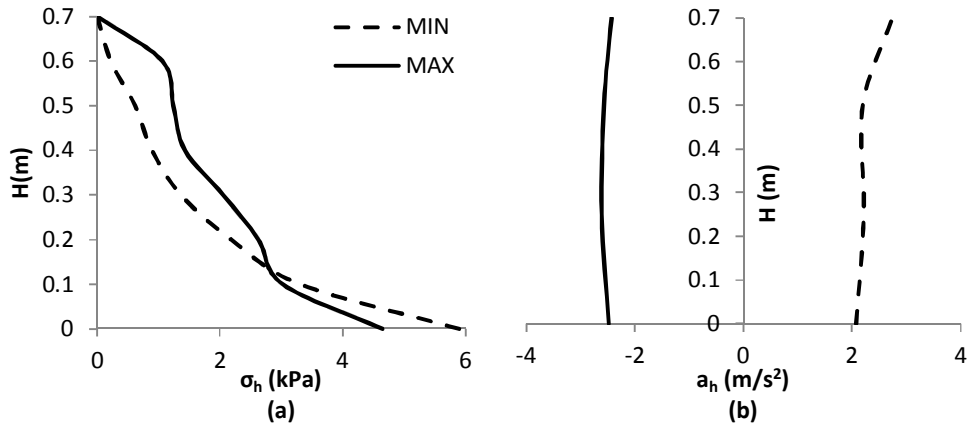

Figure 6-17 a)Earth pressure profile (b) Horizontal acceleration distribution at the instant of maximum and minimum dynamic thrust (CW-A8)

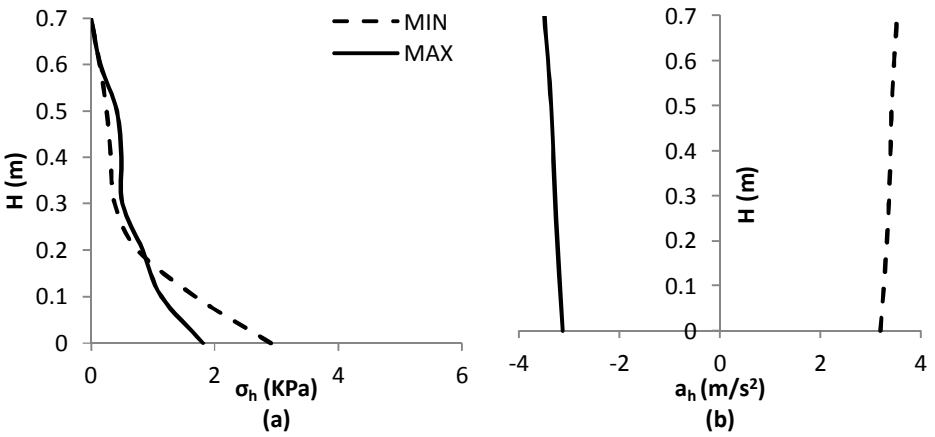

Figure 6-18 (a) Earth pressure profile (b) Horizontal acceleration distribution at the instant of maximum and minimum dynamic thrust (CW-AED8)

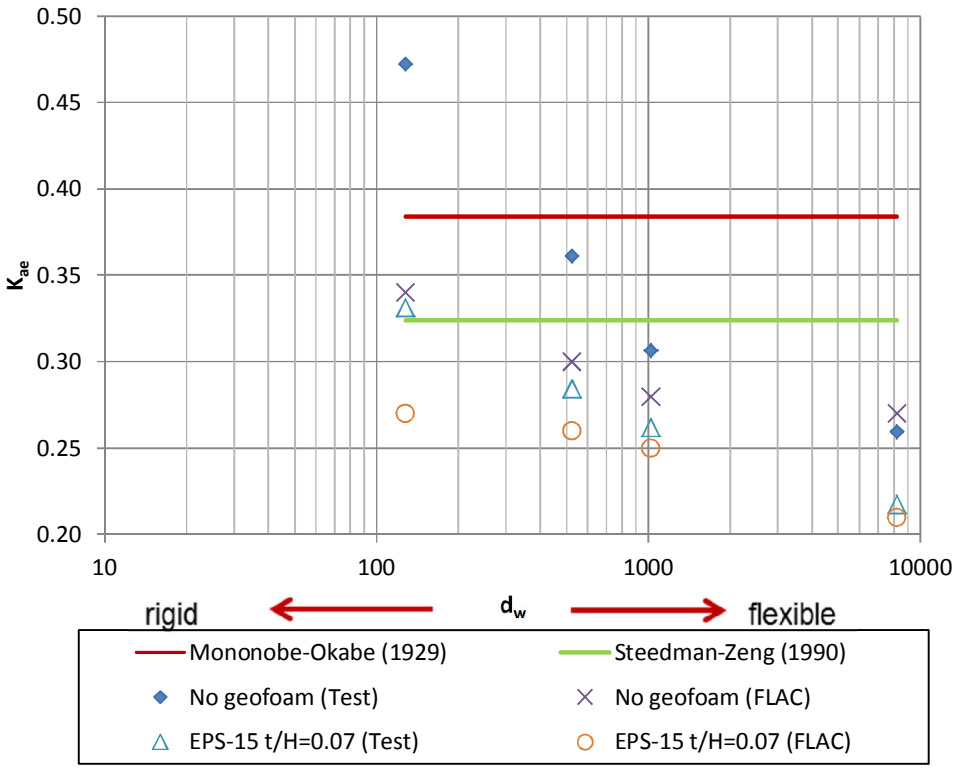

Figure 6-19 Comparison of dynamic earth pressure coefficients (PGA=0.3g) obtained from tests and numerical analyses

6.7 Seismic response of a full size cantilever retaining wall

In this section, results of a dynamic analysis carried out for a 6m high cantilever wall model subjected to a real earthquake motion was briefly discussed. In the analysis, wall model is allowed to flex, rotate and slide. The finite difference model (Figure 6-20) consisted of 6m high cohesionless backfill material retained by a reinforced concrete retaining wall and 2 m thick underlying foundation soil.

6.7.1 Overview of the model and input parameters

The model depicted in Figure 6-20 consisted of four subgrids which are attached each other. It is necessary to separate the grid into subgrid 1 and 2 due to the presence of cantilever wall base. The subgrids 3 and 4 are for the applying the free field conditions to the left and right edges of the grid. The stage construction of the wall was simulated numerically by applying the backfill in six lifts of 1m height. Similar to the model developed for the small-scale model wall described in Section 6.3, backfill and foundation soil was modeled as elasto-plastic materials in conjunction with the Mohr-Coulomb failure criterion (Table 6-3). Most of the material properties were derived from triaxial compression test results reported by Gomez (2000) on dense (relative density D_r= 92%) silica sand. The concrete retaining wall was idealized with elastic beam elements with the properties listed in Table 6-4. The geofoam was modeled as an elastic material, however confining stress dependency of the geofoam was taken into account by defining three different sets of parameters for the stress ranges of 0-30kPa, 30-60kPa and 60-90kPa (Table 6-5). These properties were assigned for the upper third, mid third and lower third of the geofoam seismic buffer.

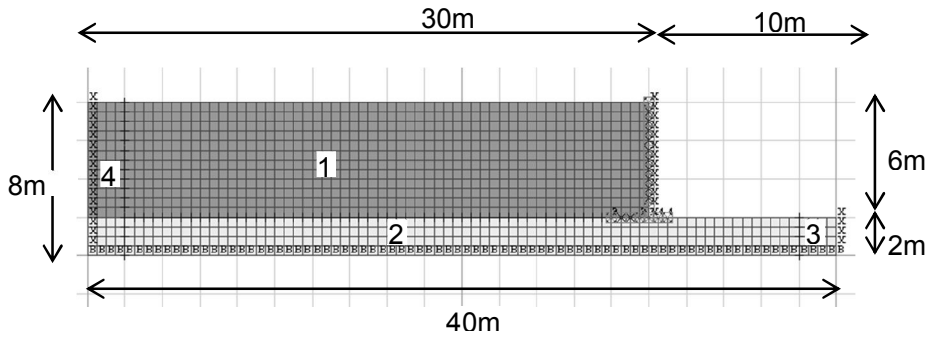

Figure 6-20 Finite difference mesh for the wall-backfill-foundation soil

For the dynamic analyses of a full scale model, implementation of the Rayleigh damping should be avoided where it is possible since incorporation of Rayleigh damping in the numerical scheme causes a drastic reduction in timestep and a consequent increase in the computational time. FLAC possesses the ability to include hysteresis damping in the analyses once the damping curves were defined in the code. In the analysis of the full scale wall, hysteretic damping function of the FLAC was implemented. The Modulus degradation and damping curves were determined according to the procedure proposed by Osso and Romo (2010). Using Eq.s 3-15 to 3-22, the cyclic strain response of EPS-24 depicted in Figure 6-21 was estimated. According to FLAC manual (Itasca, 2008), the modulus reduction and damping curves depicted in Figure 6-21 were implemented to the numerical code using sigmoidal functions. For the hysteretic response of the cohesionless material used as the backfill, the upper range modulus reduction curve for sand proposed by Seed and Idriss (1970) were applied. Elasto-plastic interfaces have been considered at the geofoam contact with the wall and the soil, characterized by interface friction angles of 45° and 26°, respectively based on the available experimental information in the literature. For the case of the wall with no geofoam inclusion, a friction angle of 32° has been utilized at the wall-soil interface. A friction angle of 28° was considered along the base of the gravity retaining wall in the present numerical study. Figure 6-22 shows the time history of the input horizontal earthquake acceleration that was applied as base excitation in the present dynamic finite-element analysis. The accelogram was recorded during the August 17, 1999 Kocaeli earthquake at a station located in Düzce, Turkey. To assess the performance of geofoam buffer, evolution of flexural wall deflections and the total dynamic earth thrust were depicted in Figure 6-23 and Figure 6-24. The numerical results indicate that the presence of an EPS panel behind the wall may result in a reduction of the permanent flexural wall deflections as well as total dynamic thrust likely to be experienced by the wall during an earthquake. Thus, the outcome of the present study demonstrates the effectiveness of EPS geofoam inclusions in improving the seismic performance of gravity retaining walls.

Table 6-3 Constitutive model properties for the geomaterials for the static phase of finite difference modeling

Parameter	*Backfill*	*Foundation*
Model	MC	MC
Unit Weight (γ) [kN/ m^3]	17	17
Young's Modulus (E) [kPa]	50000	60000
Poisson's Ratio (v)	0.33	0.33
Cohesion (c) [kPa]	3	3
Friction angle ($\varphi_{backfill}$) [°]	43.5	43.5
Dilatancy Angle (ψ) [°]	19.1	19.1

MC: Elasto-plastic model with Mohr-Coulomb yield criterion

Table 6-4 Elastic properties for the flexible wall

Property	*Wall Stem*	*Wall Base*
Unit Weight (γ) [kN/ m^3]	64	64
Thickness (t_w) [mm]	0.50	0.75
Young's Modulus (E) [GPa]	26	26
Poisson's Ratio (v)	0.21	0.21

Table 6-5 Properties of EPS-24 geofoam buffer

Parameter	*Buffer 1*	*Buffer 2*	*Buffer 3*
Stress range	*0-30kPa*	*30-60kPa*	*60-90kPa*
Model	LE	LE	LE
Unit Weight (γ) [kN/	0.24	0.24	0.24
G_{max} [kPa]	10180	9350	8516
Poisson's Ratio (v)	0.169	0.109	0.049

LE: Linear Elastic model

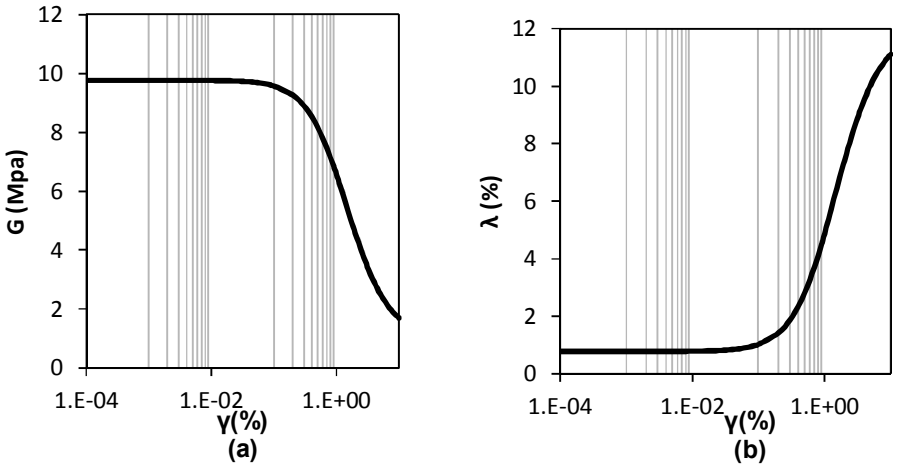

Figure 6-21 (a) Modulus reduction curve for EPS-24 (b) Damping curve for EPS-24

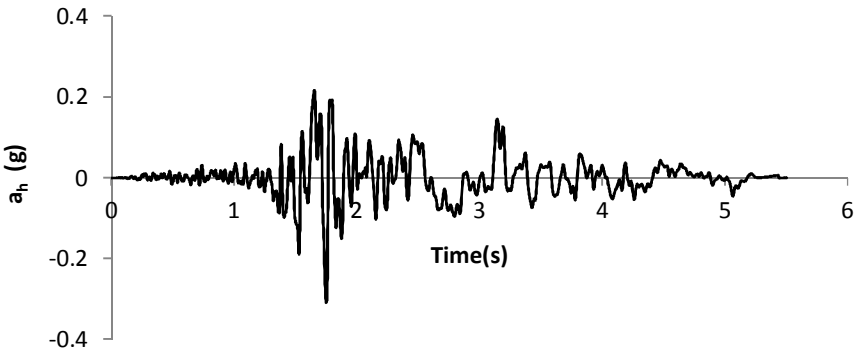

Figure 6-22 Acceleration time history used in the dynamic analysis (http://peer.berkeley.edu/nga_files/ath/KOCAELI/DZC180.AT2)

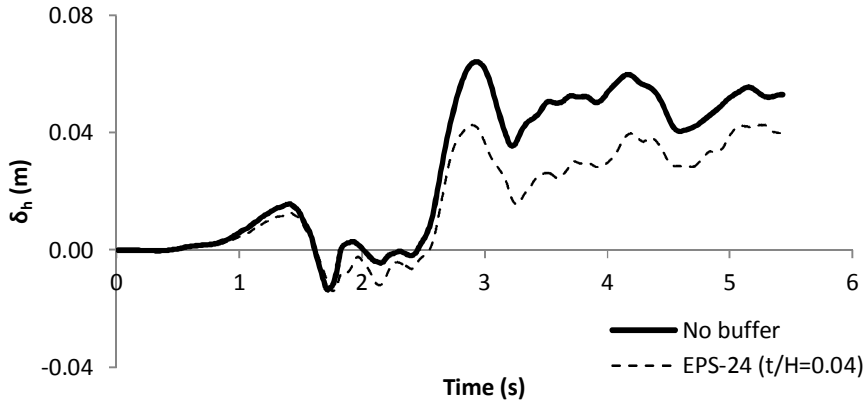

Figure 6-23 Evolution of the earthquake-induced horizontal displacements

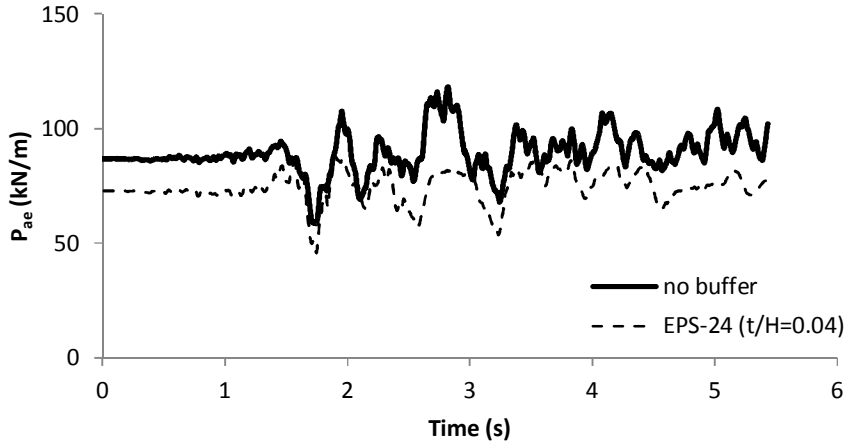

Figure 6-24 Evolution of lateral dynamic earth thrust

CHAPTER 7

SUMMARY, DISCUSSION AND CONCLUSION

7.1 Summary

In this study, results of physical model tests and numerical simulations on the static and dynamic behavior of yielding cantilever retaining walls with geofoam compressible buffers were discussed. The effect of relative flexibility of the wall and the excitation characteristics (i.e. excitation frequency, amplitude) as well as the thickness and stiffness of the compressible buffer placed between the cohesionless backfill and the wall stem were investigated in this context. A series of numerical simulations were performed using the general finite difference method software FLAC 2D v6.0 (Itasca, 2008).

For the physical modeling study, 0.7m high wall models with various stem thicknesses were instrumented. The types of geofoam used as deformable buffers in this study are expanded polystyrene (EPS) having density of 15kg/m^3 and extruded polystyrene (XPS) with density of 22kg/m^3. The static and dynamic characterization of the materials used in physical modeling study was made through extensive laboratory testing. Static and cyclic triaxial tests were performed using a state-of-the art triaxial testing machine to determine the mechanical properties of the geomaterials.

1-g model tests were performed with a laminar container (2m length × 1m width) placed on a shaking table system. Simple harmonic base excitations were applied to the base of the models since this type of excitation enables more accurate comparisons to be made about the effect of various parameters regarding the base motion. Three groups of reduced scale model tests were performed in the physical modeling study.

In the first group (control tests), compressible buffer was not present between the retaining wall model and the backfill. In the second and third sets, EPS-15 and XPS-22 type geofoam buffers of different thicknesses were installed between the model walls and the backfill. The responses of cantilever retaining walls were examined for different wall flexibilities, excitation amplitudes, and frequencies. Efficiency of various type of compressible geofoam buffers were investigated by making comparisons with control test results. The tests were repeated for two different buffer thicknesses (t/H=1/7 and t/H=2/7 where t is the thickness of the buffer and H denotes the wall height) and four different stem thicknesses (t_w=2mm, 4mm, 5mm and 8mm). Static and dynamic behaviors of model retaining walls were evaluated in terms of flexural wall deflections, lateral earth pressures, accelerations in the backfill and vertical pressures under the wall base. Static and dynamic earth pressure coefficients were back-calculated from the stresses measured in the tests. The lateral earth pressure coefficients determined from physical tests were compared with those calculated using analytical methods. Graphs were provided to estimate the static and dynamic lateral earth pressure coefficients depending on the geofoam characteristics and relative flexibility of the wall.

7.2 Discussions

According to the results of laboratory tests performed on the geofoam materials used in the reduced scale model tests, following important characteristics of the geofoam are observed. EPS geofoam samples ($h:d$ ratio of 2:1 where h is the specimen height (100mm) and d is the diameter of the specimen) having a density of 15kg/m^3 exhibited elasto-viscoplastic stress-strain behavior which is mainly linear elastic up to axial strains of 2%. Beyond this strain level, yielding occurs and this is followed by a strain hardening phase in a wide strain plateau. Behavior of XPS geofoam (density of 22kg/m^3) exhibits elasto-plastic behavior. Strain hardening is not observed after yielding of the material. The elastic limit strain is approximately 2% for XPS geofoam tested for this study. Contrary to the behavior of soils, the compressive strength of EPS and XPS geofoam decreases as the confining stress increases. The increase in the strain rate leads to an increase in the compressive strength. The Young's modulus describing the linear-elastic portion of the stress-strain curve for EPS-15 geofoam is approximately four times smaller than the secant modulus of the granular material used as the

backfill in the reduced scale model tests. Based on the results of cyclic triaxial tests, the damping ratio of the geofoam materials used for this study is found to be on the order of 2% and 5%.

According to the outcomes of the model tests, geofoam buffers exhibit the best load reduction performance when placed against rigid non-yielding walls. Since flexural wall deflections lead to development of active stress conditions in the backfill, positive contribution of the compressible buffer decreases for more flexible walls. As another note, thickness and stiffness of the buffer significantly affect the load isolation behavior. Results of the numerical analyses are in agreement with these findings. Investigation of the stress and deformation patterns captured by the finite difference model indicates that lateral deformations are induced in the soil by the compressible deformations concentrated at the lower half of the geofoam buffer. The arching effect induced in the retained soil by the lateral compression of the lower half of the geofoam deformable buffer has a positive effect, as this zone is able to absorb a portion of the total unbalanced lateral force exerted by the backfill thus causing a reduction in the lateral wall thrust compared to control case where no geofoam buffer was present.

The presence of the XPS-22 type deformable buffer does not significantly reduce the static lateral earth pressures. Since the elastic modulus of the XPS-22 geofoam is found to be 3.72 times higher than the modulus of EPS-15 geofoam, smaller compressive strains occur within XPS-22 type buffer under the same loading. Lateral earth stresses generated within the backfill are not sufficient enough to produce compressive strains in this type of geofoam buffer.

Model tests have not been extended for relative thickness (*t/H where t is the buffer thickness and H is wall height*) smaller than 0.07. It can be expected that there exist limiting combinations of relative inclusion thickness and stiffness for mobilizing the soil deformations required to initiate static active stress state in the backfill. Amount of soil deformation required to bring backfill material into active stress state depends on the shear strength characteristics of the backfill soil. Hence, the stiffness attributes and thickness of the compressible inclusion can be determined based on the shear strength characteristics of the backfill material. According to Karpurapu and Bathurst (1992), *t/H* values as low as 0.01 may provide active stress conditions in the backfill if stiffness of the deformable buffer is sufficiently small. The investigation of the buffer performance in conjunction

with the soil strength and stiffness parameters should be considered as a future research topic.

According to the outcomes of physical tests and numerical studies, seismic earth force reduction function of geofoam buffers mainly arises from the low stiffness of the material since the damping of the geofoam is not significantly high compared to the damping of the soils. For the strains well above the elastic limit strain of geofoam, damping ratio increases leading to the dissipation of a larger amount of energy occurring in the cyclic loading, however the volume of the deformable geofoam buffers in the retaining wall applications is generally much smaller than the volume of the retained soil mass. Hence, the influence of damping ratio of the seismic earth forces acting on the wall may be negligible.

It should be noted that for the best load reduction performance, the correct combination of the buffer stiffness and thickness, or in other words, the buffer relative stiffness should be determined depending on the magnitude of static and seismic lateral stresses expected for a specific case. Presence of a too soft inclusion may cause yielding of the buffer under static loads and diminish the amount of compressibility reserved in the buffer layer for a seismic loading. In this case, positive contribution of the geofoam buffers on seismic earth thrust acting on the walls may be ceased. Placement of a buffer having too high relative stiffness may also cease the load reduction performance of the buffer since deformations required for mobilizing active stress conditions and arching in the backfill may not be achieved.

It must be addressed that this study does not take into account the effect of geofoam creep and results are applicable to yielding cantilever retaining walls supporting dry granular backfills. Results are outcomes of reduced scale 1-g model tests and verified numerical analyses where backfill material is modeled by elasto-plastic Mohr-Coulomb failure criterion. In all the numerical analyses series, physical behavior of the geofoam is considered as linearly elastic since maximum expected stresses on the EPS geofoam inclusion are less than the yield strength of the material for the wall heights investigated.

7.3 Conclusions regarding the static behavior

On the basis of the physical 1-g model tests and numerical analyses, following conclusions can be made:

1. According to the test results, 30% to 60% of static earth thrust on the wall may be reduced depending on the wall flexibility and buffer stiffness.
2. Active earth pressure coefficients (K_{exp}) back-calculated for cantilever walls with EPS-15 type geofoam buffer are found to be smaller than those calculated according to Coulomb's theory. XPS-22 type buffer does not provide significant contribution to the reduction of (K_{exp}). Earth pressure coefficients obtained for this type of buffers are generally close to the values obtained for walls without buffers.
3. Lateral load reduction efficiency (i_p) of deformable geofoam buffers decrease as wall flexibility (d_w) increases. Deformable buffer made of EPS-15 having t/H ratio of 0.14 provides approximately 60% decrease in earth thrust for a rigid wall (d_w=128), however 35% decrease occurs for a more flexible wall (d_w=8200).
4. The point of application of the static wall thrust varied between 0.24H and 0.33H (measured from the base) depending on the wall flexibility and compressible buffer type. It was observed that increasing wall flexibility causes total wall thrust act at a higher elevation for the tests where geofoam buffer was not present. However, in the tests where geofoam buffers were present, wall flexibility does not cause any significant variation in the application point of static thrust.
5. Increasing wall flexibility (d_w) leads to larger flexural deflections of the wall. Deformable buffers reduce lateral deflections of the wall stem. Amount of reduction may reach up to 70% depending on relative stiffness of the deformable buffer.
6. Finite difference analyses are able to estimate the static wall deflections and earth thrust with reasonable agreement.

7.4 Conclusions regarding the dynamic behavior

1. Flexural wall deflections tend to increase for higher excitation frequencies and amplitudes as expected. In all the tests involving geofoam buffers, smaller deflections occurred in the model walls compared to tests without geofoam buffers. Amount of decrease in wall deflection varies between 10% and 35% depending on the base excitation and buffer characteristics. In all the dynamic tests, significant increase was observed in flexural wall

deflections as excitation frequency approaches to the natural frequency of the retaining wall and backfill system.

2. Wall flexibility significantly affects the performance of geofoam seismic buffers. Decrease in flexural wall deflections may reach up to 65% for the rigid wall model (d_w=128) under the influence of EPS-15 buffer having thickness of t/H=0.14 however only 20% reduction was achieved for a flexible wall model (d_w=8197).
3. Presence of a deformable buffer causes more amplification within the backfill compared to no buffer case. Soil amplification increases as relative flexibility (d_w) of the wall increases. The amplitude of the base excitation does not significantly affect the amplification behavior observed in the tests. However, increasing frequency of the excitation causes a nonlinear increase in amplification behavior.
4. It was observed that dynamic earth stresses on flexible walls are significantly lower than those acting to the rigid and non-yielding walls.
5. For the investigated frequency (f_{exc}) range, dynamic lateral stresses (p_{ae}) obtained in the tests are in good agreement with estimations of Steedman-Zeng (S-Z) approach for walls without buffer. Deformable buffer provides reductions in the p_{ae} values as expected. Positive effect of XPS-22 inclusions is not more than 5% for the investigated f/f_n range.
6. Total dynamic earth pressure coefficients $(K_{ae})_{\text{exp}}$ increase non-linearly with increasing PGA. Coefficients obtained for wall models without geofoam buffer are found to be between 0.20 and 0.67 in the PGA range of 0.1g to 0.7g. The decrease in $(K_{ae})_{exp}$ values may reach to 55% depending on PGA and buffer characteristics. Predictions of Mononobe-Okabe (M-O) and Steedman-Zeng (S-Z) methods are observed to be more conservative compared to those obtained from the tests without deformable buffers.
7. As the frequency ratio (f/f_n) increases, a nonlinear increase occurs in total dynamic earth pressure coefficients in all the tests. Significant increase may occur as excitation frequency approaches to the natural frequency of the wall. Deformable buffers reduce total dynamic earth pressure coefficients within the overall frequency range, with a slight performance increase at higher frequencies.
8. Increasing relative wall flexibility (d_w) provides reduction in total dynamic earth pressure coefficients. Predictions of the analytical methods are in better agreement for wall models having lower d_w values (more rigid walls).

Presence of geofoam buffers provides additional reduction in $(K_{ae})_{exp}$ values in the investigated relative wall flexibility range. Reduction in earth pressure coefficients by the presence of EPS-15 buffer with t/H=0.14 was found as approximately 48% for rigid wall model (d_w =128), whereas 30% reduction was observed for the flexible wall with same deformable buffer (d_w =8200).

9. Deformable geofoam buffers reduce the dynamic vertical pressures at the base of the wall. Presence of EPS-15 buffer (t/H=0.14) provides approximately 50% reduction. Residual vertical pressures accumulate at the toe side. The amount of stress accumulation depends on the amplitude of the base excitation.
10. Application point of the dynamic earth thrust occurs between 0.4H and 0.6H above the wall base. A slight increase occurs in the position of the application point with increasing frequency ratio and excitation amplitude. For the investigated acceleration amplitude range, position of the application point calculated by M-O Method are in good agreement with test results and the analytical approach captures the general trend observed in the tests; however, this method does not take into consideration of the influence of excitation frequency on the response of the retaining walls. Steedman-Zeng approach provides more reasonable estimates of the application point for different excitation frequencies.
11. In the tests, rotation and sliding of the wall are relatively small. Deflection of the wall stem was observed to be the major mode of deformation.
12. Wall deflections predicted by the finite difference method is in fairly good agreement with the test data. It was observed that presence of geofoam buffers with various thicknesses contributes to the reduction of the pre-excitation and post-excitation deflections of the wall. According to the results of the numerical modeling study, it was observed that backfill displacements are concentrated at lower mid-height of the wall when geofoam buffers are installed between the wall and the backfill.
13. Dynamic earth pressure coefficients back-calculated from the physical modeling study were compared to those predicted by the numerical model. It was observed that predictions of finite difference analyses were relatively lower than the results of the physical modeling tests. However, predictions are successful in determining the general trend for the wall models having various relative wall flexibilities.

14. Numerical simulations performed for a 6m high cantilever wall subjected to an excitation recorded in August 17, 1999 Kocaeli earthquake exhibited the contribution of geofoam buffers on seismic performance of cantilever earth retaining walls. The numerical results indicate that the presence of an EPS panel behind the wall may result in a reduction of the permanent flexural wall deflections as well as total dynamic thrust likely to be experienced by the wall during an earthquake.

The current study has shown significant contribution of deformable geofoam buffers on the seismic performance improvement of the retaining walls. However, several areas in this field require further investigation. Future research will address the influence of geofoam buffer thickness, density and associated stress-strain properties on the earthquake-induced stresses and displacements for various types of retaining structures towards optimizing the seismic buffer function of deformable geofoam inclusions

REFERENCES

AabФe, R. (2000). Evidence of EPS Long Term Performance and Durability as a Lightweight Fill. Washington,D.C.,USA: Transportation Research Board 79th Annual Meeting.

Abdelrahman, G. E., Kawabe, S., Tsukamoto, Y., Tatsuoka, F. (2008a). Small-strain stress-strain properties of expanded polystrene geofoam. Soils and Foundations, 48(1), 61-71.

Abdelrahman, G. E., Kawabe, S., Tatsuoka, F., Tsukamoto, Y. (2008b). Rate effects on the stress-strain behavior of EPS geofoam. Soils and Foundations, 48(4), 479-494.

Aggour, M. S., Brown, C. B. (1973). Retaining walls in seismic areas. Proceedings, 5th World Conference on Earthquake Engineering, (pp. 2624-2627).

Al Atik, L., Sitar, N. (2010). Seismic Earth Pressures on Cantilever Retaining Structures. J. Geotech. and Geoenvir. Engrg., 136, 1324-1334.

Alabama Department of Transportation. (2004). Foundation Report: Slide Correction on AL 44 At MP 6.4, Marion County. Montgomery: Alabama Department of Transportation.

Arellano, D., Tatum, J. B., Stark, T. D., Horvath, J. S., Leshchinsky, D. (2010). A Framework for the Design Guideline for EPS-Block Geofoam in Slope Stabilization and Repair. Transportation Research Record: Journal of the Transportation Research Board, 2170, 100-108.

Armstrong, R., Alfaro, M. (2003). Reduction of seismic induced pressures on rigid retaining structures using compressible inclusions: A numerical study. Proceedings of the 56th Canadian Geotechnical Conference (pp. 500-505). Winnipeg: The Canadian Geotechnical Society.

ASTM. (1997). ASTM D6112: Predicting the long term creep behavior of viscoelastic materials Appendix X5. Standard.

ASTM. (2005). Standard guide for use of expanded polystyrene (EPS) geofoam in geotechnical projects. Pennsylvania: American Society of Testing Materials.

ASTM. (2006). Standard specification for rigid cellular polystyrene geofoam. West Conshohocken: ASTM.

Athanasopoulos, G. A., Nikolopoulou, C. P., Xenaki, V. C. (2007). Reducing the seismic earth pressure on retaining walls by EPS geofoam-buffers-numerical parametric study. Proceedings of the 2007 Geosynthetics Conference, (p. p.15). Washington DC.

Athanasopoulos, G. A., Pelekis, P. C., Xenaki, V. C. (1999). Dynamic properties of EPS geofoam: an experimental investigation. Geosynthetics International, 6(3), 171-194.

Athanasopoulos, G., Nikolopoulou, C., Xenaki, V. (2007). Seismic Isolation of earth-retaining structures by EPS geofoam compressible inclusions-Dynamic FE Analyses. Proceedings of the 4th Conference on Earthquake Geotechnical Engineering. Thessaloniki.

Atmatzidis, D. K., Missirlis, E. G., Chrysikos, D. A. (2001). An investigation of EPS geofoam behaviour in compression. EPS Geofoam 2001- Proceedings of the 3rd International Conference. Salt Lake City.

Bakeer, R. M., Bhatia, S. K., Ishibashi, I. (1990). Dynamic earth pressure with various gravity wall problems. Design and Performance of Earth Retaining Structures, ASCE Geotechnical Special Publication No.25, pp. 887-899.

Bartlett, S. F., Farnsworth, C. B. (2004). Monitoring and modeling of innovative foundation treatment and embankment construction used on the I-15 reconstruction project, project management plan and instrument installation report. UDOT Research Rep. No. UY-04.19, Utah Department of Transportation Research Department, Salt Lake City.

BASF. (1997). Styropor Technical Information.

BASF AG. (1991). Highway Construction and Ground Insulation. Technical Info Bulletin No.1-800e.

Bathurst, R. J., Hatami, K. (1998). Seismic response analyses of a geosynthetic reinforced soil retaining wall. Geosynthetics International, 5(1), 127-166.

Bathurst, R. J., Zarnani, S. (2008). Numerical Modeling of EPS Seismic Buffers. The 12th International Conference on International Association for Computer Methods and Advances in Geomechanics, (pp. 425-432). Goa, India.

Bathurst, R. J., Keshavarz, A., Zarnani, A., Take, A. (2007b). A simple displacement model for the response analysis of EPS geofoam seismic buffers. Soil Dynamics and Earthquake Engineering, 27, 344-353.

Bathurst, R., Zarnani, S., Gaskin, A. (2007a). Shaking Table Testing of Geofoam Seismic Buffers. Soil Dynamics and Earthquake Engineering, 27(4), 324-332.

Beinbrech, G., Hillmann, R. (1998). EPS in road construction-current situation in Germany. Geotextiles and Geomembranes(15 (special issue)).

Beinbrech, G., Hohwiller, F. (2000). Cushion Foundations: Rigid expanded polystyrene foam as a deforming and cushioning layer. Ground Improvement, 4(1), 3-12.

Bolton, M. D., Steedman, R. S. (1982). Centrifugal testing of micro-concrete retaining walls subject to base shaking. Proceedings of Conference on Soil dynamics and Earthquake Engineering, (pp. 311-329). Southampton.

Bowles, J. E. (1996). Foundation analyses and design. New York: McGraw-Hill.

Buckingham, E. (1915). The principle of similitude. Nature, 396-397.

Butterfield,R.,Andrawes,K.Z. (1970). An Air Activated Sand Spreader for Forming Uniform Sand Beds. Geotechnique, 20(1):97-100.

Byrne, P. M., Salgado, F. (1981). Seismic response of retaining structures. Proceedings of the International Conference on Recent Advances in Geotechnical Earthquake Engineering and Soil Dynamics. St. Louis.

Calisan, O. (1999). Model study on the seismic behavior of gravity retaining walls. PhD. Thesis, METU, Ankara .

Chang, N. Y., Makarechi, H. (1982). Effects of gradation on shear modulus of Denver sand at small strains. Proceedings of the 1st International Conference on Soil Dynamics and Earthquake Engineering, (pp. 117-129). Southampton, USA.

Chun, B. S., Lim, H. S., Shin, Y. W. (2001). Application of constitutive model to predict the behavior of EPS geofoam. KSCE Journal of Civil Engineering, 5(2), 175-183.

Chun, B. S., Lim, S. H., Sagong, M. S., Kim, K. (2004). Development of a hyperbolic constitutive model for expanded polystyrene (EPS) geofoam under triaxial compression tests. Geotextiles and Geomembranes, 22, 223-237.

Cilingir, U. (2005). A model study on the effects of wall stiffness and surcharge on dynamic lateral earth pressures. M.Sc. Thesis, METU, Ankara.

Clough, G. W., Duncan, J. M. (1971). Finite element analysis of retaining wall behavior. Journal of Soil Mechanics and Foundation, 97, 1657-1673.

Das, B. M. (1983). Fundamentals of soil dynamics. New York: Elsevier Science Publishing Co. Inc.

Davies, M. (1994). Dynamic Soil Structure Interaction resulting from blast loading. Proceedings of the International Conference on Centrifuge Modeling, (pp. 319-324).

Dewoolkar, M. M., Ko, H., Pak, R. Y. (2001). Seismic behavior of cantilever retaining walls with liquefiable backfills. Journal of Geotechnical and Geoenvironmental Engineering, 127(5), 424-435.

Duskov, M. (1997). Materials research on EPS-20 and EPS-15 under representative conditions in pavement structures. Geotextiles and Geomembranes, 15(1-3), 147-181.

Edgar, T. V., Puckett, J. A., Dspain, R. B. (1989). Effects of geotextiles on lateral pressure and deformation in highway embankments. Geotextiles and Geomembranes, 8(4), 275-292.

Egan, J. A., Ebeling, R. M. (1985). Variation of small-strain shear modulus with undrainedshear strength of clay. Proceedings of the Second International Conference on Soil Dynamics and Earthquakes on Board the Liner, (pp. 2-27 to 2-36).

Elragi, A. F. (2000). Selected Engineering Properties and Applications of EPS Geofoam. Ph.D Thesis, State University of New York, College of Environmental Science and Forestry, New York.

Elragi, A., Negussey, D., Kyanka, G. (2000). Sample size effects on the behavior of EPS geofoam. Proceedings of the Soft Ground Technology Conference, (pp. 280-291).

Endo, O., Komanobe, K. (1998). Single and multidirectional shaking table tests of sand liquefaction. Proceedings of the International Conference on Earthquake Geotechnical Engineering, 2, pp. 675-680. Tokyo.

Ertugrul, O. L. (2006). A Finite Element Modeling Study on the Seismic Response of Cantilever Retaining Walls. M.S. Thesis, Middle East Technical University, Ankara.

Ertugrul, O. L. (2007). İstinat duvarlarının dinamik yükler altındaki davranışının sonlu elemanlar metodu kullanılarak modellenmesi. TMMOB İnşaat Müh. Odası 2. Geoteknik Sempozyumu, Kasım 2007, Adana, Sayfa 343-358.

Ertugrul, O. L., Trandafir, A. C. (2011). Reduction of lateral earth forces acting on rigid non-yielding retaining walls by EPS geofoam inclusions. ASCE Journal of Materials in Civil Engineering, doi:10.1061/(ASCE)MT.1943-5533.0000348 (in press).

Ertugrul, O. L., Ozkan, M. Y., Saglam, S. (2008). Excitation and Flexibility Effects on the Dynamic Response of Cantilever Earth Retaining Walls. Proceedings of the Geotechnical Earthquake Engineering and Soil Dynamics Conference IV, (GSP181). Sacramento.

Ertugrul, O. L.,Trandafir , A. C., Ozkan, M. Y. (2010). Reduction of lateral earth pressures on rigid retaining walls by EPS geofoam. Zemin Mekanigi ve Temel Muhendisligi 13. Ulusal Kongresi. Istanbul.

Findley, W. N., Khosla, G. (1956). An equation for tension creep of three unfilled thermoplastics. SPE Journal, 12(12), 20-25.

Finn, W. D., Yodendrakumar, M., Otsu, H., Steedman, R. S. (1989). Seismic response of cantilever retaining wall. Proc. of 4th International Conference on Soil Dynamics and Earthquake Engineering, (pp. 331-431). Southampton.

Finn, W. L. (1988). Dynamic analyses in geotechnical engineering. Earthquake Engineering and Soil Dynamics II, (pp. 523-591).

Forschungsgesellschaft für Straßen- und Verkehrswesen. (1995). Merkblatt für die verwendung von EPS-hartschaumstoffen beim bau von straßendämmen. Köln, Deutschland.

Franklin, A. G., Chang, F. K. (1977). Earthquake Resistance of Earth and Rock-Fill Dams. Vicksburg: Soil and Pavements Laboratory, U.S Army Waterways Experiment Station.

Frydenlund, T. E.,АавФе, R. (1996). Expanded Polystyrene-The Light Solution. Proceedings of the International Symposium on EPS construction method, (pp. 31-46). Tokyo, Japan.

Gaskin, A. P. (2000). An investigation into the use of expanded polystrene for seismic buffers. Kingston, Ontario: Queen's University.

Gazetas, Gazetas, G., Psarropoulos, P. N., Anastasopoulos, I., Gerolymos, N. (2004). Seismic behavior of flexible retaining walls subjected to short duration moderately strong excitation. Soil Dynamics and Earthquake Engineering, 24, 537-550.

Geotech Systems Corporation. (1999). Terralite EPS geofoam. Retrieved from http://www.geosyscorp.com/

Gibson, A. D. (1996). Physical scale modeling of geotechnical structures at one-G. Technical Report: CaltechEERL:1996.SML-97-01. California Institute of Technology.

Gnip, I. J., Kersulis, V. I., Vaitkus, S. I. (2005). Predicting the deformability of expanded polystrene in short term compression. Mechanics of Composite Materials, 41(2), 105-108.

Gnip, I. Y., Vejelis, S., Kersulis, V., Vaitkus, S. (2007). Deformability and tensile strength of expanded polystyrene under short-term loading. Polymer Testing, 26, 886-895.

Goh, A. T. (1993). Behavior of cantilever retaining walls. Journal of Geotechnical Engineering, 119, 1751-1770.

Gomez, J. E., Filz, G. M., Ebeling, R. M. (2000). Extended Load/Unload/Reload Hyperbolic Model for Interfaces: Parameter Values and Model Performance for the Contact between Concrete and Coarse Sand. US Army Corps of Engineers.

Green, R. A., Olgun, C. G. (2008). Response and modeling of cantilever retaining walls subjected to seismic motions. Computer-aided Civil and Infrastructure Engineering, 23, 309-322.

Hatami, K., Withoeft, A. (2008). A numerical study on the use of geofoam to increase the external stability of reinforced soil fills. Geosynthetics International, 15(6), 452-470.

Hausler, E. (2002). Influence of ground improvement in settlement and liquefaction: a study based on field case history evidence and geotechnical centrifuge tests. Ph.D. Thesis, University of California, Berkeley.

Hazarika, H. (2001). Mitigation of Seismic Hazard on retaining structures- A numerical Experiment. Proceedings of the 11th International Offshore and Polar Engineering Conference (pp. 459-464). Stavanger, Norway: International Society of Polar and Offshore Engineers.

Hazarika, H. (2005). A soil-structure Interaction model with multiple participating components. In G. Barla (Ed.), Proceedings of the 11th International Conference on Computer Methods and Advances in Geomechanics (pp. 659-666). Torino: Prediction Analysis and Design in Geotechnical Applications.

Hazarika, H. (2006). Stress-strain modeling of EPS geofoam for large strain applications. Geotextiles and Geomembranes, 24, 79-90.

Hazarika, H., Okuzono, S. (2004). On a performance enhancement of a soil-structure system with sandwiched inclusion. Proceedings of the 11th International Conference on Soil Dynamics and Earthquake Engineering and the 3rd International Conference on Earthquake Geotechnical Engineering, (pp. 257-263). Berkeley, CA.

Hazarika, H., Okuzono, S. (2004). On the performance enhancement of a soil-structure system with sandwiched inclusion. Proceedings of the 11th International Conference on Soil Dynamics and Earthquake Engineering, (pp. 257-263). Berkeley.

Hazarika, H., Nakazawa, J., Matsuzawa, H., Negussey, D. (2001). On the seismic earth pressure reduction against retaining structures using lightweight geofoam fill. Proceedings of the Fourth International Conference on recent advances in

geotechnical earthquake engineering and soil dynamics in Honor of Professor Liam Finn. San Diego.

Hazarika, H., Okuzono, S., Matsuo, Y. (2003). Seismic Stability Enhancement of Rigid Non-yielding Retaining Walls. Proceedings of 13th International Offshore and Polar Engineering Conference (pp. 1244-1249). Honolulu, Hawai.

Head, K. H. (1992). Manual of soil laboratory testing: Soil classification and compaction tests (Vol. 1). London: Pentech Press.

Horvath, J. (1995). Geofoam Geosynthetic. New York: P.C. Scarsdale.

Horvath, J. S. (1991a). Using geosynthetics to reduce earth loads in rigid retaining structures. Proceedings of Geosynthetics '91 Conference, (pp. 409-423). Atlanta, USA.

Horvath, J. S. (1991b). Using geosynthetics to reduce surcharge-induced stresses on rigid earth-retaining structures. Transportation Research Record, pp. 47-53.

Horvath, J. S. (1995). Geofoam Geosynthetic. New York: P.C. Scarsdale.

Horvath, J. S. (1997). Compressible inclusion function of EPS geofoam. Geotextiles and Geomembranes, 15(1), 77-120.

Horvath, J. S. (1998). Mathematical Modeling of the Stress-Strain-Time Behavior of Geosynthetics Using the Findley Equation: Geosynthetics Using the Findley Equation: CE/GE-98-3. Bronx, New York: Manhattan College School of Engineering Civil Engineering Department.

Horvath, J. S. (2008). Extended Veletsos-Younan model for geofoam compressible inclusions behind rigid, non-yielding earth-retaining structures. Geotechnical Earthquake Engineering and Soil Dynamics IV. Geotechnical Special Publication #181. Sacramento: ASCE.

Horvath, J. S. (2008). Seismic lateral earth pressure reduction on earth-retaining structures using geofoams. Geotechnical Earthquake Engineering and Soil Dynamics IV. Sacramento: American Society of Civil Engineers.

Horvath, J. S. (2008). Seismic Lateral Earth Pressure Reduction on Earth-Retaining Structures using Geofoams. Proceedings of GEESD IV. Sacramento: ASCE.

Horvath, J. S. (2010, July-August). Emerging trends in failures involving EPS-Block Geofoam Fills. Journal of Performance of Constructed Facilities, 365-372.

Hotta, H., Nishi, T., Kuroda, S. (1996). Report of results of assessment of damage caused by earthquakes. Proceedings of International Symposium On EPS Construction Method (EPS Tokyo '96), (pp. 303-318). Tokyo, Japan.

Iai, S. (1989). Similitude for shaking table tests on soil-structure-fluid model in 1-g gravitational field. Soils and Foundations, 29, 105-118.

Ikizler, B., Aytekin, M., Nas, E. (2008). Laboratory study of expanded polystyrene (EPS) geofoam used with expansive soils. Geotextiles and Geomembranes, 26, 189-195.

Inglis, D., Macleod, G., Naesgaard, E., Zergoun, M. (1996). Basement Wall With Seismic Earth Pressure and Novel Expanded Polystyrene Foam Buffer Layer. Proceedings of 10th Annual Symposium of the Vancouver Geotechnical Society. Vancouver: Vancouver Geotechnical Society.

Ishii, Y., Arai, H., Tsuchida, H. (1960). Lateral earth pressure in an earthquake. Proceedings, Earthquake Engineering, Second World Conference, 1. Tokyo, Japan.

Itasca. (2008). FLAC: Fast Lagrarian Analysis of Continua Version 6. Minneapolis, Minnesota, U.S.: Itasca Consulting Group Inc.

Itoh, K., Zeng, X., Koda, M., Murata, O., Kusakabe, O. (2005). Centrifuge simulation of wave propagation due to vertical vibration of shallow foundations and vibration attenuation countermeasures. Journal of Vibration and Control, 11, 781-800.

Jafarzadeh, F. (2004). Design and evaluation concepts of laminar shear box for 1-g shaking table tests. 13th World Conference on Earthquake Engineering . Vancouver, Canada.

Jakrapiyanun, W. (2002). Physical modeling of dynamic soil-foundation-structure-interaction using a laminar container. San Diego: University of California .

Jutkofsky, W. S., Sung, J. T., Negussey, D. (2000). Stabilization of an Embankment Slope with. Transportation Research Record, pp. 94-102.

Kagawa, T. (1978). On the similitude in model vibration tests of earth structures. Proc. of Japan Society of Civil Engineers, 275, pp. 69-77.

Karpurapu, R., Bathurst, R. J. (1992). Numerical investigation of controlled yielding of soil-retaining wall structures. Geotextiles and Geomembranes, 11, 115-31.

Koerner, R. M., (2005). Designing with Geosynthetics, Prentice Hall.

Kokusho, T., Iwatate, T. (1979). Scaled model tests and numerical analyses on nonlinear dynamic response of soft grounds. Proc. of Japanese Society of Civil Engineers, 285, pp. 57-67.

Koseki, J. (2002). Seismic performance of retaining walls-case histories and model tests. Proceedings of the 4th Forum on Implications of Recent Earthquakes on Seismic Risk, (pp. 95-107). Tokyo.

Kramer, S. (1996). Geotechnical Earthquake Engineering. NJ, USA: Prentice Hall.

Kuroda, S., Yamazaki, F., Okubo, N. (1994). Assessing Earthquake Resistance of Expanded Polystyrene Embankment Hit by Earthquakes. Basic Engineering, 22(10), 64-70.

Lambe, T. W., Whitman, R. V. (1969). Soil Mechanics. John Wiley and Sons.

Langhaar, H. (1951). Dimensional analysis and theory of models. New York: John Wiley and Sons.

Leo, C. J., Kumruzzaman, M., Wong, H., Yin, J. H. (2008). Behavior of EPS geofoam in true triaxial compression tests. Geotextiles and Geomembranes, 26, 175-180.

Ling, H. I., Mohri, Y., Leshchinsky, D., Burke, C., Matsushima, K., Liu, H. (2005). Large scale shaking table tests on modular-block reinforced soil retaining walls. Journal of Geotechnical and Geoenvironmental Engineering, 131.

Lynn, P. A., Fuerst, W. (1990). Introductory Digital Signal Processing with Computer Applications. Toronto: John Wiley and Sons.

Lysmer, J., Kuhlmeyer, R. L. (1969). Finite dynamic model for the infinite media. ASCE Journal of the Engineering Mechanics Division, 859-877.

Madabhushi, S. P. (1994). Dynamic response of the equivalent shear beam (ESB) container. Technical Report no. CUED/D-SOILS/TR.270.

Magnan, J. P., Serratice, J. F. (1989). Mechanical properties of expanded polystrene for applications in road embankment. Laboratoire Central Ponts et Chaussees, 164, pp. 25-31.

Matsuda, T., Ugai, K., Gose, S. (1996). Application of EPS to backfill of abutment for earth pressure reduction and impact absorption. Proceedings of the International Symposium on EPS Construction Method, (pp. 327-332). Tokyo, Japan.

Matsuo, H. (1941). Experimental study on the distribution of earth pressures acting on a vertical wall during earthquakes. Journal of Japanese Society of Civil Engineers, 27(2).

Matsuo, H., Ohara, S. (1960). Lateral earth pressure and stability of quay walls during earthquakes. Proceedings of the Second World Conference on Earthquake Engineering, pp. 165-181. Kyoto.

Matsuo, H., Ohara, S. (1960). Lateral earth pressure and stability of quay walls during earthquakes. Proceedings, Earthquake Engineering, Third World Conference,, 1. New Zeland.

Matsuo, O., Tsutsumi, T., Yokohama, K., Saito, Y. (1998). Shaking table tests and analysis of geosynthetic-reinforced soil retaining walls. Geosynthetics International, 5(1), 97-126.

Mcgown, A., Andrawes, K. Z. (1987). Influence of wall yielding on lateral stresses in unreinforced and reinforced fills. Crowthrone, Berkshire, UK: Transportation and Road Research Laboratory.

McGown, A., Andrawes, K. Z., Murray, R. T. (1988). Controlled Yielding of the lateral boundaries of soil retaining structures. In R. D. Holtz (Ed.), Proceedings of the ASCE symposium on geotechnics for soil improvement, (pp. 193-22).

McGown, A., Murray, R. T., Andrawes, K. Z. (1988). Controlled yielding of the lateral boundaries of soil retaining structures. Symposium on Geosynthetics for Soil Improvement (pp. 193-211). Nashville: ASCE.

Meymand, P. J. (1998). Shaking table scale model tests of nonlinear soil-pile-superstructure interaction in soft clay. PhD Thesis, Berkeley: University of California.

Missirlis, E. G., Atmatzidis, D. K., Chrysikos, D. A. (2004). Compressive creep behavior of EPS geofoam. In R. Floss, G. Brau, M. Nussbaumer, K. Laackmann (Ed.), Euro Geo3 Geosynthetics Conference. Munich, Germany.

Moghadam, A. M., Ghalandarzadeh, A., Towhata, I., Moradi, M., Ebrahimian, B., Hajialikhani, P. (2009). Studying the effects of deformable panels on the seismic displacements of gravity quay walls. Ocean Engineering, 35(15-16), 1129-1148.

Mononobe, N., Matsuo, M. (1929). On the determination of earth pressures during earthquakes. Proc. World Engrg. Congress, 9, pp. 179-187.

Mononobe, N., Matsuo, M. (1932). Experimental investigation of lateral earth pressure during earthquakes. Tokyo: Earthquake Research Institute and Research Institute for Public Works.

Murillo, C., Thorel, L., Caicedo, B. (2009). Ground vibration isolation with geofoam barriers: centrifuge modeling. Geotextiles and Geomembranes, 27(6), 423-434.

Murphy, G. P. (1997). The influence of creep on the performance of a compressible inclusion. Geotextiles and Geomembranes, 15, 121-131.

Nadim, F., Whitman, R. V. (1982). A numerical model for evaluation of seismic behavior of gravity retaining walls. M.I.T. .

Nakamura, S. (2006). Reexamination of Mononobe-Okabe theory of gravity retaining walls using centrifuge model tests. Soils and Foundations, 46(2), 135-146.

Nazarian, H. N., Hadjian, A. H. (1979, September). Earthquake-Induced Lateral Soil Pressures on Structures. ASCE Journal of Geotechnical Engineering, 105, 1049-1066.

Negussey, D. (1997). Properties and Applications of Geofoam. Society of Plastics Engineers.

Negussey, D. (1998). Putting Polystyrene to Work. Civil Engineering, pp. 43-48.

Negussey, D. (2001). Slope stabilization with geofoam. New York: Geofoam Research Center, Syracuse University.

Negussey, D., Jahanandish, M. (1993). Comparison of some engineering properties of expanded polystyrene with those of soils. Transportation Research Record, pp. 43-48.

Negussey, D., Sun, M. (1996). Reducing Lateral Pressure by Geofoam (EPS) Substitution. Proceedings of International Symposium on EPS construction method, (pp. 200-211). Tokyo, Japan.

Newman, M. P., Bartlett, S. F., Lawton, C. E. (2010, February). Numerical Modeling of Geofoam Embankments. Journal of Geotechnical and Geoenvironmental Engineering, 290-298.

Newmark, N. M. (1965). Effects of earthquakes on dams and embankments. Geotechnique, 15(2), 139-160.

Newton, H. J. (1988). TIMESLAB: A Time Series Analysis Laboratory. Pacific Groove, CA: Wadsworth and Brooks/Cole.

Okabe, S. (1926). General theory of earth pressures. J. Japan. Soc.Civil Eng., 12(1), 123-134.

Okamoto M., F. S. (2006). Geomechanics and Geotechnics of Particulate Media. In M. Hyodo, An evaluation of the dry pluviation preparation technique applied to silica sand samples (pp. 33-39). London: Taylor and Francis Group.

Ortiz, L., Scott, R. F., Lee, J. (1983). Dynamic centrifuge testing of a cantilever retaining wall. Earthquake Engineering and Structural Dynamics, 11, 251-268.

Ossa, A., Romo, M. P. (2008). A model for EPS dynamic shear modulus and damping ratio. Proceedings of First Pan American Geosynthetics Conference and Exhibition, (pp. 894-901). Cancun, Mexico.

Ossa, A., Romo, M. P. (2009). Micro- and macro-mechanical study of compressive behavior of expanded polystyrene. Geosynthetics International, 16(5), 327-338.

Ossa, A., Romo, M. P. (2010). Dynamic characterization of EPS geofoam. Geotextiles and Geomembranes, 29, 40-50.

Paik, K. H., Salgado, R. (2003). Estimation of active earth pressure against rigid retaining walls considering arching effects. Geotechnique, 53(7), 643-653.

Partos, A., Kazaniwsky, P. (1987). Geoboard reduces lateral earth pressures. Geosynthetics'97 (pp. 628-39). New Orleans: Industrial Fabrics Association International.

Pelexis, P., Xenaki, V., Athanasopoulos, G. (2000). Use of EPS geofoam for seismic isolation of earth retaining structures: Results of a FEM study. Proceedings of the 2nd European Geosynthetics Conference, (pp. 843-846). Bologna.

Prasad, S. K., Towhata , I., Chandradhara, G. P., Nanjundaswavy, P. (2004). Shaking table tests in earthquake geotechnical engineering. Geotechnics and Earthquake Hazards, 87(10), 1398-1404.

Preber, T., Bang, S., Chung, Y., Cho, Y. (1995). Behavior of Expanded Polystyrene Blocks. Transportation Research Record, 1462, pp. 36-46.

Psarrapoulos, P. N. (2005). Seismic Earth Pressures on rigid and flexible retaining walls. Soil Dynamics and Earthquake Engineering, 25, 795-809.

Reeves, J. N., Filz, G. M. (2000). Earth force reduction by a synthetic compressible inclusion. Department of Civil Eng. , Virginia Tech, Geotech Systems Corp.

Rehnman, S. E., Broms, B. B. (1972). Lateral pressures on basement wall; Results from full scale tests. Proceedings of the Fifth European Conference on Soil Mechanics and Foundation Engineering, (pp. 189-197).

Reuter, G., Rutz, J. (2001). Use of Geofoam for Landslide Stabilization, Bayfield County, Wisconsin. Proceedings of the 3rd International Geofoam Conference. Salt Lake City.

Richards, J. R., Elms, D. (1977). Seismic behavior of gravity retaining walls. Christchurch: University of Canterbury.

Rocha, M. (1957). The possibility of solving soil mechanics prbolems by the use of models. Proc. 4th I.C.S.M.F.E., Vol.1, pp. 183-188.

Roscoe, K. (1968). Soils and model tests. Journal of Strain Analysis, 3(1), 57-64.

Sanders, R. (1996). United Kingdom Design and Construction Experience with EPS. Proceedings of International Symposium on EPS Construction Method, (pp. 235-246). Tokyo, Japan.

Schnabel, P. B., Lysmer, J., Seed, H. D. (1972). Shake: A computer program for earthquake response analysis of horizontally layered sites. Berkeley: College of Engineering, UC .

Scott, R. F. (1973). Earthquake-induced earth pressures on retaining walls. Proc. of 5th World Conference on Earthquake Engineering, 2, pp. 1611-1620. Rome.

Seed, H. B., Idriss, I. M. (1970). Report No. EERC 70-10 Soil Moduli and Damping Factors for Dynamic Response Analyses. Berkeley, California: Earthquake Engineering Research Center, University of California at Berkeley.

Seed, K. B., Whitman, R. V. (1970). Design of earth retaining structures for dynamic loads. Lateral Stresses in Ground and Design of Earth Retaining Structures, ASCE Specialty Conference. New York.

Sherif, M. A., Fang, Y. S. (1984). Dynamic earth pressures on walls rotating about the top. Soils and Foundations, 24, 109-117.

Sherif, M. A., Ishibashi, I., Lee, C. D. (1982). Earth pressures against rigid retaining walls. ASCE Journal of Geotechnical Engineering, 108, 679-695.

Siddharthan, R., Maragakis, E. (1989). Performance of flexible retaining walls supporting dry cohesionless soils under cyclic loads. International Journal for Numerical and Analytical Methods in Geomechanics, 13, 309-326.

Stadler, A. T. (1996). Static and Dynamic Behavior of Cantilever Retaining Walls. Ph.D. Thesis, University of Colorado, Boulder.

Stark, T., Arellano, D., Horvath, J. S., Leshchinsky, D. (2004). Guideline and Recommended Standard for Geofoam Applications in Highway Embankments. Washington, D.C.: Transportation Research Board.

Steedman, R. S. (1984). Modeling the behavior of retaining walls in earthquakes. Ph.D. Thesis, Cambridge University.

Steedman, R. S., Zeng, X. (1990). The seismic response of waterfront retaining walls. ASCE Specialty Conference on Design and Performance of Earth Retaining Structures, Special Technical Publication 25, (pp. 872-886). New York.

Steedman, R. S., Zeng, X. (1991). Centrifuge modeling of the effects of earthquakes on free cantilever walls. Centrifuge'91, Rotterdam: Balkema.

Tajimi, H. (1973). Dynamic earth pressures on basement walls. Proc. of 5th World Conference on Earthquake Engineering, 2, pp. 1560-1569. Rome.

Taylor, C. A., Dar, A. R., Crewe, A. J. (1995). Shaking table modeling of seismic geotechnical problems. Proceedings of 10th European Conference on Eartquake Engineering, (pp. 441-446).

Terzaghi, K. (1943). Theoretical soil mechanics. New York: Wiley.

Thevanayagam, S., Kanagalingam, T., Reinhorn, A., Tharmendhira, R., Dobry, R., Pitman, M., et al. (2009). Laminar box system for 1-g physical modeling of liquefaction and lateral spreading. Geotechnical Testing Journal, 32(5), 438-449.

Trandafir, A. C., Bartlett, S. F., Lingwall, B. N. (2010b). Behavior of EPS geofoam in stress-controlled cyclic uniaxial tests, Geotextiles and Geomembranes. Geotextiles and Geomembranes, 28, 514-524.

Trandafir, A. C., Moyles, J. F., Erickson, B. A. (2010a). Finite-element analysis of lateral pressures on rigid non-yielding retaining walls with EPS geofoam inclusion. Proceedings of the Earth Retention Conference 3 (pp. 756-763). Bellevue, Washington: ASCE, Geo-Institute.

Tsukamoto, H. (1996). Slope Stabilization by the EPS Method and Its Applications. Proceedings of the International Symposium on EPS Construction Method (pp. 362-380). Tokyo: EPS Construction.

Turan, A., Hinchberger, S. D., Naggar, H. (2009). Design and commissioning of a laminar soil container for use on small shaking tables. Soil Dynamics and Earthquake Engineering, 29, 404-414.

Vaslestad, J., Johansen, T. H., Holm, W. (1994). Load reduction on rigid culverts beneath high fills. Long-term behavior Report No.74. Oslo: Norwegian Road Research Laboratory.

Veletsos, A. S., Younan, A. H. (1994a). Dynamic soil pressures on rigid retaining walls. Earthquake Engineering and Structural Dynamics, 29, 1815-1944.

Veletsos, A. S., Younan, A. H. (1994b). Dynamic modeling and response of soil-wall systems. Journal of Geotechnical Engineering, 120(12), 2155-2179.

Veletsos, A. S., Younan, A. H. (1997). Dynamic response of cantilever retaining walls. Journal of Geotechnical and Geoenvironmental Engineering, 123, 161-172.

Veletsos, A. S., Younan, A. H. (2003). Dynamic response of flexible retaining walls. Earthquake Engineering and Structural Dynamics, 29, 1815-1944.

Watanabe, K., Munaf, Y., Koseki, J., Tateyama, M., Kojima, K. (2003). Behaviours of several types of model retaining walls subjected to irregular excitation. Soils and Foundations, 43(5), 13-27.

Whitman, R. V., Liao, S. (1985). Seismic design of retaining walls. Vicksburg, Mississippi: U.S. Army Engineer Waterways Experiment Station.

Whitman, R. V., Lambe , P. C., Kutter, B. L. (1981). Initial results from a stacked ring apparatus for the simulation of a soil profile. Proceeding of International Conference on Recent Advanced Geotechnical Earthquake Engineering and Soil Dynamics, (pp. 361-366).

Wong, H., Leo, C. J. (2006). A simple elatoplastic hardening constitutive model for EPS geofoam. Geotextiles and Geomembranes, 24, 299-310.

Wood, D. M. (2004). Geotechnical Modeling. New York: Spon Press.

Wood, J. H. (1973). Earthquake-induced soil pressures on structures. Ph.D. Thesis, California Institute of Technology, Pasadena.

Wu, G. (1994). Dynamic soil structure interaction: pile foundations and retaining structures. Ph.D. Thesis. Vancouver: The University of British Columbia.

Yeh, S. T., Gilmore, J. B. (1992). Application of EPS for Slide Correction. Stability and Performance of Slopes and Embankments - II, Geotechnical Special Publication No. 31. New York: ASCE.

Younan, A. H., Veletsos, A. S. (2000). Dynamic response of flexible retaining walls. Earthquake Engineering and Structural Dynamics, 29, 1815-1844.

Yunatci, A. (2003). A model study on the seismic behavior of laterally braced sheet pile walls. M.S. Thesis, Middle East Technical University, Ankara.

Yunatci, A. A., Ozkan, M. Y. (2004). A model study on the seismic behavior of the laterally braced sheet pile walls. Proceedings of the 11th International Conference on Soil Dynamics and Earthquake Engineering, (pp. 235-242). Berkeley.

Zarnani, S., Bathurst, J. (2009a). Numerical parametric study of expanded polystyrene geofoam seismic buffers. Canadian Geotechnical Journal, 46, 318-338.

Zarnani, S., Bathurst, R. (2005). Numerical Investigation of geofoam seismic buffers using FLAC. Proceedings of the North American Geosynthetics Society. Las Vegas, Nevada: The Canadian Geotechnical Society.

Zarnani, S., Bathurst, R. (2006). Application of EPS geofoam as seismic buffer: numerical study using FLAC. Proceedings of the 59th Canadian Geotechnical Conference. Vancouver: The Canadian Geotechnical Society.

Zarnani, S., Bathurst, R. (2007). Experimental investigation of EPS geofoam seismic buffers using shake table tests. Geosynthetics International, 14(3), 165-177.

Zarnani, S., Bathurst, R. J. (2009b). Influence of constitutive model on numerical simulation of EPS seismic buffer shaking table tests. Geotextiles and Geomembranes, 27(4), 308-312.

Zarrabi-Kashani, K. (1979). Sliding of gravity retaining wall during earthquakes considering vertical accelerations and changing inclination of the failure surface. Massachusetts: Department of Civil Engineering, MIT.

Zeng, X. (1990). Modeling behavior of quay walls in earthquakes. PhD Thesis, Cambridge University, Cambridge.

Zhang, J., Shamoto, Y., Tokimatsu, K. (1998). Evaluation of earth pressures under any lateral deformation. Soils and Foundations, 38(1), 15-33.

APPENDIX A

CALIBRATION OF THE TRANSDUCERS

A.1 Frictional resistance of laminates

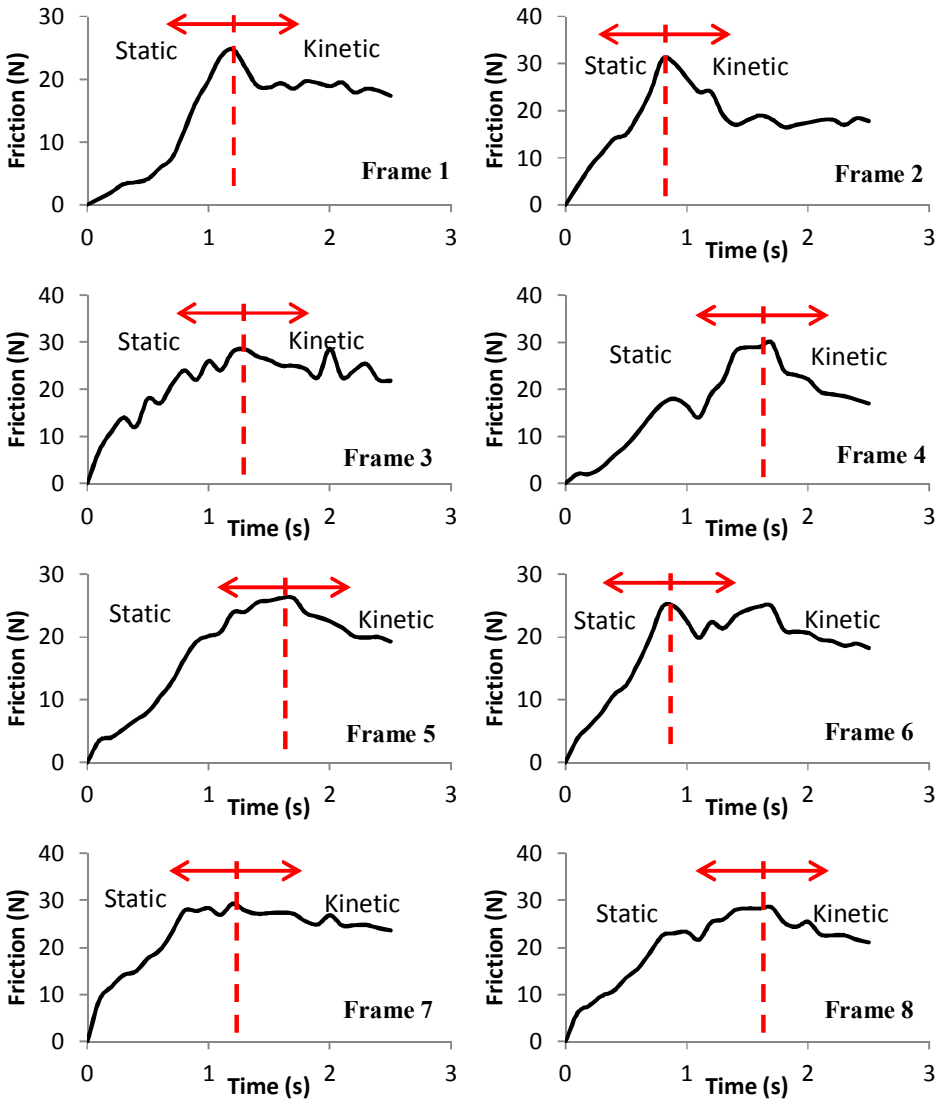

Figure A-1 Frictional forces induced by laminar frames

A.2 Available transducers from previous physical modeling studies

The available transducers which were used in the previous studies are listed in Table A-1

Table A-1 Available transducers from the previous studies

Sensor Type	Brand and Model	Serial Number	Capacity
Load Cell	TML KD2F	BP5297	200kPa
Load Cell	TML KD2F	BP2455	200kPa
Load Cell	TML KD2F	BP6324	200kPa
Load Cell	TML KD2F	BP7332	200kPa
LVDT	TML SDP-100C	623822	100mm
LVDT	TML SDP-100C	622820	100mm
Acceleration transducer	TML AR-5F	83105	5g
Acceleration transducer	TML AR-5F	83886	5g
Acceleration transducer	TML AM-2	2609	1g
Acceleration transducer	TML AR-200G	72148	200g
Acceleration transducer	TML AR-200G	72147	200g

A.3 Additional transducers purchased for the current study

New acceleration and pressure transducers were purchased for this study by BAP 2007-03-03-01 and OYP BAP-08-11-DPT-2002K120510 funding. These additional transducers are listed in Table A-2.

A.3.1 Calibration of the transducers

Accurate calibrations of all the sensors were required prior to the modeling studies. The detailed description of the calibration procedure of the sensors has been presented in Sections A.3.2 through A.3.5.

Table A.2 Additional transducers purchased in the current study

Sensor Type	Brand and Model	Serial Number	Capacity
Pressure Transducer	Honeywell ABH006PGC1B	0142HF	40kPa
Pressure Transducer	Honeywell ABH006PGC1B	0142J6	40kPa
Pressure Transducer	Honeywell ABH006PGC1B	0142J1	40kPa
Pressure Transducer	Honeywell ABH006PGC1B	0142LS	40kPa
Pressure Transducer	Honeywell ABH006PGC1B	0142L8	40kPa
Acceleration transducer	TML ARF-10A	DJB08563	1g
Acceleration transducer	TML ARF-10A	DJB08564	1g
Acceleration transducer	TML ARF-10A	DJB08565	1g
Acceleration transducer	TML ARF-10A	DJB08566	1g
Acceleration transducer	TML ARF-10A	DJB08567	1g

A.3.2 TML Acceleration Transducers

Acceleration transducers were calibrated by rotating them exactly 90° along their sensitive axes as depicted in Fig. A-2.The voltage differences for 1g, -1g and 0g acceleration values were recorded for all the transducers and linear calibration has been performed using the measured voltage differences. Calibration coefficients of the accelerometers at the specific channels are shown in Table A-3. All the values were in agreement with the factory calibration values.

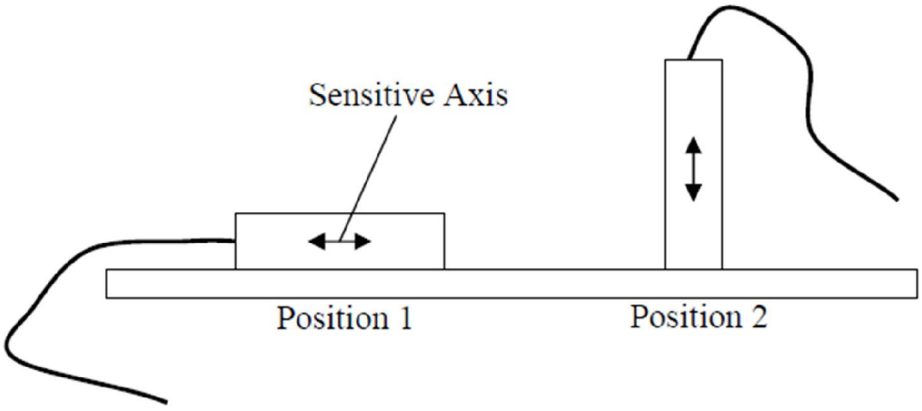

Figure A-2 Calibration of acceleration transducers

Table A-3 Calibration coefficients of the acceleration transducers

Channel #	Sensor #	0 READING (V)	1g READING (V)	-1g READING (V)	k
2	DJB08566	-1.199	-2.058	-0.038	-1.048
3	83105	-0.479	-0.054	-0.903	2.355
4	83886	0.127	0.557	-0.303	2.325
5	AM-2	-0.039	0.996	-1.079	0.963
12	DJB08563	0.000	-0.957	0.957	-1.044
13	DJB08567	-0.562	-1.523	0.381	-1.050
14	DJB08565	0.337	-0.645	1.289	-1.034
15	DJB08564	-1.103	-2.060	-0.151	-1.047

A.3.3 Displacement Transducers

Linear variable differential transformer (LVDT) type transducers having 100 mm measurement capacity are available for the physical tests. Calibration procedure was similar with the procedure explained by Calisan (1999). Displacement transducer was fixed by a stand in a vertical position and objects with known heights were put between flat surface and the sensing rod of the transducer. After taking off the object the change in voltage value was recorded. This procedure was repeated for objects with different heights and then the calibration coefficient was calculated. Calibration coefficients were in agreement with the factory calibration values (Table A-4).

Table A-4 Calibration coefficients for the LVDT's

Ch. #	Sensor #	Displacement (mm) / Voltage difference (V)						k
6	622820	10	20	30	40	50	60	50
		0.201	0.400	0.602	0.799	1.001	1.200	
7	623822	10	20	30	40	50	60	49
		0.204	0.408	0.612	0.816	1.020	1.224	

A.3.4 Honeywell Pressure Transducers

Calibration coefficients of Honeywell ABH006PGC1B transducers have been determined by applying water pressures of known magnitude on the sensing area of the sensors. For the calibration process, each transducer was installed at the bottom end of a cylindrical standpipe filled with water. By changing the height of the water column in the standpipe, output voltage differences of each sensor were measured by using the data acquisition system. Since one of the sensors (#0142L8) was malfunctioning due to an unknown reason, it was not used in the tests. The calibration graphs of the remaining Honeywell sensors are provided in Figure A-3.

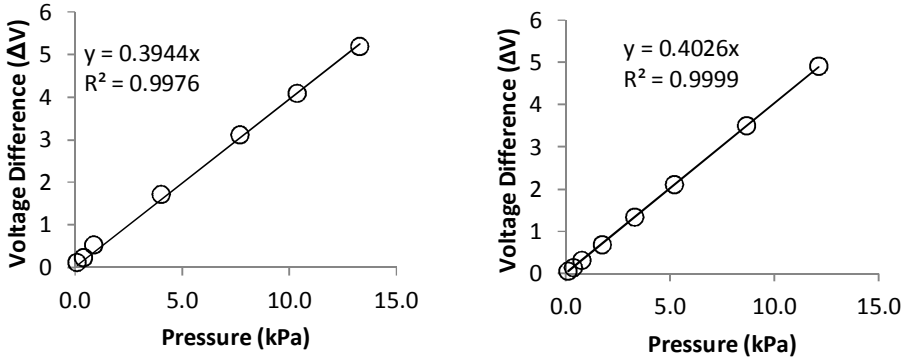

(a) (b)

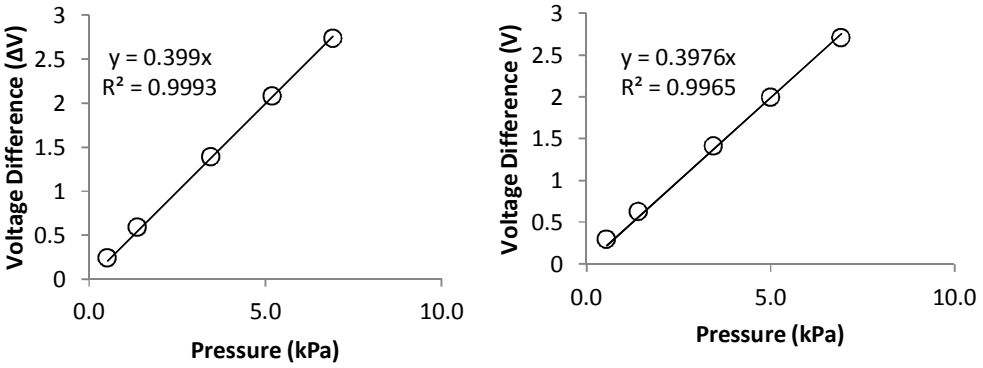

(c) (d)

Figure A-3 Calibration graphs of Honeywell pressure transducers: (a) 0142HF (b) 0142J6 (c) 0142J1 (d) 0142LS

The coefficients which are used to convert voltage differences to physical terms were determined by a linear best fit. The calibration coefficients are provided in Table A-5

Table A-5 Calibration coefficients of the Honeywell pressure transducers at their dedicated channels

Sensor No.	Channel No.	k
0142HF	8	0.3944
0142J6	9	0.4026
0142J1	10	0.3990
0142LS	11	0.3976

A.3.5 TML Earth Pressure Cells

The calibration coefficients of the strain gage type Tokyo Sokki TML KD-2F load cells were measured by placing known weights on the load sensing areas. The calibration charts and the coefficients are shown in Figure A-4Figure and Table A-6Table . Due to low confining stresses and limited overburden height in the model tests, the earth forces are quite smaller than the capacity of the KD-2F load cells (200kPa) which causes low accuracy in the measurements. For this reason, the load cells are used at the base of the model wall to monitor vertical base pressures since higher stresses were expected in this zone.

Table A-6 Calibration coefficients of the TML earth pressure cells at their dedicated channels

Sensor No.	Channel No.	k
BP-2455	1	121.23
BP-5297	2	125.93
BP-6324	3	121.23

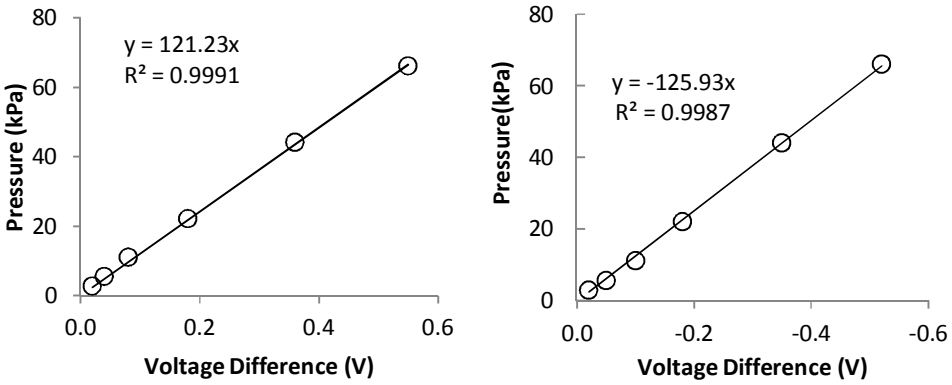

(a)

(b)

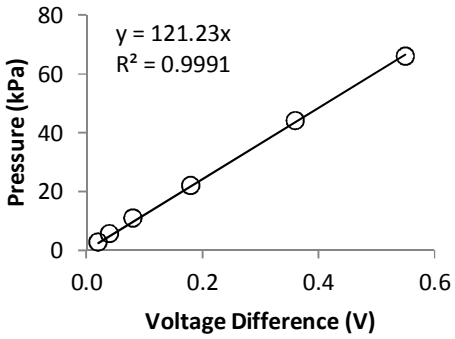

(c)

Figure A-4 Calibration graphs of TML earth pressure cells: (a) BP-2455 (b) BP-5297 (c) BP-6324

APPENDIX B

TEST SERIES

Table B-1 Test series without compressible geofoam inclusion

TEST No	Relative wall stiffness (d_w)	Geofoam inclusion	Relative inclusion thickness (t/H)	Acceleration Amplitude (g)	Acceleration Amplitude (m/s^2)	Freq. (Hz)
CW-A8	8200	Not present	N/A	0.3	2.943	4.25
CW-B8	1025	Not present	N/A	0.3	2.943	4.25
CW-C8	524	Not present	N/A	0.3	2.943	4.25
CW-D8	128	Not present	N/A	0.3	2.943	4.25
CW-C2	524	Not present	N/A	0.1	0.981	5
CW-C4	524	Not present	N/A	0.2	1.962	5
CW-C5	524	Not present	N/A	0.4	3.924	5
CW-C6	524	Not present	N/A	0.6	5.886	5
CW-C7	524	Not present	N/A	0.7	6.867	5
CW-C8	524	Not present	N/A	0.3	2.943	4.25
CW-C9	524	Not present	N/A	0.3	2.943	5.2
CW-C10	524	Not present	N/A	0.3	2.943	6.4
CW-C11	524	Not present	N/A	0.3	2.943	7.7
CW-C12	524	Not present	N/A	0.3	2.943	10

Table B-2 Test series with EPS-15 geofoam inclusion (t/H=0.07)

TEST No	Relative wall stiffness (d_w)	Geofoam inclusion	Relative inclusion thickness (t/H)	Acceleration Amplitude (g)	Acceleration Amplitude (m/s^2)	Freq. (Hz)
CW-AE8	8200	EPS-15	0.07	0.3	2.943	4.25
CW-BE8	1025	EPS-15	0.07	0.3	2.943	4.25
CW-CE8	524	EPS-15	0.07	0.3	2.943	4.25
CW-DE8	128	EPS-15	0.07	0.3	2.943	4.25
CW-CE2	524	EPS-15	0.07	0.1	0.981	5
CW-CE4	524	EPS-15	0.07	0.2	1.962	5
CW-CE5	524	EPS-15	0.07	0.4	3.924	5
CW-CE6	524	EPS-15	0.07	0.6	5.886	5
CW-CE7	524	EPS-15	0.07	0.7	6.867	5
CW-CE8	524	EPS-15	0.07	0.3	2.943	4.25
CW-CE9	524	EPS-15	0.07	0.3	2.943	5.2
CW-CE10	524	EPS-15	0.07	0.3	2.943	6.4
CW-CE11	524	EPS-15	0.07	0.3	2.943	7.7
CW-CE12	524	EPS-15	0.07	0.3	2.943	10

Table B-3 Test series with EPS-15 geofoam inclusion (t/H=0.14)

TEST No	Relative wall stiffness (d_w)	Geofoam inclusion	Relative inclusion thickness (t/H)	Acceleration Amplitude (g)	Acceleration Amplitude (m/s^2)	Freq. (Hz)
CW-AED8	8200	EPS-15	0.14	0.3	2.943	4.25
CW-BED8	1025	EPS-15	0.14	0.3	2.943	4.25
CW-CED8	524	EPS-15	0.14	0.3	2.943	4.25
CW-DED8	128	EPS-15	0.14	0.3	2.943	4.25
CW-CED2	524	EPS-15	0.14	0.1	0.981	5
CW-CED4	524	EPS-15	0.14	0.2	1.962	5
CW-CED5	524	EPS-15	0.14	0.4	3.924	5
CW-CED6	524	EPS-15	0.14	0.6	5.886	5
CW-CED7	524	EPS-15	0.14	0.7	6.867	5
CW-CED8	524	EPS-15	0.14	0.3	2.943	4.25
CW-CED9	524	EPS-15	0.14	0.3	2.943	5.2
CW-CED10	524	EPS-15	0.14	0.3	2.943	6.4
CW-CED11	524	EPS-15	0.14	0.3	2.943	7.7
CW-CED12	524	EPS-15	0.14	0.3	2.943	10

Table B-4 Test series with XPS-22 geofoam inclusion (t/H=0.07)

TEST No	Relative wall stiffness (d_w)	Geofoam inclusion	Relative inclusion thickness (t/H)	Acceleration Amplitude (g)	Acceleration Amplitude (m/s^2)	Freq. (Hz)
CW-AX8	8200	XPS-22	0.07	0.3	2.943	4.25
CW-BX8	1025	XPS-22	0.07	0.3	2.943	4.25
CW-CX8	524	XPS-22	0.07	0.3	2.943	4.25
CW-DX8	128	XPS-22	0.07	0.3	2.943	4.25
CW-CX2	524	XPS-22	0.07	0.1	0.981	5
CW-CX4	524	XPS-22	0.07	0.2	1.962	5
CW-CX5	524	XPS-22	0.07	0.4	3.924	5
CW-CX6	524	XPS-22	0.07	0.6	5.886	5
CW-CX7	524	XPS-22	0.07	0.7	6.867	5
CW-CX8	524	XPS-22	0.07	0.3	2.943	4.25
CW-CX9	524	XPS-22	0.07	0.3	2.943	5.2
CW-CX10	524	XPS-22	0.07	0.3	2.943	6.4
CW-CX11	524	XPS-22	0.07	0.3	2.943	7.7
CW-CX12	524	XPS-22	0.07	0.3	2.943	10

Table B-5 Test series with XPS-22 geofoam inclusion (t/H=0.14)

TEST No	Relative wall stiffness (d_w)	Geofoam inclusion	Relative inclusion thickness (t/H)	Acceleration Amplitude (g)	Acceleration Amplitude (m/s^2)	Freq. (Hz)
CW-AXD8	8200	XPS-22	0.14	0.3	2.943	4.25
CW-BXD8	1025	XPS-22	0.14	0.3	2.943	4.25
CW-CXD8	524	XPS-22	0.14	0.3	2.943	4.25
CW-DXD8	128	XPS-22	0.14	0.3	2.943	4.25
CW-CXD2	524	XPS-22	0.14	0.1	0.981	5
CW-CXD4	524	XPS-22	0.14	0.2	1.962	5
CW-CXD5	524	XPS-22	0.14	0.4	3.924	5
CW-CXD6	524	XPS-22	0.14	0.6	5.886	5
CW-CXD7	524	XPS-22	0.14	0.7	6.867	5
CW-CXD8	524	XPS-22	0.14	0.3	2.943	4.25
CW-CXD9	524	XPS-22	0.14	0.3	2.943	5.2
CW-CXD10	524	XPS-22	0.14	0.3	2.943	6.4
CW-CXD11	524	XPS-22	0.14	0.3	2.943	7.7
CW-CXD12	524	XPS-22	0.14	0.3	2.943	10

APPENDIX C

SUMMARY OF THE TRIAXIAL TESTS ON CINE SAND

Table C-1 Summary of the triaxial tests for the Cine Sand

σ_{3f}(kPa)	p(kPa)	q(kPa)	σ_{1f}(kPa)
10	34.45	24.48	58.90
30	97.82	68.07	165.64
50	156.14	106.73	262.28

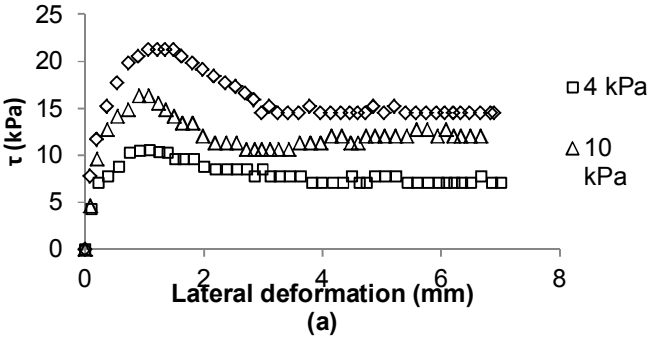

Figure C-1 Results of direct shear tests for loading rate of 0.1mm/min

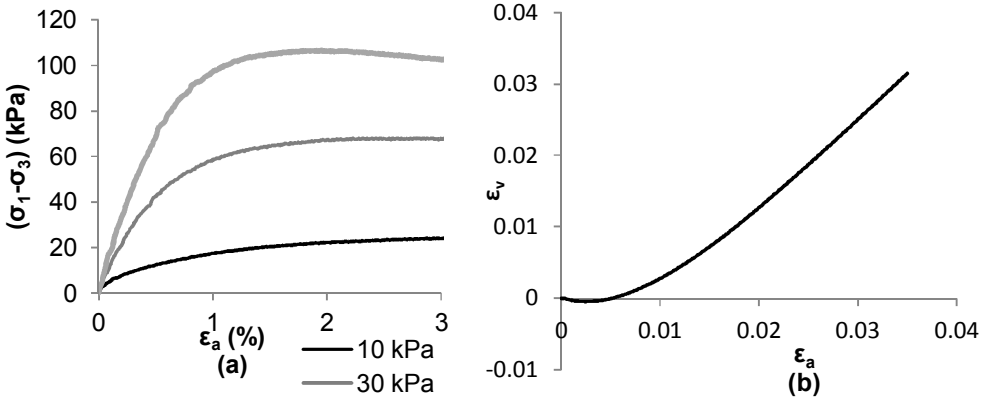

Figure C-2 (a) Test results (0.1mm/min) (b) Volumetric strain behavior

APPENDIX D

STABILITY CALCULATIONS OF THE MODEL WALLS

Using Eq.s D-1 and D-2, the factor of safety for the model types indicated in Table D-1 were calculated. Factor of safety against sliding was calculated by:

$$FS_{sliding} = \frac{\sum V \tan \delta}{0.5 K_O \gamma_{backfill} {H_W}^2} \quad \text{D-1}$$

Similarly, factor of safety against overturning is obtained by:

$$FS_{overturning} = \frac{W_S b + W_c c + P_{av} B}{P_{ah} h} \quad \text{D-2}$$

Factors of safety were calculated by taking the $\phi_{backfill}$ as 43.5° and the wall-base-foundation soil friction as 2/3 of the $\phi_{backfill}$ value.

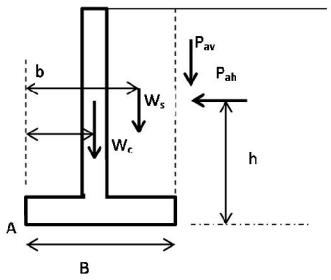

Figure D-1 Overturning safety of the wall

Table D-1 Mass of the model walls

Wall no	t_w *(mm)*	H_w *(mm)*	t_b *(mm)*	W_b*(mm)*	M_w *(kg)*	M_b *(kg)*	M_t *(kg)*
CW-A	2	700	8	500	10.70	30.58	**41.3**
CW-B	4	700	8	500	21.40	30.58	**52.0**
CW-C	5	700	8	500	32.10	30.58	**57.3**
CW-D	8	700	8	500	42.81	30.58	**73.4**

t_w=wall thickness H_w=wall height t_b=base thickness W_b=base width

APPENDIX E

SLIDING AND ROTATION OF THE WALL IN DYNAMIC TESTS

E.1 Sliding along the base

In the tests listed in Table E-1, sliding was observed depending on the characteristics of the base excitations, wall flexibility and compressible buffer type. While calculating the flexural wall deflections, the translational displacements of the wall base were deduced from measured total wall displacements.

Table E-1 Observed wall translations in the dynamic tests

TEST No	Relative wall stiffness (d_w)	Geofoam inclusion	Relative inclusion thickness (t/H)	Acceleration Amplitude (g)	Freq. (Hz)	Translation (mm)
CW-C8	524	Not present	N/A	0.3	4.25	5
CW-D8	128	Not present	N/A	0.3	4.25	8
CW-C5	524	Not present	N/A	0.4	5	3
CW-C6	524	Not present	N/A	0.6	5	5
CW-C7	524	Not present	N/A	0.7	5	8
CW-C8	524	Not present	N/A	0.3	4.25	4
CW-C9	524	Not present	N/A	0.3	5.2	6
CW-C10	524	Not present	N/A	0.3	6.4	6
CW-C11	524	Not present	N/A	0.3	7.7	7
CW-C12	524	Not present	N/A	0.3	10	9
CW-CE7	524	EPS-15	0.07	0.7	5	4
CW-CE12	524	EPS-15	N/A	0.3	10	3
CW-CX6	524	XPS-22	0.07	0.6	5	3
CW-CX7	524	XPS-22	0.07	0.7	5	5
CW-CX11	524	XPS-22	0.07	0.3	7.7	4
CW-CX12	524	XPS-22	0.07	0.3	7.7	6
CW-CXD7	524	XPS-22	0.14	0.7	5	4
CW-CXD11	524	XPS-22	0.14	0.3	7.7	6
CW-CXD12	524	XPS-22	0.14	0.3	7.7	8

E.2 Rotation of the wall base

An acceleration transducer was placed on the wall base to monitor vertical accelerations. Rotation of the wall base was measured by the procedure depicted in Figure E-1. The time history of wall rotation for CW-C7 test, where the most aggressive base acceleration in terms of amplitude and frequency is applied to the base of the model, is provided in Figure E-2. Maximum inclination of the wall is observed as 0.1° which causes 1.22mm horizontal displacement at the wall top during the excitation. The residual wall rotation was observed to be less than 0.02°.

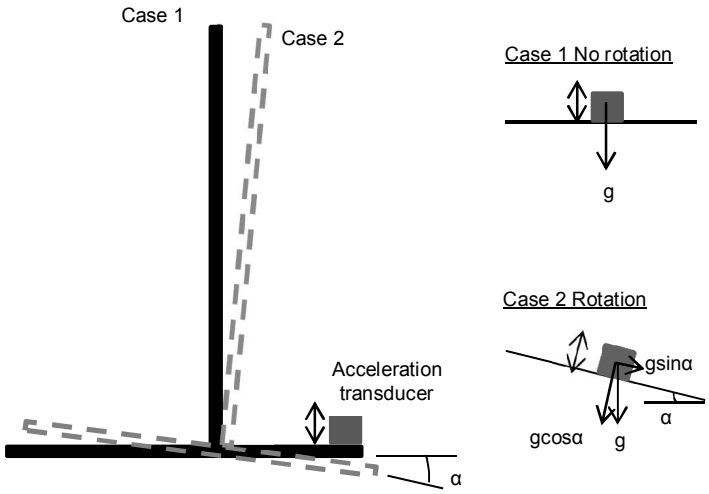

Figure E-1 Measurement of the wall rotation during tests

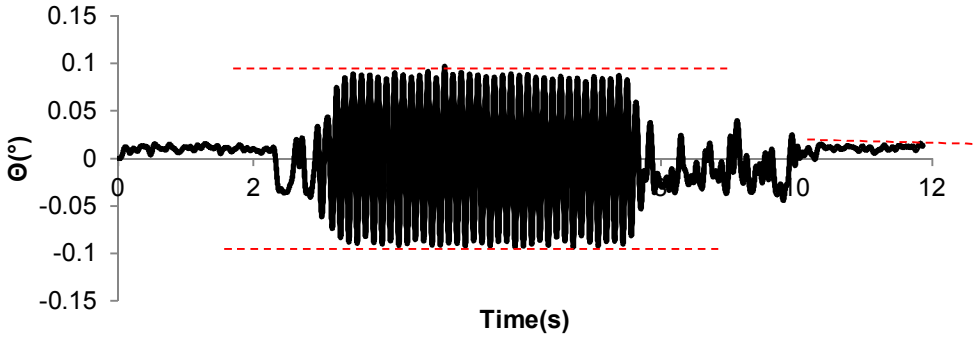

Figure E-2 Rotation of the wall base for CW-D7 test

APPENDIX F

FISH CODE FOR GENERATING SINUSOIDAL VELOCITY TIME HISTORY

```
ini xvel=0 yvel=0 xdis=0 ydis=0  ;sets initial displecements and velecities to zero
def sine_wave     ; defines velocity time history that will be applied at the base of the model
sine_wave=-0.1102*cos(2.0*pi*freq*dytime)
if dytime <(4/freq) then   ; this part causes the time history to reach full amplitude at 4 complete cycles
sine_wave=-((0.1102/4)*((dytime*freq))*cos(2.0*pi*freq*dytime))
end_if
if dytime >5  then
sine_wave = -((0.1102/4)*(((5+(4/freq))-dytime)*freq)*cos(2.0*pi*freq*dytime))
end_if
if dytime >5+(4/freq)  then
sine_wave =0
end_if
end
```

CURRICULUM VITAE

PERSONAL INFORMATION

Surname, Name: Ertuğrul, Özgür Lütfi
Nationality: Turkish
Date and Place of Birth: 1981, Ankara
Marital Status: Married
Phone: +90 (533) 393 70 66
Email: ozgurertugrul@hotmail.com

EDUCATION

Degree	Institution	Year of Graduation
PhD	METU, Civil Engineering	2011
MSc	METU, Civil Engineering	2006
BSc	METU, Civil Engineering	2003
High School	Yıldırım Beyazıt A.L.	1999

AWARDS

METU Graduate Courses Performance Award, **2005 – 2006**
Graduate School of Natural and Applied Sciences, Middle East Technical University

WORK EXPERIENCE

Year	Place	Enrollment
2003-Present	METU, Civil Engineering	Research Assistant

PUBLICATIONS

Journal Papers in Science Citation Index:

Ertugrul, O. L., Trandafir, A. C., "Reduction of Lateral Earth Forces Acting on Rigid Non-Yielding Retaining Walls by EPS Geofoam Inclusions", ASCE Journal of Materials in Civil Engineering, doi:10.1061/(ASCE)MT.1943-5533.0000348 (in press)

Ertugrul, O. L., Trandafir, A. C.,Ozkan, M.Y., “Reduction of Lateral Earth Forces by EPS Geofoam Inclusions (in Turkish)”, İMO Teknik Dergi (accepted for publication)

Peer reviewed Conference Proceedings:

Ertugrul, O.L., Trandafir, A.C., “Reduction of Lateral Earth Forces Acting on Yielding Flexible Retaining Walls By EPS Geofoam Inclusions”, Geocongress 2012, accepted for publication

Trandafir, A.C., Ertugrul, O.L., “Earthquake Response of a Gravity Retaining Wall with Geofoam Inclusion”, Proceedings of the Geo-Frontiers 2011 conference, March 13-16, 2011, Dallas, Texas, pp. 3177-3185, (doi 10.1061/41165(397)325)

Ertugrul,O.L., , Ulgen,D., “ATTENUATION OF TRAFFIC INDUCED GROUND BORNE VIBRATIONS DUE TO HEAVY VEHICLES”,Paper No:2.27, Fifth International Conference on Recent Advances in Geotechnical Earthquake Engineering and Soil Dynamics and Symposium in Honor of Professor I. M. Idriss, San Diego, CA, USA – May 24-29, 2010

Ertugrul,O.L., Ozkan, M.Y., Trandafir, A.C., “Rijit Istinat Duvarlarina Etkiyen Yanal Zemin Basinclarinin EPS Kopuk Kullanimi ile Azaltilmasi”, Zemin Mekanigi ve Temel Muhendisligi 13. Ulusal Kongresi , sf. 555-562, Istanbul, Turkiye – 30 Eylul-1 Ekim 2010

Ertugrul,O.L., Ozkan,M.Y. , Ulgen,D., “Foundation Design for Isolating a Precision Instrument from Ground- Borne Vibration”,EVACES09, Experimental Vibration Analysis for Civil Engineering Structures, October 14-16 2009, Wroclaw,Poland

Ertugrul,O.L., Bakır, B.S. , Akkar, S., “Analysis of subway induced vibrations and investigation of preventive meausres for a building structure”, COMPDYN2009, Eccomas Thematic Conference on Computational Methods in Structural Dynamics and Earthquake Engineering,Rhodes ,Greece,22-24 June 2009

Ertugrul,O.L., Ozkan,M.Y. , Ulgen,D., “Measurements and Numerical Modeling of Ground-borne Vibrations Caused by Heavy Vehicle Traffic”, 2nd International Conference on New Developments in Soil Mechanics and Geotechnical Engineering, pp. 274-281, 28-30 May 2009, Near East University, Nicosia, North Cyprus

Ertuğrul,Ö.L., Özkan,M.Y., “Dinamik yer hareketi özelliklerinin istinat duvarlarının sismik davranışına etkisi”, Zemin Mekaniği ve Temel Mühendisliği Onikinci Ulusal Kongresi 16-17 Ekim 2008,Sayfa 195-204, Selçuk Üniversitesi, Konya

Ertugrul,O.L., Ozkan,M.Y. , Saglam,S., “Excitation and Flexibility Effects on The Dynamic Response of Cantilever Earth Retaining Walls”, ASCE Proceedings of the Geotechnical Earthquake Engineering and Soil Dynamics IV Congress, GSP 181, 2008, ASCE Conf. Proc. doi:10.1061/40975(318)150 Sacramento; USA

Ertuğrul,Ö.L., Çalışan,O , Özkan,M.Y. , “İstinat Duvarlarının Dinamik Yükler Altındaki Davranışının Sonlu Elemanlar Metodu Kullanılarak Modellenmesi “ , Sayfa 343-358, TMMOB İnşaat Mühendisleri Odası 2. Geoteknik Sempozyumu, Kasım 2007, Adana, Türkiye

Ertugrul, Ö. L., Çalışan, O., Özkan, M. Y., Modelling Retaining Walls Under Dynamic Loads by Finite Element Method (in Turkish) , Yapı Dünyası, June, 2007, pp 7-13.